

Finite Element Analysis of RC beams
retrofitted with Fibre Reinforced Polymers

Giuseppe Simonelli

27/11/2005

Acknowledgements

I wish to thank Professor Luciano Rosati for his unconditional trust and guidance.

Dr. Giulio Alfano for following me strictly during the entire duration of this course.

My Director in the Mott MacDonald Group, Dr. Paul Norris for his encouragement and for giving me extra leaves to finish this work.

FEA systems for providing me a free copy of LUSAS to carry out my research.

My brother Fulvio and my parents for sorting out all the administration that I could not handle long distance.

And my girlfriend Francesca for at least a thousand of reasons.

Giuseppe Simonelli

London, 27-11-2005.

Contents

1	The use of FRPs in the strengthening of RC beams	13
1.1	Introduction	13
1.2	Materials	16
1.2.1	Fibres	16
1.2.2	Fabrics	18
1.2.3	Plates	18
1.2.4	Resins	19
1.2.5	Adhesives	21
2	A finite element model for RC beams retrofitted with FRP	23
2.1	The behaviour of RC beams retrofitted with RC	24
2.1.1	Failure modes of RC beams retrofitted with FRP	25
2.1.2	Interaction concrete-FRP	31
2.2	Finite Element Modelling of Reinforced Concrete	35
2.2.1	Introduction	35
2.2.2	Finite elements for concrete	36
2.2.3	Representation of reinforcing steel	36
2.3	Finite element models for reinforced concrete beams retrofitted with FRP	44
2.3.1	General models for beams	45
2.3.2	Models for the investigation of specific aspects	47
3	Modelling of concrete	49
3.1	Introduction	49
3.2	Mechanical behaviour of concrete	50
3.3	Mathematical model for concrete	58
3.3.1	Elastoplastic model for concrete	62
3.4	A simplified elasto-plastic model	73
3.4.1	The Menetrey-Willam concrete model	73
3.5	Solution procedure for J_3 plasticity	80
3.5.1	Introduction	80

3.5.2	Continuum formulation of the elasto-plastic problem	82
3.5.3	Stress computation	84
3.5.4	The consistent tangent operator	86
3.5.5	Assemblage of \mathbb{G}^{-1}	94
3.5.6	Specialization of the 3D return mapping to the plane stress case	98
3.5.7	Application to the Menetrey Willam material model.	109
3.6	Further simplified models for plain concrete	111
3.6.1	Damage concrete model	112
3.6.2	Cracking models	113
4	Interfaces steel/concrete and FRP/concrete	121
4.1	Introduction	121
4.2	Interface elements	123
4.2.1	INT4 element	125
4.2.2	INT6 element	129
4.3	Interface steel concrete	129
4.4	Interface FRP/concrete	136
4.4.1	Elastic approaches	136
4.4.2	Cohesive models	142
5	Modelling of cracking of concrete	153
5.1	Introduction	153
5.2	Models for crack onset and propagation	154
5.2.1	Overview	154
5.2.2	Use of the smeared crack concept for modelling lo- calised cracks.	155
5.2.3	Finite element analyses to model localised cracking	163
6	Applications	179
6.1	Introduction	179
6.2	Numerical results	180
6.2.1	Material properties	181
6.2.2	Two-dimensional Finite-element models	183
6.2.3	Three-dimensional Finite-element models	196
6.3	Conclusions	199

Introduction

Fibre reinforced polymers (FRP) have been used for many years in the aerospace and automotive industries. In the construction industry they can be used for cladding or for structural elements in an highly aggressive environment. These materials are now becoming popular mostly for the strengthening of existing structures. Strengthening of a structure can be required because of change in its use or due to deterioration. In the past, strength would be increased casting additional reinforced concrete or dowelling in additional reinforcement. More recently, steel plates have been used to enhance the flexural strength of members in bending. These plates are bonded to the tensile zone of RC members using bolts and epoxy resins. As an alternative to steel plates, fibre reinforced polymer plates, generally containing carbon fibres, can be used.

Fibre reinforced polymers can be convenient compared to steel for a number of reasons. They are lighter than the equivalent steel plates. They can be formed on site into complicated shapes. The installation is easier and temporary support until the adhesive gains its strength is not required. They can also be easily cut to length on site. Fibres are also available in the form of fabric. Fabrics are convenient instead of plates where round surfaces, like columns, need to be wrapped.

There are a number of advantages in using fibre reinforced polymers. These materials have higher ultimate strength and lower density than steel. The lower weight makes handling and installation significantly easier than steel. Works to the underside of bridges and building floor slabs can often be carried out from man-access platforms rather than full scaffolding.

The main disadvantage of externally strengthening structures with FRP materials are the risks of fire and accidental damage. A particular concern for bridges over roads is the risk of soffit reinforcement being ripped off by over height vehicles.

Experience in the long term effectiveness of this kind of intervention is not yet available. This may be perceived as a risk by some engineers and owners.

The materials are relatively expensive but generally the extra cost of the material is balanced by the reduction in labour cost. It is still difficult to find contractors with the appropriate expertise for the application of FRP. The quality of the workmanship is essential in this strengthening technique as will be seen later on.

Lack of design standards is another disadvantage. However many countries, including Italy, are developing standards and guidance manuals.

The subject of this dissertation is the numerical analyses of RC structural elements strengthened in the way described above.

The finite element method has been chosen as a basic framework for the analyses.

The main aim was to make the most effective use of the algorithms currently available for the numerical non linear analysis and to improve them, where possible, in order to reduce the number of hypothesis conditioning the results. Such results can then support the interpretation of experimental data and can be used to determine quantities that cannot be easily measured in laboratory tests.

The analysis have been carried out by using the finite element code LUSAS, widely used in both the scientific research and the design industry. However, it has been necessary to develop an enhanced solver in order to use an advanced elasto-plastic isotropic constitutive models with a yielding criterion dependent upon the three invariant of the stress tensor and kinematic isotropic hardening.

The numerical results have been used to clarify the key differences between ordinary reinforced concrete structures and reinforced concrete structures retrofitted with fibre reinforced polymers and to derive conclusions for applications.

The finite element analysis of reinforced concrete structures can be carried out using several models according to the purpose of the research and the size of the control volume relevant for the specific application. For example the analysis could be either used to calculate the deflections on the whole structure under a given loading condition or to investigate the local effects in a particular area of the structure. In the first case we can adopt a model that describes the overall stiffness of the reinforced concrete, either cracked or not, while in the second case we may find convenient to understand where the cracking will occur, how it will develop and to compute the distribution of stresses between concrete and steel and concrete and FRP. In general the overall behaviour of a structure can be successfully investigated using structural elements such as beams, shells, trusses. Their use will limit the computational onus and simplify the definition of the structure. When it comes to investigate a reduced volume of a bigger structure, solid elements

combined if necessary with structural elements are more appropriate. This is the case for our analyses as the focus is on what happens within a single structural element.

The main structural material for the systems under investigation is concrete. Concrete gives a defined shape to the structural elements and the loads are, in fact, applied directly to the concrete. The standard and FRP reinforcement, although essential, are auxiliary components. Correct modelling of the nonlinear behaviour of concrete is therefore essential. The mechanical behaviour of concrete has been investigated worldwide and today there is a general agreement among researchers on its characteristic properties [68, 39, 60, 63, 73, 120, 121, 111, 124, 125, 126, 132]. There are models to describe almost every single mechanical property of the concrete along every kind of load path. The most sophisticated ones include elasto-plastic constitutive laws with complex hardening laws, non-associative flow-rules, post yielding softening.

However these models can not be easily used within a finite element code and simplified models have been developed to take into account only the particular aspects relevant to each specific application.

Several LUSAS material models have been tested for modelling of plain concrete. Besides, a further step has been made creating in LUSAS a model that includes a more advanced constitutive law. The model is an elasto-plastic isotropic model with kinematic and isotropic hardening. Isotropy implies that the yield function depends only on the three invariants of the stress tensor. However, for many materials, this function depends only upon the first and second invariants. The dependence upon the third invariant of yield functions suitable for concrete introduces further complications. These complications have been effectively overcome by using methods recently developed and described in [90, 95, 97]. Use is made of characteristic properties of the rank-four tensors obtained as sum of dyadic and square products rank two symmetric tensors. These properties have been used for the inversion of a rank-four tensor \mathbb{G} required at every Gauss point at every iteration of every increment of the solution of the nonlinear problem. The above tensor is also required for the assemblage of a consistent tangent operator, useful to speed up the computation by exploiting the quadratic convergence rate of the Full Newton method.

The problem was originally resolved for the three dimensional case and the method can be easily adapted to the plane strain case.

The plane stress case is more complex so as to make it common practice to re-formulate the constitutive law in two-dimensions rather than deriving the solution from the three dimensional formulation.

However a general method to obtain the solution for the plane stress

elasto-plastic problem from the three-dimensional one has been recently developed [97] and has been used to implement the plane stress problem in LUSAS.

The finite step integration algorithm and the consistent tangent operator used in the method keep the formal aspect of the 3D case and only some tensor variables must be specialized. The three-dimensional formulation of the yielding function is used. Following these methods FORTRAN code has been produced to introduce the desired constitutive law in LUSAS. These routines can be applied to any isotropic yielding function; the properties of the specific yielding function are used in a single routine that is used for all the cases (full three-dimensional, plane strain, plane stress). Little modification of this routine is required to change the yield criterion. The calculation of the consistent tangent modulus has been codified, as well, to improve the convergence of the iterative process for the solution of the non-linear problem. The applications presented in this work are based on the Menetrey-William yielding function, that has been specifically derived for concrete [68, 39]. In particular, as the confining stresses increase, the shape of the Menetrey-William yield surface in the deviatoric plane changes from triangular to circular, in accordance with the experimental results (this implies the dependence upon the third stress tensor invariant). The criterion was obtained by modifying the famous Hoek and Brown criterion that was formulated for rocks and depends upon three parameters measurable by uni-axial compression, uni-axial tension and equi-bi-axial compression tests. These parameters can be specialized to obtain other criteria such as Huber-Mises, Drucker-Prager, Rankine, Leon, Mohr-Coulomb. Most of these criteria are available in the LUSAS material library, therefore the results obtained with the new routines have been validated by comparison with results obtained with the material models in the library. This test proved the new routine very efficient in terms of accuracy and convergence performances.

A very important aspect in the modelling of RC beams retrofitted with FRP is the representation of the interfacial behaviour between the different materials. Correct modelling of the interface FRP/concrete is necessary as debonding of the FRP is a typical failure mode for these systems. Moreover debonding is affected by cracking of concrete. To allow the cracks to open it is necessary to model relative displacements between concrete and reinforcement. This is possible by mean of special *interface* elements or *joint* elements. Other researchers have demonstrated that the former provide better results, therefore we have introduced interface elements in our model. Among the several constitutive models available for this kind of elements, we have adopted a cohesive-zone model.

Starting from the laboratory observations on this interface [34, 67, 79,

80, 105, 134] a cohesive model has been established. With the above model a closed form solution for the simple case of a pull off test has been derived. The numerical implementation of the interface model by means of interface elements has been, then, validated against the closed form solution, yielding excellent accordance.

The cohesive model has been successfully used in the more general and complex case of an RC beam retrofitted with FRP. Good results have been obtained managing to follow the delamination of the FRP process up to complete debonding of the reinforcing plates. Finite element analysis in conjunction with experimental data published in the literature [131] have also been used to test the robustness of the formulas given in the design guidance for the determination of the FRP/concrete interface parameters [34].

The behaviour at the interface, as mentioned, is strongly influenced by the localization of stresses due to cracking or interruption of the composite at the end of the plates. The non-uniform distribution of transverse stresses in the fibre sections appears to be relevant as well [12, 101, 129].

Because cracking is important in the analysis of the RC beams retrofitted with FRP, it has to be conveniently included in the models.

For the cases where the stress local distribution is not critical, there are models based on a uniform distribution of cracks (smeared) within a volume of cracked concrete [73, 65, 60, 58]. In this volume, assumed it is big enough to comprise several cracks, we calculate average stress and strain values taking also into account the reinforcement interaction with the concrete. In this approach cracking is reduced to a constitutive problem.

These methods have been enhanced by researchers to help local concentration of non-elastic strains and consequential stress release within narrow bands [15, 16, 17, 19, 53, 54, 88, 87, 102, 45, 35]. Basically the cracks are modelled by a sudden local stiffness loss in a band of a width comparable with the crack width. If the mesh is such to have elements of a size comparable with the crack opening, such approach is equivalent to discrete crack modelling, obtained again operating exclusively on the constitutive law for the base material. There are also methods to remove the mesh size dependency in the solution of these kind of problems [19, 53, 45, 88].

For applications to reinforced concrete beams retrofitted with FRP, the local effects at the interfaces are critical and the modelling must feature discrete cracking. Initially, the problem has been tackled by inserting preset cracks in the finite element mesh (this approach has been used also by other researches in the past [83]). This approach is justified as the crack pattern of the beams investigated was known from experiments and as the main focus was rather on the interfacial behaviour between FRP and concrete than on

the onset and propagation of cracking.

Methods for the automatic simulation of crack formation within a volume of plain concrete have also been tested. It has been found that in cases where the stress distribution within the volume is inherently uneven and a few dominant cracks govern the response, the methods are fairly effective. In the case of uniformly distributed stresses and under the distribution action of reinforcement elements, the stiffness reduction due to cracking fails to localise within narrow bands and inelastic strains tend to be spread uniformly over the analysis domain. The latter results in wrong prediction of the behaviour at the interface and makes the preset crack approach more effective. Localised crack modelling by use of a suitable constitutive law has been, however, successfully used for the prediction of failure mechanisms like covercrete debonding and failure due to plate tip shear crack propagation.

All the important aspects discussed have been represented in a number of finite element models (two and three dimensional) used to define the most convenient strategy for the analysis of the systems under investigation. The numerical results are in good accordance with experimental ones. The numerical data obtained from the analysis are obviously more comprehensive than the data from laboratory tests due to the limited number of physical measurement possible in an experimental test. The extra information gained has been used to get a better insight into the behaviour of these structures.

Chapter 1

The use of FRPs in the strengthening of RC beams

1.1 Introduction

Fibre reinforced polymers (FRP) have been used for many years in the aerospace and automotive industries. In the construction industry they can be used for cladding or for structural elements in an highly aggressive environment. These materials are now becoming popular mostly for the strengthening of existing structures. Strengthening of a structure can be required because of change in its use or due to deterioration. In the past, strength would be increased casting additional reinforced concrete or dowelling in additional reinforcement. More recently, steel plates have been used to enhance the flexural strength of members in bending. These plates are bonded to the tensile zone of RC members using bolts and epoxy resins. As an alternative to steel plates fibre reinforced polymer plates, generally containing carbon fibres, can be used.

Fibre reinforced polymers can be convenient compared to steel for a number of reasons. They are lighter than the equivalent steel plates. They can be formed on site into complicated shapes. The installation is easier and temporary support until the adhesive gains its strength is not required. They can also be easily cut to length on site. Fibres are also available in the form of fabric. Fabrics are convenient instead of plates where round surfaces, like columns, need to be wrapped. Typical applications are shown in Figure 1.1.

FRP can be applied to columns, slabs, beams, shear walls or to frame openings. They can be used to improve either the strength or the stiffness of structural elements. In most cases it is only practical to increase the live load capacity of a structure. In some situations some of the dead load can

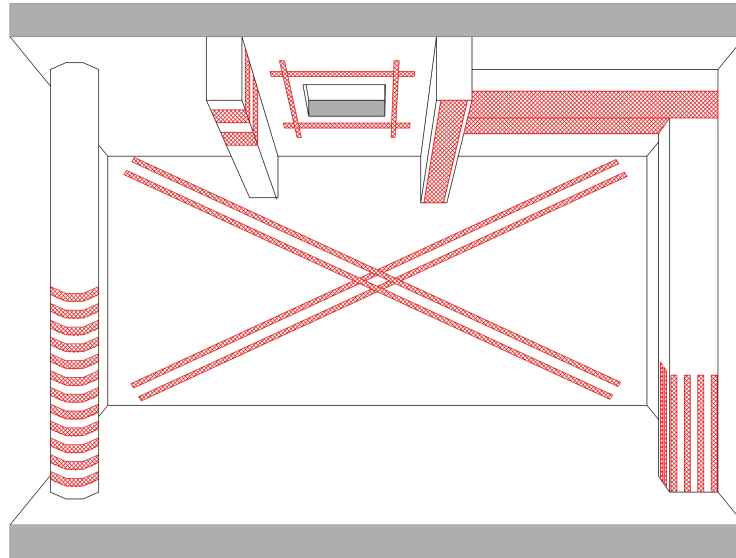


Figure 1.1: Typical applications of FRP in the strengthening of RC structures

be relieved by jacking or propping the elements before the application of the FRP plates or fabrics. This type of strengthening works is based on the following three principles:

- Increase of the bending capacity of beams and slabs by the addition of fibre composite materials to the tensile face
- Increase the shear capacity of beams by adding fibre composite materials to the sides in the shear zones
- Increase the axial and shear capacity of columns by wrapping fibre composite materials around the perimeter

There are a number of advantages in using fibre reinforced polymers. These materials have higher ultimate strength and lower density than steel. The lower weight makes handling and installation significantly easier than steel. Works to the underside of bridges and building floor slabs can often be carried out from man-access platforms rather than full scaffolding. Steel plates requires heavy lifting gear and must be held in place while the adhesive gain strength. This can be done by bolting the steel to the concrete. Bolts are usually used in the application of steel plates as a remedy to end peeling effects. The application of FRP is more like the application of wall paper.

Once it has been properly rolled to remove the entrapped air and the adhesive in excess, it may be left unsupported. Bolts should not be used as they can considerably weaken the materials. If used Additional cover plates should be bonded on. Besides, because there is no need to drill into the structure to fix bolts or other mechanical anchors there is no risk of damaging the existing reinforcement. Fibre reinforced materials are available in very long lengths while steel plates are generally limited to 6 m lengths. Their flexibility also simplifies the installation. Steel plates have their own shape and non-negligible flexural stiffness. Therefore when applied to a structural element of a slightly different shape, due to construction tolerances, initial stresses are induced in the plates and in the bonding system (resin/bolts). For curved surfaces the material needs to be bent in advance. They also need a corrosion protection system (generally coating). FRP comes in very thin layers with negligible flexural stiffness and can easily follow a curved profile without any pre-shaping. Also irregularities of the concrete surface can easily be taken up. Overlapping where strengthening is required in more than one direction is not a problem either, due to the small thickness of the plates. The material is durable and if damaged can be easily repaired by adding an additional layer. In terms of environmental impact and sustainability, studies have shown that the energy required to produce FRP materials is less than for conventional materials. Because of their light weight, the transport of FRP materials has minimal environmental impact.

The main disadvantage of externally strengthening structures with FRP materials are the risks of fire and accidental damage. A particular concern for bridges over roads is the risk of soffit reinforcement being ripped off by over-height vehicles.

Experience in the long term effectiveness of this kind of intervention is not yet available. This may be perceived as a risk by some engineers and owners.

The materials are relatively expensive but generally the extra cost of the material is balanced by the reduction in labour cost. It is still difficult to find a contractor with the appropriate expertise for the application of FRP. The quality of the workmanship is essential in this strengthening technique as will be seen later on.

Lack of design standards is another disadvantage. However many countries, including Italy, are developing standards and guidances.

1.2 Materials

Composites materials are formed of two or more materials (phases) of different nature and macroscopically distinguishable. In fibre composites the two phases are high performance fibres, and an appropriate resin.

The mechanical properties of the composites are mainly dependant on the type, amount and orientation of the fibres. The role of resin is to transfer stresses to and from the fibres. It also provide some protection from the environment.

This section provide a general introduction on the fibres and resins used for strengthening. For more information refer to the trade literature.

1.2.1 Fibres

Fibres typically used for strengthening applications are glass, carbon, or aramid (also known as Kevlar). Each is a family of fibres rather than a particular one. Typical values for the properties of fibres are given in Table 1.1. These values are for the fibres only and the correspondent values for the composite are significantly lower. All the fibres are linear elastic to failure with no significant yielding.

The selection of the type of fibre to be used for a particular application will depend on factors like the type of structure, the expected loading, the environmental conditions, and so on.

Carbon fibres

Carbon fibres are used for the fabrication of high performance composites and are characterised by high value of stiffness and strength. Failure is brittle with low energy absorption. They are not very sensible to creep and fatigue and exhibit negligible loss of strength in the long term. Fibres have a crystalline structure similar to graphite's one. Graphite's structure is hexagonal, with carbon atoms arranged in planes held together by Van Der Waals forces. Atoms in each plane are held together by covalent bonds, much stronger than Van Der Waals forces, resulting in high strength and stiffness in any direction within the plane. The modern technology of production of carbon fibres is based on the thermal decomposition in absence of oxygen of organic substances, called precursors. The most popular precursors are polyacrilonitrile and rayon fibres. Fibres are stabilised first, through a thermal treatment inducing a preferential orientation of their molecular structure, then they undergo a carbonisation process in which all components other than carbon

are eliminated. The process is completed by a graphitization during which, as the word indicate, the fibres are crystallised in a form similar to graphite. Fibres with a carbon content higher than 99% are sometime called graphite fibres.

Aramid fibres

Aramid fibres are organic fibres, made of aromatic polyamides in an extremely orientated form. Introduced for the first time in 1971 as “Kevlar”, these fibres are distinguished for their high tenacity and their resistance to manipulation. They have a strength and stiffness in between those of glass and carbon fibres. Their compression strength is usually around 1/8 the tensile one. This is due to the anisotropy of the structure of the fibre, because of which compression loads trigger localised yielding and buckling resulting in the formation of kinks. This kind of fibres undergo degradation under sunlight, with a loss of strength of up to 50%. They can also be sensitive to moisture. They exhibit creep and are fatigue sensitive. The technology of fabrication is based on the extrusion at high temperature of the polymer in a solution and subsequent rapid cooling and drying. The synthesis of polymer is done before the extruding equipment by using very acid solutions. It is finally possible to apply a thermal orientation treatment to improve the mechanical characteristics.

Glass fibres

Glass fibres are widely used in the naval industry for the fabrication of composites with medium to high performance. They are characterised by high strength. Glass is made mainly of silica (SiO_2) in tetrahedral structure (SiO_4). Alluminium and other metal oxides are added in different proportions to simplify processing or modify some properties. The technology of production is based on the spinning of a batch made essentially of sand, alumina and limestone. The components are dry mixed and melted at 1260 °C. Fibres are originated from the melted glass. Glass fibres are less stiff than carbon and aramid fibres and are sensitive to abrasion. Due to the latter care must be used when manipulating fibres before impregnation. This kind of fibres exhibit non negligible creep and are fatigue sensitive.

Fibre	Tensile strength (N/mm²)	Modulus of elasticity (kN/mm²)	Elongation (%)	Specific density
Carbon: high strength	4300-4900	230-240	1.9-2.1	1.8
Carbon: high module	2740-5490	294-329	0.7-1.9	1.78-1.81
Carbon: ultra high module	2600-4020	540-640	0.4-0.8	1.91-2.12
Aramid	3200-3600	124-130	2.4	1.44
Glass	2400-3500	70-85	3.5-4.7	2.6

Table 1.1: Typical fibre properties

Other type of fibres

There exist other type of fibres that are seldom utilised in the construction industry. Examples are: fibres of boron, alumina and silica carbide.

1.2.2 Fabrics

Fabrics are available in two basic forms:

- Sheet material, either fibres (generally unidirectional, though bi-axial and tri-axial arrangements are available) on a removable backing sheet or woven rovings.
- Fibres pre-impregnated with resin (“prepeg” material), which is cured once in place, by heat or other means.

The selection of the appropriate fabric depends on the application.

The properties of the sheet materials depend on the amount and type of fibre used. An additional consideration is the arrangement of fibres; parallel lay gives unidirectional properties while a woven fabric has two-dimensional properties. In woven fabrics, perhaps 70% of the fibres are in the ‘strong’ direction and 30% in the transverse direction. It should be noted that the kinking of the fibres in the woven material significantly reduces the strength. The thickness of the material can be as low as 0.1 mm (with the fibres fixed to a removable backing sheet) and is available in widths of 500 mm or more.

1.2.3 Plates

Unidirectional plates are usually formed by the pultrusion process. Fibres in the form of continuous rovings, are drawn off in a carefully controlled pattern through a resin bath which impregnate the fibres bundle. They are then pulled through a die which consolidates the fibres-resin combination and forms the required shape. The die is heated which sets and cure the resin,

allowing the completed composite to be drawn off by reciprocating clamps or a tension device. The process enables a high proportion of fibres (generally about 65%) to be incorporated in the cross section. Hence in the longitudinal direction, relatively high strength and stiffness are achieved, approximately 65% of the relevant figures in Table 1.1. Because most, if not all, of the fibres are in the longitudinal direction, transverse strength will be very low.

Plates formed by pultrusion are 1-2 mm thick and are supplied in a variety of widths, typically between 50 and 100 mm. As pultrusion is a continuous process, very long lengths of material are available. Thinner material is provided in the form of a coil, with a diameter of about 1 m. It can be easily cut to length on site using a common guillotine. Plates can also be produced using the prepeg process, which is widely used to produce components for the aerospace and automotive industries. Typically plates have a fiber volume fraction of 55% , and can incorporate 10% fibres (usually glass aligned at an angle of 45° to the longitudinal axis) to improve the handling strength. Lengths up to 12 m can be produced, with a thickness being tailored to the particular application. Widths up to 1.25 m have been produced and thickness up to 30 mm.

1.2.4 Resins

The most popular types of resins used for the production of FRP are polymeric thermo-hardening resins. These are available in a partially polymerised form and are liquid or creamy at ambient temperature. Mixed with an appropriate reagent they polymerise until they become a solid glassy material. Because the reaction can be accelerated heating up the material, these resin are also termed thermo-hardening resins. The advantages of their use are: low viscosity at the liquid state resulting in easy of fibre impregnation, very good adhesive properties, the availability of types capable of polymerising at ambient temperature, good chemical resistance, absence of a melting temperature, etc. The principal disadvantages, are, on the other hand, related to the range of serviceability temperatures, with an upper limit given by the glassy transition temperature, brittle fracture properties and moisture sensitivity during application.

The most common resins used in the field of civil engineering are epoxy resins. In some cases polyester or vinyl resins can be used.

If the matrix is mixed with the fibres on site (if fabrics are used) specialist contractors should be appointed.

Polymeric materials with thermo-plastic resins are also available. The have the advantage the can be heated up and bent on site at any time. This materials are more convenient for the production of bars to be embedded in

concrete like ordinary reinforcement.

Epoxy resins

Epoxy resins have good resistance to moisture and to chemicals. Besides, they have very good adhesive properties. Their maximum working temperature is depends on the type but is typically below 60 oC. However epoxy resins with higher working temperatures are available. Usually there are no limits on the minimum temperature.

The main reagent is composed by organic liquids with low molecular weight containing epoxy groups, rings composed by two atoms of carbon and one atom of oxygen.

The pre-polymer of the epoxy is a viscous fluid, with a viscosity depending on the degree of polymerisation. A polymerising agent is added to the above mix to solidify the resin. This can be done at low or high temperatures depending on practicalities and on the final properties desired.

Polyester resins

Polyester resins are characterised by a lower viscosity compared to epoxy resins. However, chemical resistance and mechanical properties are not as good as for epoxy. Polyesters are polymers with high molecular weight with double bonds between carbon atoms $C=C$, capable of reacting chemically. At ambient temperature the resin is usually solid. To be used, a solvent must be added. The latter also reduces the viscosity of the resin and facilitate the impregnation of the fibres.

The reaction is exothermal and does not generate secondary products.

Solidification can happen at low or high temperatures depending on practicalities and on the final properties desired.

Other resins

The intrinsic limits of thermo-hardening resins, described above (in particular the limited tenacity), the low service temperatures and the tendency to absorb moisture from the environment, have lead in recent years to the development of thermo-plastic resins.

These resins are characterised by their property of softening when heated up to high temperatures.

The shape of the components can be, therefore modified after heating.

Even though their use in the civil engineering field is quite limited at the moment, their use has been proposed for the production of reinforcement bars similar to the ordinary steel ones.

They have higher tenacity than epoxy and polyester resins and generally can withstand higher temperatures. Besides they are more resistant to environmental agents.

The main limitation for their application is the high viscosity that render difficult the impregnation of the fibres.

There are also special resins developed for aggressive environment and high temperatures. They are mainly vinyl-ester resins with intermediate properties between polyester and epoxy resins.

Finally, Inorganic matrices can be used. These can be cementitious, ceramic, metallic etc. Their use in civil engineering, though, pertains areas other than the retrofitting of structural elements.

1.2.5 Adhesives

FRP are bonded to the structural elements chemically through adhesives. Chemical bonding is the most practical because it does not induce stress concentrations, is easier than mechanical devices to be installed and it does not damage neither the base material nor the composite. Some disadvantages will be discussed when the mechanical behaviour of interfaces realised this way will be addressed, later on.

The most suitable adhesives for composite materials are epoxy resin based adhesives. The adhesive is made of a two component mix. The principal component is constituted of organic liquids containing epoxy groups, rings composed of an oxygen atom and two carbon atoms. A reagent is added to the above mix to obtain the final compound.

The adhesive adhere to the materials to be bonded through interlocking and the formation of chemical bonds.

The preparation of the surfaces to be bonded plays a key role for the effectiveness of the adhesive. Treatment of the surfaces are aimed to have a clean surface, free of any contaminant like: oxides, powders, oils, fat and moisture. The surface is then generally treated chemically to achieve stronger chemical bonds and always mechanically to obtain a rough surface for interlocking. Cleaning is performed using solvents and abrasion through sand blast is used for preparation of a rough surface. The surface of pre-impregnated laminates is often ready for the application of the adhesive and protected by a tape to be removed right before the application.

For porous surfaces, a priming coat may be required, which must be compatible with the adhesive. The method of application of the adhesive will depend on particular system and structural configuration. Generally hand methods are used., though machines have been developed for wrapping columns. For plates, a layer of adhesive is usually applied to the plate while

fabrics are usually pre-impregnated. The materials are then applied to the prepared concrete. Sufficient pressure is applied with rollers to ensure a uniform adhesive layer and to expel any entrapped air.

For complex surface geometries where preformed plates cannot conform, vacuum-assisted resin infusion can be used to form the composite in situ. The fibres are applied to the structure dry. The area is sealed with a rubber sheet and vacuum used to draw in the resin.

Chapter 2

A finite element model for RC beams retrofitted with FRP

For a rational and safe design of any strengthening work an appropriate analysis method is required. The choice of such a method is not uniquely determined and depends largely on the purpose of the analysis. Usually in engineering simple and conservative models are sought. Simple models have two main advantages: the first one is obviously the easy of use, but engineers are also interested in having models not very sensitive to parameters difficult to determine with the required accuracy and reliability.

The intrinsic complexity of structural problems implies that simple models are possible only if strong assumptions are made. This can be done only if there are sufficiently wide experimental grounds to prove that they are acceptable. Also assuming something arbitrarily implies that the model is stripped off of all the features that are deemed not to be relevant in the calculation of the quantities of interest. This means that even though the results calculated are sufficiently accurate the model is not encompassing all the aspects of the physics of the problem and some aspects are missed out or included together with others on an empirical basis. Besides different models are usually used to calculate different quantities pertaining the same structural element.

As an example, when we calculate the ultimate bending capacity of a section of reinforced concrete we do not bother modelling the behaviour of the interface between the steel bars and the concrete assuming perfect adherence. The consequences of this assumption are only taken into account limiting the failure strain of the reinforcement steel. If we want to calculate spacing and width of cracks we must resort to models including the bond slip behaviour at the interface.

If the model is to be used for a more thorough understanding of the

structural behaviour of the element being analysed or to carry out a design outside the boundaries of the experimentation validating the simplified models, some of the assumption must be removed and consequently the related aspects included realistically.

As the objective of this work is not the determination of a specific quantity but rather the understanding of how RC structures retrofitted with FRP work and what should be included and what not in their analysis, complex and comprehensive models are sought.

In this chapter, the modelling of FRP strengthened structures is discussed with a view to defining a model as close as possible to reality, capable of replacing or integrating laboratory testing for the investigation of the structural behaviour.

In order to do so, the physical problem is described first. Subsequently the models developed are described. Details of the different features included are given in following chapters.

2.1 The behaviour of RC beams retrofitted with RC

The role of the composite in retrofitted structures is similar to that of ordinary steel reinforcement. The composite enhances both the stiffness and the strength of the structural elements.

Methods of analysis for ordinary RC can be easily generalised to include FRP reinforcement. Accordingly the gain in the structural capacity of the strengthened structure is generally significant. However researchers have observed that the real capacity is limited by modes of failure not observed in ordinary RC structures. These failures are often brittle, involving delamination of the FRP, debonding of concrete layers, and shear collapse. Failure can occur at loads significantly lower than the theoretical strength of the retrofit system.

Specific failure criteria are therefore required for the analysis of these structures. To set these out a thorough understanding of the behaviour of these systems is required.

Until now we have referred to structural elements in general as specification of the particular structural element was not necessary. In what follows we will refer to RC beams as this is the structural element addressed by the present study.

2.1.1 Failure modes of RC beams retrofitted with FRP

Failure modes of RC beams retrofitted with FRP fall into six distinct categories Fig 2.1.

The mode of failure marked as a) in figure 2.1 is characterised by yielding of tensile steel followed by rupture of the FRP. This is a brittle failure due to the brittle nature of the FRP rupture but in this case the material is used at its maximum capacity and the failure load can be accurately predicted using strain and stress compatibility equations.

For the mode marked as b) the failure is due to the crushing of concrete in compression. In this case the maximum failure load can be accurately predicted too. Failure is still brittle.

The mode marked as c) is a shear failure mode. A shear crack initiating usually at the tip of the FRP sheets propagate until the beam fails.

Failure often occur when the laminate detaches from the beam ceasing to contribute to its strength. Failures of this type are marked as d) and e) in Fig 2.1. In case d), known as bond split, the entire covercrete is ripped off. This generally happen by formation of a shear crack that propagate along the line of the reinforcement. In case e), known as laminate peeling , the laminate detaches because of the formation and propagation of a fracture along the interface with the concrete. The fracture at the interface is usually a cohesive fracture within the concrete adjacent to the epoxy. This is usually because epoxy is stronger than concrete. In this case the same material is visible on both the fracture surfaces. The fracture can also be an adhesive fracture at the interface between epoxy and concrete. In this case the materials visible on the two fracture surfaces are different. This happen when the face of the concrete has not been properly treated before the application of the epoxy. The fracture could also be at the interface epoxy/FRP for similar reasons.

A mixed type of fracture with irregular surfaces and both the materials visible on both the fracture surface is also possible.

Laminate peeling can initiate at the tip of the laminate (end peeling) where the stiffness of the section changes and tensile forces are transferred into the laminate. Stresses at this location are essentially shear stresses but due to the little but non zero bending stiffness of the laminate, and the eccentric application of the tensile force, normal stresses can arise, activating also mode I delamination.

The stresses originating end peeling arise from the offset in position along the beam between the zero moment location (supports) and the ends of the plates. In practical single-span simply supported bridges, the presence of the bearings at the supports dictates that this offset, though small, is inevitable. Due to this offset, while zero axial strain exist at the (free) ends of the plate,

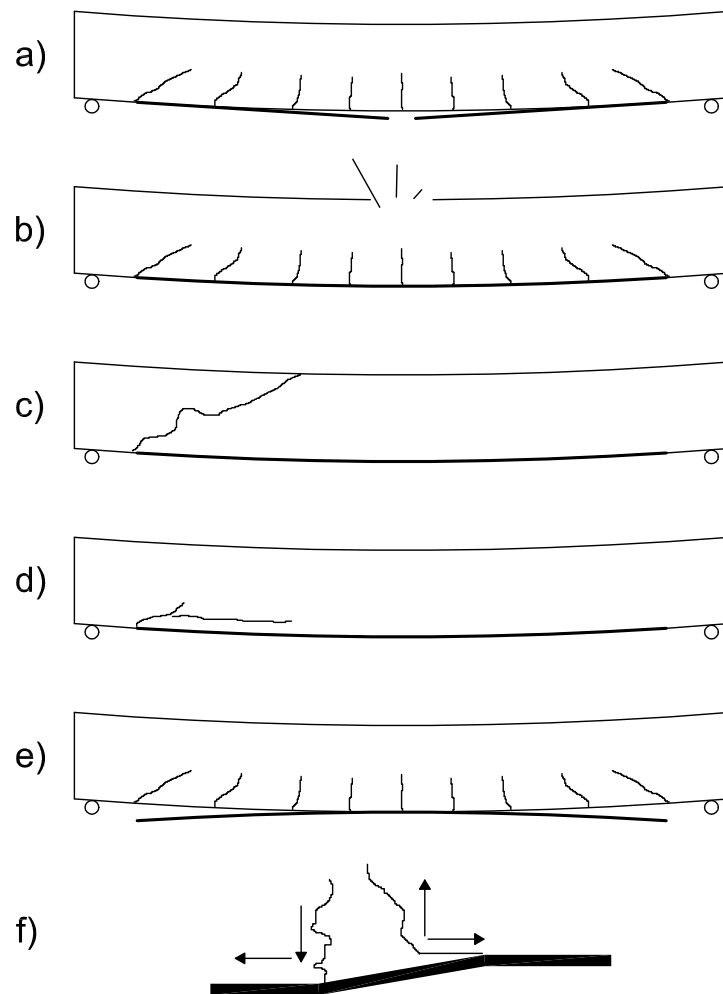


Figure 2.1: Failure Modes in FRP Retrofitted Concrete Beams: (a) Steel Yield and FRP Rupture; (b) Concrete Compression Failure; (c) Shear Failure; (d) Debond of Layer along Rebar; (e) Delamination of FRP Plate; (f) Peeling due to Shear Crack

there are non zero axial strains in the concrete immediately adjacent to the ends of the plate. Due to the shear stiffness of connective adhesive, the plate tries to catch up with the strains in the adjacent concrete by changing its axial strain from zero at the ends to a value comparable to that of the concrete at very short distances in from the ends of the plate. Hence, significant axial stress changes occur in the plates over a short distance from the ends. This requires high local equilibrating bond stresses that are transmitted from the plate through the adhesive to the adjacent covercrete. The free end boundary conditions of the plate also mean that there is zero curvature in the plates at the ends. However, nonzero moments and nonzero curvature exist in the beam at the same location. To develop zero curvature, the ends of the plate must bend away from the beam, as shown in Fig 2.2. This reversed bending of the plate, causes the adhesive to stretch vertically on the covercrete. The maximum pull occur at the end of the plates and decreases inwards. This effect is also exacerbated by the bending induced in the plate by the eccentric action of the interface shear stresses. Thus, end effects in the plate create shear stress concentrations and vertical direct stress concentrations in the covercrete. It is this coexistent stresses that trigger inclined cracking and end peel action in the covercrete attached to the plate. These effects increase as the plate curtailment away from the supports icreaises.

Whereas end peel involves the entire depth of covercrete and propagates from the ends of the plates inwards, another debond mode exists that fractures, in the main, only part of the depth of covercrete and initiates at the toes of flexural cracks in the mid span region of the beam with propagation out to the ends of the plates. This latter mode, termed midspan debond, is illustrated in Figure 2.3 for one initiating flexural crack. As shown in Figure 2.3 (a), the delaminated concrete, adhesive, and plate remain a single unit after debonding, with the remaining covercrete staying an integral part of the original beam. There are two phases to midspan debonding process, namely the initiation phase, inclined cracks form in the covercrete near the toes of flexural cracks Figure 2.3 (b) shows that opening of these inclined cracks induces local bending (or dowel action) of the plate, thereby causing the plate to exert a vertical pull on the adjacent adhesive and covercrete to one side of the inclined crack. This pull eventually fractures a thin layer of covercrete along a roughly horizontal plane. The fractured covercrete is comprised of cement paste and up to 6 mm aggregate , and will henceforth be termed mortarcrete. Note that since the FRP plates used in strengthening applications are typically very thin, the plates are quite flexible under bending in a vertical plane. Hence, propagation of mortarcrete fracture away from the base of the inclined crack due to this local bending action is limited. During the second phase, the debonding process is self propagating.

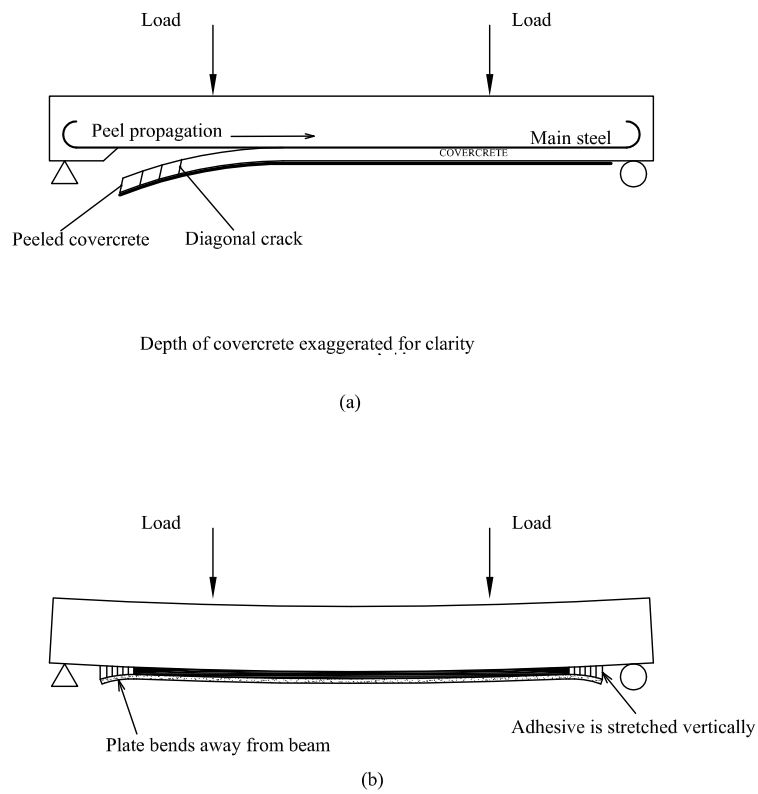


Figure 2.2: End peeling in Plated Concrete Beams: (a) Mode of failure; (b) Mechanism of Development of Vertical Stresses near Ends of Plate

The length of the mortarcrete fracture zone along the beam increases first in a stable, incremental manner with each subsequent increment of load on the beam. Eventually, the mortarcrete fracture process suddenly runs along the remaining bonded length of plate, resulting in complete unzipping of the plate from the beam. The energy released by unzipping is sometimes sufficient to dislodge from the beam the wedges of concrete bounded by the inclined crack and flexural cracks.

As we have seen then, besides the failure types commonly observed in ordinary RC beams, retrofitted beams can fail because transfer of forces between the composite and the concrete is not possible beyond a certain limit and the two structural components separate causing the FRP cease to be effective.

This mode of failure introduces a great deal of complication into the problem because its associated failure load is much more difficult to predict than those associated with crushing of concrete or rupture of the retrofit material.

Even though, with reasonable accuracy, the problem of the interface can be locally cast into a simple set of equations, considerable difficulties arise in the treatment of this aspect due to the influence of cracking of concrete in tension that continuously alter the boundary conditions.

Because of this, failure due to FRP detachment cannot be dealt with by a local stress or strain check at a certain cross section of the beam but requires analysis of the structural element as a whole.

As far as midspan debonding is concerned, currently available guidelines try to overcome this difficulty in a simplified manner introducing a limit on the *maximum* working strain of the composite as a failure criterion to be added to the usual check of the maximum compressive strain in the concrete (0.35%), maximum tensile strain in the steel (1%) and maximum stress in the FRP. The *maximum* tensile strain in the concrete to be used in the check at a given section is the one derived imposing the equilibrium at that section considering perfect adherence between the different materials and the concrete as a no tension material.

Even though this principle is sound, and the limits can be set so as to make the check conservative, it is obviously somewhat coarse and provides little understanding of the behaviour of the system.

Also delamination in the terminal zones of FRP is to be addressed. The typical approach derived by the practice for ordinary reinforced concrete is to make sure that the plates have enough anchorage length to transfer the axial forces from the concrete to the FRP.

This approach suffers from two major shortcomings:

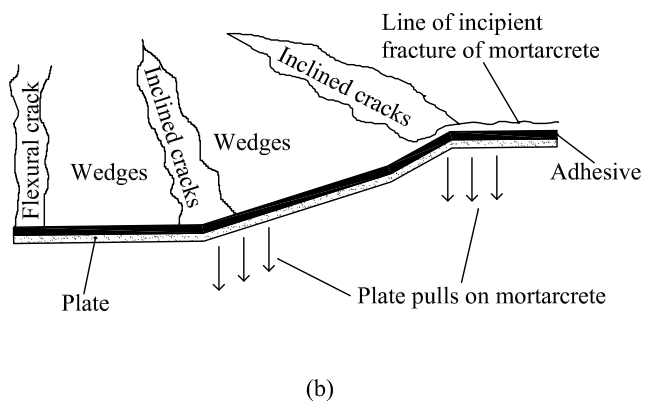
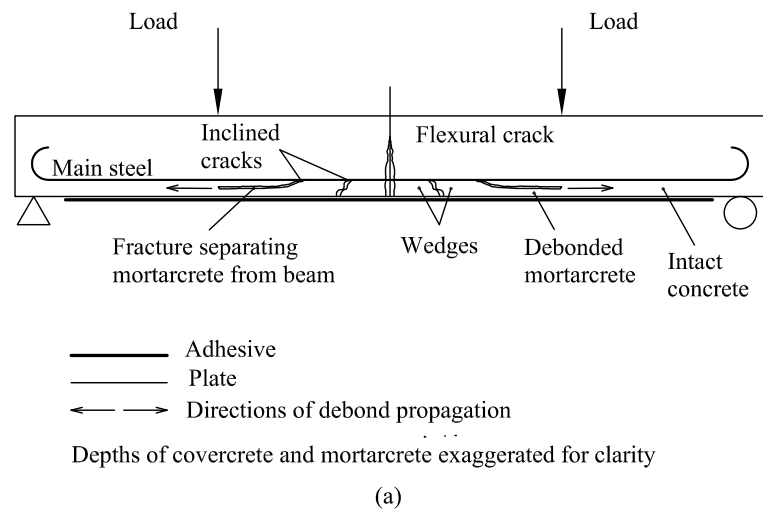


Figure 2.3: Midspan debond: (a) Mode of failure; (b) dowel effect in plate

- differently from ordinary rebars, the maximum force that can be transferred into the FRP plates does not increase indefinitely with increasing anchorage length but reaches a maximum at a specific length and then does not increase anymore
- the effects of the local distribution of stresses are much more important than in the case of the anchorage of ordinary rebars.

As a consequence of this, to predict whether end peeling is likely to occur based on the anchorage length provided to the plate is not as straight forward and reliable as in the case of ordinary rebars. This aspect is discussed in detail in the section on the interface behaviour and the one on the finite element applications carried out.

The behaviour at the interface between the different materials in an RC beam retrofitted with FRP, being to a certain extent an element of novelty with respect to ordinary RC, will be widely analysed in the following chapters. This will require the abandonment of the concept of the section and in general of the beam as opposed to the general solid.

2.1.2 Interaction concrete-FRP

It is informative at this stage to give further explanation of the mechanism of transfer of forces between the concrete and the composite. As this section is intended to be descriptive, only basic equations shall be given to clarify the physics of the problem.

Separation of concrete and FRP is generally referred to, in the literature, as *peeling* or *bond splitting* depending on whether the entire covercrete is involved or not. In the following, when it is intended to make no distinction between the two modes the term delamination will be used.

In two dimensions, two modes of delamination are recognised. They are conventionally named as mode I and mode II. Mode I is associated with normal relative displacements between the two surfaces connected by the interface and mode II is associated with transverse displacements. The two modes are generally coexistent in different proportions.

In the case of the interface FRP/concrete in structural elements in bending mode II is dominant.

Mode II generate shear stresses. These shear stresses are transmitted to the covercrete via the adhesive. Axial equilibrium of an element plate gives:

$$\tau = t_p \frac{d\sigma_{mp}}{dx} = t_p E_p \frac{d\epsilon_{mp}}{dx} \quad (2.1)$$

where τ is the shear stress; and t_p , E_p , σ_p , ϵ_{mp} , x , are the thickness of, the Young's modulus of, mean axial stress, mean axial strain, and distance along the plate respectively. For a linear strain variation through the thickness of the plate, the average strain is that at mid thickness. Hence, 2.1 shows that the shear bond stresses which trigger midspan debond action can be generated by any influence inducing axial stress gradients in the plate. For initiation of debond, one such source of axial stress gradient is tension stiffening, which refers to the axial variation of tensile stress in the concrete teeth between cracks, owing to the bond between the tension reinforcement and the cracked concrete. For equilibrium, axial stress gradients must also exist in the FRP plate bonded onto the cracked concrete, with such stresses diminishing away from the crack faces. During debond propagation, a change exists along the beam from sections with bonded plate to sections with debonded plates. The presence of yielded steel at the debonded sections and elastic steel at bonded sections exacerbates the change. This induces high axial stress gradients along the plate in the transition region between the debonded and the bonded beam sections, which in turn induces further debonding. Hence, the midspan process is self-propagating and can become particularly pronounced after yield of the embedded steel.

The elementary beam formula for the plate to beam shear bond stress is:

$$\tau = \frac{VA_p\bar{y}}{Ib_p} \quad (2.2)$$

where τ =shear bond stress; V =shear force acting on the overall section; A_p = area of the plate section; \bar{y} =distance from the neutral axis of the overall section to the centroid of the plate section; I =second moment of area of the overall section about its neutral axis; and b_p =breadth of the plate.

As it is, under four points bending, the formula erroneously predicts zero shear stresses in the area between the loaded points where shear is null.

The error lies in the fact that 2.2 assumes constant section properties along the beam. As explained, debond shear stresses are generated where sharp changes in beam section occur. If local variations of beam section are taken into account, 2.1 can be used to establish the shear stresses, provided the axial stresses at the mid thickness of the plate is used at each section. If elementary beam theory is used for this purpose, the following applies:

$$\sigma_{mp} = \frac{My_p}{I} \quad (2.3)$$

where σ_{mp} =axial stress at mid thickness of the plate: M =bending moment acting on the section; y_p = distance from the neutral axis of the

section to the mid thickness of the plate; and I =transformed second moment of area of the section.

The variation in section properties would be accounted for by determining the values of I and y_p appropriate to each section. Note that 2.3 is applicable, even if the steel has yielded and the compression concrete is nonlinear, provided that the transformed second moment of area is based on the updated secant moduli of the materials. Application of 2.3 across a flexural crack in a loaded beam gives a step change in axial stress in the plate in going from the uncracked section to the cracked one, which erroneously implies infinite shear bond stresses in accordance with 2.1.

The error occurs because elementary beam theory assumes rigid bond, or full strain compatibility, between the plate and the beam. In practice, the shear deformability of the adhesive allows the plate to slip relative to the beam, thereby generating a more gradual change of axial stress in the plate in travelling from the location of the crack to the adjacent uncracked concrete. In conclusion, any analysis of the midspan debond phenomenon should permit slip between the plate and the concrete through the adhesive and also allow for beam section changes due to cracks. This makes discrete crack modelling more suitable than the smeared one. This point will be further discussed in the following chapters. It is worth to observe that for simply supported beams, end peeling is likely to occur when the following three conditions exist:

- low shear span loading (to generate high plate-to-beam shear bond stresses near the supports)
- curtailment of the plates far from the supports (for the end effects which amplifies the shear bond stresses)
- use of a stiff plate (to attract high bond stresses near plate curtailment)

Midspan debond, by contrast, requires:

- high shear span loading (to generate large moments near midspan)
- plate curtailment very near to supports and thin plates

The latter two conditions are required to minimize end peeling tendencies. In practice uniformly distributed loads can generally be regarded as high shear span loads.

The use of arguments related to the beam theory made above in this section, is a convenient base to understand the more simple aspects of the

interaction concrete/FRP. As anticipated, there are aspects that cannot be treated within the framework of the beam theory and require a more general approach in which the beam is looked at as a two or three-dimensional continuum. As we have seen above, for instance, it is easy to understand why interfacial shear stresses are present in the zero-shear areas, looking at the retrofit structure as a beam with variable stiffness properties, but distribution of these stiffness properties along the beam is not easy to determine.

In the present work a considerable amount of numerical analysis has been carried out to gain more understanding of the interfacial behaviour. The analysis have been performed using the finite element techniques described in the following sections.

The interpretation of the behaviour of the retrofitted system by the use of the beam theory is also useful as results obtained by more general approaches can feed into the former to define convenient simplified models.

We conclude this section with a brief explanation of the local mechanism of transfer of forces between concrete and FRP. As discussed, the transfer of forces between the two materials is due to shear action of the adhesive and a small portion of concrete adjoining the FRP. At low load levels this shear action is elastic and no damage is generated. Increasing the load damage is generated (in the concrete if the adhesive has been selected and applied correctly) and progresses until the material resistance is completely lost. Therefore, the local behaviour of the interface is characterised by an initial increase of shear transfer, with increasing load, followed by a reduction, down to complete separation of the two materials.

If we disregard the distribution of stresses in the direction orthogonal to the axis of the FRP, in the volume of concrete involved in the interfacial behaviour, the interface can be reduced to the surface separating the two materials.

At such level of idealization the behaviour of the interface can be easily described by the means of the relative displacement between the two materials and the local interface stresses associated with it. Describing the behaviour of the interface in terms of the above parameters, it is seen experimentally, that cohesive fracture models are appropriate for the representation of local behaviour of the interface. It has been also shown that different cohesive models do not yield very different results if the same fracture energy G_f is used.

Numerical analysis of the damage of the volume of concrete of which the interface is representative is not practical for the investigation of the behaviour of an entire structural element. However, this type of analysis is very useful for the determination of the appropriate cohesive model and for the determination of the interfacial parameters.

The analytical description of the behaviour of the interface FRP/concrete for both the approaches mentioned in given in detail in the specific section on the interfaces.

Other aspects of the interfacial behaviour will be presented with the discussion of the numerical results.

2.2 Finite Element Modelling of Reinforced Concrete

2.2.1 Introduction

Suitable Finite Element models are required for reinforced concrete structures. Herein an overview of typical approaches, their motivations and range of applicability is given to provide background for the adopted models.

Within the framework of the finite element method reinforced concrete can be represented either by superimposition of the material models for the constituent parts (i.e., for concrete and for reinforcing steel), or by a constitutive law for the composite concrete and embedded steel considered as a continuum at the macrolevel.

Because of their wider range of applicability, models of the first type are more popular.

The finite element method is well suited for superimposition of the material models for the constituent parts of a composite material. Material models of this type can be employed for virtually all kinds of reinforced concrete structures. Depending on the type of problem to be solved, concrete can be represented by solid elements, shell or plate elements, or beam elements.

The reinforcement is modelled either by separate truss or beam elements (discrete representation) or by separate elements of the same type as the concrete elements, which are superimposed on the latter (embedded representation) or by distribution of reinforcement to thin layers of equivalent thickness (distributed representation).

Superimposition of concrete and reinforcing steel to model reinforced concrete requires constitutive models to account for bond and dowel action on the concrete-steel interface.

Discrete representation of reinforcement allows modelling of bond and dowel action by means of special elements connecting adjacent nodes of concrete and steel elements. The distributed representation and the embedded representation of the reinforcement, however, do not permit the use of bond elements, because the displacements of concrete and steel at the interface are presumed to be the same. Consequently, the effect of bond slip can only be

accounted for implicitly by modifying the constitutive relations for concrete or steel.

If reinforced concrete is modelled by a constitutive law for the composite concrete and embedded steel considered as a continuum, the material behaviour of reinforced concrete on the macrolevel is described such as if this composite material was a single material.

Constitutive models of this type are essentially based on the results of experimentation on reinforced concrete panels [124],[125],[126],[73]. Since reinforced concrete is treated as a single material, neither the reinforcement nor the steel-concrete interaction needs to be modelled separately.

Models of this type are appropriate only if reinforcement is distributed uniformly.

2.2.2 Finite elements for concrete

Depending on the application a number of finite element types can be used for concrete. These elements can be continuum elements (solids) or structural elements (shells, beams). The above elements are generally of the same type used for any other material. Special mention can be made of multilayered shells or fiber beams in which nonlinear behaviour of the main material and inhomogeneities are dealt with by subdividing an element into layers or fibres. Multilayered and fibre elements are not used in this work and therefore are not discussed but provide yet an alternative approach for modelling of reinforcement.

2.2.3 Representation of reinforcing steel

Discrete modelling

Discrete representation of the reinforcement is based on modelling the reinforcing bars as separate elements. Commonly, truss or cable elements are used for this purpose. However, for the investigation of structural details, occasionally two-dimensional or even three-dimensional elements are used. Truss and cable elements do not have rotational degrees of freedom and carry only axial forces.

The material behaviour of truss and cable elements is described by means of the one-dimensional constitutive relations. In order to guarantee compatibility of the displacements of the concrete and reinforcement, truss and cable elements must coincide with the boundaries of the concrete elements. The node points of both types of elements must also coincide. Hence, the shape

functions for the concrete elements and the truss or cable elements must be of the same order.

For instance, three-dimensional isoparametric trilinear 8-node elements and two dimensional isoparametric bilinear 4-node elements for the representation of concrete are compatible with linear 2-node truss elements for reinforcing steel. Three-dimensional isoparametric quadratic 20-node elements and two-dimensional isoparametric quadratic 8-node elements for the representation of concrete are compatible with quadratic 3- node cable elements for the reinforcing bars.

The location of the reinforcement elements is obviously determined by the layout of the reinforcement. Consequently, the boundaries of the concrete elements must follow the reinforcing bars. Thus, the layout of the reinforcement has a strong influence on the generation of the finite element mesh for a concrete structure.

Commonly, when the overall structural behaviour is investigated, coinciding nodes of concrete and steel elements are assigned the same degrees of freedom. Bond slip and dowel action are either disregarded or considered implicitly by modifying the constitutive relations of concrete or steel. However, especially for the investigation of the behaviour of structural details, it may be necessary to model bond slip and dowel action more accurately.

For this purpose, different degrees of freedom are assigned to the coinciding nodes of concrete and steel elements. Special interface elements, referred to as bond or contact elements, are employed to connect the different degrees of freedom of coinciding nodes and concrete elements. Simple interface elements connect a single node of a concrete element with a single node of a steel element and are often referred to as joint elements. Such elements are basically nonlinear springs.

An alternative to nodal interface elements are continuous interface elements [4]. Such elements are characterised by a continuous concrete-steel interface along the entire length of the reinforcing bars. Compared with nodal interface elements, their performance is better [Keuser 1987, [61]]. Obviously discrete steel elements and continuous interface elements can be combined to steel- interface elements. Such elements allow modelling of the behaviour of both the reinforcing bar and the interface. Moreover, if a discrete crack model is used, then the concrete to concrete interface behaviour at cracks, governed by aggregate interlock can be modelled by interface elements.

Interface elements are also used in this work to model the interface between FRP and concrete. They play an important role in the models developed and are further described in Chapter 4.

The main advantage of modelling reinforced concrete by superimposition of concrete and steel elements is the relatively accurate representation of the

mechanical behaviour of the reinforcement and the interface. The discrete representation is the only way of accounting for bond slip and dowel action directly. Disadvantages of this approach are the great effort required for the discretization of a structure and the significant increase of the number of degrees of freedom. These disadvantages are the consequence of having to consider each reinforcing bar in the finite element mesh. Therefore, discrete modelling of the reinforcement is generally restricted to the analysis of structural details or single structural elements as beams taken in isolation from the remainder of the structure.

It is important to note, as will be recalled later on, that opening of localised cracks can be appropriately modelled only by this approach.

Embedded modelling

Separate elements for concrete and steel are also used for the embedded representation. However, this representation of the reinforcement, the same type of elements with the same number of nodes and degrees of freedom and, consequently, the same shape functions are used for the concrete and reinforcement.

Hence, the embedded approach is characterised by incorporating the one-dimensional reinforcing bar into two- or three-dimensional elements Figure 2.4. The stiffness matrix and the internal force vector of embedded reinforcement elements only contain the contribution of reinforcement bars. They are computed by integration along the curves representing the segments of the reinforcing bars within the respective element. The embedded reinforcement elements are then superimposed on the respective concrete elements. The reinforcing bars do not have to follow the boundaries of the concrete elements. Hence, the embedded representation of the reinforcement allows generating a finite element mesh without taking much care about the layout of the reinforcement. Rather, the reinforcing bars may pass through the concrete elements in an arbitrary manner. Since the reinforcement elements and the concrete elements must be assigned the same degrees of freedom, perfect bond between concrete and steel is obtained. Hence, bond slip and dowel action can only be modelled implicitly by modifying the constitutive relations for concrete or steel. A disadvantage of this type of approach is that special reinforcement elements are required. Such elements may not exist in the available finite element program. Moreover, similar to the discrete approach, each reinforcing bar must be considered when preparing the input for the analysis.

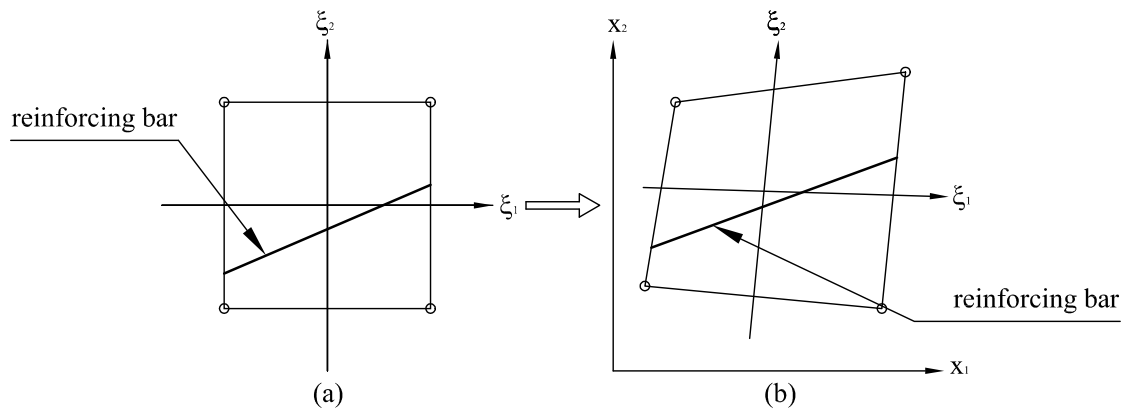


Figure 2.4: Embedded steel element: (a) in the local coordinate system, (b) in the global Cartesian coordinate system.

Distributed modelling

The distributed modelling of the reinforcement is characterised by smearing reinforcing bars over an element that is superimposed onto the main concrete element. Accordingly, for instance, membrane elements with an eccentricity can be superimposed onto shell elements to model a layer of reinforcement. The correct area of reinforcement along a unit length section of the structure is obtained assuming an equivalent thickness for the elements.

The constitutive equation for such an element with a unidirectional layer of smeared reinforcement are generally referred to the local directions of the element which are parallel and normal to the reinforcing bars.

The material relation for a two dimensional solid element for instance would be of the type:

$$\begin{bmatrix} \sigma_1 \\ \sigma_2 \\ \sigma_{12} \end{bmatrix} = \begin{bmatrix} E_T^S & 0 & 0 \\ 0 & 0 & 0 \\ 0 & 0 & 0 \end{bmatrix} \begin{bmatrix} \epsilon_1 \\ \epsilon_2 \\ \epsilon_{12} \end{bmatrix} \quad (2.4)$$

where E_T^S is the tangent material modulus of the reinforcing steel. To obtain the contribution of the steel layer to the tangent stiffness matrix of the composite element, the tangent material stiffness matrix above is transformed to the global coordinate system using the appropriate transformation for the element considered.

Thus, computation of the stresses in the reinforcing bars must be preceded by transformation of the actual strains to the direction parallel to the reinforcing bars, i.e. the local direction 1.

A combination of the distributed and the embedded representation of the reinforcement is obtained by smearing the reinforcement to thin layers, embedding the smeared layers into elements of the same type as the concrete elements and superimposing these elements on the concrete elements. This approach is convenient, for three-dimensional concrete structures with arbitrarily oriented layers of reinforcement.

Combining concrete and steel within an element requires the assumption of perfect bond between the concrete and the steel layers. Hence, bond slip and dowel action can only be modelled implicitly by modifying the constitutive relations of concrete or steel.

Note that this approach is only appropriate for uniformly distributed reinforcing bars.

Models for consideration of interface behaviour

in subsection 2.2.3 it was emphasised that the discrete representation of the reinforcing bars allows *explicit* consideration of bond slip and dowel action by means of special interface elements.

If, on the other hand, the embedded or distributed representation is chosen for the reinforcement, then the interface behaviour can only be modelled *implicitly* by means of appropriate modifications of the constitutive relations for concrete or steel.

Explicit representation has a paramount role in this work and is widely discussed in the specific sections on the constitutive laws of the interfaces and on the interface elements.

Implicit representation is deemed to be not appropriate for the investigation of the mechanical behaviour at the level of the structural element (i.e. a single beam).

The latter approach is briefly described here to clarify its shortcomings for the problem under consideration in this work and for completeness.

The effectiveness of this approach has been also tested by numerical analysis and used for a comparison with the more realistic explicit approach. The results of this comparison are presented in the chapter on the applications.

The Implicit representation of the interface behaviour is characterised by an appropriate empirical or theoretical modification of the constitutive laws for the concrete and/or the steel. Especially for the analysis of relatively large structures, where the reinforcement is modelled by the embedded or distributed approach and cracking is taken into account by a smeared crack model, the implicit approach is the only possibility to model the interface behaviour.

Aggregate interlock at cracks is considered implicitly by introducing a modified shear modulus into the constitutive relations for concrete.

The interface behaviour at concrete to steel interfaces, caused by bond slip, is modelled implicitly by relating the tension stiffening effect either to concrete or to steel. Hence, either the constitutive law for the concrete or the one for the steel is modified appropriately.

Concrete related models for consideration of tension stiffening are more popular than steel related models. In concrete related models, tension stiffening is accounted for by replacing the softening branch of the tensile stress-strain diagram for plain concrete, by the respective average stress-average strain diagram for the concrete component of reinforced concrete.

The difference between plain concrete and reinforced concrete is given by the magnitude of the ultimate strain. The values for the ultimate tensile strain of reinforced concrete reported in the literature are characterized by

a large scatter. However, as a rule of thumb, the ultimate tensile strain of reinforced concrete can be taken as one order of magnitude larger than the ultimate strain of plain concrete.

If modified constitutive relations for concrete are obtained from the examination (experimental or analytical) of the behaviour of a specimen reinforced only in the longitudinal direction and subjected to uniaxial tension the constitutive model must be extended to multiaxial case where cracks are not necessarily orthogonal to the reinforcement.

The simplest possible approach is to apply the modified uniaxial tensile post-peak constitutive law for the concrete to the principal directions of strain without consideration of the layout of the reinforcement.

However, since tension stiffening is caused by bond stresses between the concrete and the reinforcing bars, it is preferable that concrete-related tension stiffening models are referred to the directions of the reinforcement. This can be done considering tension stiffening as a function of the concrete strains in the direction of the reinforcing bars.

Alternatively, a reinforcement-related tension stiffening model can be employed. In this approach the residual tensile load-carrying capacity of cracked concrete is accounted for by a modified stress strain curve for the reinforcing steel. Consequently, the steel-related tension stiffening model is *a priori* referred to the directions of the reinforcing bars.

In Figure 2.5 basic concrete-related (a) and steel-related (b) tension stiffening models are reported. The model was derived on an experimental base [58, 59].

In the figure $\tilde{\epsilon}$ denotes the average tensile strain, σ_{ts}^C is the average residual tensile stress carried by the concrete and ρ denotes the reinforcement ratio.

If the residual tensile load-carrying capacity of the cracked concrete is related to the reinforcing steel, the additional stresses in the steel $\Delta\sigma_{ts}^S$ is computed from σ_{ts}^C and ρ , i.e., $\Delta\sigma_{ts}^S = \sigma_{ts}^C / \rho$. Hence, the material parameters for the tension stiffening models shown in Figure 2.5 are σ_{ts}^C , $\tilde{\epsilon}_{ck}$, $\tilde{\epsilon}_{ts,A}$, $\tilde{\epsilon}_{ts,B}$ and $\tilde{\epsilon}_{ts,C}$.

The experimental results on which this model is based on, indicated that the tension stiffening mainly depends on the reinforcement ratio and that is practically independent of the angle enclosed by the reinforcement and the cracks (provided the tension stiffening is evaluated in the direction of the reinforcement).

The constitutive law represented in Figure 2.5 relates to the uniaxial case. When it is generalised to the multiaxial case the direction of the cracks may not be orthogonal to the reinforcement. In this case the strain in the direction of the reinforcement at cracking is lower than $\tilde{\epsilon}_{ck}$ and can even be negative. For this reason, if the tension stiffening relation above is to be

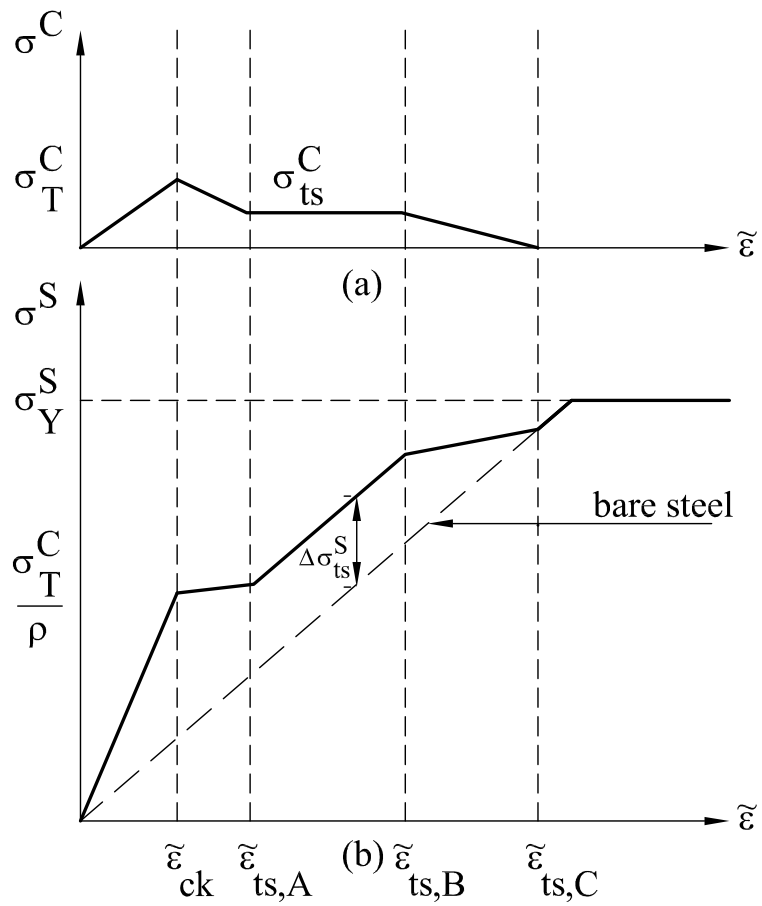


Figure 2.5: Modelling of tension stiffening by modifying the constitutive laws: (a) for concrete and (b) for steel

applied in the direction of the reinforcement, it has been proposed to assume that after cracking the initial stress in the concrete, in the direction of the reinforcement, is σ_t^C and the linear branch is omitted. In this approach there is, therefore, a discontinuity of the stresses at the initiation of cracking.

The concrete-related model of Figure 2.5 (a) yields almost the same structural response as the reinforcement-related model (Figure 2.5 (b)), provided it is formulated in terms of the concrete strain in the direction of the reinforcement. However, if the concrete related model is formulated in terms of the principal tensile strains of the concrete, the stiffening effect vanishes too early. It is also noted that in reinforcement related tension stiffening models, the compressive stresses in the concrete are somewhat overestimated. The reason for this is the neglect of the (tensile) stress-carrying capacity of the cracked concrete.

The above simple model has been described to introduce the basic principles of the implicit representation of the bond slip behaviour. There exist a large number of very refined models for implicit representation of bond slip that are derived on theoretical considerations and incorporated in a number of constitutive laws, proposed for reinforced concrete, featuring the smeared crack concept [73]. These refined models include also other aspects of concrete behaviour like, dilatancy, aggregate interlocking, reinforcement dowel action and damage accumulation under cyclic loading. This class of models will be examined in the chapter on crack modelling but the focus will be on aspects other than bond slip behaviour.

In the context of the present work, the implicit representation of the bond slip behaviour has the relevant shortcoming that it cannot be effectively combined with a discrete cracking approach and it is therefore not used in the applications.

However, the method is appealing for applications to macroscale problems because interface elements do not need to be specified.

2.3 Finite element models for reinforced concrete beams retrofitted with FRP

In the present work finite element models have been used to investigate RC beams retrofitted with FRP.

A large number of models have been set up for different purposes. Some models have been set up with the sole purpose of providing preliminary results and for the interpretation of the results yielded by more refined models. Other models have been used to investigate the behaviour of the retrofitted

structural element and the performance of different finite element approaches. Finally models have been also set up to investigate a single aspect or to validate proposed closed form solutions to particular problems.

In this section an outline of the models used and of their application is given. Only the general features of the models are described here. Details of each specific model are given in the sections where they are used.

2.3.1 General models for beams

These models have been used to explore the potential of finite element analysis in the investigation of RC beams retrofitted with FRP.

As the detailed distribution of stresses and strains within the beam is of interest, solid elements have been used. The immediate consequence of this choice is that plane sections do not have to remain plane.

In the absence of cracking the assumption that plane sections remain plane is in fact somewhat coarse for sections close to FRP plates or steel reinforcement ends.

However, the assumption is much more inadequate in presence of cracking. Actually, cracks could not open with the sections remaining plane.

Solid elements are also convenient because the better representation of multi-axial stress states enables the effective use of refined constitutive laws for concrete. Besides these elements can be attached to interface elements to model bond slip behaviour in an explicit manner. This proved to be very useful both for a good prediction of the overall behaviour of the structural elements and for an accurate evaluation of the interface stresses and strains which are critical in the delamination failure modes of these systems.

The solid elements used are:

- linear and quadratic plane strain and plane stress two-dimensional elements
- linear and quadratic three-dimensional elements

Solid elements have been used in the different models for concrete, for steel reinforcement and for FRP plates.

Alternatively truss elements have been used in two-dimensional analyses for steel bars and FRP.

Different constitutive laws have been tested for concrete. The material models used cover damage models [66, 63], elasto-plastic models [39, 132], cracking models [73, 65]. These models are described in the chapter on modelling of concrete.

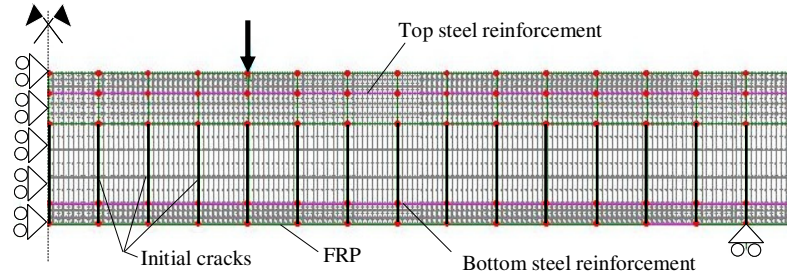


Figure 2.6: Two-dimensional finite element model for the analysis of RC beams retrofitted with FRP

Cracks have been accounted for using both a discrete and a smeared approach. In the former preset cracks have been introduced in the mesh, in the latter a material model featuring a fracture energy based smeared crack concept has been used.

Bond slip for both concrete/steel interface and concrete/FRP interface has been explicitly introduced by using interface elements. The elements and the constitutive laws adopted are described in the chapter on the interfaces. Interface elements have also been used to model unilateral contact between the faces of the preset cracks.

The constitutive law for steel is according to common practice linear perfectly plastic and the FRP are considered linear elastic up to failure.

With the features described a comprehensive and effective model encompassing all failure modes of beam retrofitted with FRP has been built. Also simplified models missing, at any one time, one of the main features have been analysed to highlight the importance of each aspect.

The complete models have been set up in a two-dimensional and in a Three-dimensional version. Details about each specific analysis are give in the sections relating to that analysis. The models are depicted in Figures 2.6 and 2.7.

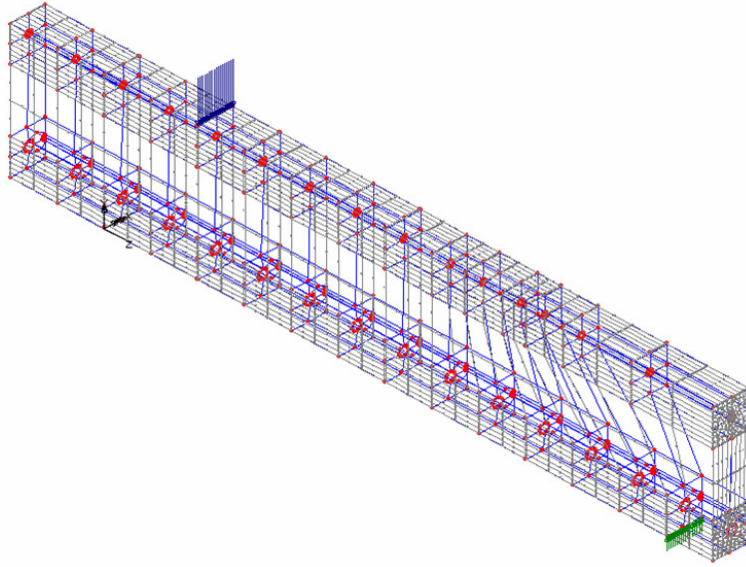


Figure 2.7: Three-dimensional finite element model for the analysis of RC beams retrofitted with FRP

2.3.2 Models for the investigation of specific aspects

Some finite element models have been set up not for the analysis of the retrofitted system but for special purposes.

The models have been used for checking the validity of a closed form solution for the interface stresses between beam and FRP, for the validation of the finite element model for the interface, and to test the potential of a fracture energy based smeared crack model for the simulation of onset and propagation of localised cracks.

The models are introduced here and presented in detail in the appropriate sections.

The closed form solution checked against results from finite element analysis pertain a beam of linear elastic material with a plate of FRP attached to its intrados. The plate does not extend to the supports. A linear elastic model in plane stress has been therefore generated. Three materials are included and they represent respectively, the concrete, the adhesive and the FRP. Only two-dimensional solid quadratic elements have been used. Perfect adherence has been considered between the different materials.

A model has also been set up to investigate the accuracy of the results obtained for the interface by using the interface elements described in Chapter 4. A closed form solution has been found for the simple problem of a

pull off test, in which a strip of FRP is attached to a block of concrete and subsequently subjected to an axial force to induce delamination in mode II. The problem has therefore been solved using a finite element model and the interface elements to be tested. The model is made of quadratic solid elements for both the concrete and FRP, and interface elements for the interface. Concrete and FRP are linear elastic in the model and the Young's modulus of concrete has been given a fictitious very high value to simulate a rigid concrete consistently with the assumptions of the closed form solution.

A number of models have been also analysed to investigate the ability of the crack models available in LUSAS to capture the onset and propagation of a single localised crack. All the models are two-dimensional and represent notched beams of different geometry and under different load conditions.

To localise the 'cracked' material within narrow bands that can be assimilated to a single crack a very fine mesh has been used. The localisation of the crack is achieved using an adequate softening law for the concrete. To keep the parameters defining the softening independent from the mesh the softening behaviour is defined by the fracture energy G_c of the concrete. In this way the program can apply automatically the appropriate softening at each gauss point based on the size of the element.

Chapter 3

Modelling of concrete

3.1 Introduction

Nonlinear analysis of reinforced concrete is essential to assess all safety aspects of a structure. This is because reinforced concrete has a very complex behaviour involving phenomena such as inelasticity, cracking, time dependency, interactive effects between concrete and reinforcement. In this chapter we first describe the mechanical behaviour of this material, than move on to mathematical modelling. We will see that very complex mathematical models are available for concrete. The most comprehensive models although useful for a better understanding of the properties of the material are not easy to use in the solution of practical problems. It is common therefore to use simplified models capturing only the aspects deemed to be relevant for the problem at hand.

For instance if the nonlinear behaviour of passively confined concrete is to be studied, dilatancy (volumetrical strain increase due to deviatoric stresses) needs to be appropriately included in the model. This, in an elasto-plastic model, requires a non-associative flow rule as it is seen experimentally that the assumption of associative behaviour would lead to over prediction of the lateral inelastic strains.

In other situations an associative flow rule can be acceptable and other aspect (like strain softening or the use of an advanced failure criterion for instance) are more important.

Bearing in mind these considerations a comprehensive mathematical model is presented to clarify the mechanical properties of concrete, already described in the first section of this chapter in a qualitative manner. A simplified model, suitable for the analysis carried out, in this work, on FRP strengthened structures is then defined and its implementation in a finite

element analysis architecture described in detail.

Finally other models used in the investigation of the behaviour of FRP structural elements in bending are described. These models feature isotropic damage and cracking of concrete and have been used for comparison with the adopted model, to find out what the consequences of its shortcomings are, and for the study of the cracking modelling options for RC beams retrofitted with FRP.

3.2 Mechanical behaviour of concrete

Concrete is a composite material mainly consisting of different sized aggregate particles embedded in a cement past matrix and its mechanical behaviour is strongly affected by the microstructure properties. In order to give physical explanations to the experimental behaviour observed during tests, the knowledge of microstructure becomes fundamental. The main aspects to consider:

1. A large number of bond micro cracks exist at the interface between coarser aggregates and mortar.
2. The cement paste has a high porosity, the pores being filled with water or air.
3. At all dimensional levels, above the molecular level, air and or water voids exists.

Many of the microcracks in concrete are caused by segregation, shrinkage or thermal expansion in the mortar and therefore exist even before any load has been applied. Some of the microcracks can be developed during loading because of the difference in stiffness between aggregates and mortar. Therefore, the aggregate-mortar interface constitutes the weakest link in the composite system. This is the primary reason for the low tensile strength of concrete materials.

For example the propagation of micro cracks during loading contributes to the non linear behaviour of concrete at low stress levels and causes volume increases near failure and uniaxial compressive state of stress. For high hydrostatic pressure the intrusion of voids and paste pores becomes increasingly important in affecting the behaviour and strength of concrete. The conclusion is that in order to create an appropriate mathematical model it is essential to understand the behaviour of plain concrete under uniaxial, biaxial and triaxial states of stress. Typical tests results are illustrated in

the next paragraph and they all refer to normal weight concrete under short term quasi static loading conditions.

Uniaxial compression behaviour

Results from uniaxial compression tests are generally represented as stress strain curves as shown in Figure 3.1. The shape of stress strain curves is similar for low-, normal-, and high strength concretes as shown in Figure 3.2. The key observations are :

1. The concrete behaviour is nearly linear elastic up to about 30% of its maximum compressive strength f_t_c . For stresses above $0.3f_t_c$ concrete begins to soften and the stress-strain curve shows a gradual increase in curvature up to about $0.75f_t_c$ to $0.9f_t_c$, after which the curve bends more sharply until it approaches the peak point at f_t_c . Beyond this point the curve has a descending part until crushing failure occurs at some ultimate strain value ϵ_u Fig.3.1.
2. The volumetric strain $\epsilon_v = \epsilon_1 + \epsilon_2 + \epsilon_3$ is almost linear up to about $0.75f_t_c$ to $0.9f_t_c$. At this point the direction of the volumetric strain is reversed and the material starts dilating Fig.3.1. The stress corresponding to the minimal volumetric strain is defined as *critical stress* (Richart et al., 1929).
3. Concrete with higher strength behave as linear to a higher stress level than low strength concrete, but seems to be more brittle on the descending portion of the stress strain curve. All peak point correspond approximately to a value of 0.002 Figure 3.2.

The first two points are associated with the mechanism of internal progressive micro cracking. When the stress is still in the region of $0.3f_t_c$ the internal energy is not sufficient to create new micro crack surfaces and the cracking existing in the concrete before loading remain nearly unchanged. The stress level corresponding to $0.3f_t_c$ has been defined as *onset of localized cracking* and has been proposed as the limits of elasticity (Kotsovos and Newman, 1977). For stress between 30 and 50 % of f_t_c the bond cracks start to extend because of the stress concentration at the crack tips. Mortar cracks remain negligible and the available internal energy is approximately balanced by the required crack release energy. At this stage the crack propagation is stable in the sense that cracks rapidly reach their final lengths, if the applied stress is maintained constant.

For the next stress range 50-70 % of f_t_c some cracks at nearby aggregates surfaces start to bridge in the form of mortar cracks. Meanwhile other bond

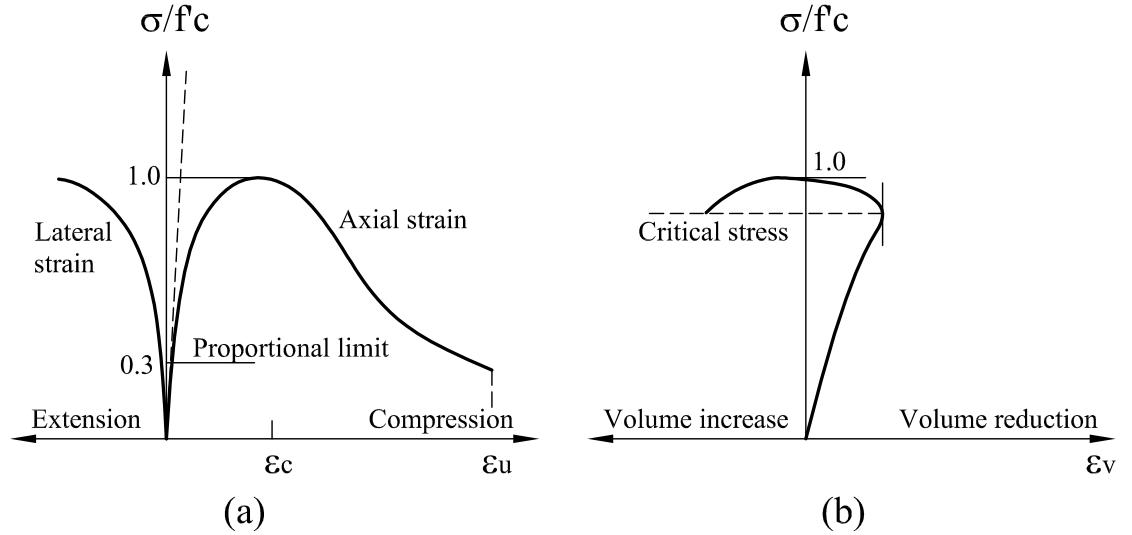


Figure 3.1: Typical stress-strain curves for concrete in uniaxial compression test. (a) Axial and lateral strains. (b) Volumetric strain ($\epsilon_v = \epsilon_1 + \epsilon_2 + \epsilon_3$)

cracks keep growing. If the load is maintained constant the crack continue to propagate with a decreasing rate to their final lengths.

For higher stress levels the system is unstable and complete disruption can occur even if the load is maintained constant. Microcracks through the mortar in the direction of the applied stress bridge together the bond microcracks at the surface of the nearby aggregates and form macroscopic cracks. This stage correspond to the descending portion of the concrete stress-strain curve (softening). The stress level of about $0.75f_c$ is termed as *onset of unstable fracture propagation* or *critical stress* since it corresponds to the minimum value of the volumetric strain ϵ_v .

The initial modulus of elasticity E_0 is generally correlated to the uniaxial compressive strength and can be approximated with the empirical formula:

$$E_0 = 5700\sqrt{f_c} \text{ N/mm}^2 \quad (3.1)$$

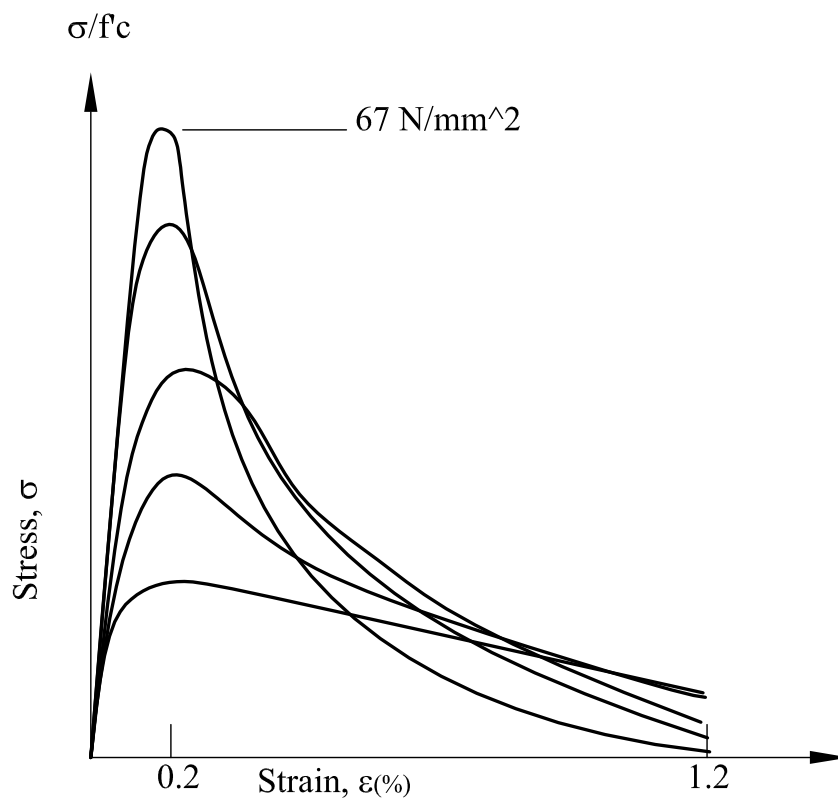


Figure 3.2: Uniaxial compressive stress-strain curves for concrete with different strengths

which gives a reasonable accuracy. The poisons ratio ν also varies with the compressive strength f'_c , with 0.19 or 0.20 being representative values.

Uniaxial tension behaviour

The stress-strain curves for uniaxial tension tests are similar in shape to those observed for uniaxial compression Figure 3.3. However the tensile strength f'_t is significantly lower than the corresponding strength in compression f'_c , with a ratio of 0.05-0.1. The concrete behaviour is nearly linear elastic up to about 60% of its maximum tension strength f'_t . The following interval of stable crack propagation is very short and the system becomes unstable around $0.75f'_t$. The direction of cracks propagation is transversal to the applied stress direction. The descending portion of the stress-strain curve is difficult to follow because the crack propagation is very rapid. The value of f'_t is difficult to measure experimentally and there are several formulae to estimate it from the corresponding value of the compression strength.

The modulus of elasticity and the poisons ratio under uniaxial tension are respectively higher and lower than the case of uniaxial compression.

Biaxial behaviour

The strength and ductility of the concrete under biaxial states depends on the nature of stress state: compressive type or tensile type. The biaxial strength envelope Fig.3.4 represented by Kupfer et al. (1969) [62] suggest that the biaxial compression strength of the material increases compared to the equivalent uniaxial state. Equally from the stress-strain curves it is possible to recognize that the tensile ductility of concrete is greater under biaxial compression state than uniaxial compression Fig.3.5 .

The biaxial tension strength is very similar to what measured for uniaxial tension state. Under biaxial compression-tension state the compressive strength decreases almost linearly as the applied tensile strength is increased.

Some studies suggest that the maximum strength envelope is almost independent of load path (Nelissen,1972).

The growth of major microcracks is associated with an inelastic volume increase defined dilatancy. This phenomenon becomes visible when the failure point is approached. The failure will occur along surfaces orthogonal to the direction of the maximum tensile stress or strain. In particular the tensile strains are critical in defining the failure criterion of concrete.

Triaxial behaviour

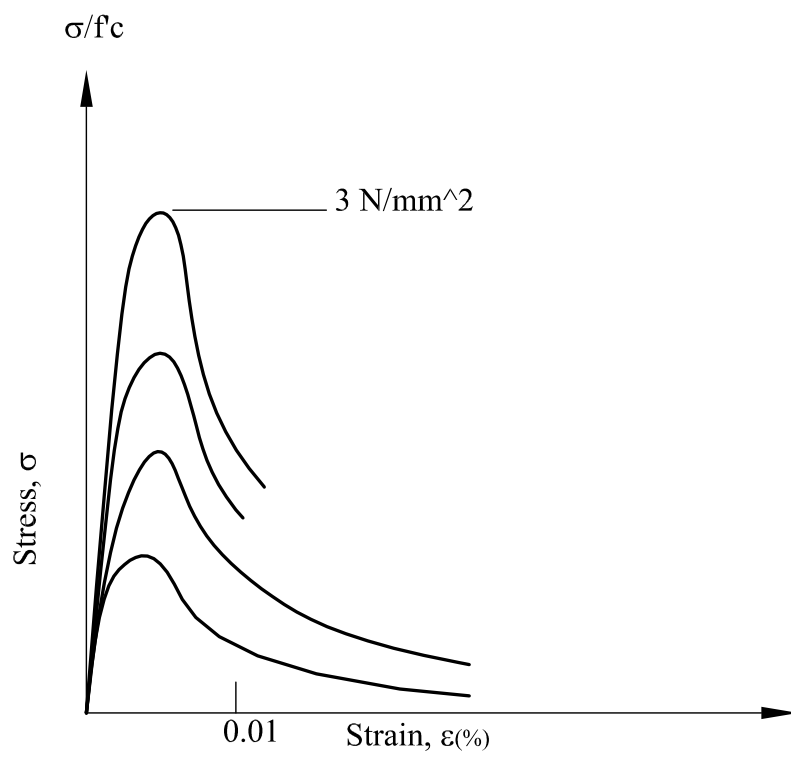


Figure 3.3: Typical tensile stress-strain curves for concrete

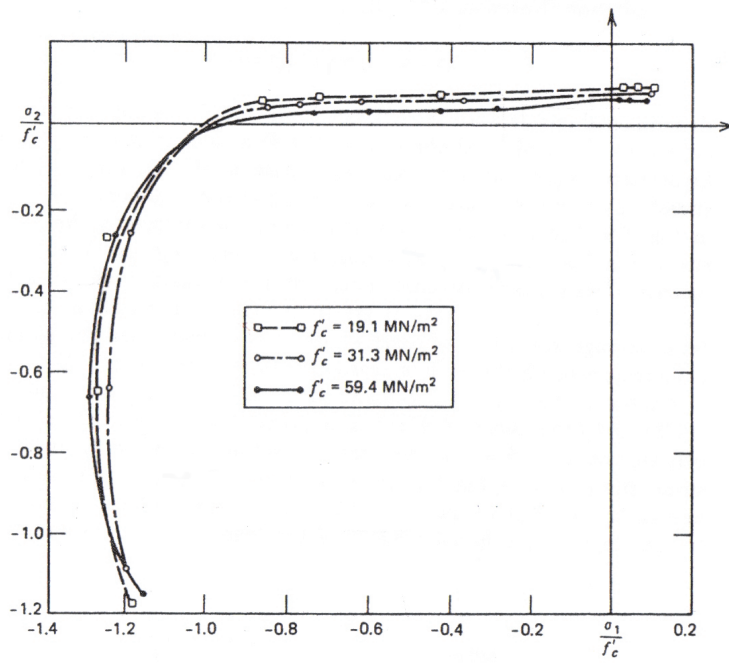


Figure 3.4: Biaxial strength envelope of concrete (Kupfer et al.,1969).

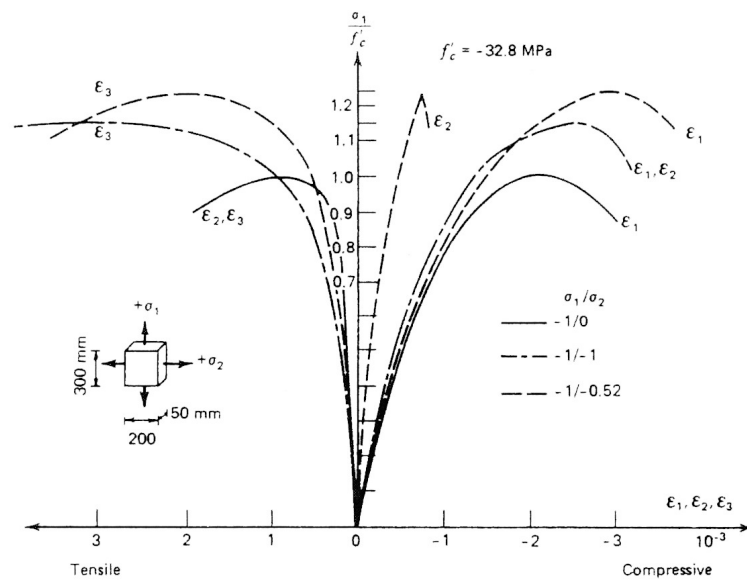


Figure 3.5: Stress-strain relationships for concrete under biaxial compression (Kupfer et al.,1969).

Typical stress-strain results from triaxial tests on concrete indicate that the ultimate axial strength increases considerably with the confining stress Figure 3.6. As the hydrostatic stress increases, the behaviour of the concrete moves from quasi-brittle to plastic softening to plastic hardening. This happens because under higher hydrostatic stresses the possibility of bond cracking is reduced and the failure rather explained with the crushing of cement paste. During hydrostatic compression tests the concrete behaves as nonlinear during the loading stages, while upon unloading the slope of the curve is almost constant and approximately equal to the initial tangent of the loading curve Figure 3.7. The failure surface can be defined as a function of the three principal stresses. The elastic limit and failure surfaces of concrete representation in the three principal stresses space is shown indicatively in Figure 3.7, assuming the material is isotropic. For small hydrostatic pressures the deviatoric sections are convex and non circular, becoming more or less circular for increasing compressions (along the $\sigma_1 = \sigma_2 = \sigma_3$ axis). Finally, the failure surface appears to be independent of the load path (Gerste et al,1978; Kotzovos,1979).

3.3 Mathematical model for concrete

There exist an incredible amount of models for concrete. Although the physical properties of the material are relatively well established, regularly, researchers develop new variants of existing models and there are not two commercial software adopting the same formulation.

This is probably because as anticipated, and as it will be self evident in the next section, to model concrete effectively into a program for structural analysis is not an easy matter. Available models are usually tailored around a specific application. To complicate the matter, as concrete is usually used in RC, there exist models for the composite material concrete with embedded reinforcement. The latter are usually derived as modified versions of a model for plain concrete.

Because we are looking into the behaviour of a single structural element (a beam), where concrete and reinforcement are represented independently, we only need a model for plain concrete.

There are two basic approaches to nonlinear modelling of concrete: *finite* (or *total*) material characterization in the form of *secant* formulation and *incremental* (or *differential*) models in the form of *tangential* stress-strain relations. Finite constitutive equations of the first category are restricted to path-independent, reversible processes causing a uniqueness problem in the case of non-proportional loading. The most prominent models of this class

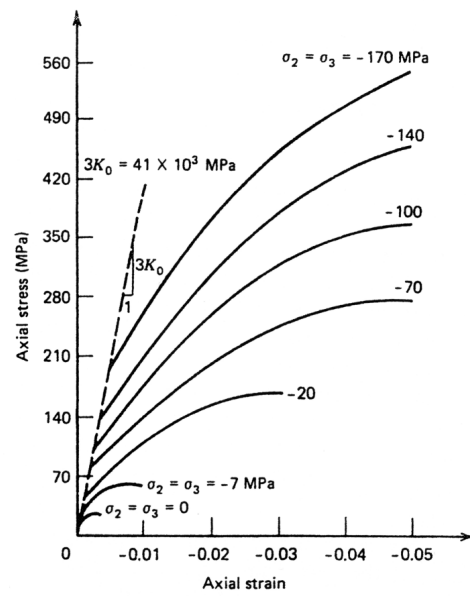


Figure 3.6: Triaxial stress-strain relationship for concrete (Balmer,1949).

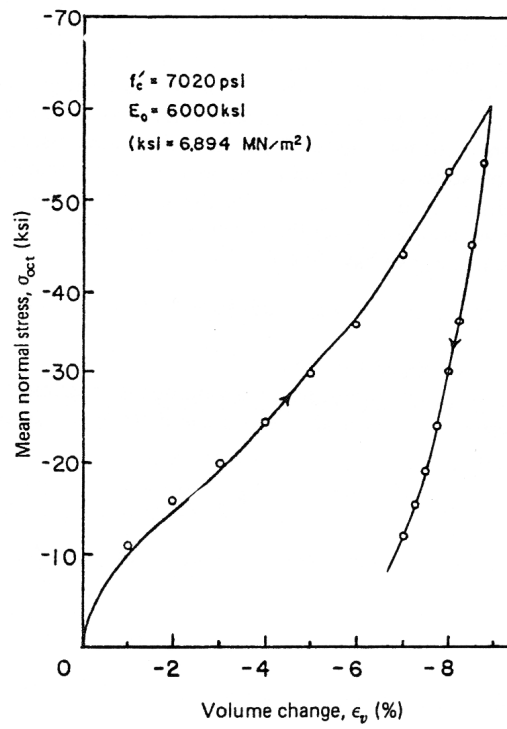


Figure 3.7: Behaviour of concrete in hydrostatic compression test (Green and Swanson, 1973).

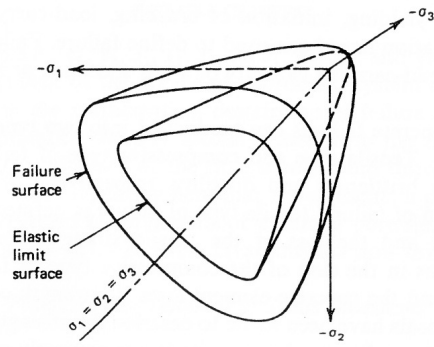


Figure 3.8: Schematic representation of the elastic limit and failure surfaces of concrete in the three dimensional principal space.

are hyperelastic formulation and the deformation theory of plasticity.

In contrast, differential or incremental material descriptions of the second category do not exhibit the shortcomings of reversibility and path dependency. The most prominent models of this class are hypoelastic models and models based on the flow theory of plasticity.

There are also models based on elastic degradation in the form of continuum damage mechanics.

3.3.1 Elastoplastic model for concrete

The model described here, used as a base to discuss the main aspects of concrete modelling, is an incremental one and is based on the flow theory of elasticity. The model has been introduced by Etse and Willam in [39] and is an attempt to define an omni-comprehensive representation of the material.

The model features refined failure criterion and plastic loading conditions, a nonassociated flow rule, and specifically designed hardening and softening rules. Softening is based on a fracture energy formulation.

Failure criterion

The proposed failure criterion uses the Hoek and Brown criterion, originally developed for rock materials, as a backbone

The criterion is expressed in terms of three scalar invariants $\sigma = I_1/3$, $\rho = \sqrt{2J_2}$, $\cos(3\theta) = \sqrt{27}J_3/(2J_2)^{3/2}$ directly related to the Haigh-Westergaard coordinates $\xi = \sqrt{3}\sigma, \rho, \theta$, which, as known, permit a convenient geometric representation of the failure surfaces.

The meridional sections of the failure surface are, in fact, readily traced, for different values of θ in the (ξ, ρ) plane, and the sections in the deviatoric planes can be also represented in a polar diagram.

The expression for the failure criterion proposed in [39] is:

$$F(\sigma, \rho, \theta) = \frac{3}{2} \left[\frac{\rho r(\theta)}{f'_c} \right]^2 + \frac{m_o}{f'_c} \left[\sigma + \frac{\rho r(\theta)}{\sqrt{6}} \right] - 1 = 0 \quad (3.2)$$

where $r(\theta)$ is the Klisinsky function

$$r(\theta) = \frac{4(1 - e^2) \cos^2(\theta) + (2e - 1)^2}{2(1 - e^2) \cos(\theta) + (2e - 1)\sqrt{4(1 - e^2) \cos^2(\theta) + 5e^2 + 4e}} \quad (3.3)$$

with $0.5 \leq e \leq 1$ to preserve convexity of the yield function. The parameter e is called eccentricity and represent the ratio between the radius of the deviatoric section along tensile and compressive meridians ρ_t/ρ_c (tensile

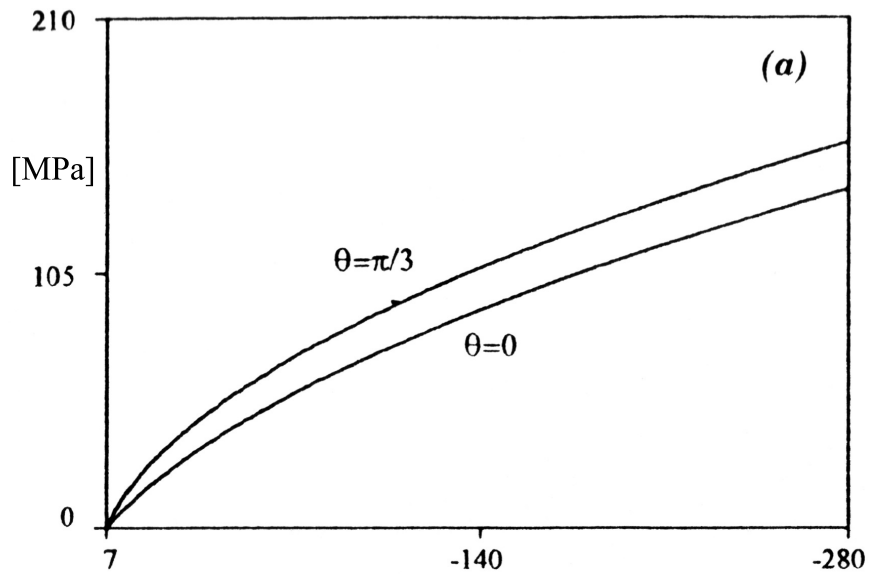


Figure 3.9: Meridional sections of concrete failure surface

and compressive meridians correspond to $\theta = 0$ and $\theta = \pi/3$ and are represented in Figure 3.9). The Klisinsky function was introduced to smoothen the Hoek and Brown failure surface and its effect can be seen in Figure 3.10. The difference between the proposed criterion and the Hoek and Brown's one is best appreciated by comparing the failure locus in plane stress (Figure 3.11). Note that the Klisinsky function is used to obtain a smooth surface also in the Menetrey Willam criterion used in the simplified elastoplastic model described in the next section and implemented LUSAS.

Loading surface

Also the loading function was derived by modifying the Hoek and Brown criterion. The same loading function is used for pre-peak and post-peak response.

The model is isotropic and remain isotropic during the loading history

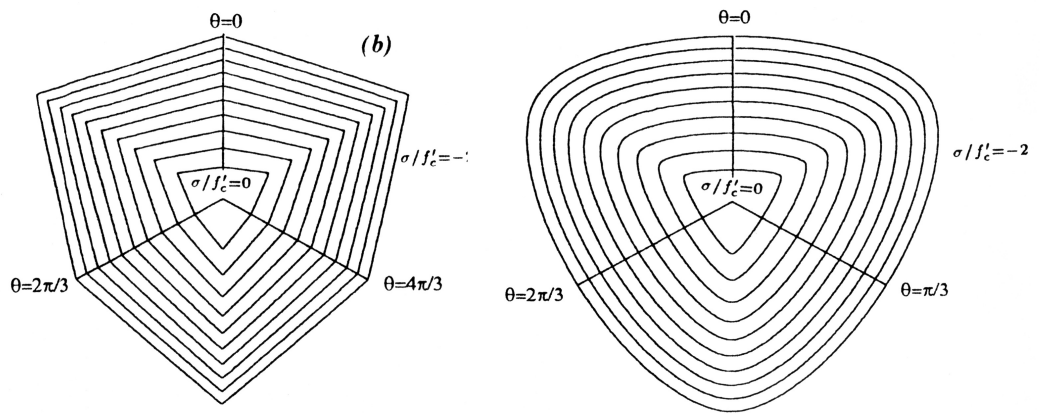


Figure 3.10: Deviatoric sections of Hoek and Brown failure criterion (left) and the proposed Extended Leon Criterion (right).

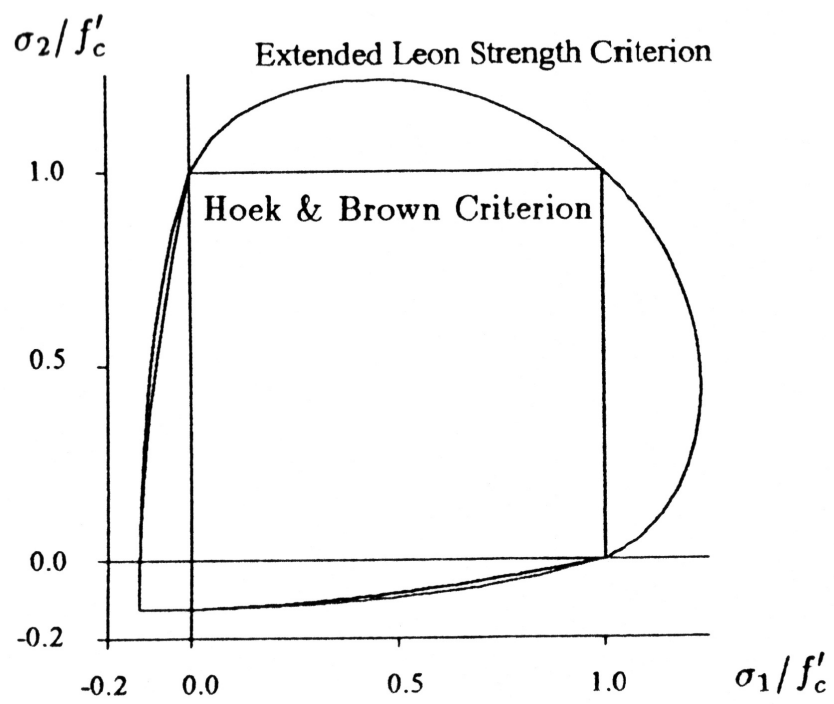


Figure 3.11: Plane stress sections of smoothed and polygonal failure envelopes.

and degradation of the elastic properties during plastic flow is neglected.

The total strain is composed of a plastic and an elastic component according to

$$\dot{\boldsymbol{\varepsilon}} = \dot{\boldsymbol{\varepsilon}}_e + \dot{\boldsymbol{\varepsilon}}_p$$

The elastic response is linear, and the plastic response is governed by the flow rule

$$\dot{\boldsymbol{\varepsilon}}_p = \dot{\lambda} \mathbf{m}; \quad \text{with} \quad \mathbf{m} = \frac{\partial Q}{\partial \boldsymbol{\sigma}} \quad (3.4)$$

where $\dot{\lambda}$ denotes the plastic multiplier and Q is the plastic potential. A non associative flow rule is used to avoid overprediction of dilatancy. Therefore Q differs from the loading function.

The expression of the loading function proposed in [39] is:

$$\begin{aligned} F(\sigma, \rho, \theta, k, c) &= \left\{ (1 - k) \left[\frac{\sigma}{f'_c} + \frac{\rho r(\theta)}{\sqrt{6} f'_c} \right]^2 + \sqrt{\frac{3}{2}} \frac{\rho r(\theta)}{f'_c} \right\}^2 \\ + \frac{k^2 m}{f'_c} \left[\sigma + \frac{\rho r(\theta)}{\sqrt{6}} \right] - k^2 c &= 0 \end{aligned} \quad (3.5)$$

In the hardening regime the evolution of the loading surface is varied by the parameter k ($0 \leq k \leq 1$), named the normalized strength parameter. For hardening c and m remain constant.

The linear elastic response is therefore bounded by the initial value of k (for instance $k_o = 0.1$).

Softening is represented varying the decohesion parameter c from unity to zero. The friction parameter m is also varied but is dependent on m as described in the sequel. Note that for $k = 1$ the loading function reduces to the failure one.

The shape of the hardening surfaces for different values of k is depicted in Figure 3.12. Note that initially the loading surface are closed to allow for cap action. The hardening function is smooth everywhere except at its intersection with the hydrostatic axis. In Figure 3.13 the same surface are represented during softening ($c = 0 \rightarrow 1$).

Flow rule

A non associated flow rule is used to control inelastic dilatancy. This is required because it is seen experimentally that the use of an associative flow rule, overpredicting the dilatation, overpredicts the confinement, as well, leading to overestimation of structural element affected by passive confinement.

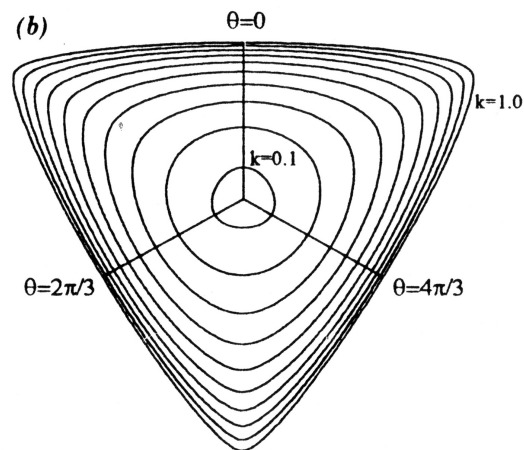
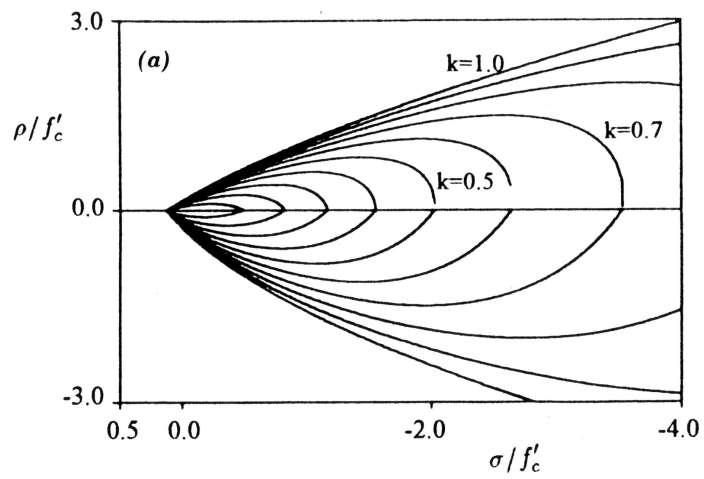


Figure 3.12: Loading surface of ELM in Hardening regime: (a) Meridional sections; (b) deviatoric sections at $\sigma/f'_c = -0.3$.

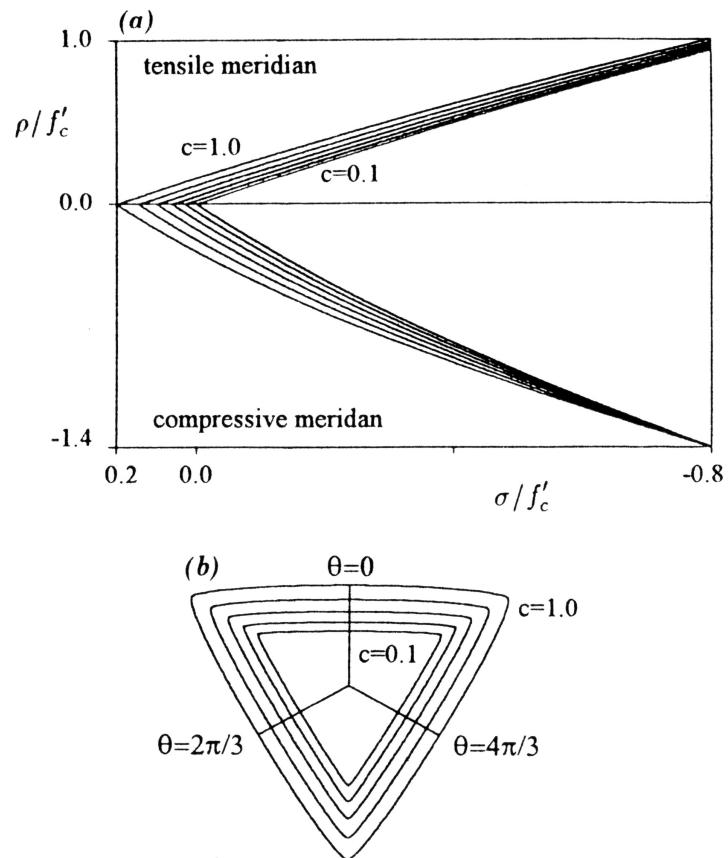


Figure 3.13: Loading surface of ELM in Softening regime: (a) Meridional sections; (b) deviatoric sections at $\sigma/f'_c = 0$.

The plastic potential used is based on a volumetric modification of the yield condition. Therefore, the deviatoric component of the plastic strain rate follows an associated flow rule. The plastic potential has the following form:

$$Q(\sigma, \rho, \theta, k, c, m_Q) = \left\{ (1-k) \left[\frac{\sigma}{f'_c} + \frac{\rho r(\theta)}{\sqrt{6} f'_c} \right]^2 + \sqrt{\frac{3}{2}} \frac{\rho r(\theta)}{f'_c} \right\}^2 + \frac{k^2}{f'_c} \left[m_Q + m \frac{\rho r(\theta)}{\sqrt{6}} \right] - k^2 c = 0 \quad (3.6)$$

where m_Q is defined in terms of its gradient

$$\frac{\partial m_Q}{\partial \sigma} = D \exp(E x^2) + G; \quad \text{where } x = \frac{-\sigma + f'_t/3}{f'_c} \quad (3.7)$$

The material parameters D, E, G are to be calibrated from three different experiments using dilatancy measurements at different levels of the hydrostatic component of the stress.

Hardening formulation

The model for hardening is as follows. A scalar variable α is introduced such that

$$\dot{\alpha} = \frac{1}{x_p} \dot{\epsilon}_p \quad (3.8)$$

where $\dot{\epsilon}_p$ is the Euclidean norm of the of the plastic strain rate

$$\dot{\epsilon}_p = \sqrt{\dot{\boldsymbol{\epsilon}}_p \cdot \dot{\boldsymbol{\epsilon}}_p} = \dot{\lambda} \|\mathbf{m}\| \quad (3.9)$$

x_p is a function of the confinement through the stress invariant $\boldsymbol{\sigma}$ and have the following polynomial expression:

$$x_p = x_p(\boldsymbol{\sigma}) = \mathbf{A} \left(\frac{\boldsymbol{\sigma}}{f'_c} \right)^2 + B \left(\frac{\boldsymbol{\sigma}}{f'_c} \right) + C \quad (3.10)$$

therefore,(3.8) defines the rate of strain hardening α in terms of x_p and $\dot{\epsilon}_p$, with $\alpha = 0$ at the beginning of the inelastic deformation process. The peak strength is reached for $\alpha = 1$.

The normalized strength parameter k which controls the evolution of the yield surface in the pre-peak regime, is finally expressed by the following function of the variable α

$$k = k(\alpha) = k_o + (1 - k_o) \sqrt{\alpha(2 - \alpha)} \quad (3.11)$$

Softening

Correct modelling of softening is a very important aspect of concrete modelling. It is widely recognized, in fact, that the most relevant source of non-linearity in structural problems involving concrete is cracking of concrete. In the smeared crack concept, in which the cracked medium is represented as an equivalent continuum, a good representation of the softening of the material in tension is of key importance for the correct prediction of crack propagation and spacing. However, softening does not occur only in tension and its different characteristics for different confinement regimes determine brittle or ductile response of the material in compression.

Concrete softening is the manifestation of drastic changes of the micro- and mesostructure of the heterogeneous material, when microdefects propagate and coalesce into macrodefects. Softening is then a structural phenomenon rather than a material property.

Because of this, in a smeared crack based formulation for softening behaviour there is a difficulty in determining softening relations that are independent on test configuration and boundary conditions.

A possible strategy is the use of a fracture energy base softening description. Note that It is recognise in the source of the model that we are about to describe, that there is still a problem associated with localization in the form of discontinuous bifurcation.

The proposed model, however, assures consistent energy dissipation at the formation of spatial discontinuities.

Softening is represented through a reduction of the decohesion parameter c and the friction parameter m and is assumed to take place only for values of confinement below a determined transition point TP. The decohesion factor c varies from 1 to 0 during the softening process and the shear parameter m is a function of the decohesion one as the deviatoric strength at the transition point is assumed to be constant during the softening process.

The intermediate softening surface after failure is defined by

$$F_s(\sigma, \rho, \theta, c) = \frac{3}{2} \left[\frac{\rho r(\theta)}{f'_c} \right]^2 + \frac{m_s}{f'_c} \left[\sigma + \frac{\rho r(\theta)}{\sqrt{6}} \right] - c_s = 0 \quad (3.12)$$

Imposing the constraint that the deviatoric strength at the transition point is fixed we get that the parameter m_s have the following expression

$$m_s = m_r - (m_r - m_o)c_s \quad (3.13)$$

where m_r is the residual shear parameter and m_o is the initial one.

$$c_s = \frac{\sigma_t}{f'_t}; \quad \text{where} \quad 1 \geq c_s \geq 0 \quad (3.14)$$

Fracture energy based softening

In the decohesive crack formulation of the fictitious crack concept, the degrading tensile strength σ_t is a function of the crack opening displacement and not a function of the tensile strain. The following expression for this has been experimentally determined

$$\sigma_t(u_f) = f'_t \exp\left(-5\frac{u_f}{u_r}\right) \quad (3.15)$$

As a result the fracture energy release rate for tensile cracking reduces to

$$G_f^I = \int_0^{u_r} \sigma_t(u_f) du_f = f'_t \frac{u_r}{5} \left[1 - \exp\left(-5\frac{u_f}{u_r}\right) \right] \quad (3.16)$$

It is possible to combine the fracture based strength degradation with the homogenised crack opening displacement of an equivalent elastoplastic continuum such that

$$\sigma_t = \sigma_t(u_f); \quad \text{where} \quad u_f = u_f(\varepsilon_f). \quad (3.17)$$

The relationship between u_f and ε_f involves the crack spacing h_t in tension

$$\dot{u}_f = h_t \dot{\varepsilon}_f. \quad (3.18)$$

Conceptually this corresponds to the fracture energy concept of tensile softening that is extended below to shear faulting in order to also maintain constant fracture energy during compressive splitting and shear slipping. From physical observations, the crack spacing h_t in tension is a multiple of that in compression h_s . The relation between both characteristic lengths can be evaluated in terms of the ratio between the fracture energy release rate in tension and G_f^I and that in shear G_f^{II} . Thereby it is understood that G_f^{II} is already the result of representing distributed tensile cracking by a single inclined shear band. In the present formulation, the crack spacing is described with the fracture energy based softening parameter β which accounts for the variation of crack spacing in mode I type tensile cracking and mode II type shear faulting as

$$\dot{\beta} = \frac{G_f^I}{G_f^{II}} h_t \dot{\varepsilon}_f = \frac{1}{x_f} \dot{\varepsilon}_f. \quad (3.19)$$

Thereby the softening ductility measure x_f is defined as a function of the mean stress

$$x_f = x_f(\sigma) = \frac{G_f^{II}}{G_f^I} \frac{1}{h_t}.$$

This ductility measure plays the role of the microcrack density that increases rapidly with increasing confining pressure and accounts for diffuse type failure without strength degradation beyond the point TP of brittle-ductile transition. The magnification of the microcrack density in shear compared with direct tension is described by the fracture energy ratio G_f^{II}/G_f^I , which is expressed in terms of the volumetric stress as

$$\frac{G_f^{II}}{G_f^I} = A_f R(\sigma)^4 + B_f R(\sigma)^2 + 1; \quad \text{where} \quad R(\sigma) = \frac{\sigma - f'_t/3}{f'_c} \quad (3.20)$$

and where the softening parameters A_f and B_f are calibrated from low and high confined compression tests.

It remains to formulate the equivalent failure strain ε_f , which provides a natural strain softening measure in terms of the components of the inelastic failure strain $\boldsymbol{\varepsilon}_f$. During softening, growth law defines the direction and the magnitude of inelastic failure strains in the homogenized continuum analogous to the plastic flow rule as

$$\dot{\boldsymbol{\varepsilon}}_f = \dot{\lambda} \mathbf{m} = \frac{\partial Q_s}{\partial \boldsymbol{\sigma}} \quad (3.21)$$

According to the nonassociated flow rule, the failure potential Q_s is obtained by setting $k = 1$ in the 3.6

$$Q_s = \frac{3}{2} \left[\frac{\rho r(\theta)}{f'_c} \right]^2 + \frac{1}{f'_c} \left[m_Q + m \frac{\rho r(\theta)}{\sqrt{6}} \right] - c_s = 0 \quad (3.22)$$

where m_Q is given by 3.7.

The equivalent failure strain plays the role of the damage metric in the energy equivalent continuum, which should experience the same amount of cracking as the discontinuum. In particular, increments of ε_f should only take place if the existing microcracks are activated and result in an increase of failure strain due to microcrack opening. Mathematically this situation may be expressed by requiring that the rate of failure strain $\dot{\boldsymbol{\varepsilon}}_f$ has at least one positive eigenvalue. Considering the principal components of $\dot{\boldsymbol{\varepsilon}}_f^p$, and introducing the orthogonal projection P^+ of the $\dot{\boldsymbol{\varepsilon}}_f^p$ onto the positive cone C^+ in Figure 3.14, $P^+ \dot{\boldsymbol{\varepsilon}}_f^p$ represents the closest point projection of $\dot{\boldsymbol{\varepsilon}}_f^p$ onto C^+ . The effect of P^+ is simply to remove the negative principal components from $\dot{\boldsymbol{\varepsilon}}_f^p$,

$$P^+ \dot{\boldsymbol{\varepsilon}}_f^p = \langle \dot{\lambda} \mathbf{m}^p \rangle \quad (3.23)$$

where

$$\langle \dot{\lambda} \mathbf{m}^p \rangle = \langle m_I \rangle \mathbf{e}_1 \otimes \mathbf{e}_1 + \langle m_{II} \rangle \mathbf{e}_2 \otimes \mathbf{e}_2 + \langle m_{III} \rangle \mathbf{e}_3 \otimes \mathbf{e}_3$$

The components of \mathbf{m}^p are defined as

$$\mathbf{m}^p = \begin{pmatrix} m_I = \frac{\partial Q}{\partial \sigma_I} \\ m_{II} = \frac{\partial Q}{\partial \sigma_{II}} \\ m_{III} = \frac{\partial Q}{\partial \sigma_{III}} \end{pmatrix} = \begin{pmatrix} \frac{\partial Q}{\partial \sigma} \frac{\partial \sigma}{\partial \sigma_I} + \frac{\partial Q}{\partial \rho} \frac{\partial \rho}{\partial \sigma_I} + \frac{\partial Q}{\partial \theta} \frac{\partial \theta}{\partial \sigma_I} \\ \frac{\partial Q}{\partial \sigma} \frac{\partial \sigma}{\partial \sigma_{II}} + \frac{\partial Q}{\partial \rho} \frac{\partial \rho}{\partial \sigma_{II}} + \frac{\partial Q}{\partial \theta} \frac{\partial \theta}{\partial \sigma_{II}} \\ \frac{\partial Q}{\partial \sigma} \frac{\partial \sigma}{\partial \sigma_{III}} + \frac{\partial Q}{\partial \rho} \frac{\partial \rho}{\partial \sigma_{III}} + \frac{\partial Q}{\partial \theta} \frac{\partial \theta}{\partial \sigma_{III}} \end{pmatrix} \quad (3.24)$$

The rate of the equivalent fracture strain defines the length of the projection $P^+ \dot{\boldsymbol{\varepsilon}}_f^p$

$$\dot{\varepsilon}_f = \|P^+ \dot{\boldsymbol{\varepsilon}}_f^p\| = \sqrt{\langle \dot{\boldsymbol{\varepsilon}}_f^p \rangle \cdot \langle \dot{\boldsymbol{\varepsilon}}_f^p \rangle} = \dot{\lambda} \|\langle \mathbf{m}^p \rangle\| \quad (3.25)$$

Thereby (3.19) redefines the softening parameter β in terms of the reciprocal value of the characteristic length for tensile cracking resembling a scalar valued crack opening rule.

Substituting β for u_f , which describes the crack opening in the softening regime, into (3.15), the degradation of the tensile strength due to tensile cracking or due to shear failure reduces to

$$\sigma_t(u_f) = f'_t \exp\left(-5 \frac{\beta}{u_r}\right) = f'_t \exp\left(-5 \frac{1}{x_f} \frac{\varepsilon_f}{u_r}\right) \quad (3.26)$$

Figure 3.15 shows the softening behaviour of σ_t for tensile failure and for shear failure for different levels of confinement.

3.4 A simplified elasto-plastic model

3.4.1 The Menetrey-Willam concrete model

The model described in the previous section include all the main aspects characterizing the behaviour of plain concrete. A model of this type can be implemented in a computer program to trace, given a straining history, the corresponding stress history. This operation is not easy but accomplishable. However a program of this kind does not necessarily have the stability and efficiency required for the inclusion within a finite element architecture. Also the computational time is not an issue if the sole purpose of the program is to reproduce a stress history for a given strain history, in order to validate a constitutive law, whereas it can lead to inapplicability of the model when used in the solution of a finite element problem in which the stresses are to be integrated at each gauss point at each time step, at each iteration.

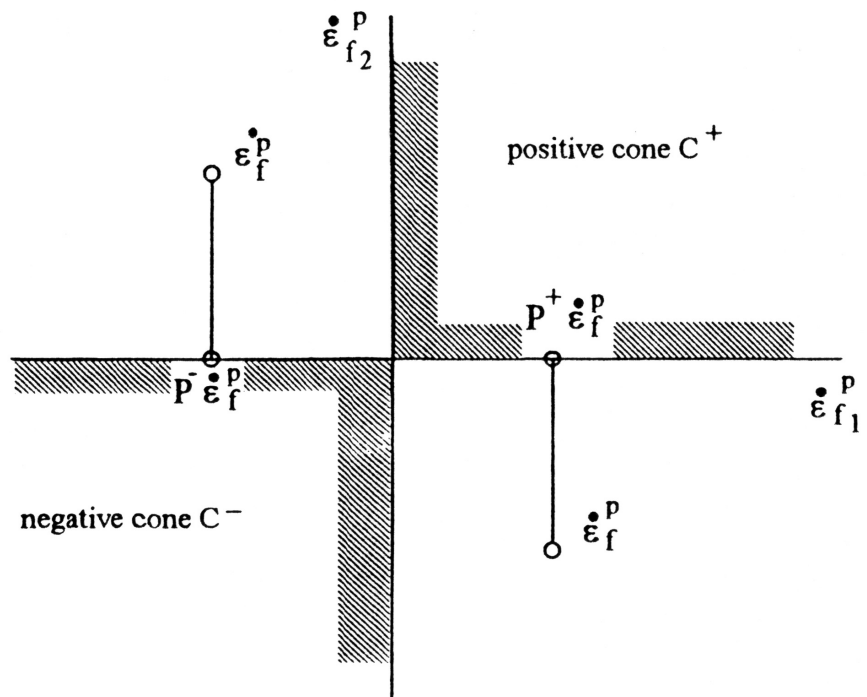


Figure 3.14: Orthogonal Projections of Failure strain rates onto Positive and Negative Cone.

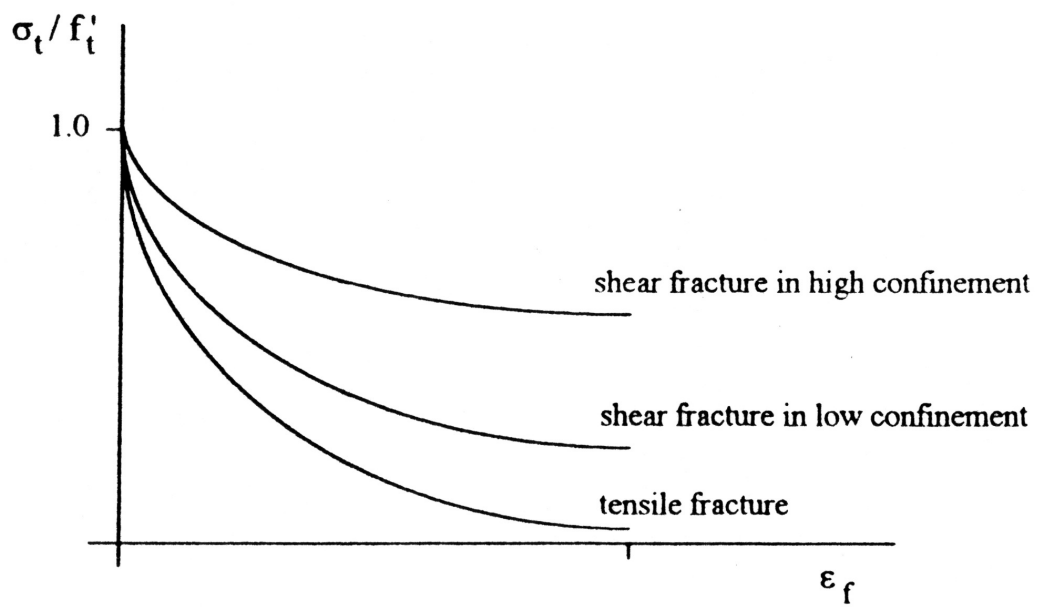


Figure 3.15: Exponential degradation of Tensile Strength

Also in a finite element model it is desirable to assemble a tangent operator necessary for the use of a Full Newton Raphson solution algorithm. This tangent modulus should be assembled in efficient manner to speed up, rather than slowing down, the solution. On the other hand softening, as it is well known, leads to negative stiffnesses in local areas whose propagation in the analysed domain renders the tangential stiffness of the problem singular and leads to failure of the procedures for solving non linear problems.

To circumvent these issues, as typical in engineering, may be convenient to renounce to completeness and make use of a model embodying only the aspects deemed to be decisive. The consequences of lack of completeness can be assessed a posteriori by examination of the results obtained. Also the model of the structure can be set up in such a way to render the inclusion of some aspects redundant. For instance if the location and extension of cracks is known from preliminary analysis or observation (for existing pre-cracked structures), and the cracks are included in the finite element mesh as local discontinuities, the omission of even such an important aspect like strain softening is justifiable. Obviously exclusion of the softening would be very inadequate if the crack generation and propagation were the purpose of the analysis. In conclusion the choice of the characteristics of a model depends on implementation issues, computational effort required, numerical convergence performance, but also on the purpose of the analysis and the range of application of the model. Models with different characteristics can finally be used for clarification of the consequences of the assumptions made, by comparison of results.

Bearing in mind the above considerations a simplified model for concrete has been defined, implemented and used for the main bulk of the analysis carried out. The results obtained with this model have been cross checked with those obtained with other simplified models already available in the LUSAS (as mentioned already LUSAS is the software used as a base for the finite element applications carried out).

The model adopted is an isotropic elastoplastic model with standard isotropic and kinematic hardening. It features an associative flow rule as dilatancy is not thought to be a key parameter for the investigation carried out (limited passive confinement is involved). The yield function used is the failure function proposed for concrete by Menetrey Willam in [68] as this reflects closely the real behaviour of concrete. The expression of the Menetrey Willam yield criterion has been slightly modified for the inclusion of isotropic and kinematic hardening according to the procedure explained in detail in the following section on the implementation of the model.

The Menetrey-Willam plasticity model is based on the hypothesis of material isotropy, whereby the yield function can be expressed in terms of the

three invariants, I_1 , J_2 and J_3 of the stress state, $\boldsymbol{\sigma}$:

$$I_1 = \text{tr } \boldsymbol{\sigma} = \boldsymbol{\sigma} \cdot \mathbf{1} \quad J_2 = \frac{1}{2} \text{tr } \mathbf{S}^2 = \frac{1}{2} \mathbf{S}^2 \cdot \mathbf{1} \quad J_3 = \frac{1}{3} \text{tr } \mathbf{S}^3 = \frac{1}{3} \mathbf{S}^3 \cdot \mathbf{1} \quad (3.27)$$

with \mathbf{S} denoting the deviatoric part of $\boldsymbol{\sigma}$, $\mathbf{1}$ the rank-two identity tensor and the symbol \cdot indicating the operation of scalar product.

For geometrical interpretation it is convenient to introduce the three Haigh-Westergaard cylindrical coordinates [22]:

$$\xi = \frac{1}{\sqrt{3}} I_1 \quad \rho = \sqrt{2 J_2} \quad \theta = \frac{1}{3} \cos^{-1} \left(\frac{3 \sqrt{3} J_3}{2 J_2^{\frac{3}{2}}} \right) \quad (3.28)$$

where ξ represents the mean stress, ρ is the norm of the deviatoric stress, and θ denotes the Lode angle.

The Menetrey-Willam yield function can then be written as follows:

$$\phi(\xi, \rho, \theta) = (A \rho)^2 + m [B \rho r(\theta, e) + C \xi] - c \quad (3.29)$$

where A , B , C , m and e represent material parameters, c accounts for isotropic hardening and r indicates the Klisinski function, defined for $\theta \in [0, \pi/3]$ by:

$$r(\theta, e) = \frac{4(1 - e^2) \cos^2 \theta + (2e - 1)^2}{2(1 - e^2) \cos \theta + (2e - 1) \sqrt{4(1 - e^2) \cos^2 \theta + 5e^2 - 4e}}; \quad (3.30)$$

for $\theta \notin [0, \pi/3]$ the following symmetry conditions are assumed:

$$r\left(\theta + n \frac{2\pi}{3}, e\right) = r(\theta, e) \quad r(-\theta, e) = r(\theta, e) \quad (3.31)$$

with n being an arbitrary integer.

From the definition of the yield function (3.29) the following remarks on the yield surface can be made:

- It is convex and smooth everywhere except at a vertex located along the hydrostatic axis, that is for any value of θ , $\rho = 0$ and $\xi = c/(mC)$;
- its sections with the planes $\theta = \theta_o = \text{const.}$ are parabolic curves;
- if $A = 0$, its section with the plane $\xi = \xi_o = \text{const.}$ is a curve whose equation in polar coordinates ρ, θ is given by:

$$\rho = \rho(\theta) = \frac{c - mC\xi_o}{mB} \frac{1}{r(\theta, e)} \quad (3.32)$$

Hence, to within the factor $(c - mC\xi_o)/(mB)$, the function defined by equation (3.32) coincides with the inverse of the Klisinski function (3.30), which is plotted in the polar diagram of Figure 3.16.

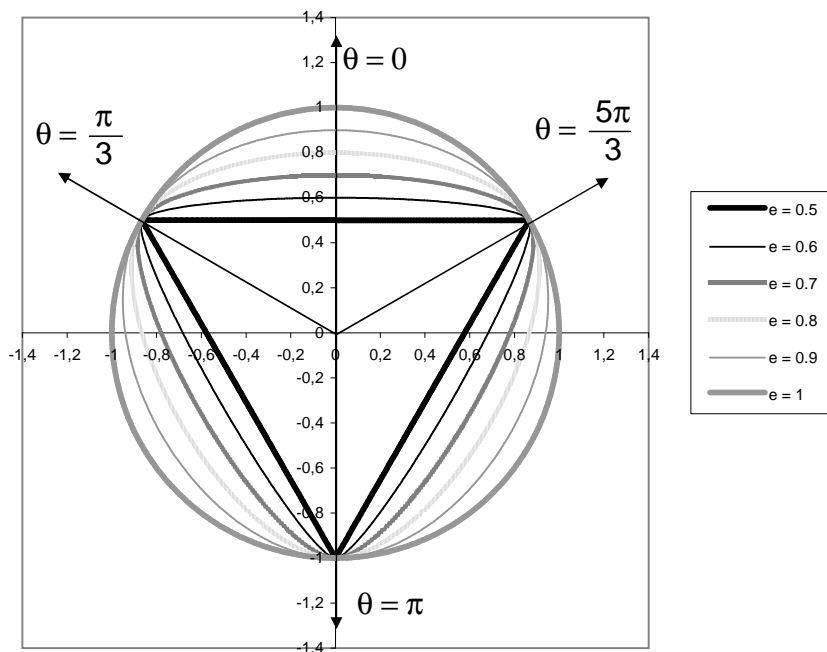


Figure 3.16: Polar diagram of the inverse of the Klisinski function.

It has been shown in [68] that the parameters in expression (3.29) can be suitably fixed so as to specialize the Menetrey-Willam yield criterion to the Hencky-von Mises, Drucker-Prager, Rankine and Leon criteria. Mohr-Coulomb criterion can also be well approximated.

Numerical implementation of the Menetrey-Willam model

The Menetrey-Willam yield function also depends upon the third invariant J_3 of the stress deviator, so that its implementation is considerably more complicated than that pertaining to models which only depend on I_1 and J_2 . An efficient and general approach to the solution of the constitutive problem and to the evaluation of the consistent tangent operator for isotropic elastoplastic models depending upon all the stress invariants has been presented in [90]. The subsequent version [98], formulated in terms of the eigenvalues of the stress tensor by adopting a spectral decomposition of the rank-four tensors appearing in the constitutive problem, is adopted here. To apply this procedure it is only required to evaluate the first and second derivatives of the yield function (3.29) with respect to the stress invariants, whose expressions are reported in the appendix for completeness.

For J_3 models the constitutive problem necessarily has to be solved it-

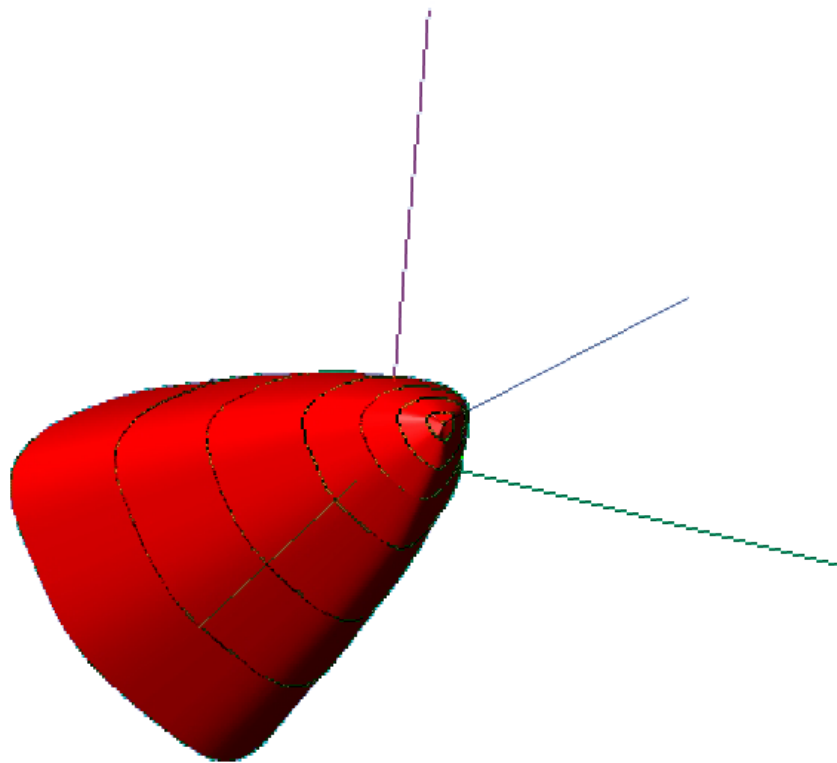


Figure 3.17: Spatial representation of the Menetrey Willam yield surface

eratively and, using a fully implicit integration scheme, this requires the inversion of a fourth-order positive-definite tensor \mathbf{G} , which changes at each iteration. This tensor is isotropic, as it is the sum of the elastic compliance tensor and of the product between the second derivative of the yield function and the plastic multiplier. Within each iteration of the solution algorithm, the tensor \mathbf{G}^{-1} is required at each ‘yielded’ integration point of the structural model and for each iteration of the local inner constitutive loop. Furthermore, it is also required for the evaluation of the consistent tangent operator, in accordance with the general formula presented in [2]. A very effective way of evaluating \mathbf{G}^{-1} in closed form as a function of the eigenvectors and eigenprojectors of the stress deviator has been given in [98] and therein applied to the Willam-Warnke plasticity model. The same approach described in [98] has been successfully employed here for the case of the Menetrey-Willam criterion.

Although only the Yield function has been formulated by Menetrey and Willam the model will be referred to as Menetrey Willam model for simplicity in the sequel.

3.5 Solution procedure for J_3 plasticity

3.5.1 Introduction

As anticipated a yield criterion suitable for concrete must depend on all the three invariants of the stress tensor. In particular in the Menetrey Willam criterion selected for the applications presented in this work this dependence is expressed by the Klisinsky function $r(\theta, e)$ as θ is a function of J_3 .

In the following we will refer to elasto-plastic problems governed by a yield function dependant on the third principal invariant of the stress tensor as J_3 plasticity and to elasto-plastic problems independent on J_3 as J_2 plasticity .

In J_3 plasticity contrary to 3D and plane strain problems in J_2 plasticity, in which the numerical integration of the constitutive problem is reducible to the solution of a scalar equation, a local nonlinear system must be solved.

Note that the elasto-plastic problem is formulated in incremental form. Integration of the stresses for a given strain path cannot be done in closed form. To overcome this difficulty (pseudo)time discretization is required and the load (and therefore the iterative strain) is increased in finite steps.

At each time (strain) increment the stresses corresponding to the current value of the total strain must be evaluated. Note that the above stresses depend not only on the current total strains but also on the strain history. Also note that we are discussing the elasto-plastic problem as strain driven. This

is because we are referring to the common displacement based formulation the finite element method in which at the beginning of each iteration of each increment in the nonlinear solution algorithm (in the present case, the full Newton-Raphson) the total strain is known and the corresponding stress are to be evaluated.

The algorithm yielding the stresses at each iteration at each load increment is called return mapping because if the total stresses due to an elastic increment violates the yield condition, the stresses are returned onto the yield surface by application of plastic strains.

In this section it is shown how the return mapping can be carried out efficiently in the case of J_3 plasticity and an expression of the consistent tangent operator for the use of the full Newton-Raphson algorithm is given. The Newton-Raphson algorithm and its application to the solution of nonlinear finite element problems are not discussed as assumed well known to the reader.

In [90, 98] it is shown how the assumptions of isotropic elastic behaviour and the isotropy of the yield function allow one to obtain in intrinsic form the inverse of an elasto-plastic compliance tensor \mathbb{G} required in the exact linearization of the constitutive problem. The approach is presented in [90] and moved from an original representation formula for the inverse of tensor \mathbb{G} which expresses it as a linear combination of dyadic and square tensor products of the rank two identity $\mathbf{1}$, the stress deviator \mathbf{S} and its square \mathbf{S}^2 .

The assemblage of the inverse of the mentioned fourth order tensor \mathbb{G} is of key importance in the finite element procedure as it is required at each gauss point at each iteration of each load increment. A fast and robust algorithm for its computation is therefore essential.

The evaluation of \mathbb{G}^{-1} according to the proposed methodology allows one to perform the return mapping algorithm and to compute the consistent tangent operator very efficiently since the required operations are multiplications between 3×3 matrices and the construction of the matrix representation of the fourth-order tensors $(\mathbf{S}_i \otimes \mathbf{S}_j + \mathbf{S}_j \otimes \mathbf{S}_i)$ and $(\mathbf{S}_k \boxtimes \mathbf{S}_l + \mathbf{S}_l \boxtimes \mathbf{S}_k)$.

Besides, in the adopted approach one can directly express the consistent tangent operator in the given reference frame; computationally heavy transformations of fourth-order tensors with respect to the reference frame associated with the eigenvectors of \mathbf{S} can thus be completely avoided.

The method described can be applied to any isotropic J_3 elasto-plastic model. Isotropic and Kinematic hardening are also included.

The specific yield criterion enter this formulation only by means of scalar coefficients here referred to as $e_1, e_2, e_3, e_4, e_5, e_6, e_7, e_8$. The expressions of these coefficients for the case of Menetrey Willam Yield function are also given in this section.

3.5.2 Continuum formulation of the elasto-plastic problem

To set the stage, we outline the basic continuum equations for elastoplasticity. Under the small strain hypothesis the total strain $\boldsymbol{\epsilon}$ can be additively decomposed into its elastic component \mathbf{e} and its plastic component \mathbf{p} :

$$\boldsymbol{\epsilon} = \mathbf{e} + \mathbf{p} \quad (3.33)$$

According to such relation, the stored energy function can be introduced in fully decoupled form [49] as:

$$\psi(e, \boldsymbol{\alpha}) = \psi_{el}(\mathbf{e}) + \psi_h(\boldsymbol{\alpha}) \quad (3.34)$$

where $\psi_{el} : \mathcal{D} \mapsto \mathfrak{R}$ and $\psi_h : \mathcal{X} \mapsto \mathfrak{R}$ represent, respectively, the elastic energy and the hardening potential, this last one characterising the inelastic response in terms of a set of kinematic internal variables $\boldsymbol{\alpha} \in \mathcal{X}$.

A suitable form of the potential ψ_h and of the internal variables $\boldsymbol{\alpha}$ allows one to account for several hardening behaviours; in particular, we shall make reference in the sequel to a hardening law which describes the combined kinematic and isotropic hardening while mechanisms. To this end the internal variable $\boldsymbol{\alpha}$ is partitioned as:

$$\boldsymbol{\alpha} = (\boldsymbol{\eta}, \zeta)$$

where $\boldsymbol{\eta} \in \mathcal{D}$ denotes a tensorial variable accounting for kinematic hardening while ζ is a scalar variable referring to the isotropic one. As a particular choice, the stored energy function $\psi : \mathcal{D} \times \mathcal{D} \times \mathfrak{R} \mapsto \mathfrak{R}$ can be defined as the positive definite quadratic form:

$$\psi(\mathbf{e}, \boldsymbol{\eta}, \zeta) = \frac{1}{2} \mathbb{E} \mathbf{e} \cdot \mathbf{e} + \frac{1}{2} \mathbb{H}_{kin} \boldsymbol{\eta} \cdot \boldsymbol{\eta} + \frac{1}{2} h_{iso} \zeta^2 \quad (3.35)$$

where, for isotropy, the elastic tensor \mathbb{E} is given by:

$$\mathbb{E} = K(\mathbf{1} \otimes \mathbf{1}) + 2G \left[\mathbb{I} - \frac{1}{3}(\mathbf{1} \otimes \mathbf{1}) \right] \quad (3.36)$$

with K and G representing the bulk and the shear moduli respectively; besides, \mathbb{H}_{kin} and h_{iso} denote in turn a positive definite isotropic tensor and a scalar. By making use of the standard thermodynamic arguments the constitutive relations for the stress $\boldsymbol{\sigma} \in \mathcal{S}$ and the thermodynamic forces are thus identified as:

$$\begin{cases} \boldsymbol{\sigma} = d_e \psi_{el}(\mathbf{e}) = \mathbb{E} \mathbf{e} \\ \boldsymbol{\beta} = d_\eta \psi_h(\boldsymbol{\alpha}) = \mathbb{H}_{kin} \boldsymbol{\eta} \\ \boldsymbol{\rho} = d_\zeta \psi_h(\boldsymbol{\alpha}) = h_{iso} \boldsymbol{\zeta} \end{cases} \quad (3.37)$$

where $\boldsymbol{\beta} \in \mathcal{S}$ is the back-stress tensor and $\rho \in \mathfrak{R}$ is a stress-like scalar measure of the homothetic expansion of the yield locus \mathbf{C} . This last one is given by:

$$\mathbf{C} = \{(\boldsymbol{\sigma}, \boldsymbol{\beta}, \rho) \in \mathcal{S} \times \mathcal{S} \times \mathfrak{R} : \phi(\boldsymbol{\sigma}, \boldsymbol{\beta}, \rho) \leq 0\} \quad (3.38)$$

is defined in terms of a convex yield mode ϕ which in accordance with the meaning attributed to the internal variables, is given the expression:

$$\phi(\boldsymbol{\sigma}, \boldsymbol{\beta}, \rho) = \phi(\boldsymbol{\tau}, \rho) = \varphi(I_1, J_2, J_3) - \rho - Y_o = 0 \quad (3.39)$$

where Y_o depends upon the initial uniaxial yield limit of the material,

$$I_1 = tr(\boldsymbol{\tau}) \quad J_2 = \frac{1}{2} tr(\mathbf{S}^2) \quad J_3 = \frac{1}{3} tr(\mathbf{S}^3),$$

are the principal stress invariants and $\mathbf{S} = \boldsymbol{\tau} - \frac{1}{3} tr(\boldsymbol{\tau}) \mathbf{1}$ is the deviator of the relative stress $\boldsymbol{\tau} = \boldsymbol{\sigma} - \boldsymbol{\beta}$.

The definition of the model is completed by introducing the evolution equation for the plastic strain and the internal variables. In standard plasticity formulations they are provided by the maximum dissipation principle [49] which, for the case at hand, yields:

$$\begin{cases} \dot{\mathbf{p}} = \dot{\boldsymbol{\eta}} = \dot{\lambda} d_\tau \phi(\boldsymbol{\tau}, \rho) = \dot{\lambda} \mathbf{n} \\ \dot{\boldsymbol{\zeta}} = \dot{\lambda} d_\rho \phi(\boldsymbol{\tau}, \rho) = \dot{\lambda} \end{cases} \quad (3.40)$$

where \mathbf{n} is the normal to the yield surface:

$$\begin{aligned} \mathbf{n} = d_\tau \phi &= \frac{\partial \varphi}{\partial I_1} \mathbf{1} + \frac{\partial \varphi}{\partial J_2} \mathbf{S} + \frac{\partial \varphi}{\partial J_3} (\mathbf{S}^2 - \frac{2}{3} J_2 \mathbf{1}) = \\ &= (d_1 \varphi - \frac{2}{3} J_2 d_3 \varphi) \mathbf{1} + (d_2 \varphi) \mathbf{S} + (d_3 \varphi) \mathbf{S}^2 = \\ &= n_1 \mathbf{1} + n_2 \mathbf{S} + n_3 \mathbf{S}^2; \end{aligned} \quad (3.41)$$

$\dot{\lambda}$ is the plastic consistency parameter which represents a Lagrange multiplier obeying the loading/unloading conditions in Kuhn-Tucker form:

$$\phi(\boldsymbol{\tau}, \rho) \leq 0 \quad \dot{\lambda} \geq 0 \quad \dot{\lambda} \phi(\boldsymbol{\tau}, \rho) = 0, \quad (3.42)$$

along with Prager's consistency rule:

$$\dot{\lambda} \dot{\phi}(\boldsymbol{\tau}, \rho) = 0. \quad (3.43)$$

The above constitutive equations define a unilaterally constrained problem of evolution which, in an algorithmic framework, is transformed into a sequence of constrained optimization problems by means of a suitable integration algorithm. In particular, we shall adopt in the sequel the fully implicit (*backward Euler*) integration scheme according to which the fulfilment of the discrete flow equations is enforced at the end of the time step.

Summarizing the constitutive equations governing an associative elasto-plastic material model endowed with linear kinematic and isotropic hardening are:

$$\begin{cases} \boldsymbol{\sigma} = \mathbb{E}\mathbf{e} = \mathbb{E}(\boldsymbol{\varepsilon} - \mathbf{p}) \\ \boldsymbol{\beta} = \mathbb{H}_{kin}\boldsymbol{\eta} \\ \boldsymbol{\rho} = h_{iso}\boldsymbol{\zeta} \\ \dot{\mathbf{p}} = \lambda d_{\boldsymbol{\tau}}\phi(\boldsymbol{\tau}, \boldsymbol{\rho}) \\ \dot{\boldsymbol{\zeta}} = \lambda d_{\boldsymbol{\rho}}\phi(\boldsymbol{\tau}, \boldsymbol{\rho}) = \dot{\lambda} \\ \phi(\boldsymbol{\tau}, \boldsymbol{\delta}) \leq 0 \quad \dot{\lambda} \geq 0 \quad \dot{\lambda}\phi(\boldsymbol{\tau}, \boldsymbol{\delta}) = 0 \end{cases} \quad (3.44)$$

3.5.3 Stress computation

The solution of the problem defined in section 3.5.2 is not achievable in closed form. However, as anticipated, the problem can be solved numerically through (pseudo-) time discretization. The time discretization amounts to subdividing the time interval of interest, say $[0, T]$, into a sequence of non-overlapping time steps $[t_n, t_{n+1}]$; for each one of these and at each point x of the body, one has to construct and solve the discrete counterpart of the constitutive equations by approximating the evolution laws. This problem is *local* and amounts to compute the updated local state variables $\{\boldsymbol{\varepsilon}_{n+1}, \mathbf{p}_{n+1}, \boldsymbol{\sigma}_{n+1} \dots\}$ at the time t_{n+1} starting with their known values at t_n and from the incremental total strains obtained by the iteration solution of the global equilibrium problem.

Accordingly, considering the initial conditions :

$$\boldsymbol{\varepsilon}(t_n) = \boldsymbol{\varepsilon}_o; \quad \mathbf{p}(t_n) = \mathbf{p}_o; \quad \boldsymbol{\zeta}(t_n) = \boldsymbol{\zeta}_o \quad (3.45)$$

The discrete counterpart of the problem defined in section 3.5.2 is:

$$\begin{cases} \boldsymbol{\tau}^{tr} = \mathbb{E}\boldsymbol{\varepsilon} - (\mathbb{E} + \mathbb{H}_{kin})\mathbf{p}_o \\ \boldsymbol{\rho}^{tr} = h_{iso}\boldsymbol{\zeta}_o \\ \phi^{tr} = \phi(\boldsymbol{\tau}^{tr}, \boldsymbol{\rho}^{tr}) \\ \mathbf{p} - \mathbf{p}_o = \lambda d_{\boldsymbol{\tau}}\phi(\boldsymbol{\tau}, \boldsymbol{\rho}) \\ \boldsymbol{\zeta} - \boldsymbol{\zeta}_o = -\lambda d_{\boldsymbol{\rho}}\phi(\boldsymbol{\tau}, \boldsymbol{\rho}) \\ \phi(\boldsymbol{\tau}, \boldsymbol{\rho}) < 0 \quad \lambda > 0 \quad \lambda\phi(\boldsymbol{\tau}, \boldsymbol{\rho}) = 0 \end{cases} \quad (3.46)$$

The first three equations in 3.46 define the *trial state* i.e. the stress state obtained freezing the state variables to their value at the end of the previous increment. The trial state can be easily computed without any iterative procedure as it is seen from the equations. Accordingly, if $\phi^{tr} \leq 0$ the trial state coincides with the final one and nothing else needs to be computed. If $\phi^{tr} > 0$, instead, plastic consistency has to be restored by solving the plastic equations.

For plastic loading, the last three equations in 3.46 define a nonlinear system for which the trial state provide the starting value of the iterative process. By adopting a full Newton's scheme, the last three equations in 3.46 are linearized around the k-th estimate of the solution to get:

$$\begin{cases} \mathbf{r}_{\mathbf{p}}^{(k)} - \delta \mathbf{p}_k^{(k+1)} + \lambda^{(k)} d_{\tau\tau}^2 \phi^{(k)} \delta \boldsymbol{\tau}_k^{(k+1)} + d_{\tau} \phi^{(k)} \delta \lambda_{(k)}^{(k+1)} = \mathbf{0} \\ \mathbf{r}_{\boldsymbol{\zeta}}^{(k)} \delta \boldsymbol{\zeta}_k^{(k+1)} - \delta \lambda_{(k)}^{(k+1)} = \mathbf{0} \\ \mathbf{r}_{\phi}^{(k)} + d_{\tau} \phi^{(k)} \delta \boldsymbol{\tau}_k^{(k+1)} - \delta \boldsymbol{\rho}_k^{(k+1)} = \mathbf{0}, \end{cases} \quad (3.47)$$

where the residuals are defined by :

$$\begin{cases} \mathbf{r}_{\mathbf{p}}^{(k)} = -\mathbf{p}^{(k)} + \mathbf{p}_o + \lambda^{(k)} d_{\tau} \phi^{(k)} \\ \mathbf{r}_{\boldsymbol{\zeta}}^{(k)} = \boldsymbol{\zeta}^{(k)} - \boldsymbol{\zeta}_o - \lambda^{(k)} \\ \mathbf{r}_{\phi}^{(k)} = \phi(\boldsymbol{\tau}^{(k)}, \boldsymbol{\rho}^{(k)}) - \phi^{(k)}; \end{cases} \quad (3.48)$$

in which the symbol $\delta(\cdot)_{(k)}^{(k+1)} = (\cdot)^{(k+1)} - (\cdot)^{(k)}$ denotes the iterative increments of (\cdot) . The solution of 3.47 is obtained by observing that the linearization of the state equations around $(\boldsymbol{\tau}^{(k)}, \boldsymbol{\rho}^{(k)})$ yields:

$$\delta \mathbf{p}_k^{(k+1)} = -[\mathbb{E} + \mathbb{H}_{kin}]^{-1} \delta \boldsymbol{\tau}_k^{(k+1)} \quad \delta \boldsymbol{\zeta}_k^{(k+1)} = \frac{1}{h_{iso}} \delta \boldsymbol{\rho}_k^{(k+1)}$$

so that equations 3.47 can be recast in the form:

$$\begin{bmatrix} \mathbf{r}_{\mathbf{p}}^{(k)} \\ \mathbf{r}_{\boldsymbol{\zeta}}^{(k)} \\ \mathbf{r}_{\phi}^{(k)} \end{bmatrix} + \begin{bmatrix} \mathbb{G}^{(k)} & \mathbf{0} & d_{\tau} \phi^{(k)} \\ \mathbf{0} & \frac{1}{h_{iso}} & -1 \\ d_{\tau} \phi^{(k)} & -1 & 0 \end{bmatrix} \begin{bmatrix} \delta \boldsymbol{\tau}_k^{(k+1)} \\ \delta \boldsymbol{\rho}_k^{(k+1)} \\ \delta \lambda_{(k)}^{(k+1)} \end{bmatrix} = \mathbf{0} \quad (3.49)$$

where $\mathbb{G}^{(k)}$ is the fourth order tensor defined by:

$$\mathbb{G}^{(k)} = [\mathbb{E} + \mathbb{H}_{kin}]^{-1} + \lambda^{(k)} d_{\tau\tau}^2 \phi^{(k)}. \quad (3.50)$$

Due to the convexity of the yield function \mathbb{G} is positive-definite so that the system 3.49 can be reduced and solved for $\delta \lambda_{(k)}^{(k+1)}$:

$$\delta\lambda_{(k)}^{(k+1)} = \frac{\mathbf{r}_\phi^{(k)} - [\mathbb{G}^{(k)}]^{-1}\mathbf{r}_\mathbf{p}^{(k)} \cdot d_\tau\phi^{(k)} + h_{iso}\mathbf{r}_\zeta^{(k)}}{[\mathbb{G}^{(k)}]^{-1}d_\tau\phi^{(k)} \cdot d_\tau\phi^{(k)} + h_{iso}} \quad (3.51)$$

from which the iterative values of the state variables can be easily updated:

$$\begin{cases} \lambda^{(k+1)} = \lambda^{(k)} + \delta\lambda_{(k)}^{(k+1)} \\ \boldsymbol{\tau}^{(k+1)} = \boldsymbol{\tau}^{(k)} - [\mathbb{G}^{(k)}]^{-1}(\mathbf{r}_\mathbf{p}^{(k)} + \delta\lambda_{(k)}^{(k+1)}d_\tau\phi^{(k)}) \\ \boldsymbol{\rho}^{(k+1)} = \boldsymbol{\rho}^{(k)} + h_{iso}(\delta\lambda_{(k)}^{(k+1)} - \mathbf{r}_\zeta^{(k)}) \\ \mathbf{p}^{(k+1)} = \mathbf{p}_o + [\mathbb{E} + \mathbb{H}_{kin}]^{-1}(\boldsymbol{\tau}^{tr} - \boldsymbol{\tau}^{(k+1)}) \\ \boldsymbol{\zeta}^{(k+1)} = \frac{1}{h_{iso}}\boldsymbol{\rho}^{(k+1)}. \end{cases}$$

3.5.4 The consistent tangent operator

To use a full Newton's approach in the solution of the nonlinear finite element problem the consistent tangent operator needs to be computed. The term consistent is used to highlight that the operator is not associated with the continuum formulation of the elastoplastic problem but with its discrete counterpart (3.44).

The consistent tangent operator for the problem expressed by (3.44) \mathbb{E}^{tan} is given by the expression:

$$\mathbb{E}^{\text{tan}} = d_\epsilon\boldsymbol{\sigma},$$

In order to find a convenient expression for this operator let us rewrite (3.44) in the following form:

$$\begin{cases} \boldsymbol{\sigma} = d\psi_{el}(\boldsymbol{\epsilon} - \mathbf{p}) \\ \boldsymbol{\beta} = d\psi_{kin}(\boldsymbol{\eta}) \\ \rho = d\psi_{iso}(\boldsymbol{\zeta}) \\ \mathbf{p} - \mathbf{p}_o = \lambda d_\sigma\phi(\boldsymbol{\sigma}, \boldsymbol{\beta}, \rho) \\ \boldsymbol{\eta} - \boldsymbol{\eta}_o = \lambda d_\beta\phi(\boldsymbol{\sigma}, \boldsymbol{\beta}, \rho) \\ \boldsymbol{\zeta} - \boldsymbol{\zeta}_o = \lambda d_\rho\phi(\boldsymbol{\sigma}, \boldsymbol{\beta}, \rho) \\ \phi(\boldsymbol{\sigma}, \boldsymbol{\beta}, \rho) \leq \mathbf{0} \quad \lambda \geq 0 \quad \lambda = \phi(\boldsymbol{\sigma}, \boldsymbol{\beta}, \rho) \end{cases} \quad (3.52)$$

In equation (3.52) $d\psi_{el}$, $d\psi_{kin}$, $d\psi_{iso}$ are the three terms on the right hand side of equation (3.52).

To find the tangent operator of the problem under consideration we will define a generalized standard material (GSM) as introduced by Halphen and Nguyen in [6]. This allows us to handle plasticity with hardening in the same formal way as we do for perfect plasticity. Then we derive the consistent

tangent operator for the GSM. Finally we derive the desired operator from the latter.

The generalized standard material

The constitutive model for the generalized standard material is defined grouping the kinematic and static internal variables in the vector $\alpha \in \mathcal{X} = \mathcal{D} \times \mathfrak{R}$ and $\chi \in \mathcal{X}' = \mathcal{S} \times \mathfrak{R}$:

$$\alpha = \begin{bmatrix} \eta \\ \zeta \end{bmatrix} \quad \chi = \begin{bmatrix} \beta \\ \rho \end{bmatrix}, \quad (3.53)$$

The key of the GSM consists in defining the generalized total, elastic and plastic strains, denoted by $\tilde{\varepsilon}$, $\tilde{\mathbf{e}}$ and $\tilde{\mathbf{p}}$ and the generalized stress $\tilde{\sigma}$, belonging in turn to the product spaces $\tilde{\mathcal{D}} = \mathcal{D} \times \mathcal{X}$ and $\tilde{\mathcal{S}} = \mathcal{S} \times \mathcal{X}'$, as follows:

$$\tilde{\varepsilon} = \begin{bmatrix} \varepsilon \\ \mathbf{0} \end{bmatrix} \quad \tilde{\mathbf{e}} = \begin{bmatrix} \mathbf{e} \\ \mathbf{0} \end{bmatrix} \quad \tilde{\mathbf{p}} = \begin{bmatrix} \mathbf{p} \\ -\alpha \end{bmatrix} \quad \tilde{\sigma} = \begin{bmatrix} \sigma \\ \chi \end{bmatrix}. \quad (3.54)$$

In the sequel we shall use the notation $\tilde{\sigma} = (\sigma, \chi)$. The plastic consistency condition is now enforced on the generalized stress $\tilde{\sigma}$ and states that $\tilde{\sigma}$ must belong to the closed *generalized convex elastic domain* $\tilde{\mathcal{C}} \subseteq \tilde{\mathcal{S}}$ defined by:

$$\tilde{\mathcal{C}} = \{ \tilde{\sigma} \in \tilde{\mathcal{S}} : \tilde{\phi}(\tilde{\sigma}) \leq 0 \iff (\sigma, \chi) \leq 0 \}. \quad (3.55)$$

where $\tilde{\phi} : \tilde{\mathcal{S}} \rightarrow \mathfrak{R}$ is the yield function expressed in terms of generalized stresses. The duality product between the generalized variables is induced by the corresponding ones between \mathcal{D} and \mathcal{S} as well as the ones between \mathcal{X} and \mathcal{X}' :

$$\tilde{\sigma} \cdot \tilde{\varepsilon} = \sigma \cdot \varepsilon \quad \tilde{\sigma} \cdot \tilde{\mathbf{e}} = \sigma \cdot \mathbf{e} + \chi \cdot \alpha \quad \tilde{\sigma} \cdot \tilde{\mathbf{p}} = \sigma \cdot \mathbf{p} - \chi \cdot \alpha \quad (3.56)$$

where, for simplicity, the same symbol has been used to denote duality products defined on different pairs of dual linear spaces. In terms of the generalized variables, equations (3.52) are rewritten in a more compact form:

$$\begin{cases} \tilde{\sigma} = d\tilde{\psi}(\tilde{\varepsilon} - \tilde{\mathbf{p}}) \\ \tilde{\mathbf{p}} - \tilde{\mathbf{p}}_o = \lambda d\tilde{\phi}(\tilde{\sigma}) \\ \tilde{\phi}(\tilde{\sigma}) \leq 0 \quad \lambda \geq 0 \quad \lambda \tilde{\phi}(\tilde{\sigma}) = 0 \end{cases} \quad (3.57)$$

thus assuming the same formal expression of perfect plasticity.

The function $\tilde{\psi}$, is given by

$$\tilde{\psi}(\tilde{\mathbf{e}}) = \psi_{el}(\mathbf{e}) + \psi_{kin}(\boldsymbol{\eta}) + \psi_{iso}(\boldsymbol{\varsigma}) \quad (3.58)$$

represent the Helmotz free energy and it is assumed to be strictly convex and smooth as a consequence of the same properties of the elastic and hardening potentials ψ_{el} , ψ_{kin} and ψ_{iso} .

The consistent tangent operator for the GSM

We now derive the expression of the consistent tangent operator for the generalized standard material.

To this end, differentiating equation (3.57) with respect to $\tilde{\mathbf{e}}$, we get

$$(d_{\tilde{\mathbf{e}}}\tilde{\boldsymbol{\sigma}})\tilde{\boldsymbol{\varepsilon}}^* = d_{\tilde{\mathbf{e}}\tilde{\mathbf{e}}}^2\tilde{\psi}[\tilde{\boldsymbol{\varepsilon}}^* - (d_{\tilde{\mathbf{e}}}\tilde{\mathbf{p}})\tilde{\boldsymbol{\varepsilon}}^*], \quad \forall \tilde{\boldsymbol{\varepsilon}}^* \in \tilde{\mathcal{D}}. \quad (3.59)$$

From equation (3.57) we get the expression:

$$(d_{\tilde{\mathbf{e}}}\tilde{\mathbf{p}})\tilde{\boldsymbol{\varepsilon}}^* = \lambda(d_{\tilde{\sigma}\tilde{\sigma}}^2\tilde{\phi})(d_{\tilde{\mathbf{e}}}\tilde{\boldsymbol{\sigma}})\tilde{\boldsymbol{\varepsilon}}^* + (d_{\tilde{\mathbf{e}}}\lambda \cdot \tilde{\boldsymbol{\varepsilon}}^*)d_{\tilde{\sigma}}\tilde{\phi}, \quad \forall \tilde{\boldsymbol{\varepsilon}}^* \in \tilde{\mathcal{D}}. \quad (3.60)$$

which, substituted into equation (3.59), provides

$$\begin{aligned} (d_{\tilde{\mathbf{e}}}\tilde{\boldsymbol{\sigma}})\tilde{\boldsymbol{\varepsilon}}^* &= (d_{\tilde{\mathbf{e}}\tilde{\mathbf{e}}}^2\tilde{\psi})\tilde{\boldsymbol{\varepsilon}}^* - \lambda(d_{\tilde{\mathbf{e}}\tilde{\mathbf{e}}}^2\tilde{\psi})(d_{\tilde{\sigma}\tilde{\sigma}}^2\tilde{\phi})(d_{\tilde{\mathbf{e}}}\tilde{\boldsymbol{\sigma}})\tilde{\boldsymbol{\varepsilon}}^* - (d_{\tilde{\mathbf{e}}}\lambda \cdot \tilde{\boldsymbol{\varepsilon}}^*)(d_{\tilde{\mathbf{e}}\tilde{\mathbf{e}}}^2\tilde{\psi})d_{\tilde{\sigma}}\tilde{\phi}, \\ \forall \tilde{\boldsymbol{\varepsilon}}^* &\in \tilde{\mathcal{D}}. \end{aligned} \quad (3.61)$$

Grouping together the terms multiplying $d_{\tilde{\mathbf{e}}}\tilde{\boldsymbol{\sigma}}$ and pre multiplying by the compliance operator $(d_{\tilde{\mathbf{e}}\tilde{\mathbf{e}}}^2\tilde{\psi})^{-1}$ we get

$$[(d_{\tilde{\mathbf{e}}\tilde{\mathbf{e}}}^2\tilde{\psi})^{-1} + \lambda(d_{\tilde{\sigma}\tilde{\sigma}}^2\tilde{\phi})](d_{\tilde{\mathbf{e}}}\tilde{\boldsymbol{\sigma}})\tilde{\boldsymbol{\varepsilon}}^* = \tilde{\boldsymbol{\varepsilon}}^* - (d_{\tilde{\mathbf{e}}}\lambda \cdot \tilde{\boldsymbol{\varepsilon}}^*)d_{\tilde{\sigma}}\tilde{\phi}, \quad \forall \tilde{\boldsymbol{\varepsilon}}^* \in \tilde{\mathcal{D}}. \quad (3.62)$$

and hence:

$$(d_{\tilde{\mathbf{e}}}\tilde{\boldsymbol{\sigma}})\tilde{\boldsymbol{\varepsilon}}^* = \tilde{\mathbb{W}}\tilde{\boldsymbol{\varepsilon}}^* - (d_{\tilde{\mathbf{e}}}\lambda \cdot \tilde{\boldsymbol{\varepsilon}}^*)\tilde{\mathbb{W}}d_{\tilde{\sigma}}\tilde{\phi}, \quad \forall \tilde{\boldsymbol{\varepsilon}}^* \in \tilde{\mathcal{D}}. \quad (3.63)$$

where $\tilde{\mathbb{W}}$ denotes the operator

$$\tilde{\mathbb{W}} = [(d_{\tilde{\mathbf{e}}\tilde{\mathbf{e}}}^2\tilde{\psi})^{-1} + \lambda(d_{\tilde{\sigma}\tilde{\sigma}}^2\tilde{\phi})]^{-1}. \quad (3.64)$$

notice that $\tilde{\mathbb{W}}$ is symmetric and positive definite. Actually it is the sum of the tangent generalized elastic compliance $(d_{\tilde{\mathbf{e}}\tilde{\mathbf{e}}}^2\tilde{\psi})^{-1}$ and the quantity $\lambda(d_{\tilde{\sigma}\tilde{\sigma}}^2\tilde{\phi})$ which is symmetric and positive semidefinite since $\tilde{\phi}$ is convex and λ is non negative. In order to get the expression of $(d_{\tilde{\mathbf{e}}}\lambda \cdot \tilde{\boldsymbol{\varepsilon}}^*)$ the fulfillment of Prager's condition is enforced:

$$(d_{\tilde{\varepsilon}}\tilde{\sigma})\tilde{\varepsilon} \cdot d_{\tilde{\sigma}}\tilde{\phi} = 0 \iff d_{\tilde{\varepsilon}}\lambda \cdot \tilde{\varepsilon}^* = \frac{\tilde{\mathbb{W}}\tilde{\varepsilon}^* \cdot d_{\tilde{\sigma}}\tilde{\phi}}{\tilde{\mathbb{W}}d_{\tilde{\sigma}}\tilde{\phi} \cdot d_{\tilde{\sigma}}\tilde{\phi}}, \quad \forall \tilde{\varepsilon}^* \in \tilde{\mathcal{D}}. \quad (3.65)$$

by substituting equation (3.65) into equation (3.64) and by exploiting the symmetry of $\tilde{\mathbb{W}}$ we get

$$(d_{\tilde{\varepsilon}}\tilde{\sigma})\tilde{\varepsilon} = \tilde{\mathbb{W}}\tilde{\varepsilon}^* - \frac{\tilde{\mathbb{W}}\tilde{\varepsilon}^* \cdot d_{\tilde{\sigma}}\tilde{\phi}}{\tilde{\mathbb{W}}d_{\tilde{\sigma}}\tilde{\phi} \cdot d_{\tilde{\sigma}}\tilde{\phi}}\tilde{\mathbb{W}}d_{\tilde{\sigma}}\tilde{\phi} = \tilde{\mathbb{E}}^{\text{tan}}\tilde{\varepsilon}^*, \quad \forall \tilde{\varepsilon}^* \in \tilde{\mathcal{D}}. \quad (3.66)$$

Introducing the following notations:

$$\tilde{\mathbf{N}} = \tilde{\mathbb{W}}d_{\tilde{\sigma}}\tilde{\phi} \quad \beta = \tilde{\mathbb{W}}d_{\tilde{\sigma}}\tilde{\phi} \cdot d_{\tilde{\sigma}}\tilde{\phi}, \quad (3.67)$$

the consistent tangent operator for the GSM assumes the compact expression:

$$\tilde{\mathbb{E}}^{\text{tan}} = \tilde{\mathbb{W}} - \frac{1}{\beta}\tilde{\mathbf{N}} \otimes \tilde{\mathbf{N}}. \quad (3.68)$$

Note that from a mechanical point of view, the operator $\tilde{\mathbb{W}}$ represents a reduced stiffness with respect to the generalized elastic one $d_{\tilde{\varepsilon}\tilde{\varepsilon}}^2\tilde{\psi}$. Actually, reasoning in terms of compliances, the positive semidefiniteness of $\lambda(d_{\tilde{\sigma}\tilde{\sigma}}^2\tilde{\phi})$ yields

$$\tilde{\mathbb{W}}^{-1}\tilde{\sigma} \cdot \tilde{\sigma} \geq \lambda(d_{\tilde{\sigma}\tilde{\sigma}}^2\tilde{\phi})^{-1}\tilde{\sigma} \cdot \tilde{\sigma} \quad \forall \tilde{\sigma}. \quad (3.69)$$

Specialization to elastoplasticity with kinematic and isotropic hardening

Recalling the definitions of $\tilde{\sigma}$ and $\tilde{\varepsilon}$, $\tilde{\mathbb{W}}$ and $\tilde{\mathbf{N}}$ can be conveniently partitioned as follows:

$$\tilde{\mathbb{W}} = \begin{bmatrix} \tilde{\mathbb{W}}_{11} & \tilde{\mathbb{W}}_{12} & \tilde{\mathbb{W}}_{13} \\ \tilde{\mathbb{W}}_{21} & \tilde{\mathbb{W}}_{22} & \tilde{\mathbb{W}}_{23} \\ \tilde{\mathbb{W}}_{31} & \tilde{\mathbb{W}}_{32} & \tilde{\mathbb{W}}_{33} \end{bmatrix} \quad \tilde{\mathbf{N}} = \begin{bmatrix} \tilde{\mathbf{N}}_1 \\ \tilde{\mathbf{N}}_2 \\ \tilde{\mathbf{N}}_3 \end{bmatrix}, \quad (3.70)$$

so that the consistent tangent operator for the GSM can be represented in the form:

$$\tilde{\mathbb{E}}^{\text{tan}} = \begin{bmatrix} \tilde{\mathbb{E}}_{11}^{\text{tan}} & \tilde{\mathbb{E}}_{12}^{\text{tan}} & \tilde{\mathbb{E}}_{13}^{\text{tan}} \\ \tilde{\mathbb{E}}_{21}^{\text{tan}} & \tilde{\mathbb{E}}_{22}^{\text{tan}} & \tilde{\mathbb{E}}_{23}^{\text{tan}} \\ \tilde{\mathbb{E}}_{31}^{\text{tan}} & \tilde{\mathbb{E}}_{32}^{\text{tan}} & \tilde{\mathbb{E}}_{33}^{\text{tan}} \end{bmatrix}. \quad (3.71)$$

Denoting by q the dimension of \mathcal{D} and \mathcal{S} , the entries $\tilde{\mathbb{E}}_{ij}^{\text{tan}}$, for $i,j=1,2$, are $q \times q$ matrices while the matrices associated with the terms $\tilde{\mathbb{E}}_{i3}^{\text{tan}}$ and $\tilde{\mathbb{E}}_{3i}^{\text{tan}}$, for $i=1,2$, have dimension $q \times 1$ and $1 \times q$, respectively. Finally, the term $\tilde{\mathbb{E}}_{33}^{\text{tan}}$ turns out to be a scalar.

The consistent tangent operator, which has to be used in the solution algorithm for the elastoplastic structural problem, coincides with the term $\tilde{\mathbb{E}}_{11}^{\text{tan}}$:

$$\mathbb{E}^{\text{tan}} = \tilde{\mathbb{E}}_{11}^{\text{tan}} = d_{\epsilon} \boldsymbol{\sigma}, \quad (3.72)$$

or equivalently:

$$\mathbb{E}^{\text{tan}} = \tilde{\mathbb{W}}_{11} - \frac{\tilde{\mathbf{N}}_1 \otimes \tilde{\mathbf{N}}_1}{\beta}. \quad (3.73)$$

By virtue of equation (3.64) evaluation of \mathbb{E}^{tan} rests on the inversion of the operator $\tilde{\mathbb{W}}$ whose associated matrix has dimension $(2q + 1) \times (2q + 1)$. However, the expression of $\tilde{\mathbb{W}}$ can be conveniently manipulated so that only the inversion of a $q \times q$ matrix is really needed .

From the computational stand point the reduction of the dimension of the matrix to invert is particularly relevant. Actually, referring for instance to a finite element solution of the elastoplastic structural problem, the consistent tangent operator must be evaluated at each yielded Gauss point of the mesh, for each structural iteration and each load increment.

In order to illustrate the steps which allow one to simplify the evaluation of the consistent tangent operator we express $\tilde{\mathbb{W}}$ in a more explicit form. Recalling the definition (3.58) and the expression (3.39) of the yield function we have

$$\tilde{\mathbb{W}} = \left\{ \left[\begin{array}{ccc} (d^2\psi_{el})^{-1} & \mathbf{0} & \mathbf{0} \\ \mathbf{0} & (d^2\psi_{kin})^{-1} & \mathbf{0} \\ \mathbf{0} & \mathbf{0} & (d^2\psi_{iso})^{-1} \end{array} \right] + \right. \quad (3.74)$$

$$\left. + \lambda \left[\begin{array}{ccc} d_{\sigma\sigma}^2\phi & d_{\sigma\beta}^2\phi & d_{\sigma\rho}^2\phi \\ d_{\beta\sigma}^2\phi & d_{\beta\beta}^2\phi & d_{\beta\rho}^2\phi \\ d_{\rho\sigma}^2\phi & d_{\rho\beta}^2\phi & d_{\rho\rho}^2\phi \end{array} \right] \right\}$$

The assumed definition (3.39) of the yield function implies that the partial derivatives $d_{\beta}\phi$ and $d_{\rho}\phi$ are given by

$$d_{\beta}\phi = -d_{\sigma}\phi \quad d_{\rho}\phi = -1, \quad (3.75)$$

and

$$d_{\beta\beta}^2\phi = -d_{\beta\sigma}^2\phi = -d_{\sigma\beta}^2\phi = d_{\sigma\sigma}^2\phi$$

$$d_{\beta\rho}^2\phi = [d_{\rho\beta}^2\phi]^t = d_{\sigma\rho}^2\phi = [d_{\rho\sigma}^2\phi]^t = \mathbf{0} \quad d_{\rho\rho}^2\phi = \mathbf{0}. \quad (3.76)$$

Hence setting

$$\mathbb{E} = d^2\psi_{el} \quad \mathbb{H}_{kin} = d^2\psi_{kin} \quad h_{iso} = d^2\psi_{iso}, \quad (3.77)$$

the expression of $\tilde{\mathbb{W}}$ is explicitly given by

$$\begin{aligned} \tilde{\mathbb{W}} &= \left\{ \begin{bmatrix} \mathbb{E}^{-1} & \mathbf{0} & \mathbf{0} \\ \mathbf{0} & \mathbb{H}_{kin}^{-1} & \mathbf{0} \\ \mathbf{0} & \mathbf{0} & h_{iso}^{-1} \end{bmatrix} + \begin{bmatrix} \lambda d_{\sigma\sigma}^2\phi & -\lambda d_{\sigma\sigma}^2\phi & \mathbf{0} \\ -\lambda d_{\sigma\sigma}^2\phi & \lambda d_{\sigma\sigma}^2\phi & \mathbf{0} \\ \mathbf{0} & \mathbf{0} & 0 \end{bmatrix} \right\}^{-1} = \\ &= \begin{bmatrix} \tilde{\mathbb{W}}_r & \mathbf{0} \\ \mathbf{0} & h_{iso}^{-1} \end{bmatrix}, \end{aligned} \quad (3.78)$$

where

$$\tilde{\mathbb{W}}_r = \left\{ \begin{bmatrix} \mathbb{E}^{-1} & \mathbf{0} \\ \mathbf{0} & \mathbb{H}_{kin}^{-1} \end{bmatrix} + \begin{bmatrix} \lambda d_{\sigma\sigma}^2\phi & -\lambda d_{\sigma\sigma}^2\phi \\ -\lambda d_{\sigma\sigma}^2\phi & \lambda d_{\sigma\sigma}^2\phi \end{bmatrix} \right\}^{-1}, \quad (3.79)$$

For a nonlinear elastic behaviour, as well as for nonlinear hardening, \mathbb{E} , \mathbb{H}_{kin}^{-1} , h_{iso}^{-1} are not constant and depend upon the values \mathbf{e} , $\boldsymbol{\eta}$, $\boldsymbol{\zeta}$, respectively.

By introducing the following vector notation:

$$\mathbb{A} = \begin{bmatrix} \mathbb{E}^{-1} & \mathbf{0} \\ \mathbf{0} & \mathbb{H}_{kin}^{-1} \end{bmatrix} \quad \mathbb{U} = \begin{bmatrix} \lambda d_{\sigma\sigma}^2\phi & \lambda d_{\sigma\sigma}^2\phi \\ -\lambda d_{\sigma\sigma}^2\phi & -\lambda d_{\sigma\sigma}^2\phi \end{bmatrix} \quad \mathbb{V}^t = \begin{bmatrix} \mathbb{I} & \mathbf{0} \\ \mathbf{0} & -\mathbb{I} \end{bmatrix}, \quad (3.80)$$

It turns out to be

$$\tilde{\mathbb{W}}_r = (\mathbb{A} + \mathbb{U}\mathbb{V}^t)^{-1}. \quad (3.81)$$

Accordingly, the Sherman-Morrison-Woodbury formula, yields

$$(\mathbb{A} + \mathbb{U}\mathbb{V}^t)^{-1} = \mathbb{A}^{-1} - \mathbb{A}^{-1}\mathbb{U}(\mathbb{I} + \mathbb{V}^t\mathbb{A}^{-1}\mathbb{U})^{-1}\mathbb{V}^t\mathbb{A}^{-1}. \quad (3.82)$$

Being

$$\mathbb{A}^{-1}\mathbb{U} = \begin{bmatrix} \lambda\mathbb{E}d_{\sigma\sigma}^2\phi & \lambda\mathbb{E}d_{\sigma\sigma}^2\phi \\ -\lambda\mathbb{H}_{kin}d_{\sigma\sigma}^2\phi & -\lambda\mathbb{H}_{kin}d_{\sigma\sigma}^2\phi \end{bmatrix} \quad \mathbb{V}^t\mathbb{A}^{-1} = \begin{bmatrix} \mathbb{E} & \mathbf{0} \\ \mathbf{0} & -\mathbb{H}_{kin} \end{bmatrix}. \quad (3.83)$$

and

$$\mathbb{V}^t \mathbb{A}^{-1} \mathbb{U} = \begin{bmatrix} \lambda(\mathbb{E} + \mathbb{H}_{kin})d_{\sigma\sigma}^2\phi & \mathbf{0} \\ \mathbf{0} & \lambda(\mathbb{E} + \mathbb{H}_{kin})d_{\sigma\sigma}^2\phi \end{bmatrix}, \quad (3.84)$$

and

$$\begin{aligned} \mathbb{I} + \mathbb{V}^t \mathbb{A}^{-1} \mathbb{U} &= \begin{bmatrix} \mathbb{I} + \lambda(\mathbb{E} + \mathbb{H}_{kin})d_{\sigma\sigma}^2\phi & \mathbf{0} \\ \mathbf{0} & \mathbb{I} + \lambda(\mathbb{E} + \mathbb{H}_{kin})d_{\sigma\sigma}^2\phi \end{bmatrix} = \\ &= \begin{bmatrix} \mathbb{F} & \mathbf{0} \\ \mathbf{0} & \mathbb{F} \end{bmatrix}, \end{aligned} \quad (3.85)$$

we get

$$\begin{aligned} \tilde{\mathbb{W}}_r &= \begin{bmatrix} \mathbb{E} & \mathbf{0} \\ \mathbf{0} & \mathbb{H}_{kin} \end{bmatrix} + \\ &- \begin{bmatrix} \lambda\mathbb{E}d_{\sigma\sigma}^2\phi & \lambda\mathbb{E}d_{\sigma\sigma}^2\phi \\ -\lambda\mathbb{H}_{kin}d_{\sigma\sigma}^2\phi & -\lambda\mathbb{H}_{kin}d_{\sigma\sigma}^2\phi \end{bmatrix} \begin{bmatrix} \mathbb{F}^{-1} & \mathbf{0} \\ \mathbf{0} & \mathbb{F}^{-1} \end{bmatrix} \begin{bmatrix} \mathbb{E} & \mathbf{0} \\ \mathbf{0} & -\mathbb{H}_{kin} \end{bmatrix} \end{aligned} \quad (3.86)$$

Hence, the only matrix which needs to be inverted is the following one:

$$\mathbb{F} = \mathbb{I} + \lambda(\mathbb{E} + \mathbb{H}_{kin})d_{\sigma\sigma}^2\phi. \quad (3.87)$$

Expanding the matrix product in equation 3.86 the following expression of $\tilde{\mathbb{W}}$ is finally obtained:

$$\tilde{\mathbb{W}} = \begin{bmatrix} \mathbb{E} - \lambda\mathbb{E}d_{\sigma\sigma}^2\phi\mathbb{F}^{-1}\mathbb{E} & \lambda\mathbb{E}d_{\sigma\sigma}^2\phi\mathbb{F}^{-1}\mathbb{H}_{kin} & \mathbf{0} \\ \lambda\mathbb{H}_{kin}d_{\sigma\sigma}^2\phi\mathbb{F}^{-1}\mathbb{E} & \mathbb{H}_{kin} - \lambda\mathbb{H}_{kin}d_{\sigma\sigma}^2\phi\mathbb{F}^{-1}\mathbb{H}_{kin} & \mathbf{0} \\ \mathbf{0} & \mathbf{0} & h_{iso} \end{bmatrix}. \quad (3.88)$$

So the term in expression 3.73 is given by

$$\tilde{\mathbb{W}}_{11} = \mathbb{E} - \lambda\mathbb{E}d_{\sigma\sigma}^2\phi\mathbb{F}^{-1}\mathbb{E}. \quad (3.89)$$

To complete the evaluation of the consistent tangent operator (3.73) we still need the expression of $\tilde{\mathbf{N}}$ and β appearing in (3.68). They can be obtained from the relation:

$$\tilde{\mathbf{n}} = (d_{\bar{\sigma}}\tilde{\phi})^t = [\mathbf{n} \quad -\mathbf{n} \quad -1] \quad (3.90)$$

where $\mathbf{n} = d_{\sigma}\phi$. hence, recalling 3.39 and 3.88, we obtain

$$\tilde{\mathbf{N}} = \tilde{\mathbb{W}} d_{\tilde{\sigma}} \tilde{\phi} = \begin{bmatrix} [\mathbb{E} - \lambda \mathbb{E} d_{\sigma\sigma}^2 \phi \mathbb{F}^{-1} (\mathbb{E} + \mathbb{H}_{kin})] \mathbf{n} \\ -[\mathbb{H}_{kin} - \lambda \mathbb{H}_{kin} d_{\sigma\sigma}^2 \phi \mathbb{F}^{-1} (\mathbb{E} + \mathbb{H}_{kin})] \mathbf{n} \\ -h_{iso} \end{bmatrix} \quad (3.91)$$

and

$$\begin{aligned} \beta &= \tilde{\mathbb{W}} \tilde{\mathbf{n}} \cdot \tilde{\mathbf{n}} = \tilde{\mathbf{N}} \cdot \tilde{\mathbf{n}} = \\ &= [(\mathbb{E} + \mathbb{H}_{kin}) - \lambda(\mathbb{E} + \mathbb{H}_{kin}) d_{\sigma\sigma}^2 \phi \mathbb{F}^{-1} (\mathbb{E} + \mathbb{H}_{kin})] \mathbf{n} \cdot \mathbf{n} + h_{iso} \end{aligned} \quad (3.92)$$

Being $\tilde{\mathbf{N}}_1 = [\mathbb{E} - \lambda \mathbb{E} d_{\sigma\sigma}^2 \phi \mathbb{F}^{-1} (\mathbb{E} + \mathbb{H}_{kin})] \mathbf{n}$, the expression of the elastoplastic tangent operator is finally obtained:

$$\begin{aligned} \mathbb{E}^{\text{tan}} &= \mathbb{E} - \lambda \mathbb{E} d_{\sigma\sigma}^2 \phi \mathbb{F}^{-1} \mathbb{E} + \\ &\quad - \frac{[\mathbb{E} - \lambda \mathbb{E} d_{\sigma\sigma}^2 \phi \mathbb{F}^{-1} (\mathbb{E} + \mathbb{H}_{kin})] \mathbf{n} \otimes [\mathbb{E} - \lambda \mathbb{E} d_{\sigma\sigma}^2 \phi \mathbb{F}^{-1} (\mathbb{E} + \mathbb{H}_{kin})] \mathbf{n}}{[(\mathbb{E} + \mathbb{H}_{kin}) - \lambda(\mathbb{E} + \mathbb{H}_{kin}) d_{\sigma\sigma}^2 \phi \mathbb{F}^{-1} (\mathbb{E} + \mathbb{H}_{kin})] \mathbf{n} \cdot \mathbf{n} + h_{iso}} \end{aligned} \quad (3.93)$$

Finally, indicating $\lambda d_{\sigma\sigma}^2 \phi \mathbb{F}^{-1}$ as \mathbb{F}_{ϕ}^{-1} and $(\mathbb{E} + \mathbb{H}_{kin})$ as \mathbb{E}_H the consistent tangent operator can be written as:

$$\begin{aligned} \mathbb{E}^{\text{tan}} &= \mathbb{E} - \mathbb{E} \mathbb{F}_{\phi}^{-1} \mathbb{E} + \\ &\quad - \frac{[\mathbb{E} - \mathbb{E} \mathbb{F}_{\phi}^{-1} \mathbb{E}_H] \mathbf{n} \otimes [\mathbb{E} - \mathbb{E} \mathbb{F}_{\phi}^{-1} \mathbb{E}_H] \mathbf{n}}{[\mathbb{E}_H - \mathbb{E}_H \mathbb{F}_{\phi}^{-1} \mathbb{E}_H] \mathbf{n} \cdot \mathbf{n} + h_{iso}} \end{aligned} \quad (3.94)$$

applying the Sherman-Morrison-Woodbury formula to the (3.87) we get

$$\mathbb{F}^{-1} = \mathbb{I} - \lambda \mathbb{E}_H (\mathbb{I} + \lambda d_{\sigma\sigma}^2 \phi \mathbb{E}_H)^{-1} d_{\sigma\sigma}^2 \phi \quad (3.95)$$

hence

$$\begin{aligned} \mathbb{F}_{\phi}^{-1} &= \lambda d_{\sigma\sigma}^2 \phi - \lambda^2 d_{\sigma\sigma}^2 \phi \mathbb{E}_H (\mathbb{I} + \lambda d_{\sigma\sigma}^2 \phi \mathbb{E}_H)^{-1} d_{\sigma\sigma}^2 \phi = \\ &= \lambda d_{\sigma\sigma}^2 \phi - \lambda d_{\sigma\sigma}^2 \phi \mathbb{E}_H (\mathbb{I} + \lambda d_{\sigma\sigma}^2 \phi \mathbb{E}_H)^{-1} \lambda d_{\sigma\sigma}^2 \phi \end{aligned} \quad (3.96)$$

Recalling (3.50) and applying Sherman-Morrison-Woodbury formula to it

$$\mathbb{G}^{-1} = \mathbb{E}_H - \lambda \mathbb{E}_H (\mathbb{I} + \lambda d_{\sigma\sigma}^2 \phi \mathbb{E}_H)^{-1} d_{\sigma\sigma}^2 \phi \mathbb{E}_H. \quad (3.97)$$

Applying the formula again, to the expression $\mathbb{E}_H (\mathbb{I} + \lambda d_{\sigma\sigma}^2 \phi \mathbb{E}_H)^{-1}$ we get

$$\begin{aligned}
\mathbb{E}_H(\mathbb{I} + \lambda d_{\sigma\sigma}^2 \phi \mathbb{E}_H)^{-1} &= \mathbb{E}_H[\mathbb{I} - d_{\sigma\sigma}^2 \phi (\mathbb{I} + \lambda \mathbb{E}_H d_{\sigma\sigma}^2 \phi)^{-1} \lambda \mathbb{E}_H] = \\
&= \mathbb{E}_H - \lambda \mathbb{E}_H (\mathbb{I} + \lambda d_{\sigma\sigma}^2 \mathbb{E}_H)^{-1} d_{\sigma\sigma}^2 \phi \mathbb{E}_H = \mathbb{G}^{-1} \quad (3.98)
\end{aligned}$$

In rearranging the above expressions the symmetry of $d_{\sigma\sigma}^2 \phi$ has been exploited. By comparison between (3.96) and (3.98) we get

$$\mathbb{F}_\phi^{-1} = \lambda d_{\sigma\sigma}^2 \phi - \lambda d_{\sigma\sigma}^2 \phi \mathbb{G}^{-1} \lambda d_{\sigma\sigma}^2 \phi. \quad (3.99)$$

Therefore as anticipated we see that the fourth order tensor \mathbb{G}^{-1} is also needed to compute the consistent tangent operator \mathbb{E}^{tan} . The crucial assemblage of this fourth order tensor can be carried out very effectively as described in the next section.

3.5.5 Assemblage of \mathbb{G}^{-1}

For the evaluation of \mathbb{G}^{-1} one has to compute the product of the second derivative of the yield function and of the plastic consistency parameter $\lambda d_{\tau\tau}^2 \phi$. Note that in the return mapping algorithm we have used the second derivatives of the yield function with respect to the relative stress τ , $d_{\tau\tau}^2 \phi$ whilst in the formulation of the consistent tangent operator the second derivative with respect to the actual stresses $d_{\sigma\sigma}^2 \phi$ appears. By use of the chain rule it is seen that the two derivatives coincides and therefore can be introduced in the formulas indifferently.

In the sequel we will use the notation associated with relative stress $d_{\tau\tau}^2 \phi$ for consistency with the notation used for the return mapping.

Recalling (3.39), the needed expression is provided by:

$$\begin{aligned}
\lambda d_{\tau\tau}^2 \phi &= e_1 \mathbb{I} + e_2 (\mathbf{S} \boxtimes \mathbf{1} + \mathbf{1} \boxtimes \mathbf{S}) + \\
&+ e_3 (\mathbf{1} \otimes \mathbf{1}) + e_4 (\mathbf{S} \otimes \mathbf{1} + \mathbf{1} \otimes \mathbf{S}) + e_5 (\mathbf{S}^2 \otimes \mathbf{1} + \mathbf{1} \otimes \mathbf{S}^2) + \\
&+ e_6 (\mathbf{S} \otimes \mathbf{S}) + e_7 (\mathbf{S}^2 \otimes \mathbf{S} + \mathbf{S} \otimes \mathbf{S}^2) + e_8 (\mathbf{S}^2 \otimes \mathbf{S}^2), \quad (3.100)
\end{aligned}$$

for which the coefficients are given by:

$$\begin{aligned}
e_1 &= \lambda d_2 \varphi = \lambda n_2 \\
e_2 &= \lambda d_3 \varphi = \lambda n_3 \\
e_3 &= \lambda (d_{11} \varphi - \frac{1}{3} d_2 \varphi - \frac{4}{3} J_2 d_{13} \varphi + \frac{4}{9} J_2^2 d_{33} \varphi) \\
e_4 &= \lambda (d_{12} \varphi - \frac{2}{3} d_3 \varphi - \frac{2}{3} J_2 d_{23} \varphi) \\
e_5 &= \lambda (d_{13} \varphi - \frac{2}{3} J_2 d_{33} \varphi) \\
e_6 &= \lambda d_{22} \varphi \\
e_7 &= \lambda d_{23} \varphi \\
e_8 &= \lambda d_{33} \varphi. \quad (3.101)
\end{aligned}$$

The symbol \boxtimes denotes the square tensor product defined as [38]:

$$(\mathbf{A} \boxtimes \mathbf{B})\mathbf{C} = \mathbf{ACB}^t, \quad (3.102)$$

for every second order tensor \mathbf{A} , \mathbf{B} and \mathbf{C} .

The approach proposed here for the evaluation of \mathbb{G}^{-1} is based upon the results contributed in [98]. To this end consider the spectral decomposition of the stress deviator:

$$\mathbf{S} = s_1 \mathbf{S}_1 + s_2 \mathbf{S}_2 + s_3 \mathbf{S}_3, \quad (3.103)$$

where s_i is the generic eigenvalue, \mathbf{s}_i the associated eigenvector and $\mathbf{S}_i = \mathbf{s}_i \otimes \mathbf{s}_i$ the corresponding eigenprojector. It has been shown in [98] that every fourth order tensor given as a linear combination of the dyadic and square products of $\mathbf{1}$, \mathbf{A} and \mathbf{A}^2 , where \mathbf{A} is a generic rank two symmetric tensor, can be expressed as a linear combination of fourth order tensors obtained as dyadic and square tensor products of the eigenprojectors of \mathbf{A} . For instance:

$$\begin{aligned} \lambda d_{\tau\tau}^2 \phi &= [\mathbf{F}^\otimes] \cdot [\mathbf{S}^\otimes] + [\mathbf{F}^\boxtimes] \cdot [\mathbf{S}^\boxtimes] = \\ &= \begin{bmatrix} f_{11}^\otimes & f_{12}^\otimes & f_{13}^\otimes \\ f_{12}^\otimes & f_{22}^\otimes & f_{23}^\otimes \\ f_{13}^\otimes & f_{23}^\otimes & f_{33}^\otimes \\ 0 & f_{12}^\boxtimes & f_{13}^\boxtimes \\ f_{12}^\boxtimes & 0 & f_{23}^\boxtimes \\ f_{13}^\boxtimes & f_{23}^\boxtimes & 0 \end{bmatrix} \cdot \begin{bmatrix} \mathbf{S}_1 \otimes \mathbf{S}_1 & \mathbf{S}_1 \otimes \mathbf{S}_2 & \mathbf{S}_1 \otimes \mathbf{S}_3 \\ \mathbf{S}_2 \otimes \mathbf{S}_1 & \mathbf{S}_2 \otimes \mathbf{S}_2 & \mathbf{S}_2 \otimes \mathbf{S}_3 \\ \mathbf{S}_3 \otimes \mathbf{S}_1 & \mathbf{S}_3 \otimes \mathbf{S}_2 & \mathbf{S}_3 \otimes \mathbf{S}_3 \\ \mathbb{O} & \mathbf{S}_1 \boxtimes \mathbf{S}_2 & \mathbf{S}_1 \boxtimes \mathbf{S}_3 \\ \mathbf{S}_2 \boxtimes \mathbf{S}_1 & \mathbb{O} & \mathbf{S}_2 \boxtimes \mathbf{S}_3 \\ \mathbf{S}_3 \boxtimes \mathbf{S}_1 & \mathbf{S}_3 \boxtimes \mathbf{S}_2 & \mathbb{O} \end{bmatrix} + \end{aligned} \quad (3.104)$$

where the entries of the matrices $[\mathbf{F}^\otimes]$ and $[\mathbf{F}^\boxtimes]$ are given by:

$$\begin{cases} f_{ii}^\otimes &= e_1 + e_3 + 2(e_2 + e_4)s_i + (2e_5 + e_6)s_i^2 + 2e_7s_i^3 + e_8s_i^4 \\ f_{ij}^\otimes &= e_3 + e_4(s_i + s_j) + e_5(s_i^2 + s_j^2) + e_6s_is_j + e_7(s_i^2s_j + s_is_j^2) + e_8s_i^2s_j^2 \\ f_{ij}^\boxtimes &= e_1 + e_2(s_i + s_j) \\ i, j &= 1, 2, 3 \quad i \neq j. \end{cases} \quad (3.105)$$

and the symbol \cdot stands for the sum of the products of the terms which have the same position in both arrays.

Analogously, the elastic operator (3.36) can be represented in the form:

$$\mathbb{E} = [\mathbf{D}^\otimes] \cdot [\mathbf{S}^\otimes] + [\mathbf{D}^\boxtimes] \cdot [\mathbf{S}^\boxtimes] \quad (3.106)$$

where:

$$[\mathbf{D}^\otimes] = \begin{bmatrix} d_1 + d_2 & d_2 & d_2 \\ d_2 & d_1 + d_2 & d_2 \\ d_2 & d_2 & d_1 + d_2 \end{bmatrix}, \quad [\mathbf{D}^\boxtimes] = \begin{bmatrix} 0 & d_1 & d_1 \\ d_1 & 0 & d_1 \\ d_1 & d_1 & 0 \end{bmatrix}, \quad (3.107)$$

being $d_1 = 2G$ and $d_2 = K - 2G/3$.

Further, the fourth order tensor \mathbb{E}_H is amenable to the representation:

$$\mathbb{E}_H = [\mathbf{D}_H^\otimes] \cdot [\mathbb{S}^\otimes] + [\mathbf{D}_H^\boxtimes] \cdot [\mathbb{S}^\boxtimes] \quad (3.108)$$

where the matrix $[\mathbf{D}_H^\otimes]$ coincides with $[\mathbf{D}^\otimes]$, except for d_1 being replaced by $d_1 + h_{kin}$, and $[\mathbf{D}_H^\boxtimes] = [\mathbf{D}^\boxtimes]$. Hence, it turns out to be [98]:

$$[\mathbb{E}_H^{-1}] = [\tilde{\mathbf{D}}_H^\otimes] \cdot [\mathbb{S}^\otimes] + [\tilde{\mathbf{D}}_H^\boxtimes] \cdot [\mathbb{S}^\boxtimes], \quad (3.109)$$

where:

$$[\tilde{\mathbf{D}}_H^\otimes] = \begin{bmatrix} \tilde{h}_1 + \tilde{h}_2 & \tilde{h}_2 & \tilde{h}_2 \\ \tilde{h}_2 & \tilde{h}_1 + \tilde{h}_2 & \tilde{h}_2 \\ \tilde{h}_2 & \tilde{h}_2 & \tilde{h}_1 + \tilde{h}_2 \end{bmatrix}, \quad [\tilde{\mathbf{D}}_H^\boxtimes] = \begin{bmatrix} 0 & \tilde{h}_1 & \tilde{h}_1 \\ \tilde{h}_1 & 0 & \tilde{h}_1 \\ \tilde{h}_1 & \tilde{h}_1 & 0 \end{bmatrix}, \quad (3.110)$$

and:

$$\tilde{h}_1 = \frac{1}{2G + h_{kin}} \quad \tilde{h}_2 = -\frac{1}{3} \frac{3K - 2G}{(2G + h_{kin})(3K + h_{kin})}. \quad (3.111)$$

Finally, according to (3.104) and (3.109), one has form (3.50):

$$\mathbb{G} = [\mathbf{G}^\otimes] \cdot [\mathbb{S}^\otimes] + [\mathbf{G}^\boxtimes] \cdot [\mathbb{S}^\boxtimes], \quad (3.112)$$

where the entries g_{ij}^\otimes ($i, j \in \{1, 2, 3\}$) of $[\mathbf{G}^\otimes]$ and g_{ij}^\boxtimes ($i \neq j$) of $[\mathbf{G}^\boxtimes]$ are given by:

$$\begin{cases} g_{ii}^\otimes = f_{ii}^\otimes + \tilde{h}_1 + \tilde{h}_2 & (\text{no sum}) \\ g_{ij}^\otimes = f_{ij}^\otimes + \tilde{h}_2 & (i \neq j) \\ g_{ij}^\boxtimes = f_{ij}^\boxtimes + \tilde{h}_1 & (i \neq j). \end{cases} \quad (3.113)$$

It can be proved that the matrix $[\mathbf{G}^\otimes]$ is positive definite and that the non zero entries of $[\mathbf{G}^\boxtimes]$ are positive if and only if \mathbb{G} is positive definite; in this case the inverse of \mathbb{G} is obtained as [98]:

$$\mathbb{G}^{-1} = [\mathbf{G}^\otimes]^{-1} \cdot [\mathbb{S}^\otimes] + [\mathbf{G}^\boxtimes]^{-1} \cdot [\mathbb{S}^\boxtimes]; \quad (3.114)$$

This amounts to compute the inverse of the 3×3 matrix $[\mathbf{G}^\otimes]$ while the matrix $[\mathbf{G}^\boxtimes]^{-1}$ collects the reciprocals of the scalars g_{ij}^\boxtimes , ($i \neq j$).

Consistent tangent operator

Based on the previous results it is now an easy matter to evaluate the tangent operator \mathbb{E}^{tan} . To this end we first recast the normal \mathbf{n} to the yield surface (3.41) in the form:

$$\mathbf{n} = n_1 \mathbf{1} + n_2 \mathbf{S} + n_3 \mathbf{S}^2 = [\mathbf{n}_p] \cdot [\mathbf{E}_S] = \begin{bmatrix} n_1 s_1 + n_1 s_1 + n_1 s_1^2 \\ n_1 s_2 + n_1 s_2 + n_1 s_2^2 \\ n_1 s_3 + n_1 s_3 + n_1 s_3^2 \end{bmatrix} \begin{bmatrix} \mathbf{S}_1 \\ \mathbf{S}_2 \\ \mathbf{S}_3 \end{bmatrix}.$$

By defining :

$$\begin{aligned} [\mathbf{P}^\otimes] &= [\mathbf{F}^\otimes] - [\mathbf{F}^\otimes][\mathbf{G}^\otimes]^{-1}[\mathbf{F}^\otimes]; & [\mathbf{P}^\boxtimes] &= [\mathbf{F}^\boxtimes] - [\mathbf{F}^\boxtimes] * [\mathbf{G}^\boxtimes]^{-1} * [\mathbf{F}^\boxtimes]; \\ [\mathbf{T}^\otimes] &= [\mathbf{D}^\otimes] - [\mathbf{D}^\otimes][\mathbf{P}^\otimes][\mathbf{D}_H^\otimes]; & [\mathbf{T}^\boxtimes] &= [\mathbf{D}^\boxtimes] - [\mathbf{D}^\boxtimes] * [\mathbf{P}^\boxtimes] * [\mathbf{D}_H^\boxtimes]; \end{aligned}$$

where the symbol $*$ denotes the matrix product performed component-wise, i.e. $([\mathbf{A}] * [\mathbf{B}])_{ij} = \mathbf{A}_{ij} \mathbf{B}_{ij}$ (no sum), the numerator of (3.93) can be expressed as follows:

$$[\mathbb{E} - \mathbb{E} \mathbb{F}_\phi^{-1} \mathbb{E}_H] \mathbf{n} = [\mathbf{T}^\otimes] [\mathbf{n}_p] \cdot [\mathbf{E}_S] = [\mathbf{t}] \cdot [\mathbf{E}_S].$$

so that the final expression of the consistent tangent operator is obtained as:

$$\begin{aligned} \mathbb{E}^{\text{tan}} &= \left([\mathbf{D}^\otimes] - [\mathbf{D}^\otimes][\mathbf{P}^\otimes][\mathbf{D}^\otimes] - \frac{([\mathbf{T}^\otimes] [\mathbf{n}_p]) \otimes ([\mathbf{T}^\otimes] [\mathbf{n}_p])}{[\mathbf{T}^\otimes] [\mathbf{n}_p] \cdot [\mathbf{n}_p]} \right) \cdot [\mathbb{S}^\otimes] + \\ &+ ([\mathbf{D}^\boxtimes] - [\mathbf{D}^\boxtimes] * [\mathbf{P}^\boxtimes] * [\mathbf{D}^\boxtimes]) \cdot [\mathbb{S}^\boxtimes]. \end{aligned} \quad (3.115)$$

With reference to the precious formula three considerations are worth being emphasized. First, the consistent tangent operator has been obtained in closed form for an arbitrary isotropic yield criterion given in the form (3.39); only the coefficients n_i and e_i of the first and second derivative of φ , need to be computed in advance.

Second, the computational burden required by the proposed approach consists in the inversion of a positive semidefinite 3×3 matrix, matrix multiplications between 3×3 matrices and the construction of the matrix representation of the six dyadic products $2\text{sym}(\mathbf{S}_i \otimes \mathbf{S}_j)$, $(i, j = 1, 2, 3)$, along with the three square products $(\mathbf{S}_k \boxtimes \mathbf{S}_l + \mathbf{S}_l \boxtimes \mathbf{S}_k)$, $(k, l = 1, 2, 3, k \neq l)$.

Third and more important, the consistent tangent operator is directly expressed in the given reference frame: this avoids the costly transformations of \mathbb{E}^{tan} with respect to the reference frame associated with the eigenvectors

of \mathbf{S} . Obviously, the same considerations apply to the computations required to perform the return mapping algorithm.

The methods presented are restricted to the case of a single surface return. The appropriate modification for treating a problem governed by multiple surfaces and the treatment of the corner regions can be found in [11]

3.5.6 Specialization of the 3D return mapping to the plane stress case

At first sight the solution of two dimensional problems should be simpler than the three-dimensional one. This is certainly true in elasticity but things are rather different in elasto/visco-plasticity. To be convinced about this striking occurrence it is sufficient to think about the return mapping algorithm for elastoplastic models depending upon the second principal invariant J_2 of the stress deviator: it admits a close form solution in the 3D and plain strain case endowed with linear kinematic and isotropic hardening since it amounts to solving a linear scalar equation in the plastic multiplier [115]. On the contrary, in the plane stress case, the closed form solution has been established by Simo and Govindjee [114] only for perfect plasticity or linear isotropic hardening. Although the inclusion of Kinematic hardening has been subsequently achieved in [3], the closed form solution of the plane stress problem is represented by a quartic equation whose solution algorithm is well known to be numerically unstable. The anomalous character of the plain stress problem is witnessed by the variety of algorithm which have been presented in the literature [36], [37], [43], [64], [113], see e.g. the review paper by Millard [78]. Rather surprisingly, neither the solution algorithms for plain stress have the same formal structure as the corresponding three-dimensional problem nor any relationship between the two solution procedures has been previously looked for or established, the only remarkable exception being that in the paper [103]. Actually, each one of the previously mentioned algorithms is directly conceived for plane stress thus introducing *ab-initio* special assumptions which hinder from developing a unified approach with the three-dimensional problem. This is further strengthened by the fact that all such algorithms, apart from the paper from Fuschi et al. [42], directly address the case of von Mises plasticity. This naturally prompts, due to the simplicity of von Mises criterion, the adoption of very special relations such as the one occurring between the in-plane components of the back-stress and the plastic strain tensors. In this section we show how, following the approach by Rosati and Valoroso [96, 97], the gap existing between 2D and 3D elastoplastic formulations can be bridged and that the connection of the

former with the solution procedure for 3D isotropic elastoplastic models of arbitrary type yields a great generality in the solution of the plain stress problem and a considerable simplification of the computational procedure is in [96],[90].

Derivation of an integration algorithm for plane strain is very straightforward and amounts to imposing zero value to the out of plane components of the strain tensor. Derivation of an algorithm for the plain stress case from the general three-dimensional problem is non trivial instead. It is common practice to reformulate the problem in two dimensions to circumvent this problem. A direct formulation of the plane stress elastoplastic problems is possible by expressing the invariants in terms of the in-plane stress components in the expression of the yield function. The 2D yield function that is thus obtained needs to be doubly differentiated with respect to each component. This task results laborious especially for J_3 -dependent yield functions [42]. The solution procedure for plane stress elastoplastic problems, endowed with isotropic yield criteria of arbitrary type, can be directly derived from the corresponding 3D one and it fits the same algorithmic framework. Moreover, reference can always be made to the 3D yield function, i.e. to the expression formulated in terms of invariants. In a plane stress problem the tensors appearing in the finite-step constitutive equations have the following matrix representation:

$$[\sigma_p] = \begin{pmatrix} \sigma_{11} & \sigma_{12} & 0 \\ \sigma_{21} & \sigma_{22} & 0 \\ 0 & 0 & 0 \end{pmatrix} \quad (3.116)$$

$$[\epsilon_p] = \begin{pmatrix} \epsilon_{11} & \epsilon_{12} & 0 \\ \epsilon_{21} & \epsilon_{22} & 0 \\ 0 & 0 & \epsilon_{33} \end{pmatrix} \quad (3.117)$$

$$[p_p] = \begin{pmatrix} p_{11} & p_{12} & 0 \\ p_{21} & p_{22} & 0 \\ 0 & 0 & p_{33} \end{pmatrix} \quad (3.118)$$

in the given reference frame. Hence, the constitutive problem can be naturally expressed in terms of the in-plane components of the stress tensor:

$$[\hat{\sigma}] = \begin{pmatrix} \sigma_{11} & \sigma_{12} \\ \sigma_{21} & \sigma_{22} \end{pmatrix} \quad (3.119)$$

assuming:

$$[\hat{\epsilon}] = \begin{pmatrix} \epsilon_{11} & \epsilon_{12} \\ \epsilon_{21} & \epsilon_{22} \end{pmatrix} \quad (3.120)$$

as driving variable. Actually, once the constitutive model has been solved, the component p_{33} can be evaluated as λn_{33} . This last quantity is in turn obtained from (3.41) provided that all quantities are associated with the value of the stress tensor at solution. Moreover, ϵ_{33} is obtained from the 3D elastic relation (3.36) by enforcing the plane stress condition $\sigma_{33}=0$.

The symbols σ_p and $\hat{\epsilon}$ denote respectively 3D and 2D tensors even if the non-zero entries of the former are exactly the same as the entries of the latter.

More generally, given a symmetric 3D tensor $\mathbf{A} \in Lin$, we shall use the symbol \mathbf{A}_c to denote the 3D tensor collecting the components of \mathbf{A} spanning the subspace S_c of Lin complementary to the subspace S_p defined by the in-plane components of \mathbf{A} .

In other words we shall write:

$$A = A_p + A_c, \quad (3.121)$$

to synthetically indicate the decomposition of \mathbf{A} whose associated matrix decomposition is:

$$\begin{bmatrix} A_{11} & A_{12} & A_{13} \\ A_{21} & A_{22} & A_{23} \\ A_{13} & A_{23} & A_{33} \end{bmatrix} = \begin{bmatrix} A_{11} & A_{12} & 0 \\ A_{21} & A_{22} & 0 \\ 0 & 0 & 0 \end{bmatrix} + \begin{bmatrix} 0 & 0 & A_{13} \\ 0 & 0 & A_{23} \\ A_{13} & A_{23} & A_{33} \end{bmatrix}. \quad (3.122)$$

Further, the symbol \mathbf{A} will be used to denote the 2D tensor collecting the out-of-plane components of \mathbf{A} and we shall write:

$$A_p \rightleftharpoons \hat{A} \quad A_c \rightleftharpoons \check{A} \quad (3.123)$$

where the symbol \rightleftharpoons has been used to emphasize that the 3D tensors on the left are isometrically mapped to the 2D tensors on the right.

A matrix representation for $\check{\mathbf{A}}$ could be:

$$[\check{A}] = \begin{bmatrix} A_{13} & A_{33} \\ A_{33} & A_{23} \end{bmatrix} \quad (3.124)$$

but, as it will be clear in the sequel, it does not to be really invoked. Sometimes, to fully grasp the meaning of our calculations, it can be convenient to think of fourth-order 3D tensors of 6x6 matrices and second order 3D tensors of 6x1 vectors according to the following vector representation of stress (\mathbf{T}) and strain-like (\mathbf{D}) rank-two symmetric tensors:

$$\begin{aligned}
[\mathbf{T}] &= [\mathbf{T}_{11}, \mathbf{T}_{22}, \mathbf{T}_{12}, \mathbf{T}_{33}, \mathbf{T}_{23}, \mathbf{T}_{13}]^t \\
[\mathbf{D}] &= [\mathbf{D}_{11}, \mathbf{D}_{22}, 2\mathbf{D}_{12}, \mathbf{D}_{33}, 2\mathbf{D}_{23}, 2\mathbf{D}_{13}]^t.
\end{aligned}
\tag{3.125}$$

As a consequence, we can represent two-dimensional second-order tensor in the form:

$$[\hat{T}] = \begin{bmatrix} T_{11} \\ T_{22} \\ T_{12} \end{bmatrix} \quad [\check{T}] = \begin{bmatrix} T_{33} \\ T_{23} \\ T_{13} \end{bmatrix} \quad [\hat{D}] = \begin{bmatrix} D_{11} \\ D_{22} \\ 2D_{12} \end{bmatrix} \quad [\check{D}] = \begin{bmatrix} D_{33} \\ 2D_{23} \\ 2D_{13} \end{bmatrix}.
\tag{3.126}$$

However, as a general rule, the vector (matrix) representation rank-two (-four) tensors can be left in the backstage since it really needs to be invoked only for implementation.

As a matter of fact we shall make reference to 2D tensors, rather than to their matrix representation, for two reasons. First, tensor relations involving 2D entities can be consistently derived from the ones associated with 3D tensors as shown further on. Second, the systematic use of tensor algebra brings to a more effective solution procedure from the computational point of view.

Let's recall the 3D yield function ϕ :

$$\phi(\sigma, \beta, \rho) = \phi(\tau, \rho) = \varphi(I_1, J_2, J_3) - \rho - Y_o = 0
\tag{3.127}$$

where Y_o is related to the initial uniaxial yield limit of the material,

$$I_1 = tr(\tau) \quad J_2 = \left(\frac{1}{2}trS^2\right) \quad J_3 = \left(\frac{1}{3}trS^3\right)
\tag{3.128}$$

are the principal stress invariants and $S = \tau - \frac{1}{3}tr(\tau)1$ is the deviator of the relative stress $\tau = \sigma - \beta$.

The derivative $d_\tau\phi$ is the rank-two 3D tensor collecting the derivatives of ϕ with respect to the stress components while

$$d_{\hat{\tau}}\phi \quad \text{and} \quad d_{\check{\tau}}\phi
\tag{3.129}$$

denote in turn the rank-two tensors collecting the derivatives of ϕ with respect to the in-plane and out-of-plane components.

They are associated with $d_\tau\phi$ as follows:

$$d_\tau\phi = (d_\tau\phi)_p + (d_\tau\phi)_c = d_{\tau_p}\phi + d_{\tau_c}\phi.
\tag{3.130}$$

The 3D tensor on the right-end side of the previous formula should be considered as 2D tensor by writing:

$$d_{\tau_p}\phi \rightleftharpoons d_{\hat{\tau}}\phi \quad d_{\tau_c}\phi \rightleftharpoons d_{\hat{\tau}}\phi. \quad (3.131)$$

The second derivative $d_{\tau\tau}\phi$ is the rank-four 3D tensor collecting the second derivatives of ϕ with respect to the stress components while:

$$d_{\hat{\tau}\hat{\tau}}^2\phi \quad d_{\hat{\tau}\hat{\tau}}^2\phi = (d_{\hat{\tau}\hat{\tau}}^2\phi)^t \quad d_{\hat{\tau}\hat{\tau}}^2\phi \quad (3.132)$$

are rank-four tensors, where $d_{\hat{\tau}\hat{\tau}}^2\phi = (d_{\hat{\tau}\hat{\tau}}^2\phi)^t$ collects the nine components $d_{\tau_i\tau_j}^2\phi$ where τ_i ranges in the set $\{\tau_{11}, \tau_{22}, \tau_{12}\}$ and τ_j ranges in the set $\{\tau_{33}, \tau_{13}, \tau_{23}\}$.

Thinking of $d_{\tau\tau}^2\phi$ as a 6x6 matrix and the tensor in (6.12) as 3x3 matrices resulting from the ordering of components detailed in (3.125), it is immediate to verify that:

$$[d_{\tau\tau}^2\phi] = \begin{bmatrix} d_{\hat{\tau}\hat{\tau}}^2\phi & : & d_{\hat{\tau}\hat{\tau}}^2\phi \\ \dots\dots\dots & & \\ d_{\hat{\tau}\hat{\tau}}^2\phi & : & d_{\hat{\tau}\hat{\tau}}^2\phi \end{bmatrix}; \quad (3.133)$$

in the tensor form the previous relation is written as:

$$d_{\tau\tau}^2\phi = d_{\tau_p\tau_p}^2\phi + d_{\tau_p\tau_c}^2\phi + d_{\tau_c\tau_p}^2\phi + d_{\tau_c\tau_c}^2\phi. \quad (3.134)$$

Remark 1 In spite of the fact that we are addressing plane stress, the rank-four two-dimensional tensors $d_{\hat{\tau}\hat{\tau}}^2\phi = (d_{\hat{\tau}\hat{\tau}}^2\phi)^t$ and $d_{\hat{\tau}\hat{\tau}}^2\phi$ are different from zero. This is evident when the matrix representation of $d_{\tau\tau}^2\phi$ is explicitly provided as sum of eight addends depending upon the unit tensor $\mathbf{1}$ and the stress deviator \mathbf{S} .

We are now in the position to provide a consistent derivation of the plane stress elasto-plastic problem from the 3D one according to the general ideas detailed ahead. The rank-two symmetric tensor \mathbf{P} has the following matrix representation:

$$[\mathbf{P}] = \begin{bmatrix} 1 & 0 & 0 \\ 0 & 1 & 0 \\ 0 & 0 & 1 \end{bmatrix} \quad (3.135)$$

in the given reference frame.

It is immediate to verify that the rank four symmetric tensor \mathbb{P} :

In the sequel we shall synthetically address the diagonal terms of the matrix representation in (3.141) by adopting the following terminology:

$$\mathbb{P}\mathbb{A}\mathbb{P}^t \rightleftharpoons \hat{\mathbb{A}} \quad \mathbb{P}_c\mathbb{A}\mathbb{P}_c^t \rightleftharpoons \check{\mathbb{A}} \quad (3.142)$$

where the symbol \rightleftharpoons denotes the isometric isomorphism between the rank-four 3D tensor on the left-hand side and the the rank-four 2D tensor on the right.

To show the usefulness of the previous definitions, let us derive the plane stress elastic relation from the 3Done. We can write:

$$\mathbb{E}^{-1}\boldsymbol{\sigma} = \boldsymbol{\epsilon} - \mathbf{p} \quad (3.143)$$

which yields, upon premultiplication by \mathbb{P} and \mathbb{P}_c ,

$$\begin{aligned} \mathbb{P}\mathbb{E}^{-1}\boldsymbol{\sigma} &= \mathbb{P}\boldsymbol{\epsilon} - \mathbb{P}\mathbf{p} \\ \mathbb{P}_c\mathbb{E}^{-1}\boldsymbol{\sigma} &= \mathbb{P}_c\boldsymbol{\epsilon} - \mathbb{P}_c\mathbf{p} \end{aligned}$$

Invoking the decomposition (34) and recalling that, in planestress, $\boldsymbol{\sigma} = \boldsymbol{\sigma}_p = \mathbb{P}\boldsymbol{\sigma} = \mathbb{P}^t\boldsymbol{\sigma}$, one gets:

$$\begin{aligned} \mathbb{P}\mathbb{E}^{-1}\mathbb{P}^t\boldsymbol{\sigma} &= \mathbb{P}\boldsymbol{\epsilon}_p + \mathbb{P}\boldsymbol{\epsilon}_c - \mathbb{P}\mathbf{p}_p - \mathbb{P}\mathbf{p}_c \\ \mathbb{P}_c^t\mathbb{E}^{-1}\mathbb{P}^t\boldsymbol{\sigma} &= \mathbb{P}_c\boldsymbol{\epsilon}_p + \mathbb{P}_c\boldsymbol{\epsilon}_c - \mathbb{P}_c\mathbf{p}_p - \mathbb{P}_c\mathbf{p}_c \end{aligned} \quad (3.144)$$

By definition, $\mathbb{P}\boldsymbol{\epsilon}_c = \mathbb{P}\mathbf{p}_c = 0$ so that the former of the relations above becomes:

$$\hat{\mathbb{E}}^{-1}\hat{\boldsymbol{\sigma}} = \hat{\boldsymbol{\epsilon}} - \hat{\mathbf{p}} \quad (3.145)$$

To be specific the elastic relation can be written as follows:

$$\hat{\boldsymbol{\sigma}} = \hat{\mathbb{E}}(\hat{\boldsymbol{\epsilon}} - \hat{\mathbf{p}}) \quad (3.146)$$

and detail the expression of $\hat{\mathbb{E}}$.

The elastic compliance operator \mathbb{E}^{-1} consistent with the tensor-to-matrix mapping (3.125) has the matrix representation:

$$\mathbb{E}^{-1} = \begin{bmatrix} \frac{1}{E} & -\frac{\nu}{E} & 0 & -\frac{\nu}{E} & 0 & 0 \\ -\frac{\nu}{E} & \frac{1}{E} & 0 & -\frac{\nu}{E} & 0 & 0 \\ 0 & 0 & \frac{1}{G} & 0 & 0 & 0 \\ -\frac{\nu}{E} & -\frac{\nu}{E} & 0 & \frac{1}{E} & 0 & 0 \\ 0 & 0 & 0 & 0 & \frac{1}{G} & 0 \\ 0 & 0 & 0 & 0 & 0 & \frac{1}{G} \end{bmatrix} \quad (3.147)$$

where E is the Young modulus and ν the Poisson's ratio.

Hence, according to (3.141), the plane stress compliance operator is defined by:

$$\mathbb{P}\mathbb{E}^{-1}\mathbb{P}^t \rightleftharpoons \hat{\mathbb{E}}^{-1}, \quad [\mathbb{E}^{-1}] = \begin{bmatrix} \frac{1}{E} & -\frac{\nu}{E} & 0 \\ -\frac{\nu}{E} & \frac{1}{E} & 0 \\ 0 & 0 & \frac{1}{G} \end{bmatrix} \quad (3.148)$$

and the elastic operator \mathbb{E} is the rank-four two-dimensional tensor whose associated matrix is obtained by inverting $[\hat{\mathbb{E}}^{-1}]$. Thus, for isotropic elasticity we can write:

$$[\hat{\mathbb{E}}] = \begin{bmatrix} 1 & \nu & 0 \\ \nu & 1 & 0 \\ 0 & 0 & \frac{1-\nu}{2} \end{bmatrix}. \quad (3.149)$$

The second relation of (3.144) establishes a linear relation between the 33 components of $\boldsymbol{\epsilon}$, \mathbf{p} and the in-plane components of the stress tensor. Actually, recalling (3.138) one has:

$$\mathbb{P}\mathbb{E}^{-1}\mathbb{P}^t \boldsymbol{\sigma} = \boldsymbol{\epsilon}_c - \mathbf{p}_c \quad (3.150)$$

since, by definition, $\mathbb{P}_c \boldsymbol{\epsilon}_p = \mathbb{P}_c \mathbf{p}_p = 0 = \mathbb{P} \boldsymbol{\epsilon}_c = \mathbb{P} \mathbf{p}_c = 0$. In the case of linear isotropic elasticity, we can represent the previous equation as follows:

$$\begin{bmatrix} -\frac{\nu}{E} & -\frac{\nu}{E} & 0 \\ 0 & 0 & 0 \\ 0 & 0 & \frac{1}{G} \end{bmatrix} \begin{bmatrix} \boldsymbol{\sigma}_{11} \\ \boldsymbol{\sigma}_{22} \\ \boldsymbol{\sigma}_{12} \end{bmatrix} = \begin{bmatrix} \boldsymbol{\epsilon}_{33} \\ 2\boldsymbol{\epsilon}_{23} \\ 2\boldsymbol{\epsilon}_{13} \end{bmatrix} + \begin{bmatrix} \mathbf{p}_{33} \\ 2\mathbf{p}_{23} \\ 2\mathbf{p}_{13} \end{bmatrix} \quad (3.151)$$

according to (3.126), (3.141) and (3.147) thus recovering the well known relation:

$$\boldsymbol{\epsilon}_{33} - \mathbf{p}_{33} = -\nu \frac{\boldsymbol{\sigma}_{11} + \boldsymbol{\sigma}_{22}}{E}. \quad (3.152)$$

Reasoning as for the elastic relation addressed above, we can derive the two kinematic hardening relations associated, in turn, with the in-plane and out-of-plane components of the back-stress and plasticstrain tensors. Specifically, on account of definition (3.142), we get from the 3D kinematic hardening relation (3.37) the two ones:

$$\hat{\boldsymbol{\beta}} = \hat{\mathbb{H}}_{kin} \hat{\mathbf{p}} \quad \check{\boldsymbol{\beta}} = \check{\mathbb{H}}_{kin} \check{\mathbf{p}}. \quad (3.153)$$

Subtracting the first one of the previous relation for (3.146) and setting $\hat{\boldsymbol{\tau}} = -\hat{\boldsymbol{\beta}}$, we get:

$$\begin{aligned}\hat{\boldsymbol{\tau}} &= \hat{\mathbb{E}}\hat{\boldsymbol{\epsilon}} - (\hat{\mathbb{E}} + \hat{\mathbb{H}}_{kin})\hat{\boldsymbol{p}} = \hat{\mathbb{E}}\hat{\boldsymbol{\epsilon}} - \hat{\mathbb{E}}_H\hat{\boldsymbol{p}} \\ \check{\boldsymbol{\tau}} &= -\hat{\mathbb{H}}_{kin}\check{\boldsymbol{p}}.\end{aligned}$$

Finally, we can split the finite-step normality rule in the form:

$$\hat{\boldsymbol{p}} - \hat{\boldsymbol{p}}_0 = \lambda d_{\hat{\boldsymbol{\tau}}}\phi \quad \check{\boldsymbol{p}} - \check{\boldsymbol{p}}_0 = \lambda d_{\check{\boldsymbol{\tau}}}\phi. \quad (3.154)$$

To sum up, the finite-step plane stress elastoplastic problem in a fully implicit form can be written as follows:

$$\left\{ \begin{array}{l} \hat{\boldsymbol{\tau}} = \hat{\mathbb{E}}\hat{\boldsymbol{\epsilon}} - \hat{\mathbb{E}}_H\hat{\boldsymbol{p}} \\ \check{\boldsymbol{\tau}} = -\hat{\mathbb{H}}_{kin}\check{\boldsymbol{p}} \\ \boldsymbol{\rho} = h_{iso}\boldsymbol{\zeta} \\ \hat{\boldsymbol{p}} - \hat{\boldsymbol{p}}_0 - \lambda d_{\hat{\boldsymbol{\tau}}}\phi(\hat{\boldsymbol{\tau}}, \check{\boldsymbol{\tau}}, \boldsymbol{\rho}) = 0 \\ \check{\boldsymbol{p}} - \check{\boldsymbol{p}}_0 - \lambda d_{\check{\boldsymbol{\tau}}}\phi(\hat{\boldsymbol{\tau}}, \check{\boldsymbol{\tau}}, \boldsymbol{\rho}) = 0 \\ \boldsymbol{\zeta} - \boldsymbol{\zeta}_0 + \lambda d_{\boldsymbol{\rho}}\phi(\hat{\boldsymbol{\tau}}, \check{\boldsymbol{\tau}}, \boldsymbol{\rho}) = 0 \\ \phi(\hat{\boldsymbol{\tau}}, \check{\boldsymbol{\tau}}, \boldsymbol{\rho}) \leq 0 \quad \lambda \geq 0 \quad \lambda\phi(\hat{\boldsymbol{\tau}}, \check{\boldsymbol{\tau}}, \boldsymbol{\rho}) = 0 \end{array} \right. \quad (3.155)$$

where dependence of ϕ upon the in-plane $\hat{\boldsymbol{\tau}}$ and out-of-plane $\check{\boldsymbol{\tau}}$ components of $\boldsymbol{\tau}$ has been emphasized by writing $\phi(\hat{\boldsymbol{\tau}}, \check{\boldsymbol{\tau}}, \boldsymbol{\rho})$. It is worth noting that references is always made to the 3D yield function.

The previous set of equations represents a non linear system to be solved for a given value of $\hat{\boldsymbol{\epsilon}}$. Pursuing a Newton's approach we stagger (3.155) by considering separately the equations related to the out of plane and in-plane components:

$$\left\{ \begin{array}{l} \check{\boldsymbol{\tau}} = -\hat{\mathbb{H}}_{kin}\check{\boldsymbol{p}} \\ \check{\boldsymbol{p}} - \check{\boldsymbol{p}}_0 - \lambda d_{\check{\boldsymbol{\tau}}}\phi(\hat{\boldsymbol{\tau}}, \check{\boldsymbol{\tau}}, \boldsymbol{\rho}) = 0 \end{array} \right. \quad (3.156)$$

$$\left\{ \begin{array}{l} \hat{\boldsymbol{\tau}} = \hat{\mathbb{E}}\hat{\boldsymbol{\epsilon}} - \hat{\mathbb{E}}_H\hat{\boldsymbol{p}} \\ \boldsymbol{\rho} = h_{iso}\boldsymbol{\zeta} \\ \hat{\boldsymbol{p}} - \hat{\boldsymbol{p}}_0 - \lambda d_{\hat{\boldsymbol{\tau}}}\phi(\hat{\boldsymbol{\tau}}, \check{\boldsymbol{\tau}}, \boldsymbol{\rho}) = 0 \\ \boldsymbol{\zeta} - \boldsymbol{\zeta}_0 + \lambda d_{\boldsymbol{\rho}}\phi(\hat{\boldsymbol{\tau}}, \check{\boldsymbol{\tau}}, \boldsymbol{\rho}) = 0 \\ \phi(\hat{\boldsymbol{\tau}}, \check{\boldsymbol{\tau}}, \boldsymbol{\rho}) \leq 0 \quad \lambda \geq 0 \quad \lambda\phi(\hat{\boldsymbol{\tau}}, \check{\boldsymbol{\tau}}, \boldsymbol{\rho}) = 0 \end{array} \right. \quad (3.157)$$

Actually, the variables in the former set of equations are non-linear functions of the variable in the latter. In particular, the linearization of the equations in (3.156) moves its steps from the following considerations.

The relative stress $\boldsymbol{\tau}$ has the following matrix representation:

$$[\boldsymbol{\tau}] = \begin{bmatrix} \boldsymbol{\tau}_{11} & \boldsymbol{\tau}_{12} & \boldsymbol{\tau}_{13} \\ \boldsymbol{\tau}_{21} & \boldsymbol{\tau}_{22} & \boldsymbol{\tau}_{23} \\ \boldsymbol{\tau}_{13} & \boldsymbol{\tau}_{23} & \boldsymbol{\tau}_{33} \end{bmatrix} = \begin{pmatrix} \sigma_{11} - \beta_{11} & \sigma_{12} - \beta_{12} & 0 \\ \sigma_{21} - \beta_{21} & \sigma_{22} - \beta_{22} & 0 \\ 0 & 0 & -\beta_{33} \end{pmatrix}. \quad (3.158)$$

Hence:

$$[\mathbf{S}] = \begin{pmatrix} 2\tau_{11} - \tau_{22} - \beta_{33} & 3\tau_{12} - \beta_{12} & 0 \\ 3\tau_{21} - \beta_{21} & -\tau_{11} + 2\tau_{22} - \beta_{33} & 0 \\ 0 & 0 & -\tau_{11} - \tau_{22} - 2\beta_{33} \end{pmatrix} \quad (3.159)$$

and it is immediate to verify that \mathbf{S}^2 has the same matrix representation as the previous tensor, i.e. the (3.46) and (3.91) entries are zero.

Accordingly, (3.156)2 establishes a non linear relation between the out of plane components of the plastic strain, as a matter of fact \mathbf{p}_{33} , and the components of the stress tensor, both the in-plane and the out of plane ones. We thus get:

$$d_{\hat{\boldsymbol{\tau}}}\check{\mathbf{p}} = \lambda d_{\hat{\boldsymbol{\tau}}\hat{\boldsymbol{\tau}}}^2\boldsymbol{\phi} + \lambda(d_{\hat{\boldsymbol{\tau}}\hat{\boldsymbol{\tau}}}^2\boldsymbol{\phi})d_{\hat{\boldsymbol{\tau}}}\check{\boldsymbol{\tau}} + d_{\hat{\boldsymbol{\tau}}}\boldsymbol{\phi} \otimes d_{\hat{\boldsymbol{\tau}}}\lambda; \quad (3.160)$$

the derivative of (3.156)1 with respect to $\boldsymbol{\tau}$, combined with the previous expression, provides:

$$d_{\hat{\boldsymbol{\tau}}}\check{\boldsymbol{\tau}} = -\check{\check{\mathbb{A}}}_H^{-1}[\lambda d_{\hat{\boldsymbol{\tau}}\hat{\boldsymbol{\tau}}}^2\boldsymbol{\phi} + d_{\hat{\boldsymbol{\tau}}}\boldsymbol{\phi} \otimes d_{\hat{\boldsymbol{\tau}}}\lambda] \quad (3.161)$$

where it has been set:

$$\check{\check{\mathbb{A}}}_H = \check{\check{\mathbb{H}}}_{kin} + \lambda d_{\hat{\boldsymbol{\tau}}\hat{\boldsymbol{\tau}}}^2\boldsymbol{\phi}. \quad (3.162)$$

Let us now linearize (3.157)1-4 and the condition

$$\boldsymbol{\phi}(\hat{\boldsymbol{\tau}}, \check{\boldsymbol{\tau}}, \boldsymbol{\rho}) \quad (3.163)$$

around the k -th estimate of the solution. Defining:

$$\mathbf{r}_{\hat{\mathbf{p}}}^{(k)} = -\hat{\mathbf{p}}^{(k)} + \hat{\mathbf{p}}_0^{(k)} + \lambda^{(k)} d_{\hat{\boldsymbol{\tau}}}\boldsymbol{\phi}^{(k)} \quad (3.164)$$

in place of (3.48)1, we get:

$$\mathbf{r}_{\hat{\mathbf{p}}}^{(k)} - \delta\hat{\mathbf{p}}^{(k+1)} + \lambda^{(k)} d_{\hat{\boldsymbol{\tau}}}\boldsymbol{\phi}^{(k)} \delta\hat{\boldsymbol{\tau}}^{(k+1)} + \lambda^{(k)} d_{\hat{\boldsymbol{\tau}}}\boldsymbol{\phi}^{(k)} (d_{\hat{\boldsymbol{\tau}}}\check{\boldsymbol{\tau}}) \delta\hat{\boldsymbol{\tau}}^{(k+1)} + d_{\hat{\boldsymbol{\tau}}}\boldsymbol{\phi}^{(k)} \delta\lambda^{(k+1)} = 0. \quad (3.165)$$

Taking into account (3.155)1 and (3.161) the previous equation becomes:

$$\mathbf{r}_{\hat{\mathbf{p}}}^{(k)} + \hat{\mathbb{G}}_H^{(k)} \delta \hat{\boldsymbol{\tau}}_{(k)}^{(k+1)} + \delta \lambda_{(k)}^{(k+1)} \hat{\mathbf{n}}_H^{(k)} = 0. \quad (3.166)$$

where:

$$\hat{\mathbb{G}}_H = \hat{\mathbb{E}}_H^{-1} + \lambda d_{\hat{\boldsymbol{\tau}}\hat{\boldsymbol{\tau}}}^2 \boldsymbol{\phi} - (\lambda d_{\hat{\boldsymbol{\tau}}\hat{\boldsymbol{\tau}}}^2 \boldsymbol{\phi})(\hat{\mathbb{A}}_H)^{-1} (\lambda d_{\hat{\boldsymbol{\tau}}\hat{\boldsymbol{\tau}}}^2 \boldsymbol{\phi}) \quad (3.167)$$

and:

$$\hat{\mathbf{n}}_H = d_{\hat{\boldsymbol{\tau}}}\boldsymbol{\phi} - (\lambda d_{\hat{\boldsymbol{\tau}}\hat{\boldsymbol{\tau}}}^2 \boldsymbol{\phi})(\hat{\mathbb{A}}_H)^{-1} d_{\hat{\boldsymbol{\tau}}}\boldsymbol{\phi}. \quad (3.168)$$

It is worth noting that, in absence of hardening $\hat{\mathbf{n}}_H$ callapses to $\hat{\mathbf{n}} = d_{\hat{\boldsymbol{\tau}}}\boldsymbol{\phi}$; moreover, at the beginning of the constitutive iterations ($\lambda^{(k=0)} = 0$), it turns out to be $\hat{\mathbb{G}}_H^{(k=0)} = \hat{\mathbb{E}}$ as much as the inverse of its 3D counterpart, reported in (3.50), coincides with the 3D elastic operator.

The linearization of (3.163) yields:

$$\boldsymbol{\phi}^{(k)} + d_{\hat{\boldsymbol{\tau}}}\boldsymbol{\phi}^{(k)} \cdot \delta \hat{\boldsymbol{\tau}}_{(k)}^{(k+1)} + d_{\hat{\boldsymbol{\tau}}}\boldsymbol{\phi}^{(k)} \cdot (d_{\hat{\boldsymbol{\tau}}}\check{\boldsymbol{\tau}})^{(k)} \delta \hat{\boldsymbol{\tau}}_{(k)}^{(k+1)} - \delta \boldsymbol{\rho}_{(k)}^{(k+1)} = 0. \quad (3.169)$$

so that, on account of (3.161) and (3.168) , one gets:

$$\boldsymbol{\phi}^{(k)} + \hat{\mathbf{n}}_H \cdot \delta \hat{\boldsymbol{\tau}}_{(k)}^{(k+1)} - [(\check{\mathbb{A}}_H^{(k)})^{-1} d_{\hat{\boldsymbol{\tau}}}\boldsymbol{\phi}^{(k)} \cdot d_{\hat{\boldsymbol{\tau}}}\boldsymbol{\phi}^{(k)}] \delta \hat{\boldsymbol{\lambda}}_{(k)}^{(k+1)} - \delta \boldsymbol{\rho}_{(k)}^{(k+1)} = 0. \quad (3.170)$$

Finally, the linearization of (3.48)2 for plane stress is completely similar to the 3D case. In order to emphasize the perfect analogy between the plane stress and the three-dimensional returning map we re-formulate the previous equations in matrix form by adopting the same formalism employed in the formula (3.49)

$$\begin{bmatrix} \mathbf{r}_{\hat{\mathbf{p}}}^{(k)} \\ \mathbf{r}_{\hat{\boldsymbol{\zeta}}}^{(k)} \\ \mathbf{r}_{\boldsymbol{\phi}}^{(k)} \end{bmatrix} + \begin{bmatrix} \hat{\mathbb{G}}_H^k & 0 & \hat{\mathbf{n}}_H \\ 0 & \frac{1}{h_{iso}} & -1 \\ \hat{\mathbf{n}}_H & -1 & -(\check{\mathbb{A}}_H^{(k)})^{-1} d_{\hat{\boldsymbol{\tau}}}\boldsymbol{\phi}^{(k)} \cdot d_{\hat{\boldsymbol{\tau}}}\boldsymbol{\phi}^{(k)} \end{bmatrix} + \begin{bmatrix} \delta \hat{\boldsymbol{\tau}}_{(k)}^{(k+1)} \\ \delta \boldsymbol{\rho}_{(k)}^{(k+1)} \\ \delta \boldsymbol{\lambda}_{(k)}^{(k+1)} \end{bmatrix} = \begin{bmatrix} \check{\mathbf{0}} \\ 0 \\ 0 \end{bmatrix}. \quad (3.171)$$

Condensation of the previous system with respect to $\delta \boldsymbol{\lambda}_{(k)}^{(k+1)}$ yields:

$$\delta \boldsymbol{\lambda}_{(k)}^{(k+1)} = \frac{\mathbf{r}_{\boldsymbol{\phi}}^{(k)} - (\hat{\mathbb{G}}_H^{(k)})^{-1} \mathbf{r}_{\hat{\mathbf{p}}}^{(k)} \cdot \hat{\mathbf{n}}_H^{(k)} + h_{iso} \mathbf{r}_{\hat{\boldsymbol{\zeta}}}^{(k)}}{(\hat{\mathbb{G}}_H^{(k)})^{-1} \hat{\mathbf{n}}_H^{(k)} \cdot \hat{\mathbf{n}}_H^{(k)} + (\check{\mathbb{A}}_H^{(k)})^{-1} d_{\hat{\boldsymbol{\tau}}}\boldsymbol{\phi}^{(k)} \cdot d_{\hat{\boldsymbol{\tau}}}\boldsymbol{\phi}^{(k)} + h_{iso}}, \quad (3.172)$$

and it is proved that $\hat{\mathbb{G}}_H$ and $\check{\mathbb{A}}_H$ are positive-definite; hence, being also $h_{iso} \geq 0$, the previous relation is always well defined. The associated quantities are then updated at the end of the k-th constitutive iteration on the basis of (3.171)2-3.

3.5.7 Application to the Menetrey Willam material model.

The methods described above for the implementation of an elasto-plastic isotropic material model into a finite element program, have been used to program the user supplied material model described in section 3.4.1 for its use in LUSAS. The FORTRAN routines codified (that cover the use of the material in full three dimensional, plane strain and plane stress problems) are reported in the Appendix.

In what follows the derivatives of the Menetrey Willam yield function required for the calculation of the coefficients n_i and e_i are reported.

The first and second derivatives of the yield function (3.29) with respect to the stress invariants represent the basic ingredients of the procedure developed in [98].

The first derivatives of (3.29) have the following expressions:

$$\left\{ \begin{array}{l} d_1\varphi = \frac{\partial\varphi}{\partial I_1} = mC \frac{1}{\sqrt{3}} \\ d_2\varphi = \frac{\partial\varphi}{\partial J_2} = \frac{\partial\varphi}{\partial\rho} \frac{\partial\rho}{\partial J_2} + \frac{\partial\varphi}{\partial\theta} \frac{\partial\theta}{\partial J_2} = 2A^2\rho \frac{\partial\rho}{\partial J_2} + mBr \frac{\partial\rho}{\partial J_2} + mB\rho \frac{\partial r}{\partial\theta} \frac{\partial\theta}{\partial J_2} \\ d_3\varphi = \frac{\partial\varphi}{\partial J_3} = \frac{\partial\varphi}{\partial\theta} \frac{\partial\theta}{\partial J_3} = mB\rho \frac{\partial r}{\partial\theta} \frac{\partial\theta}{\partial J_3} \end{array} \right. \quad (3.173)$$

The required non-zero derivatives of ρ and θ with respect to the invariants J_2 and J_3 are given by:

$$\left\{ \begin{array}{l} \frac{\partial\rho}{\partial J_2} = \frac{1}{\sqrt{2J_2}} \\ \frac{\partial\theta}{\partial J_2} = \frac{1 \cos 3\theta}{2J_2 \sin 3\theta} \quad \frac{\partial\theta}{\partial J_3} = -\frac{1 \cos 3\theta}{3J_3 \sin 3\theta} \end{array} \right. \quad (3.174)$$

while the derivative of r with respect to θ are evaluated by rewriting equation (3.30) as follows:

$$r(\theta, e) = \frac{N}{D} \quad (3.175)$$

with N and D being:

$$N = N(\theta) = 4(1 - e^2) \cos^2 \theta + (2e - 1)^2$$

$$D = D(\theta) = 2(1 - e^2) \cos \theta + (2e - 1) \sqrt{4(1 - e^2) \cos^2 \theta + 5e^2 - 4e} \quad (3.176)$$

so that we get:

$$\frac{\partial r}{\partial \theta} = \frac{N'D - ND'}{D^2} \quad (3.177)$$

with N' and D' given by:

$$\begin{aligned} N' &= -8(1 - e^2) \cos \theta \sin \theta \\ D' &= -2(1 - e^2) \sin \theta - \frac{4(2e - 1)(1 - e^2) \cos \theta \sin \theta}{\sqrt{4(1 - e^2) \cos^2 \theta + 5e^2 - 4e}} \end{aligned} \quad (3.178)$$

The second derivatives of the yield function have the following expressions:

$$\left\{ \begin{aligned} d_{11}\varphi &= d_{12}\varphi = d_{13}\varphi = 0 \\ d_{22}\varphi &= 2A^2 \left(\frac{\partial \rho}{\partial J_2} \right)^2 + 2A^2 \rho \frac{\partial^2 \rho}{\partial J_2^2} + mBr \frac{\partial^2 \rho}{\partial J_2^2} + 2mB \frac{\partial r}{\partial \theta} \frac{\partial \theta}{\partial J_2} \frac{\partial \rho}{\partial J_2} + \\ &\quad + mB\rho \frac{\partial^2 r}{\partial \theta^2} \left(\frac{\partial \theta}{\partial J_2} \right)^2 + mB\rho \frac{\partial r}{\partial \theta} \frac{\partial^2 \theta}{\partial J_2^2} \\ d_{23}\varphi &= mB\rho \frac{\partial^2 r}{\partial \theta^2} \frac{\partial \theta}{\partial J_3} \frac{\partial \theta}{\partial J_2} + mB\rho \frac{\partial r}{\partial \theta} \frac{\partial^2 \theta}{\partial J_3 \partial J_2} + mB \frac{\partial \rho}{\partial J_2} \frac{\partial r}{\partial \theta} \frac{\partial \theta}{\partial J_3} \\ d_{33}\varphi &= mB\rho \frac{\partial^2 r}{\partial \theta^2} \left(\frac{\partial \theta}{\partial J_3} \right)^2 + mB\rho \frac{\partial r}{\partial \theta} \frac{\partial^2 \theta}{\partial J_3^2} \end{aligned} \right. \quad (3.179)$$

where the second derivatives of ρ and θ with respect to the stress deviator invariants J_2 and J_3 are given by:

$$\begin{aligned} \frac{\partial^2 \rho}{\partial J_2^2} &= \frac{-1}{\sqrt{(2J_2)^3}} & \frac{\partial^2 \theta}{\partial J_2^2} &= -\frac{1}{2J_2^2} \frac{\cos 3\theta}{\sin 3\theta} \left[1 + \frac{3}{2} \frac{1}{\sin^2 3\theta} \right] \\ \frac{\partial^2 \theta}{\partial J_2 \partial J_3} &= \frac{1}{2J_2 J_3} \frac{\cos 3\theta}{\sin^3 3\theta} & \frac{\partial^2 \theta}{\partial J_3^2} &= -\frac{1}{3J_3^2} \frac{\cos^3 3\theta}{\sin^3 3\theta} \end{aligned} \quad (3.180)$$

while the expression of the second derivative of r with respect to θ is as follows:

$$\frac{\partial^2 r}{\partial \theta^2} = \frac{N''D^2 - D''DN + 2D'^2N - 2N'DD'}{D^3} \quad (3.181)$$

with N'' and D'' provided by:

$$N'' = -8(1 - e^2)(\cos^2 \theta - \sin^2 \theta) \quad (3.182)$$

$$D'' = -2(1 - e^2) \cos \theta - 4(2e - 1)(1 - e^2) f(\theta)$$

and

$$f(\theta) = \{(2 \cos^2 \theta - 1)[4(1 - e^2) \cos^2 \theta + 5e^2 - 4e]^{-\frac{1}{2}} + 4(1 - e^2) \sin^2 \theta \cos^2 \theta [4(1 - e^2) \cos^2 \theta + 5e^2 - 4e]^{-\frac{3}{2}}\} \quad (3.183)$$

3.6 Further simplified models for plain concrete

Beside the model described in the preceding sections, other simplified models have been used. They have been used for testing the validity of the assumptions inherent in the Menetrey Willam elastoplastic model (such as that softening is not activated in the cracked concrete domain) and to investigate particular aspects, like crack onset and propagation, within a plain concrete volume.

Although several models have been tested (some of them using the computer package ADINA instead of LUSAS) only the results obtained with two of them, alongside with those obtained with the new developed model, are reported in this dissertation. These models fall under the two categories usually addressed as damage models and cracking models. In the first category we find models in which the stiffness properties of the material are degraded as damage, due to stressing or straining, is accumulated whilst in the second one the principal source of nonlinearity of concrete, i.e. cracking, is addressed by making use of the smeared crack concept. Both the models include a fracture energy based softening model but the characteristics of the material response to a given strain history are different. The main difference is related to the direction in which the material softens and then to the anisotropic properties of the material after onset of damage/cracking.

In the following the main features of the two models are explained together with the motivation for their use. The details of their implementation are not given as they are outside the scope of this work.

3.6.1 Damage concrete model

Damage models have become, recently, popular techniques for simulating various nonlinear effects in materials.

The LUSAS program incorporates an isotropic damage model, based on a publication by Oliver et al. (1991), [87]. This isotropic damage model, includes degradation of the material both in tension and in compression. The onset of damage is established by imposing a damage condition similar to a yield function in elastoplasticity.

Different tensile and compressive strengths can be specified and the model, even though very simple, has been used, also by others, to attempt a smeared crack type modelling of concrete [92].

Damage accumulation is represented by using a function of the complementary energy

$$G(r_t) = 1 - \frac{r_o}{r_t} \exp[A(1 - \frac{r_o}{r_t})] \quad (3.184)$$

where r_o is called the damage threshold and has the expression

$$r_o = [(\sigma_t)/(E_o)^{1/2}] \quad (3.185)$$

and r_t (the term containing the complementary energy) is the current damage strength and has the expression

$$r_t = \max\{r_o, \quad \gamma(\sigma_t^T \mathbb{E}^{-1} \sigma)^{\frac{1}{2}}\} \quad (3.186)$$

where \mathbb{E} denotes as usual the elastic compliance tensor of the undamaged material and γ is a scalar function of the stresses (in a similar model by Simo $\gamma = 1$).

For the case of no damage $G(r_t) = G(r_o) = 0$.

The parameter A in (3.184) is a material parameter and has the following expression in Oliver's model

$$A = [(G_f E_o / \sigma_d^t) - 0.5]^{-1} \quad (3.187)$$

With E_o initial modulus of elasticity of concrete and G_f fracture energy in mode I of concrete.

Eventually, the secant stiffness matrix of the material is given as

$$E^{\text{sec}} = (1 - G)E_o \quad (3.188)$$

From which the current stresses can be easily calculated.

The model has been used because no difficulty whatsoever has been encountered in terms of convergence. It is, admittedly too simplistic, for concrete, but was useful to obtain preliminary results against which to compare those obtained with more sophisticated models.

It is worth noting that at the beginning of this work it was, also, the only nonlinear model allowing different strengths in compression and tension, available in LUSAS, yielding convergence for advanced loading stages. The more sophisticated multicrack concrete model failed to yield convergence at load levels too low for the purposes of the investigation intended. More recently with the release of version 13.7 of LUSAS by FEA the convergence limitations of the above model have been overcome by the introduction of a new model for concrete.

With the new tool the use of the smeared crack concept in the analysis of RC beams retrofitted with FRP has been further explored.

3.6.2 Cracking models

As mentioned several times the principal source of non-linearity for concrete is cracking. By natural emulation of reality modelling of cracking has been first attempted by introducing discontinuities in the mesh [83]. These discontinuities can be preset or automatically generated. In the first case we have the obvious limitation that the crack pattern must be predetermined by preliminary analysis and cracks configuration is not variable during the analysis. Even with these major drawbacks this approach can still be useful in the investigation of particular aspects as will be shown in the chapter on cracking modelling. The second case presents, obviously, very onerous operative complications related to remeshing and to modelling of local behaviour at crack tips.

On the other hand, even though cracking is physically the generation of a discontinuity in the material, within the framework finite element method, it would be appealing to model its consequences without losing the continuity of the analysed spatial domain.

To achieve this, as we do not want to touch the element introducing discontinuities in it (this is a possible approach that will be briefly discussed later on), we have to operate at the material level.

This means defining a constitutive law that enables a stress release over the volume that is affected by cracking. It is immediately apparent, then, that the main ingredient required is softening of the material.

As by using the above strategy discontinuities are suppressed the modelling of cracking must involve necessarily some space averaging. It is for this reason that the approaches that we are outlining are called smeared crack approaches. More precisely models of this kind are referred to as models using the smeared crack concept. The denomination is due to the fact that cracks are somehow smeared into a finite volume rather than localised as discrete discontinuity.

It is opportune, now, to clarify that such an approach is currently used in two, quite different, contexts.

One case is the modelling of a large portion of a structure in which a finite element is representative of a volume actually containing series of parallel cracks in one or more directions, for which the smearing is quite a natural operation. In this context the control volume includes generally also reinforcement uniformly spread in different directions and the constitutive law used is representative of the entire assemblage of uncracked concrete, cracks and reinforcement (note that we deliberately refer to cracks like to a sort of fictitious structural unit).

The other case is the modelling of the onset and growth of localised cracks into a plain concrete volume.

Although the two applications of the smeared crack concept are quite different they are both developed on the same basic framework. The main difference being mainly the strategy used, in the latter, for the localization of the strains representative of cracking within narrow bands (ideally with the width of a single element).

As our aim is the detailed investigation of the behaviour of a single structural element, the modelling of localised cracks, is the situation of interest for us.

In this section we outline the basic features of this manner of modelling concrete and leave the discussion of the details concerning localization for the section on crack modelling.

The smeared crack approach may be divided into the fixed smeared crack and the rotating smeared crack approach. In the latter the direction of the crack is updated during the analysis and is always considered normal to the tensile principal stress exceeding the cracking criterion. This greatly simplify the implementation but has evident limitations above all about modelling of shear transfer through cracks due to aggregate interlocking..

To formulate a smeared crack concrete model let us consider a concrete element with one or more parallel cracks in one arbitrary direction only (the extension to multiple crack directions will be discussed later). We refer in what follows to the two-dimensional plane stress case for simplicity of representation.

The averaged stress-strain relation required, can be formulated from the mechanics of nonlinearity of the cracks and the elasticity of the uncracked concrete.

The secant stiffness operator relating the average stress to the average strain of the element, can be obtained considering the equilibrium and compatibility conditions of the cracks and the uncracked concrete acting as a serial chain see Figure 3.18.

The behaviour of uncracked concrete can be represented by the elastic compliance tensor \mathbb{E} while the mechanics of nonlinearity of the cracks can be represented by introducing the following

$$\left\{ \begin{array}{c} \sigma_n \\ \tau \end{array} \right\} = [\mathbb{D}^*] \boldsymbol{\varepsilon}_{ck}^*, \quad D = \begin{bmatrix} E_n & EG \\ 0 & \beta G \end{bmatrix} \quad (3.189)$$

with the entries in \mathbb{D}^* being appropriate nonlinear functions of the current stress-strain state. The stress-strain relation (3.189) is expressed in a local orthogonal reference frame (\mathbf{n}, \mathbf{t}) with the \mathbf{n} axis normal to the crack. The term E_n describes the direct relation between crack opening strain and stress transfer across the crack. The term βG expresses the effect of aggregate shear interlocking (is generally expressed as product of the shear modulus G of the uncracked material by the scalar nonlinear function of the internal variables β called shear retention factor). The term EG , if non zero, accounts for the shear/normal stress coupling (dilatancy).

The strain $\boldsymbol{\varepsilon}_{ck}^*$ represents the average strain in the element associated with the crack, expressed in the local frame. The relation for the modelling of cracking given in a local reference frame can be easily transformed to the global reference frame by applying a transformation \mathbb{T} such that

$$\mathbb{D} = (\mathbb{T} \boxtimes \mathbb{T})[\mathbb{D}^*]$$

from which we obtain the stress-strain relation for the crack in the global reference frame

$$\boldsymbol{\sigma} = \mathbb{D} \boldsymbol{\varepsilon}_{ck} \quad (3.190)$$

thus we can write

$$\boldsymbol{\sigma} = \mathbb{E} \boldsymbol{\varepsilon}_c = \mathbb{D} \boldsymbol{\varepsilon}_{ck} = \mathbb{E}_{\text{sec}} \boldsymbol{\varepsilon}; \quad \boldsymbol{\varepsilon} = \boldsymbol{\varepsilon}_c + \boldsymbol{\varepsilon}_{ck}. \quad (3.191)$$

where the first one is an equilibrium equation in which $\boldsymbol{\varepsilon}_c$ is the average strain associated with the uncracked concrete, \mathbb{E}_{sec} is the secant modulus of the cracked material and $\boldsymbol{\varepsilon}$ is the total average strain of the composite material.

The second equation in (3.191) is obviously a compatibility equation.

From (3.191)

$$\boldsymbol{\varepsilon}_c = \boldsymbol{\varepsilon} - \boldsymbol{\varepsilon}_{ck}; \quad \mathbb{D}\boldsymbol{\varepsilon}_{ck} = \boldsymbol{\sigma} = \mathbb{E}\boldsymbol{\varepsilon}_c = \mathbb{E}\boldsymbol{\varepsilon} - \mathbb{E}\boldsymbol{\varepsilon}_{ck}; \quad (\mathbb{D} + \mathbb{E})\boldsymbol{\varepsilon}_{ck} = \mathbb{E}\boldsymbol{\varepsilon} \quad (3.192)$$

and therefore

$$\boldsymbol{\varepsilon}_{ck} = (\mathbb{D} + \mathbb{E})^{-1}\mathbb{E}\boldsymbol{\varepsilon} \quad (3.193)$$

and considering the third of (3.191) again

$$\boldsymbol{\varepsilon}_c + (\mathbb{D} + \mathbb{E})^{-1}\mathbb{E}\boldsymbol{\varepsilon} = \boldsymbol{\varepsilon}. \quad (3.194)$$

Applying \mathbb{E} to both sides of the above equation, substituting $\boldsymbol{\sigma}$ for $\mathbb{E}\boldsymbol{\varepsilon}_c$, and rearranging, we finally obtain the expression for the average stress-average strain relation, of the cracked concrete :

$$\boldsymbol{\sigma} = [\mathbb{E} - \mathbb{E}(\mathbb{D} + \mathbb{E})^{-1}\mathbb{E}]\boldsymbol{\varepsilon} = \mathbb{E}_{\text{sec}}\boldsymbol{\varepsilon} \quad (3.195)$$

where \mathbb{E}_{sec} is a secant modulus relating directly the total average strain in the finite element with the average stress.

Note that the reinforcement could be easily superimposed by adding a term of the kind

$$\mathbb{D}_r = (\mathbb{R}_r \boxtimes \mathbb{R}_r)[\mathbb{D}_r^*]; \quad \mathbb{D}_r^* = \begin{bmatrix} \rho_x E_s & 0 & 0 \\ 0 & \rho_y E_s & 0 \\ 0 & 0 & 0 \end{bmatrix}$$

With E_s elastic modulus of steel and ρ_x and ρ_y ratios of steel to concrete area in two orthogonal directions x and y . Again \mathbb{R}_r is a rotation and the superscript * denotes quantities referred to a local reference frame.

With the above positions, different cracking concrete models can be defined specifying the terms E_n , EG and β as appropriate nonlinear functions of a given set of internal variables.

In the above approach a local reference frame is generated on onset of cracking. Orthogonal cracks can be handled by using a single local reference frame and adding an appropriate entry for $\sigma_{n\perp}$ in (3.189). If, more than two, or non orthogonal, crack directions are required, additional reference frames must be introduced. This can be computationally onerous as the total strain is to be distributed into concrete and crack strains, solving iteratively a nonlinear set of equations and a number of approximation strategies have been devised.

The introduction of a crack or a series of parallel cracks into an element by using the (3.189) implies that stresses are not immediately released to zero when crack strains begin to be accumulated. In models for reinforced

concrete a residual stress can be maintained even for large strains, due to the reinforcement bridging action. In plain concrete a stress free crack is generated after a softening phase. The softening phase has actually a physical meaning because a macrocrack in plain concrete, as already pointed out, forms by coalescence of a number of microcracks. Differently from what happens with metals the area interested by microcracking (process zone) and therefore by softening, at the level of the control volume, is relatively large compared to the overall dimensions of the structural element (Figure 3.19). On the other hand, if the stresses across a crack were considered to drop immediately to zero, completely stress free cracks could appear simultaneously in adjacent elements resulting in an unstable structure and impossible convergence due to the presence of multiple solutions. The softening model is to be defined in such a way to prevent also the occurrence of the above situation. There are also problems related to mesh dependency of the solution that will be addressed in Chapter 5.

Using the outlined framework as a backbone very comprehensive smeared crack concrete models can be defined. The cracking crushing criteria can be chosen as desired, plasticity can be introduced for uncracked concrete, degradation of the concrete stiffness/resistance in the direction parallel to cracks can be accounted for and, above all, different strategies can be used to control localization of crack strains. These strategies range from the use of fracture energy based softening relations to the introduction of a nonlocal continuum and will be discussed in the section on crack modelling.

The Smeared crack model of LUSAS (model multicrack 92) has been used to explore the modelling of localised cracks in concrete for the application to RC beams retrofitted with FRP. Notched plain concrete specimens have been analysed first obtaining a satisfactory strain localization. The analysis of the full system has been therefore attempted. In the presence of uniform moments on part of the beam, and due to the force spreading action of FRP and steel reinforcement, the desired localization has not been achieved in the models representing a complete retrofitted system. This has, as will be seen in the following sections, a major effect on the interfacial stresses between concrete and FRP and, in turn, on the performance of the interface and on the prediction of possible mechanisms of debonding failure.

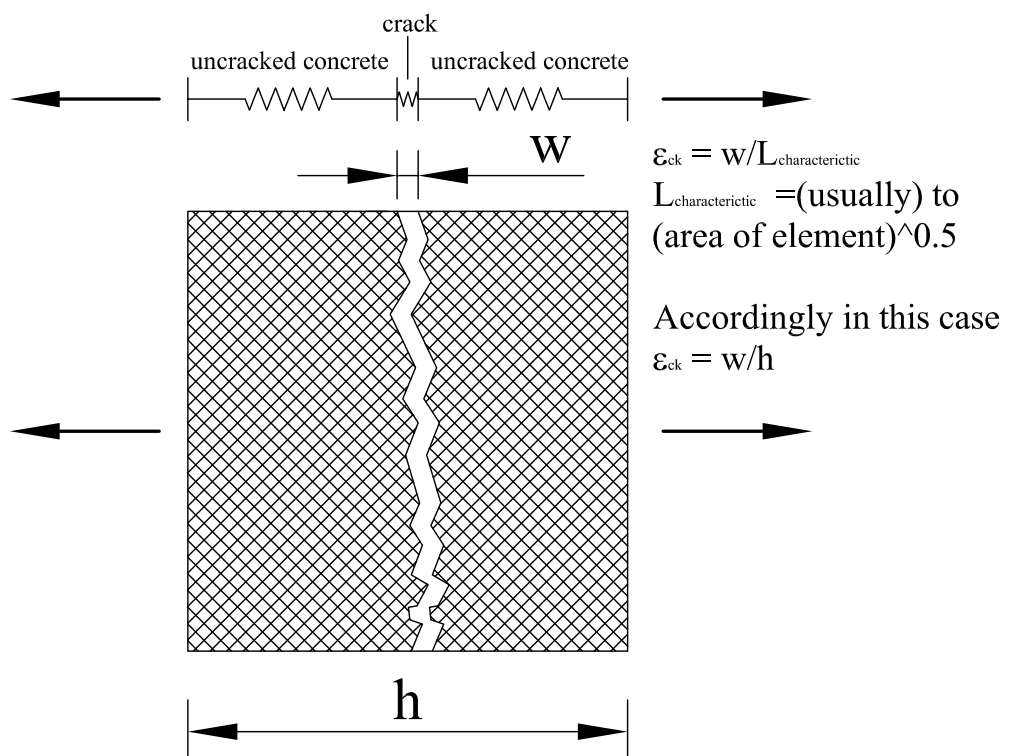


Figure 3.18: Crack modelling in the smeared crack approach

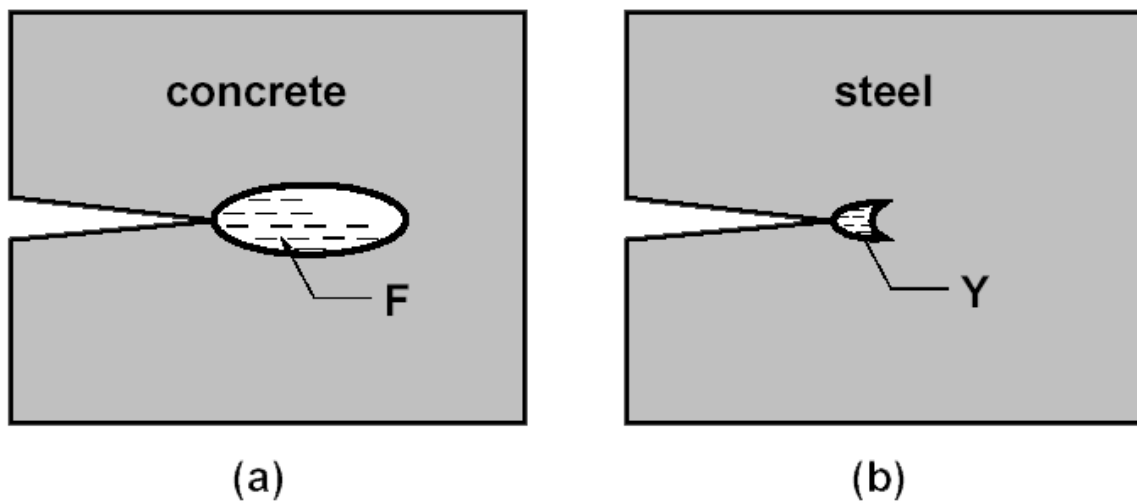


Figure 3.19: Relative size of crack process zone. (a) fracture zone (F) of concrete;(b) yielding zone (Y) of steel.

Chapter 4

Interfaces steel/concrete and FRP/concrete

4.1 Introduction

The main element of novelty of RC beams retrofitted with FRP, with respect to ordinary reinforced concrete beams, are the failure modes associated with debonding of the FRP external reinforcement.

In fact, for an embedded steel bar, due to the nature of the mechanism of force transfer rebar/concrete, is always possible to increase the amount of force transferred from concrete (the directly loaded material) into the steel (Fig4.1 (a)). Therefore, provided the reinforcement has been correctly detailed, failure due to ineffective interaction between concrete and rebar cannot happen and is not to be taken into account.

For FRP external plates, instead, there is a maximum anchorage length beyond which the force that can be transferred cannot be further (Fig4.1 (b)) increased. The problem is also complicated by stress concentrations due to cracking, stress concentrations at the plates'ends and debonding effects due relative slip at shear cracks (see Chapter 2).

This new aspect is recognised in the international guidelines for the design of this type of strengthening works, which give indications on how to calculate the *effective anchorage length*, that is the anchorage length corresponding to the maximum possible force transfer, and provide a limit strain for FRP to prevent midspan debonding (see Chapter 2).

A good model for RC beams retrofitted with FRP must be therefore capable of predicting debonding failure modes. Besides, as we have already explained, the model we are setting up is intended to be the more realistic and comprehensive is possible. This is because the model is not only intended

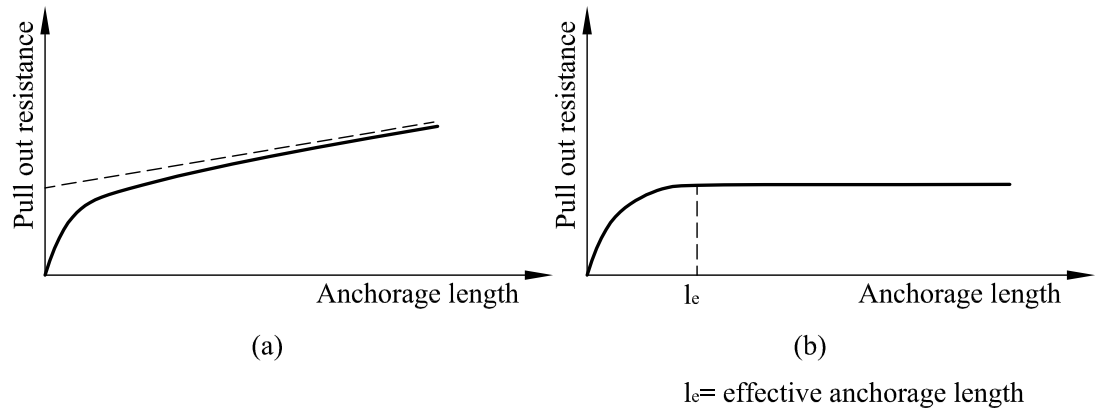


Figure 4.1: Qualitative diagram of pull out resistance versus anchorage length:(a) steel rebar;(b) FRP plate.

for the assessment of the element capacity but also to supply informations on these systems difficult to obtain experimentally.

A good model for the interfaces is therefore of key importance. This does not apply only to the sensitive interface FRP/concrete but also to the more robust one, steel rebar/concrete. This is due to the fact that bond slip of steel rebars largely influence crack opening and spacing, and in turn, as already explained, the performance of the FRP/concrete interface.

The correct modelling of the interfaces affects significantly also the stiffness performance of the system, that is also of interest, as often FRP are used to increase the stiffness of a structural element rather than its capacity.

In this chapter we explain how the interfacial behaviour can be incorporated into a finite element model. We then describe the behaviour of the interface steel rebar/concrete and give a mathematical model for it. Finally we discuss the interfacial behaviour of FRP/concrete.

4.2 Interface elements

The interfacial behaviour FRP/ concrete and the bond slip behaviour of steel rebars can be effectively modelled by using interface elements. Using this approach we define a surface of separation (a line in two-D problems) between different materials and describe their interaction by defining a relative displacement at each contact point and the associated dual stress component. As we will see, in reality, the interfacial interaction is not a phenomenon localised at the physical joint between the two materials but involves a small volume around it. The observable slip between the materials is due in reality to inelastic deformation of a small portion of concrete (and of the adhesive for the FRP case). Simulation of the interaction between the two materials explicitly modelling the local mechanism of force transfer would require a model capable of operating at the same time at the microscale and at the mesoscale. This is not practical in a finite element analysis involving such a number of sources of nonlinearity as the analysis of RC beams retrofitted with FRP. Therefore it is convenient to represent the interfacial interaction in global terms through the introduction of an interfacial stress and a relative slip between the two materials which is a measure of the relative movement between two points in the two material associated with the location at which the interfacial stress is evaluated. The definition of one of the points is very straightforward as it is the contact point on the FRP or the steel, which do not generally undergo any damage. The definition of the other point is instead somewhat vague as it should be on the boundary of volume of concrete considered interface, which is not well defined. Models for the interaction between the materials based on the actual simulation of the stress, strain and damage accumulation in the vicinity of the interface, are used for the analyses of a small portion of the structure, isolated from the rest by introducing appropriate boundary conditions. In this way it is possible to operate only at the microscale. The information derived by using this approach can be then used to characterize the global interface model to be used in the mesoscale and macro scale problems.

To introduce the interface elements let us focus the attention on two-dimensional problems. In the interface-elements approach to debonding and delamination problems it is assumed that the interface has a null thickness, whereby the interface can be viewed as a couple of lines which exactly occupy the same position in the initial configuration domain. These two lines will be indicated as bottom (b) line and top (t) line so that, on each point of the initial configuration of the interface, there exist two points, one point on the bottom line and one other on the top line. Accordingly, two displacement vectors can be defined, namely a displacement \mathbf{u}_b of the point on the bottom

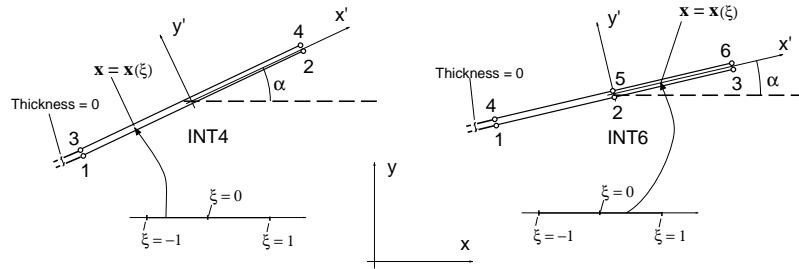


Figure 4.2: Initial configuration.

line and a displacement \mathbf{u}_t of the point of the top line.

In this way, a discontinuity for the displacement field is introduced on the interface and the relative displacement vector, or displacement jump, at each point of the interface is indicated as \mathbf{s} and is given by $\mathbf{s} = \mathbf{u}_t - \mathbf{u}_b$. The relative displacement is obviously null in the initial configuration.

A local reference system is pointwise introduced, with axis x' tangent and axis y' normal to the interface, and the relative displacement can be decomposed into two components along the axes, s'_x and s'_y . The component s'_y physically represents the ‘opening’ component of the relative displacement, usually named mode-*I*, and will be later indicated as s_I , while the component s'_x represents the ‘sliding’ component, usually named mode-*II*, and will be later indicated as s_{II} .

In a finite-element model, the interface is discretized into a finite number of interface elements. Each element is characterised by an even number N of nodes, because for each node placed on the bottom line of the element there must exist an other node on the top part of it. Here 4-noded (INT4) and 6-noded (INT6) interface elements will be considered. For the INT4 element the initial configuration must necessarily be a straight line, while the initial shape of the INT6 element can also describe a curved line. However, also for the INT6 element it will be initially assumed, for the sake of simplicity, that the three couples of nodes initially stay on a straight line.

For both elements a reference element domain is defined, consisting in the interval $[-1, 1]$ of \mathfrak{R} . An isoparametric mapping relates the abscissas ξ in the reference element to the position $\mathbf{x}(\xi)$ of the points in the interface element (see figure 4.2).

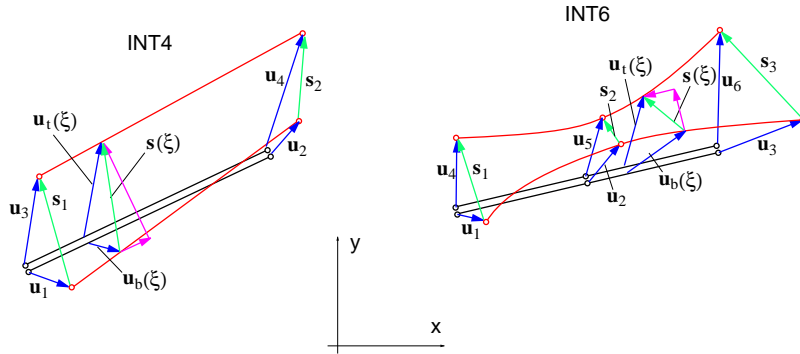


Figure 4.3: Deformed configuration.

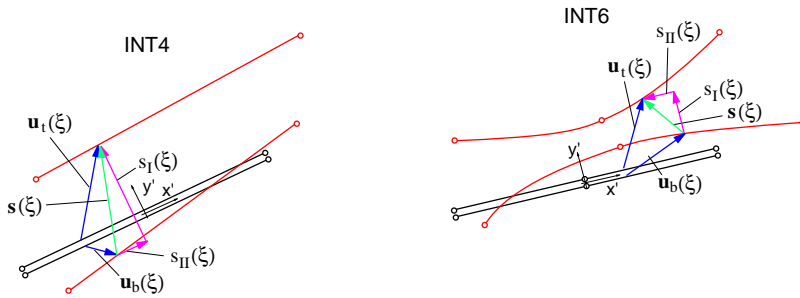


Figure 4.4: Decomposition of the relative displacement $\mathbf{s}(\xi)$ into its components, or 'modes', that is the opening mode s_I and the sliding mode s_{II} .

4.2.1 INT4 element

Let us focus the attention on the INT4 element, as all the results obtained for this element will easily be extended to the case of the INT6 element. The isoparametric mapping is given by:

$$\mathbf{x}(\xi) = \sum_1^{N/2} \Phi_i(\xi) \mathbf{x}_i = \frac{1-\xi}{2} \mathbf{x}_1 + \frac{1+\xi}{2} \mathbf{x}_2 \quad (4.1)$$

where \mathbf{x}_1 is the initial (coincident) position vector of nodes 1 and 3 with respect to a preset origin O of the 2D Euclidean space, \mathbf{x}_2 is the initial position vector of nodes 2 and 4 while Φ_1 and Φ_2 are the shape functions and $N/2 = 2$ in this case.

The relative displacement at each point \mathbf{x} of the initial configuration can be defined as a function of ξ through the isoparametric mapping (4.1) as

follows:

$$\mathbf{s}(\xi) = \sum_1^{N/2} \Phi_i(\xi) \mathbf{s}_i \quad (4.2)$$

with \mathbf{s}_i being the nodal relative displacements. More in detail it results:

$$\begin{aligned} \mathbf{s}(\xi) &= \begin{bmatrix} s_{II}(\xi) \\ s_I(\xi) \end{bmatrix} = \Phi_1(\xi) \begin{bmatrix} s_{1,II} \\ s_{1,I} \end{bmatrix} + \Phi_2(\xi) \begin{bmatrix} s_{2,II} \\ s_{2,I} \end{bmatrix} = \\ &= \Phi_1(\xi) (\mathbf{u}'_3 - \mathbf{u}'_1) + \Phi_2(\xi) (\mathbf{u}'_4 - \mathbf{u}'_2) = \\ &= \Phi_1(\xi) \begin{bmatrix} u'_{3x} - u'_{1x} \\ u'_{3y} - u'_{1y} \end{bmatrix} + \Phi_2(\xi) \begin{bmatrix} u'_{4x} - u'_{2x} \\ u'_{4y} - u'_{2y} \end{bmatrix} \end{aligned} \quad (4.3)$$

and then

$\mathbf{s}(\xi) =$

$$\begin{aligned} &= \left[\begin{array}{cc|cc} -\Phi_1(\xi) & 0 & -\Phi_2(\xi) & \\ 0 & -\Phi_1(\xi) & 0 & -\Phi_2(\xi) \end{array} \middle| \begin{array}{cc|cc} \Phi_1(\xi) & 0 & \Phi_2(\xi) & 0 \\ 0 & \Phi_1(\xi) & 0 & \Phi_2(\xi) \end{array} \right] \begin{bmatrix} u'_{1x} \\ u'_{1y} \\ \hline u'_{2x} \\ u'_{2y} \\ \hline u'_{3x} \\ u'_{3y} \\ \hline u'_{4x} \\ u'_{4y} \end{bmatrix} = \\ &= \left[-\Phi_1(\xi) \quad -\Phi_2(\xi) \quad \Phi_1(\xi) \quad \Phi_2(\xi) \right] \begin{bmatrix} \mathbf{u}'_1 \\ \mathbf{u}'_2 \\ \mathbf{u}'_3 \\ \mathbf{u}'_4 \end{bmatrix} \end{aligned} \quad (4.4)$$

where

$$\Phi_i = \begin{bmatrix} \Phi_i(\xi) & 0 \\ 0 & \Phi_i(\xi) \end{bmatrix} \quad \text{and} \quad \mathbf{u}'_i = \begin{bmatrix} \mathbf{u}'_{ix} \\ \mathbf{u}'_{iy} \end{bmatrix} \quad (4.5)$$

It is now convenient to introduce the transformation from the global system $\{x, y\}$ to the local system $\{x', y'\}$:

$$\mathbf{u}'_i = \mathbf{R} \mathbf{u}_i \quad (4.6)$$

and more in detail:

$$\mathbf{u}'_i = \begin{bmatrix} \mathbf{u}'_{ix} \\ \mathbf{u}'_{iy} \end{bmatrix} = \begin{bmatrix} \cos \alpha & \sin \alpha \\ -\sin \alpha & \cos \alpha \end{bmatrix} \begin{bmatrix} \mathbf{u}_{ix} \\ \mathbf{u}_{iy} \end{bmatrix} \quad (4.7)$$

where α is the angle formed by x' with x (see figure 4.2).

The 2×8 matrix $\mathbf{B}(\xi)$ which relates the element nodal displacements to the relative displacement $\mathbf{s}(\xi)$ is then obtained as follows:

$$\begin{aligned} \mathbf{B}(\xi) &= [-\Phi_1(\xi) \mathbf{R} \quad -\Phi_2(\xi) \mathbf{R} \quad \Phi_1(\xi) \mathbf{R} \quad \Phi_2(\xi) \mathbf{R}] = \\ &= \begin{bmatrix} -\Phi_1 \cos \alpha & -\Phi_1 \sin \alpha & -\Phi_2 \cos \alpha & -\Phi_2 \sin \alpha & \Phi_1 \cos \alpha & \Phi_1 \sin \alpha & \Phi_2 \cos \alpha & \Phi_2 \sin \alpha \\ \Phi_1 \sin \alpha & -\Phi_1 \cos \alpha & \Phi_2 \sin \alpha & -\Phi_2 \cos \alpha & -\Phi_1 \sin \alpha & \Phi_1 \cos \alpha & -\Phi_2 \sin \alpha & \Phi_2 \cos \alpha \end{bmatrix} \end{aligned} \quad (4.8)$$

having omitted the dependence on ξ for lack of space.

In a displacement-based finite-element analysis the internal work in the interface element is then given by:

$$\begin{aligned} W_{int} &= \int_{\xi=-1}^{\xi=1} \mathbf{t}[\mathbf{s}(\xi), history] \cdot \delta \mathbf{s}(\xi) J(\xi) d\xi = \\ &= \int_{\xi=-1}^{\xi=1} \mathbf{t}[\mathbf{B}(\xi) \mathbf{u}, history] \cdot \mathbf{B}(\xi) \delta \mathbf{u} J(\xi) d\xi \end{aligned} \quad (4.9)$$

where $\delta \mathbf{s}(\xi)$ denotes the virtual relative displacement at the interface and $\mathbf{t}(\mathbf{s}, history)$ is the value of the traction obtained for an assigned relative displacement \mathbf{s} and an assigned history [70, 71, 4, 5]. Furthermore, $J(\xi)$ represents the jacobian $\|d\mathbf{x}/d\xi\|$ of the isoparametric mapping.

By transposing matrix \mathbf{B} and omitting the dependence of \mathbf{t} on the history of the relative displacement one then obtains:

$$W_{int} = \int_{\xi=-1}^{\xi=1} \mathbf{B}(\xi)^T \mathbf{t}(\xi) J(\xi) d\xi \cdot \delta \mathbf{u} = \mathbf{q}_{int} \cdot \delta \mathbf{u} \quad (4.10)$$

The internal force vector is then given by:

$$\mathbf{q}_{int} = \int_{\xi=-1}^{\xi=1} \mathbf{B}(\xi)^T \mathbf{t}(\xi) J(\xi) d\xi \quad (4.11)$$

By differentiating the function $\mathbf{t} = \mathbf{t}(\mathbf{s}, \text{history})$ with respect to \mathbf{s} the tangent material stiffness $d\mathbf{t}/d\mathbf{s}$ is obtained. By the chain rule of differentiation the element tangent stiffness is then given by the following expression:

$$\mathbf{K}_t = \int_{\xi=-1}^{\xi=1} \mathbf{B}(\xi)^T \frac{d\mathbf{t}}{d\mathbf{s}} \mathbf{B}(\xi) J(\xi) d\xi \quad (4.12)$$

Numerical integration

The integrals contained in equations (4.11) and (4.12) must of course be numerically evaluated. To this end, Newton-Cotes integration rule is typically used instead of the Gauss rule, because spurious traction oscillations have been often observed with the latter [117]. Denoting by M the number of integration points and by ξ_i and W_i the abscissa and the weighting factor associated with the i -th integration point, one obtains:

$$\mathbf{q}_{int} = \sum_{i=1}^M W_i J(\xi_i) \mathbf{B}(\xi_i)^T \mathbf{t}(\xi_i) \quad (4.13)$$

$$\mathbf{K}_t = \sum_{i=1}^M W_i J(\xi_i) \mathbf{B}(\xi_i)^T \frac{d\mathbf{t}}{d\mathbf{s}} \mathbf{B}(\xi_i) \quad (4.14)$$

Implementation

From an operative point of view, the implementation of the INT4 element can be summarized as follows:

- Loop on the element integration points $i = 1, \dots, M$;
- For each integration point compute the value of the shape function:

$$\phi_1 = \frac{1 - \xi_i}{2} \quad \phi_2 = \frac{1 + \xi_i}{2}; \quad (4.15)$$

- For each integration point evaluate the Jacobian. In this case the jacobian is constantly equal to:

$$J(\xi) = J = \frac{\|\mathbf{x}_2 - \mathbf{x}_1\|}{2} = \frac{L}{2} \quad (4.16)$$

with L being the length of the element in its initial configuration;

- Compute matrix $\mathbf{B}(\xi_i)$ by substituting expressions (4.15) into equation (4.8)
- Evaluate the relative displacement $\mathbf{s}(\xi_i)$ with the formula:

$$\mathbf{s}(\xi_i) = \mathbf{B}(\xi_i) \mathbf{u} \quad (4.17)$$

$$\text{with } \mathbf{u}^T = [\mathbf{u}_1^T \quad \mathbf{u}_2^T \quad \mathbf{u}_3^T \quad \mathbf{u}_4^T]$$

- Compute the traction \mathbf{t} and the material stiffness as a function of the current relative displacement $\mathbf{s}(\xi_i)$ and also of the history of the relative displacements. This last point is fully detailed in [4] [5].

Apart from the last point of the bullet point list of operations detailed above, all the other steps are valid whatever interface law is used.

Interesting contributions, where many different interface models are either proposed or revisited, are given in [86, 122, 123, 116, 28, 8, 9, 11, 32, 10, 30, 31, 29].

4.2.2 INT6 element

For the INT6 element the shape function are the following quadratic functions:

$$\Phi_1(\xi) = \frac{1}{2} \xi (\xi - 1) \quad \Phi_2(\xi) = 1 - \xi^2 \quad \Phi_3(\xi) = \frac{1}{2} \xi (1 + \xi) \quad (4.18)$$

The matrix $\mathbf{B}(\xi)$ is then given by:

$$\begin{aligned} \mathbf{B}(\xi) &= \\ &= [-\Phi_1(\xi) \mathbf{R} \quad -\Phi_2(\xi) \mathbf{R} \quad -\Phi_3(\xi) \mathbf{R} \quad \Phi_1(\xi) \mathbf{R} \quad \Phi_2(\xi) \mathbf{R} \quad \Phi_3(\xi) \mathbf{R}] \end{aligned} \quad (4.19)$$

with \mathbf{R} again given by (4.7).

The relative displacement $\mathbf{s}(\xi)$ is then given by:

$$\mathbf{s}(\xi) = \mathbf{B}(\xi) \mathbf{u} \quad (4.20)$$

$$\text{with } \mathbf{u}^T = [\mathbf{u}_1^T \quad \mathbf{u}_2^T \quad \mathbf{u}_3^T \quad \mathbf{u}_4^T \quad \mathbf{u}_5^T \quad \mathbf{u}_6^T].$$

All the remaining part follows analogously as for the INT4 element.

4.3 Interface steel concrete

Steel concrete interaction influences the crack behaviour of the beam and therefore the performance of the FRP concrete interface and eventually of

the entire retrofitted structural element. The mechanism by which forces are transferred between concrete and reinforcement has been widely investigated since reinforced concrete was introduced as a construction material and a detailed discussion of this topic is outside the scope of this work. However, the bond slip behaviour of steel reinforcement is briefly described for completeness and to give the relations used in the FEM models.

The interaction between concrete and rebars is characterized by four different stages Figure 4.5.

Stage I (*uncracked concrete*): in this stage the bond action is due mainly to chemical adhesion. The bond stresses are characterized by low value, but highly localized stresses may arise close to lug tips (Figure 4.5, 4.7).

Stage II (*first cracking*): in this stage the chemical adhesion breaks down and the stress transfer is due to mechanical interlocking of the lugs in the surrounding concrete. Large bearing stresses are generated in the concrete at the lugs figure(4.7). Due to these bearing stresses micro cracks originate at the tips of the lugs allowing the bar to slip as the bond stresses increase.

Stage III (*conical struts action*): for higher bond stress values, longitudinal cracks start to form originating from initial micro cracks, generating conical struts, Figure 4.5, 4.7. The outward component of the strut action Figure 4.7 is resisted by the hoop stresses in the surrounding concrete. The surrounding concrete will exert therefore a confinement action on the bar. Thus, the bond strength and the stiffness are due mostly to the interlocking among the lugs and the surrounding concrete.

Stage IV (*residual friction*): at this stage the conical struts have failed and only a residual frictional stress transfer is active.

The interfacial stresses associated with the interaction mechanisms described, are of different nature and very variable along the bar. For the purpose of the analysis of a reinforced concrete structural element these stresses need to be spatially averaged. By carrying out this spatial averaging we define a bond stress that can be used to define a bond slip relation that simplify considerably the treatment of this problem Figure 4.5, 4.6, 4.7.

The mechanisms of stress transfer of stages one to three are considered primary mechanisms as they can be found within the serviceability load limits of the structure. The residual frictional stress transfer of stage IV is considered a secondary mechanism (whose effect combined with all the others is present since the beginning of the loading process anyway) as steel bars are considered debonded if this is the only resistance mechanism active. In Figure 4.6 typical failure modes of the concrete surrounding the rebars are shown.

We now need to establish an appropriate constitutive law for the interface.

The bond slip relation should depend, in principle, upon the type of

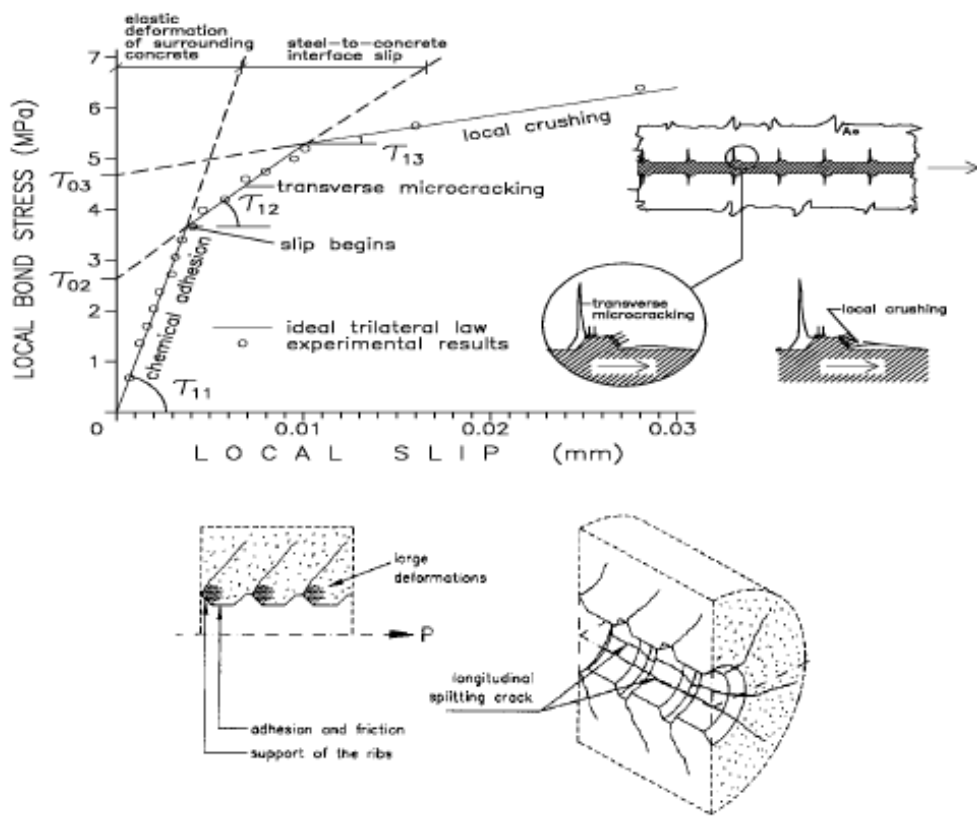


Figure 4.5: Local bond slip behaviour (Tassios,1979).

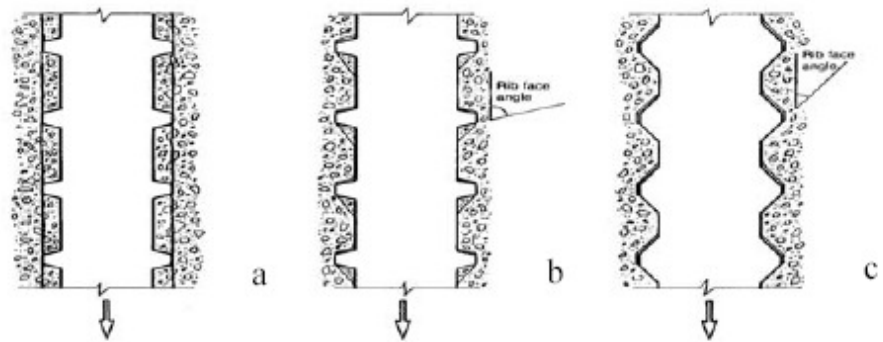


Figure 4.6: Modes of bond failure: (a) pull out; (b) splitting-induced pull out accompanied by crushing and/or shearing-off in the concrete under the rib action; (c) splitting accompanied by slip on the rib faces (Coirus, Andreasen, 1992).

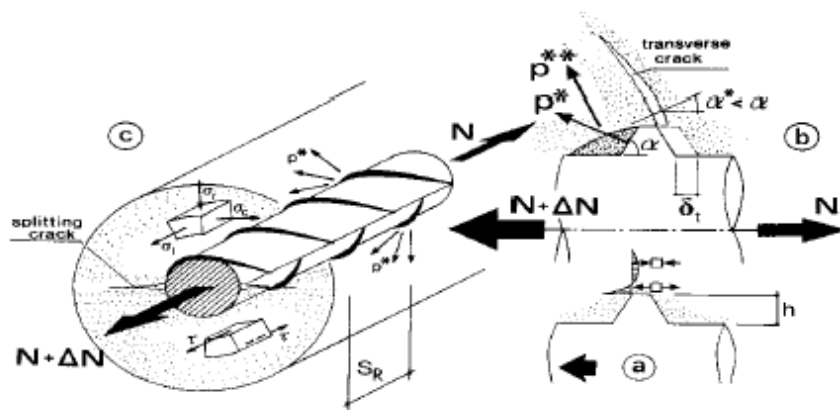


Figure 4.7: Bond splitting in reinforced concrete (deformed bars): (a) typical stress peak in the elastic phase; (b) bar concrete slip and wedging action of the bar; (c) main parameters.

	s_1 (mm)	s_2 (mm)	s_3 (mm)	τ_1 (MPa)	τ_2 (MPa)	Ω
Confined conc.	1	3	Clear rib spacing	$2.5(f_{ck})^{1/2}$	$(f_{ck})^{1/2}$	0.4
Unconfined conc.	0.6	0.6	10	$2.0(f_{ck})^{1/2}$	$0.6(f_{ck})^{1/2}$	0.4

Table 4.1: Bond slip law parameters

bar, the concrete strength, the confinement regime and the conditions of the materials (rusting of steel, carbonation of concrete). Workmanship of the structure is also relevant.

However, a constitutive law depending only on the concrete strength and confinement regime is given in the CEB-FIP Model Code 1990. This is based on a work by Ciampi et al.. In this model the primary zone is non linear and it is modeled by:

$$\tau = \rho_1 s^\Omega \quad (4.21)$$

where

$$\rho_1 = \frac{\tau_1}{\rho_1^\Omega} \quad (4.22)$$

Ω is an empirical constant ($\Omega < 1$) that describe the shape of the bond-stress-slip curve. The model includes a plateau at the peak stresses (τ_1), followed by a linear degradation zone. The bond stress due to the secondary bond mechanism is assumed constant.

The model is characterised by the parameters: s_1 , s_2 , s_3 , τ_1 , τ_2 , and Ω ; refer to Figure 4.8 for the meaning of these parameters.

These parameters are given in the Model Code as functions of the clear rib spacing of the rebars, the concrete strength and the confinement regime. Their expression is reported in Table 4.1

For implementation reasons the above relation has been simplified, in the FEM models, to the one with a linear initial branch followed by linear softening described in Figure 4.9.

The parameters characterizing the model adopted have been derived imposing the same peak stress as in the CEB-FIP model, a slip displacement at the peak stress (s_o) equal to s_1 and a fracture energy G_c equal to the energy obtained integrating the CEB-FIP relation between zero and the slip displacement s_3 . This is equivalent to neglecting the the residual bond stresses.

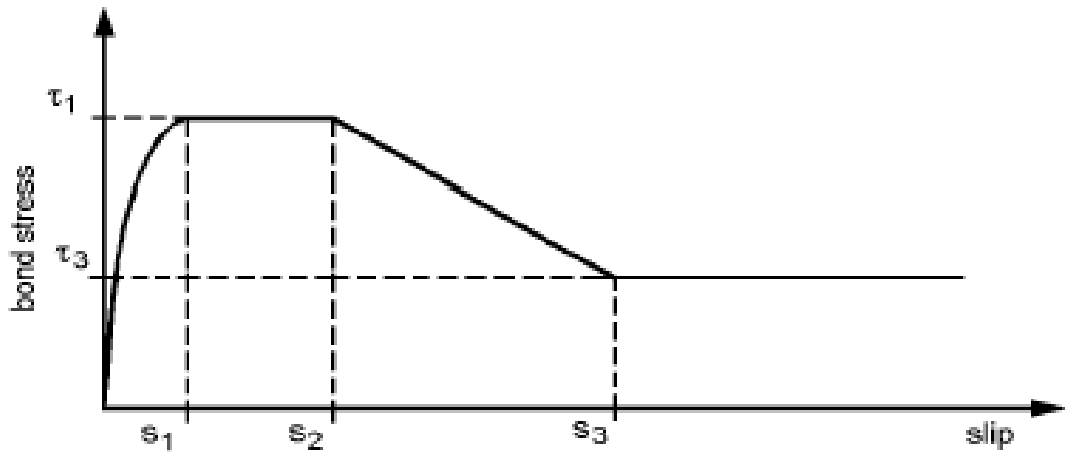


Figure 4.8: Analytical model for local bond stress-slip relationship (Ciampi et al., 1981; Eligehausen et al., 1983); monotonic loading.

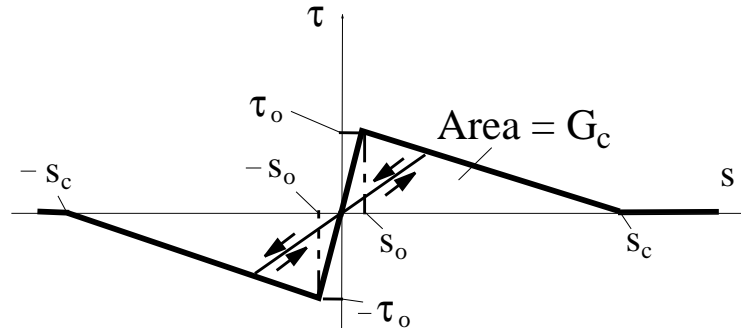


Figure 4.9: Bond slip relation used in the FEM models.

4.4 Interface FRP/concrete

4.4.1 Elastic approaches

A variety of possible approaches have been proposed for the problem of the interface between concrete and FRP. Closed form solutions have been found for highly idealised linear elastic models [101], [135] in which the relative movement between the two materials is due to elastic deformation of the bonding agent (epoxy) assumed with a finite thickness. At this level of idealization a closed form solution to the interface problem can be derived as follows.

The problem can be greatly simplified if the following assumptions are made:

- Linear elastic behaviour of all components
- Unidirectional FRP plates with their fibres aligned with the beam axis
- Bond line has no axial and bending stiffnesses
- The adhesive is homogeneous and uniform along the bond line
- Linear strain distribution is assumed in the beam and strengthening plate sections

With reference to Fig.4.10 the following relation can be written:

$$-\gamma t_i = d(v' - \phi) \quad (4.23)$$

where γ is the shear strain in the adhesive layer, t_i is the thickness of the adhesive, d is the distance of the axis of the FRP plate from the axis of the concrete section, v' is the rotation of the concrete section and ϕ is the average cross sectional rotation defined by the difference of the axial displacement of the concrete section and the plate and the distance between their axes d (see Fig. 4.10). Assuming small deformations:

$$\phi = \frac{u_2 - u_1}{d} \quad (4.24)$$

According to the convention used in the figure v' and ϕ are counter clockwise while γ is a clockwise angle.

The axial strains of beams and plate are given by:

$$u_1' = \frac{C}{EA_B}, \quad u_2' = \frac{T}{EA_p} \quad (4.25)$$

where C is the compressive axial force in the concrete, T is the tensile axial force in the FRP and all other symbols have their usual meaning with the suffix B for beam and p for plate.

Since the deflection is assumed to be the same for all points in the section, the curvature (v'') may be directly used to define the bending moments in the beam and the FRP plate, respectively (Fig.4.11(a)).

$$M_B = EI_B v'', \quad M_p = EI_p v'' \quad (4.26)$$

The interface shear stress τ is related to the shear strain γ through the shear modulus G .

$$\tau = G\gamma \quad (4.27)$$

The equilibrium of an elemental segment of plate yields:

$$\tau = \frac{1}{b} \frac{dT}{dx} \quad (4.28)$$

where b denotes the width of the FRP plate.

Taking the equilibrium of forces and moments at any cross section

$$C = -T \quad (4.29)$$

$$M(x) = M_b + M_p + Td \quad (4.30)$$

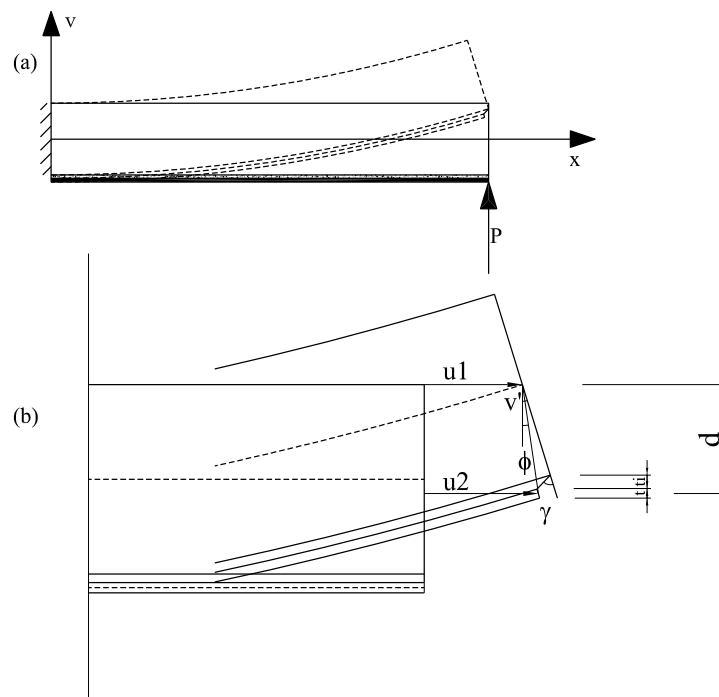


Figure 4.10: FRP strengthened beam considering interface slip: (a) beam layout; (b) cross section kinematics

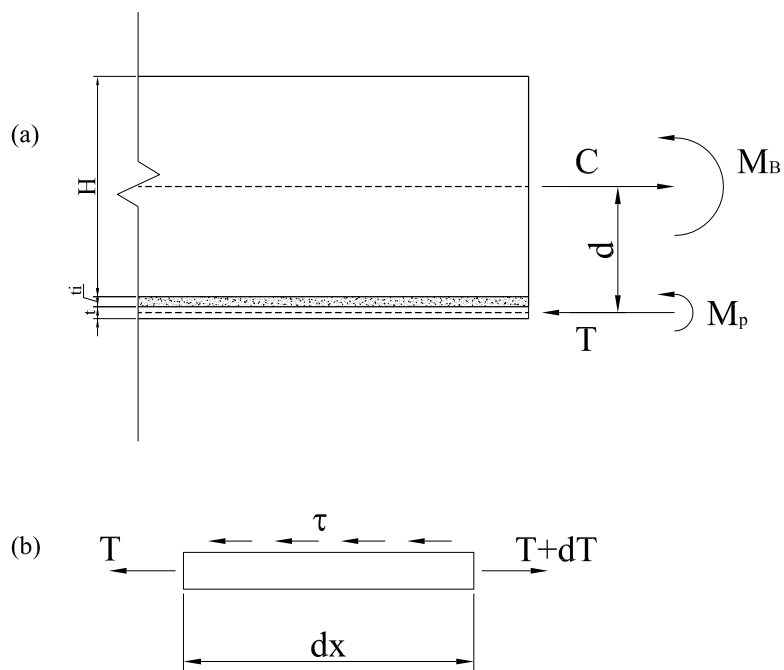


Figure 4.11: Equilibrium of forces: (a) force/moment distribution in cross section; (b) interface shear stress on differential plate element

Differentiating ϕ with respect to x and using equation 4.29 we get:

$$\phi' = \frac{T}{dEA_s} \quad (4.31)$$

where $EA_s = 1/EA_b + 1/EA_p$. Substituting equation 4.26 into 4.30 and rearranging

$$T = \frac{M(x) - EI_s v''}{d} \quad (4.32)$$

where $EI_s = EI_b + EI_p$. Differentiating equation 4.32 with respect to x and substituting into 4.28

$$v''' = \frac{M'(x) - bd\tau(x)}{EI_s} \quad (4.33)$$

Differentiating equation 4.23 twice with respect to x , substituting equation 4.31 and rearranging

$$\gamma'' + \frac{d}{t_i} \left(v''' - \frac{T'}{dEA_s} \right) = 0 \quad (4.34)$$

Substituting equation 4.28 and 4.33 into 4.34, The shear differential equation is obtained:

$$\tau''(x) - \alpha^2 \tau(x) = -\frac{dG}{t_i EI_s} M'(x) \quad (4.35)$$

where $\alpha^2 = bG/t_i[1/EA_s + d^2/EI_s]$.

The solution of the above linear differential equation with constant coefficients has the well known form:

$$\tau(x) = A \cosh(\alpha x) + B \sinh(\alpha x) + \tau_p(x) \quad (4.36)$$

where τ_p is a particular solution.

To calculate the shear stresses as a function of x it is necessary to find a particular solution $\tau_p(x)$ and impose the appropriate boundary conditions.

In the case of a simply supported partially plated beam under uniform loading the solution has the following form:

$$\begin{aligned}
\tau(x) = & \frac{dG}{\alpha^2 t_i EI_s} w \left[\left(\frac{L}{2} - x_p \right) \right. \\
& \left. + \frac{\sinh(\alpha x_p) - \tanh(\alpha L_p/2) \cosh(\alpha x_p)}{\alpha} \right] \\
& - \frac{dG}{2\alpha^2 t_i EI_s} w (L - L_p) \frac{\cosh(\alpha x_p)}{\cosh(\alpha L_p/2)} \\
& + \frac{Gw}{8\alpha t_i dEA_s} (L^2 - L_p^2) \left(1 - \frac{EI}{EI_b} \right) [(\sinh(\alpha x_p) \\
& - \tanh(\alpha L_p/2) \cosh(\alpha x_p))
\end{aligned} \tag{4.37}$$

The results obtained by using the above approach have been compared to those obtained by using a more general FEM technique. The structural scheme is simplified in both cases (all materials are homogeneous, isotropic and linear elastic, as required by the analytical approach) and steel reinforcement is not included. However the kinematical assumptions of the FEM model are less stringent and it can be used to test the assumptions of the analytical method.

Different shear moduli G have been used in the analyses. The values of G have been kept lower than typical values for the adhesive to reduce the effect of its axial stiffness (lower G implies lower E) in the FEM model. In fact, axial forces in the adhesive cannot be excluded in the latter. Note that the analyses have been carried out only to check a mathematical method and not to provide results on a specific structure.

The details of the modelled beam are reported in Fig 4.12 and the results are reported in Fig 4.13. The stress distribution predicted by the two methods are generally in good accordance. However, local stresses at the tip of the laminate are fairly different. This is a critical point as these local stresses are often responsible for end peeling. We note that it is not demonstrated, although likely, that FEM results obtained are better than the analytical ones.

Other approaches [135] with less stringent kinematical assumptions giving also the possibility of considering more than three layers of different materials involve the use of Fourier series and are not reported for brevity.

We conclude this section observing that elastic approaches, although appealing for their simplicity, have little relevance for practical applications. This is because the strongly nonlinear behaviour of cracked concrete in the range of loading conditions of practical interest and the nonlinear proper-

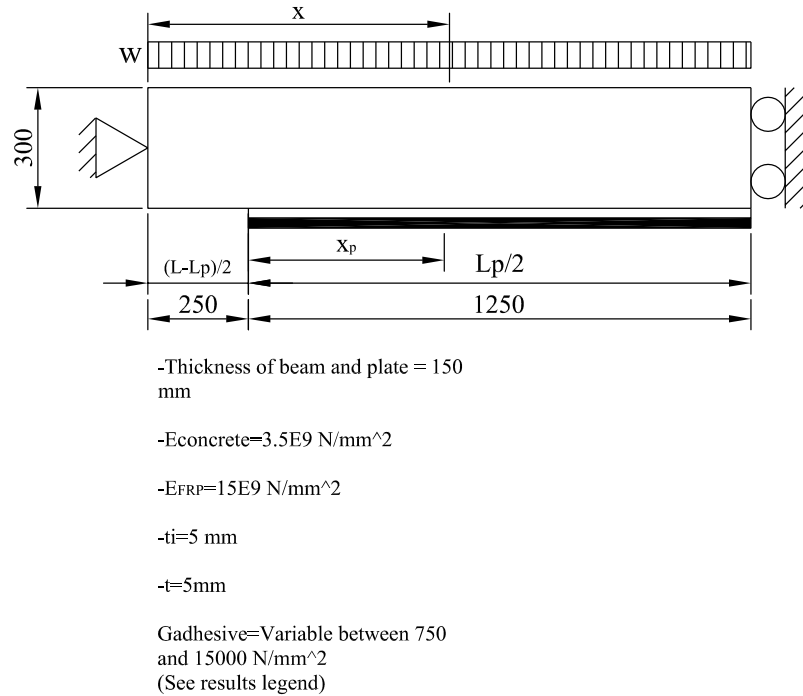


Figure 4.12: Elastic interface: Model structure used for solution validation

ties of the interface play a key role in the behaviour of retrofitted structures at both Serviceability and Ultimate limit states. A more appropriate approach to the problem of the interface involves the use of cohesive models as described in the following section.

4.4.2 Cohesive models

In reality the bond slip involves not only the adhesive but also a small portion of the adjoining concrete and is not elastic in nature. Also the closed form solutions refer to uncracked structural elements and find their applicability more in the choice of an appropriate stiffness for the adhesive rather than in the evaluation of the ultimate capacity of a structural element. More sophisticated approaches resort to *cohesive zone models* for an interface of zero thickness representative of the overall behaviour of the volume interested by the bond slip process. Using such an approach the actual stresses, strain and damage in the adhesive and adjoining concrete are not computed but their overall effect on the RC element and the FRP plating can be effectively

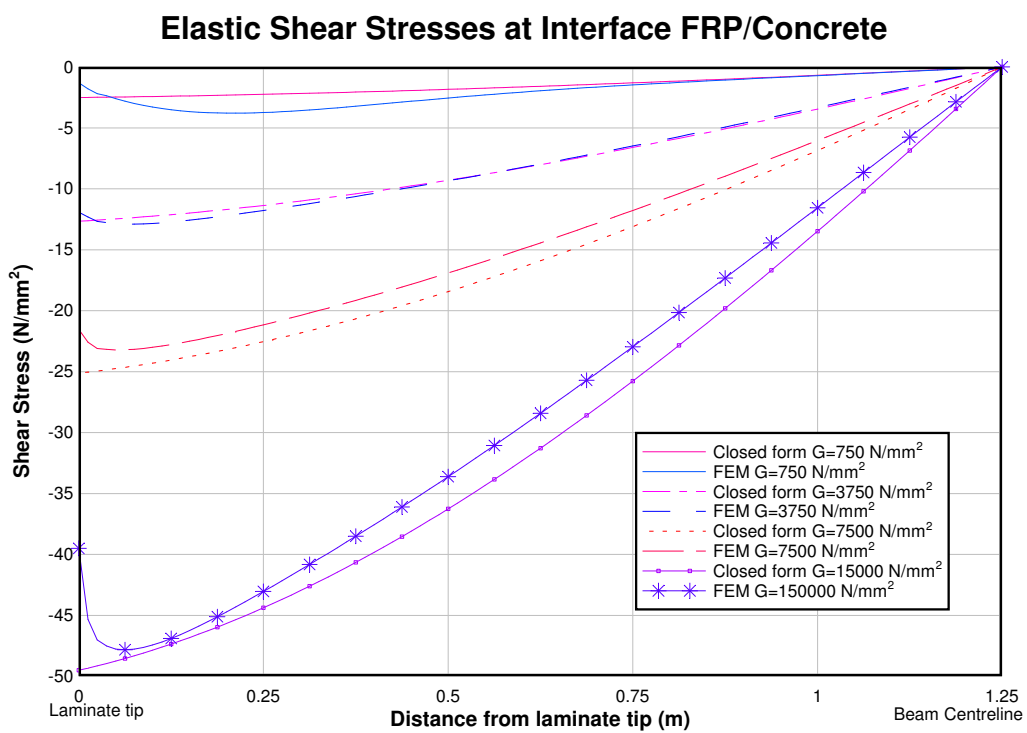


Figure 4.13: Elastic interface: comparison between analytical and FEM models

reproduced. The interface is in turn kinematically characterised by a relative displacement between FRP and concrete and statically by the associated stresses. The relative displacement is represented through its components normal (mode I) and tangential (mode II and III) to the interface surface. In the present context mode II is generally the only relevant component of displacement. Mode I can be included to take into account the effects of direct stresses arising from the difference in curvature between the laminate and the concrete mentioned above. Mode three can only be present in three dimensions and its inclusion in the model is not necessary as this mode is not activated (it would be associated with different transversal displacement between concrete and FRP, generally negligible due to the small width of the FRP sheeting).

Behaviour of the interface

The behaviour of the interface has been mainly studied based on observations on pull tests. Existing studies suggest that the main failure mode of FRP to concrete bonded joints, in pull tests, is concrete failure under shear occurring generally a few millimetres from the adhesive layer. The ultimate load depends strongly on the strength of the concrete. In addition, the plate to concrete member width ratio also has a significant effect. A very important aspect of the behaviour of these bonded joints is that there exist an effective bond length l_e beyond which an extension of the bond length cannot increase the ultimate load. This is a fundamental difference between an externally bonded plate and an internal reinforcing bar, for which sufficiently long anchorage can always be found so that the full tensile strength of the reinforcement can be achieved. The interfacial cracks in concrete can be classified into three types: (a) interfacial shallow cracks; (b) interfacial deep cracks; and (c) microcracks within a cracked zone under the FRP plate. The depths of the interfacial shallow cracks are about 0.5 to 1 mm, and their widths are small and relatively uniform. This thin layer is subject to high tensile stresses as well as high shear stresses as it is directly under the FRP plate. The depths of the interfacial deep cracks are about 2 to 5 mm. The widths of these cracks are relatively large. They are caused by interfacial shear stresses which control the final debonding strength and slip of the interface. The overall depth of the cracked zone of concrete is about 5 to 15 mm. In this zone microcracks of the type (c) are present. They are also due to the interfacial shear stresses and some of them develop into interfacial deep cracks as the deformation is further increased. The failure process of the interface may be explained as follows. At low level of loading, the formation of interfacial shallow cracks at angles of 45° to 60° to the interface

leads to the appearance of small cantilever teeth. With further increase in loading, these cantilever may grow longer as the shallow cracks grow into deep cracks, or may fail in shear. The shear force on these inclined teeth leads to axial compressive failure or flexural failure at the root. Laboratory observations show that debonding corresponds to progressive flexural failure of these cantilevering teeth, except near the loaded end where debonding is mainly due to crushing of concrete.

The experimental observation that the pull off force does increase increasing the anchorage length above a certain limit can therefore be explained as follows. Loading the specimen cantilevering teeth are generated due to oblique cracking of concrete. The tooth closest to the loaded point in the one in which the largest tip displacement is induced. As a consequence this is also the one with the maximum flexural action at the root. At a certain load level this tooth fail in flexure and ceases to transfer any load between FRP and concrete. When this happen there is no significant shear stress mobilization, yet, far from the loaded point. In this situation The interfacial stress distribution is shifted towards the unloaded end of the plate. Imposing an increasing displacement at the loaded end of the plate, other teeth will fail shifting the interfacial stress distribution towards the unloaded end of the plate without an increase in the load carried. Eventually cracking and flexural failing of the cantilevering teeth generated will reach the unloaded end and the plate will detach completely.

From a certain point of view this mechanism of interaction is not very different from the one of the internal steel bars for which the conical struts play the role of cantilevering teeth. The difference is that for the internal rebars the confinement due to the hoop stresses in the concrete surrounding the bar, result in a stress transfer due to strut action rather than bending of cantilevers. This results in a much more robust and ductile bond behaviour. Also for external FRP plates once a tooth has failed it detaches completely and cannot transfer any force. When the conical struts around the embedded bars fail, because they are still kept in contact with the rebar by the covercrete, stress transfer due to friction is still possible. This explain the non negligible residual bond stresses observed for internal rebars even under very large relative displacements.

Cohesive model for the FRP/concrete interface

Based on the observations in the previous section we can now define a cohesive model for the interface FRP/concrete. The first requirement of such a model is that, in accordance with the experimental observations, there must be a maximum relative displacement s_c at which the two materials detach

completely. There must also be a maximum effective anchorage length l_e such that no increase in the anchorage force is gained increasing the anchorage length. This second condition is fulfilled if the first one mentioned is. It is actually difficult to determine experimentally the actual shape of the stress-slip curve for an FRP to concrete joint. This is due to the fact that the effective anchorage length (which depends mainly on the strength of the concrete) is generally only 80 to 200 mm and that the measurement of the strains at a sufficient number of locations is not practical within such a limited space. Also, the constitutive law we are seeking is an averaged one. In reality, as seen, the behaviour of the interface is governed by cracking of the concrete adjoining the interface. The real stresses at this interface, therefore, cannot be smoothly distributed. The experimental curves are, therefore, affected by the positioning of the strain gauges. However, some qualitative features of the stress-slip curves have been experimentally established by researchers [105].

The first part of the stress-slip curve is almost linear up to half the peak stress and then there is a nonlinear branch with reducing stiffness up to the peak. Data on the softening branch are too scattered for a good appreciation of the most appropriate shape but a linear softening branch seems to be a reasonable approximation.

It is worth mentioning that in decohesion problems, often, determining the correct shape of the stress slip curve is not very important compared to getting an accurate value of the fracture energy.

Based on the above, a linear up to peak-linear softening curve (Figure 4.14) has been adopted to represent the interfacial behaviour FRP/concrete. Unloading has been assumed along the secant to the origin. Where more than one opening mode has been considered the different modes have been modelled as uncoupled (i.e. no interaction is allowed for).

The model is characterised by the three parameters: fracture energy G_c , the peak stress τ_o and the slip corresponding to the peak stress s_o .

The three parameters could be selected by measuring experimentally the maximum pull off force, of a specimen, and the effective anchorage length. One more condition would be required but because the stiffness of the prepeak branch is not very important, as long as it is set as relatively high, the ratio τ_o/s_o can be imposed by the analyst.

To get a better insight into the model and to provide formulas to determine the parameters of the interfacial law by the mentioned procedure a closed form solution for the pull off test has been determined. The formula has also been used to test the accuracy of the finite element implementation of the interface model.

The solution has been obtain as follows.

A plate of FRP bonded to an infinitely stiff block of concrete is considered (Figure 4.15). The bond slip law is simplified to an infinitely stiff-linear softening one (Figure 4.15). The origin of the reference frame is set at the location where the relative slip switches from zero to a finite value and the slip displacement has been indicated as $u(x)$. Bending and shear stiffnesses of the FRP are neglected and, because of the assumed infinite stiffness of the concrete block, the slip displacement $u(x)$ coincides with the axial displacement of the FRP at x . The maximum peak stress is τ_o and the ultimate slip displacement is s_c . All the other quantities involved are as indicated in Figure 4.15.

Writing the expression of the $\tau - u$ relationship:

$$\tau(u) = \frac{\tau_o}{s_c}u - \tau_o \quad (4.38)$$

and enforcing the horizontal equilibrium, we get the following differential equation:

$$u''(x) = -\frac{1}{Et} \left(\frac{\tau_o}{s_c}u(x) - \tau_o \right) \quad (4.39)$$

which can be rewritten as follows:

$$u''(x) + \frac{\tau_o}{Ets_c}u(x) = \frac{\tau_o}{Et} \quad (4.40)$$

The boundary conditions can be written at $x = 0$ as follows:

$$\begin{cases} u(0) = 0 \\ u'(0) = \varepsilon_p(0) = \frac{\sigma_p(0)}{E} = 0 \end{cases} \quad (4.41)$$

In the above expressions E is the elastic modulus of the FRP, t is the thickness of the plate and ε_p is the strain of the FRP.

Denoting $\varpi^2 = \frac{\tau_o}{Ets_c}$ and $k = \frac{\tau_o}{Et}$ the solution of the above problem has the well known expression:

$$u(x) = \frac{k - k \cos(\varpi x)}{\varpi^2} \quad (4.42)$$

from which

$$u'(x) = \frac{k \sin(\varpi x)}{\varpi} \quad (4.43)$$

$$u''(x) = k \cos(\varpi x) \quad (4.44)$$

and therefore

$$\tau(x) = -Etu''(x) = -Etk \cos(\varpi x). \quad (4.45)$$

We find l_e imposing that $\tau(x) = 0$. Therefore:

$$l_e = \frac{\pi}{2\varpi} \quad (4.46)$$

The pull off force is calculated integrating $\tau(x)$ between 0 and l_e .

$$F = - \int_0^{\frac{\pi}{2\varpi}} \tau(x) dx = \int_0^{\frac{\pi}{2\varpi}} Etk \cos(\varpi x) dx = \frac{Etk \sin(l_e/\varpi)}{\varpi} = \frac{Etk}{\varpi} \quad (4.47)$$

since $G_c = \tau_o s_c / 2$ the (4.46) and (4.47) can be expressed in terms of the fracture energy G_c and τ_o as follows

$$l_e = \frac{\pi}{\sqrt{2}\tau_o} \sqrt{EtG_c} \quad (4.48)$$

$$F = \sqrt{2EtG_c}. \quad (4.49)$$

The above expressions are the ones to be used for determining τ_o and G_c , known F and l_e from testing.

In Figure 4.16 we report a comparison between the analytical results obtained by the above approach and the corresponding numerical results. The data on the problem analysed are also reported in the figure. We can see that the numerical model is very accurate.

With the validated numerical model the complex case of the delamination of concrete beams retrofitted with FRP has been tackled. We will show in the chapter on the applications that the model yields results in good accordance with experiments. Note that direct comparison of the interfacial stresses calculated with experimental results was not possible, for the beams examined, as no measurement of these stresses was available. The predictions of the model have been assumed accurate based on indirect comparison, through the experimentally measured parameters, like load displacement curves, failure load and mode of failure. Inspection of the results seems to bring reliability to them as they are qualitatively realistic and in accordance with the expected behaviour. Note that as interfacial stresses are very difficult to be directly measured experimentally a good finite element model is a useful research tool for the integration and interpretation of experimental data.

Parameters characterizing the interface

Part of the finite element work undertaken during this study was devoted to testing the indications in the international guidelines for the design of

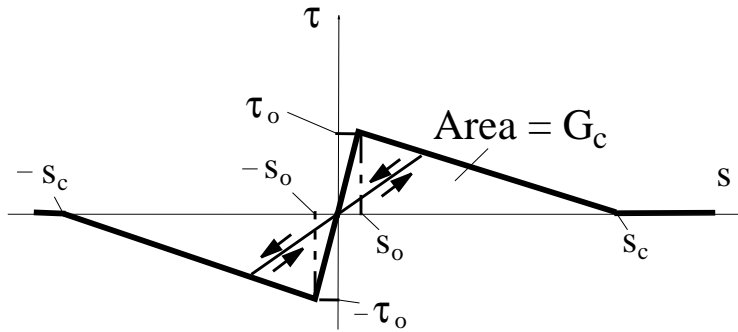


Figure 4.14: Cohesive model for FRP to concrete interface.

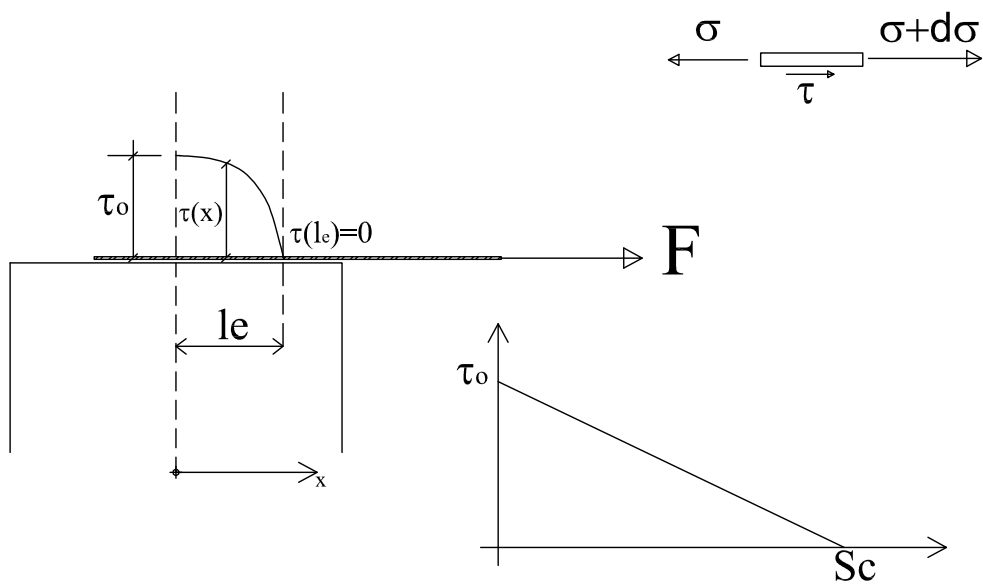


Figure 4.15: Closed form approach for a pull off test.

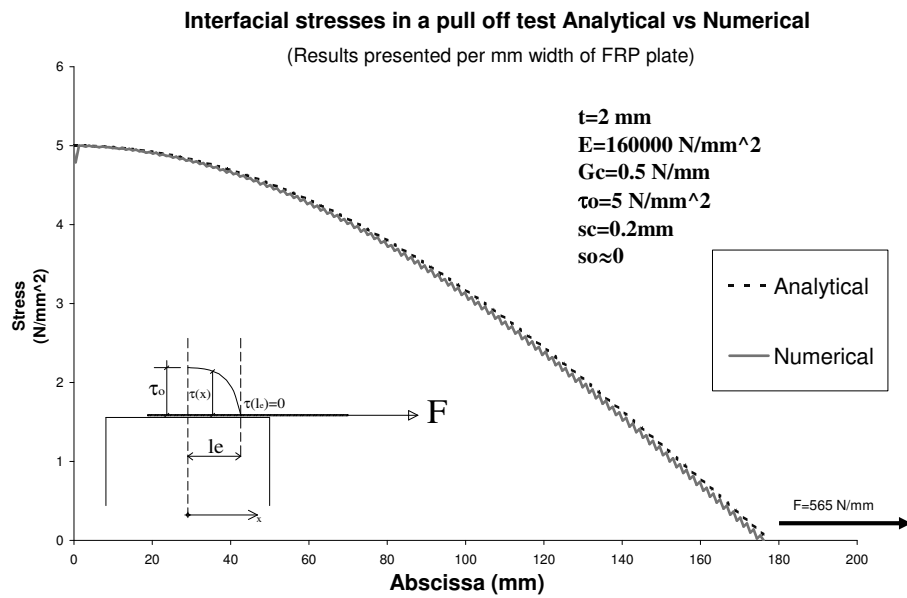


Figure 4.16: Comparison of closed form solution and Finite Element solution for a pull off test.

RC structures retrofitted with FRP. As far as the interface is concerned the British Report 55 by the Concrete Society [34] and the Italian recommendations by the CNR [33] are consistent. They recommend the following.

The cohesive model to be used is a linear model up to peak stress followed by a linear softening branch down to complete detachment.

The peak interface stress should be assumed as:

$$\tau_o = 0.3k_b\sqrt{f_{ck}f_{tm}} \quad [f \text{ in } N/mm^2]$$

in which f_{ck} and f_{tm} are the characteristic compressive strength of concrete and its mean tensile strength, and k_b is a geometrical factor and allow for the influence of the interface performance of the ratio breadth of the beam to width of the FRP plate b/b_f . Its value is given by

$$k_b = \sqrt{\frac{2 - \frac{b_f}{b}}{1 + \frac{b_f}{400}}} \quad [\text{lengths in } mm].$$

The stiffness of the initial linear branch K_1 can be estimated by

$$K_1 = \frac{c_1}{t_a/G_a + t_c/G_{conc}}$$

in which G_a and G_c are the shear moduli of the adhesive and the concrete; t_a and t_c are the thicknesses of the adhesive and the concrete taking part in the interface deformation (the latter being between 20 and 30 mm); the constant c_1 can be taken as any value between 0.5 and 0.7.

The slip displacement corresponding to the entire delamination s_c can be assumed as 0.2 mm. Finally the fracture energy of the interface can be taken as:

$$G_c = \frac{1}{2}\tau_o s_c = 0.03k_b\sqrt{f_{ck}f_{tm}}$$

The notation reported in the referenced sources has been slightly adjusted to be consistent with the notation used herein.

The analysis proved (see the section on the applications) that although some of these parameters have been derived in quite a simplistic manner they are robust parameters for the design of this type of strengthening works.

Chapter 5

Modelling of cracking of concrete

5.1 Introduction

Because of its influence on the mechanism of stress transfer between the FRP and the concrete, cracking of concrete has a great influence on the behavior of RC beams retrofitted with FRP. Within the framework of the finite element method, there exist several techniques to model crack onset and propagation.

For problems in which the local distribution of stresses is not very important, methods considering the cracks like uniformly spread on a portion of material affected by cracking have become popular. Stresses and strains in such a volume (large enough to contain a few cracks) are represented by averaged values, calculated in some cases taking into account also the reinforcement and its interaction with the base material. In this approach cracking is reduced to a constitutive problem.

By using a suitable constitutive law, anyway, it is also possible to induce local concentrations of inelastic strains, and a stress release within narrow bands. Basically, a single discrete crack can be modelled by introducing a sharp loss of stiffness within a strip, one or two elements wide. If the mesh adopted is such that the dimensions of the element are of the same order of magnitude as the crack opening a model of this kind is equivalent to a discrete cracking model. Note that this is achieved operating on the constitutive model only. The continuity is not lost at the element or mesh level with obvious advantages from the implementation point of view.

As far as the reinforced concrete beams retrofitted with FRP are concerned local effects are relevant as they largely influence the behaviour of

the interface. Therefore a discrete crack approach is necessary. Initially, in the finite element analysis carried out in this work, cracking of concrete has been dealt with by introducing preset cracks in the finite element mesh. This approach was justified because the crack pattern on the beams analysed was known from experimental records and because the main focus was not on the prediction of the formation and propagation of cracks, but on their effect on the performance of the structure once formed and fully developed.

Methods for the simulation of crack formation and propagation, yielding a discrete crack type of results, have been tested later in the investigation program. It has been found that in the case of a simple notched beam under a load condition determining uneven distribution of stresses reasonable results can be obtained with a constitutive law featuring a fracture energy based softening model. In the case of uniform stress distribution and under the spreading action exerted by the reinforcement (both ordinary and external FRP reinforcement) inelastic strains do not localise in the zones where cracks are expected, but tend to spread over the volume, missing to give a good representation of local effects. This behaviour of this kind of model is known to researchers, who recognise that the problem cannot be effectively solved without the introduction a random dishomogeneity of the material [52].

Because of this tendency to spread the damage into the volume interested by tensile stresses, the cracking models mentioned proved to be not suitable for the detailed investigation of the behaviour of RC beams retrofitted with FRP and in particular for the prediction of the interfacial behaviour at the FRP to concrete joint. The initial approach of resorting to preset cracks proved to be therefore more adequate. This will be discussed in detail in the next chapter.

It is important to note that there exist, nowadays, techniques enabling the introduction of discontinuities in the displacement field within a finite element and therefore a more realistic modelling of cracking. The implementation of these techniques, likewise that of others involving automatic generation of a new mesh, when a crack forms, is outside the scope of this research work.

5.2 Models for crack onset and propagation

5.2.1 Overview

The nonlinear response of concrete is often dominated by progressive cracking which results in localized failure. Since cracking is the major source of material nonlinearity in the serviceability range of reinforced concrete structures,

realistic cracking models need to be developed in order to accurately predict the load-deformation behaviour of reinforced concrete members. The selection of a cracking model depends on the purpose of the finite element analysis. If overall load-deflection behaviour is of primary interest, without much concern for crack patterns and estimation of local stresses, the "smeared" crack model is probably the best choice. If detailed local behaviour is of interest, the adoption of a "discrete" crack model might be necessary.

The first reinforced concrete finite element model which includes the effect of cracking was developed by Ngo and Scordelis (1967) [83], who carried out a linear elastic analysis of beams with predefined crack patterns. The cracks were modelled by separating the nodal points of the finite element mesh and thus creating a discrete crack model (Figure 5.1). Although, the lack of generality in crack orientation has made the discrete crack model unpopular, the use of discrete crack models in finite element analysis offers certain advantages over other methods. For those problems that involve a few dominant cracks, the discrete crack approach offers a more realistic description of the cracks, which represent strain discontinuities in the structure. Such discontinuities are correctly characterized by the discrete crack model.

The need for a crack model that offers automatic generation of cracks and complete generality in crack orientation, without the need of redefining the finite element topology, has led the majority of investigators to adopt the smeared crack concept also to model discrete cracks.

Rather than representing a single crack, as shown in Figure 5.1 a, the smeared crack model represents many finely spaced cracks perpendicular to the principal stress direction, as illustrated in Figure 5.1 b. This approximation of cracking behaviour of concrete is quite realistic, since the fracture behaviour of concrete is very different from that of metals. In concrete, fracture is preceded by microcracking of material in the fracture process zone, which manifests itself as strain softening. This zone is often very large relative to the cross section of the member due to the large size of aggregate (Figure 5.2a). On the contrary, in a steel member fracture is preceded by yielding of material in the process zone which is concentrated near the crack tip and has a relatively small size (Figure 5.2b). In this case a discrete crack model is a more realistic representation of actual behaviour.

5.2.2 Use of the smeared crack concept for modelling localised cracks.

The smeared crack model first used by Rashid (1968) [104] represents cracked concrete as an elastic orthotropic material with reduced elastic modulus in

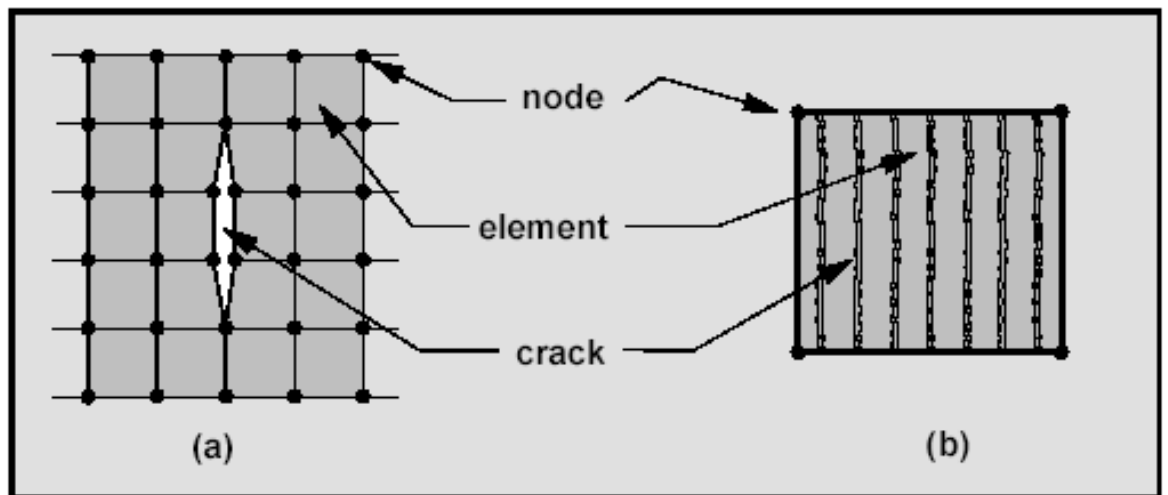


Figure 5.1: Cracking models: (a) discrete; (b) smeared

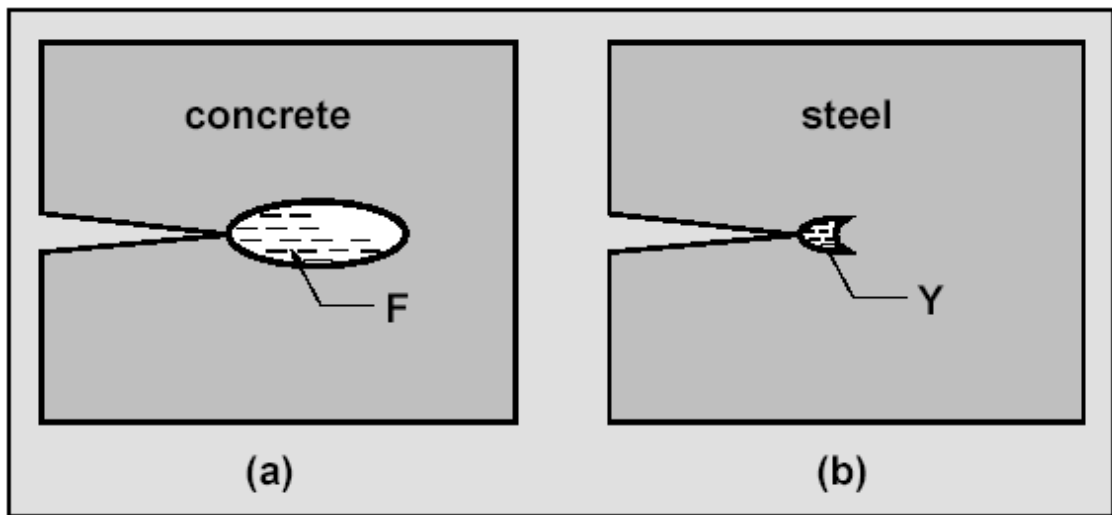


Figure 5.2: Relative size of process zone: (a) Fracture zone (F) of concrete ;
(b) Yielding zone (Y) of steel

the direction normal to the crack plane. With this continuum approach the local displacement discontinuities at cracks are distributed over some tributary area within the finite element and the behavior of cracked concrete can be represented by average stress-strain relations. In contrast to the discrete crack concept, the smeared crack concept fits the nature of the finite element displacement method, since the continuity of the displacement field remains intact.

Although this approach is simple to implement and is, therefore, widely used, it has nevertheless a major drawback, which is the dependency of the results on the size of the finite element mesh used in the analysis [15, 16, 17]. When large finite elements are used, each element has a large effect on the structural stiffness. When a single element cracks, the stiffness of the entire structure is greatly reduced. Higher order elements in which the material behavior is established at a number of integration points do not markedly change this situation, because, in most cases, when a crack takes place at one integration point, the element stiffness is reduced enough so that a crack will occur at all other integration points of the element in the next iteration. Thus, a crack at an integration point does not relieve the rest of the material in the element, since the imposed strain continuity increases the strains at all other integration points. The overall effect is that the formation of a crack in a large element results in the softening of a large portion of the structure. The difficulty stems from the fact that a crack represents a strain discontinuity which cannot be modelled correctly within a single finite element in which the strain varies continuously. Many research efforts have been devoted to the solution of this problem based, in particular, on fracture mechanics concepts [15, 16]. In order to define the strain softening branch of the tensile stress-strain relation of concrete by fracture mechanics concepts three important parameters need to be defined:

- the tensile strength of concrete at which a fracture zone initiates;
- the area under the stress-strain curve;
- the shape of the descending branch (Reinhardt 1986).

Among these parameters, the first two can be considered as material constants, while the shape of the descending branch varies in the models that have been proposed [53, 17]. Before discussing two of the most prominent models, a relation between the area under the tensile stress-crack strain diagram in Figure 5.3 and the fracture energy G_f is needed. This relation can be readily derived by the following procedure.

The area g_f under the curve in Figure 5.2a can be expressed as:

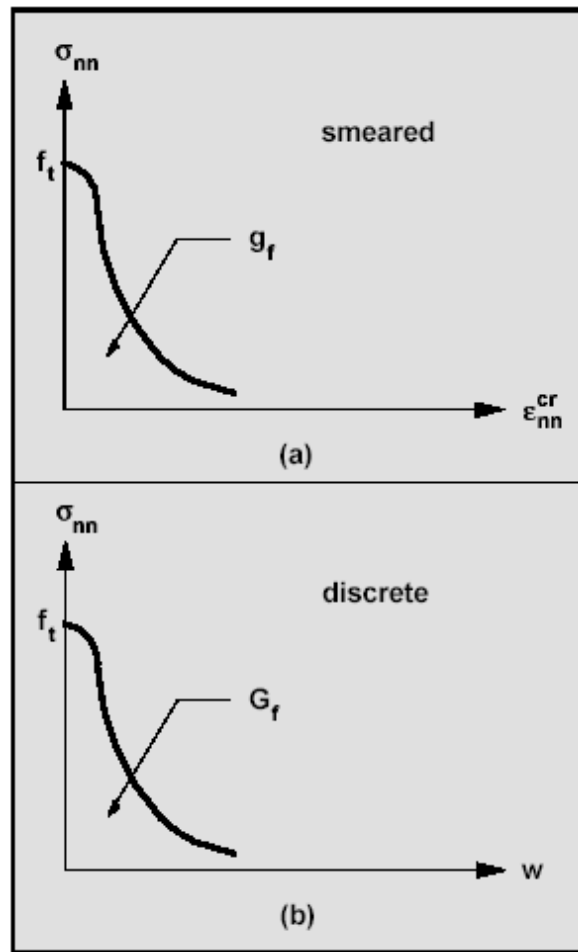


Figure 5.3: Strain softening behaviour of concrete: (a) tensile stress vs. crack strain relation ; (b) tensile stress vs. crack opening displacement relation

$$g_f = \int \sigma_{nn} d\epsilon_{nn}^{cr} \quad (5.1)$$

The fracture energy G_f is defined as the amount of energy required to crack one unit of area of a continuous crack and is considered a material property. This definition results in the following expression for the fracture energy G_f

$$G_f = \int \sigma_{nn} dw \quad (5.2)$$

where w represents the sum of the opening displacements of all microcracks within the fracture zone. Eq. 5.2 is schematically shown in Figure 5.3b. In the smeared crack model w is represented by a crack strain which acts over a certain width within the finite element called the crack band width b . Since w is the accumulated crack strain, this is represented by the following relation

$$w = \int \epsilon_{nn}^{cr} dn \quad (5.3)$$

Assuming that the microcracks are uniformly distributed across the crack band width, Eq. 5.3 reduces to:

$$w = b\epsilon_{nn}^{cr} \quad (5.4)$$

The combination of Eq. 5.4 with Eqs. 5.1 and 5.2 yields the relation between G_f and g_f :

$$G_f = bg_f \quad (5.5)$$

The simplicity of Eq. 5.5 is misleading, because the actual size of the crack band width b depends on the selected element size, the element type, the element shape, the integration scheme and the problem type to be solved. Strains are assumed uniform within the band. In this case the final equation for determining the tensile fracture strain ϵ_o takes the form (Figure 5.3a)

$$\epsilon_o = \frac{2G_f}{f_t b} \quad (5.6)$$

where b is the element width and G_f is the fracture energy required to form a crack. After an extensive experimental study Hillerborg et. al. (1976) proposed a bilinear descending branch for the tensile strain softening behavior of concrete (Figure 5.3b). Using the assumption that the microcracks are uniformly distributed over the crack band width and combining the area g_f

with the fracture energy G_f according to Eq. 5.5 the following equation is derived for the tensile fracture strain

$$\epsilon_o = \frac{18 G_f}{5 f_t b} \quad (5.7)$$

Both models have been extensively used in the analysis of RC members and yield very satisfactory results when the size of the finite element mesh is relatively small. The analytical results, however, differ significantly from the experimental data when the finite element mesh size becomes very large. This happens because both models assume a uniform distribution of microcracks over a significant portion of a relatively large finite element while the actual microcracks are concentrated in a much smaller cracked region of the element. Thus Eqs. 5.6 and 5.7 cannot be directly applied to the numerical analysis of RC structures with relatively large finite elements.

Fracture and crack propagation in concrete depends to a large extent on the material properties in tension and the post-cracking behavior. Experimental studies [21] indicate that the behavior of concrete after cracking is not completely brittle and that the cracked region exhibits some ductility. As the applied loads are increased the tensile stress in the critical cross section of the member reaches the tensile strength f_t . At this stage microcracks develop and form a fracture zone.

This process is characterized by the strain softening behavior of the section which ends when the microcracks coalesce to form one continuous macrocrack and stresses in the section reduce to zero. In order to account for the fact that microcracks are concentrated in a fracture process zone which may be small compared to the size of the finite element mesh a distribution function for the microcracks across the element width can be introduced. The distribution should be such that it can represent the concentration of microcracks near the crack tip when the finite element mesh size becomes fairly large (Figure 5.4).

Note that the above methodology rely mainly on an appropriate softening model and can be easily implemented within the framework outlined in section 3.6.

There exist, however, a very large number of methods to solve the problem of crack localization. For instance methods using the so called “Extended Finite Elements” are becoming popular. In this approach the problems associated with the stress transfer between different Gauss points in an element, due to the averaging of the strains between nodes due the limited representation capabilities of the shape functions, mentioned above, are solved introducing the possibility of displacement discontinuities (displacement jumps) into the element. Within this class different options are available. In some

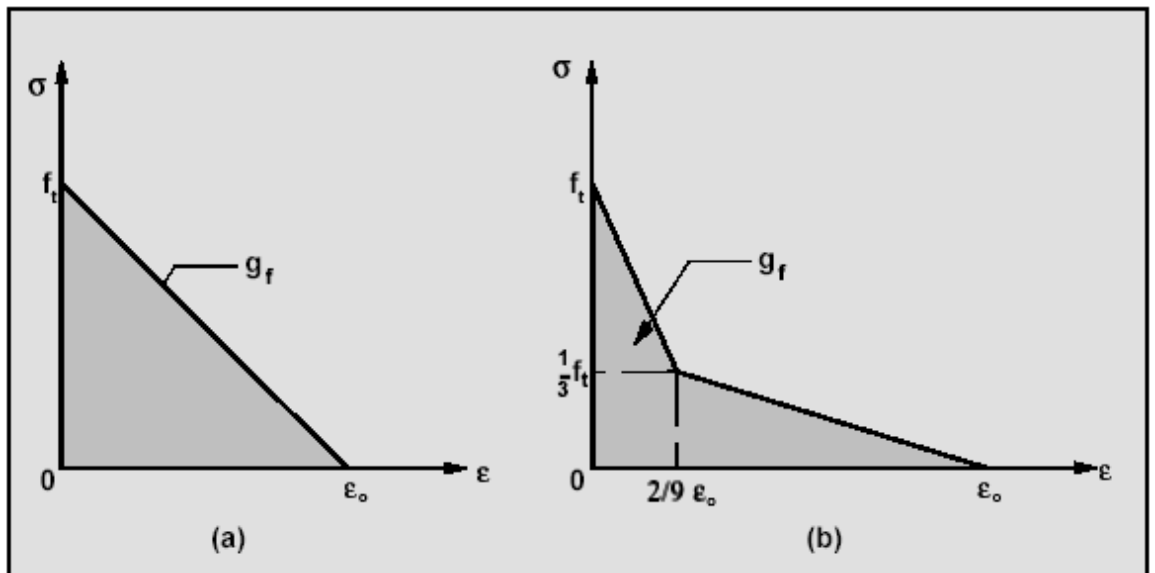


Figure 5.4: Typical shapes of softening branch for concrete: (a) Bazant and Oh; (b) Hillerborg

formulation additional degrees of freedom are not introduced in the element as the magnitude of the displacement jump is solved at the element level by applying equilibrium conditions. In other formulations additional nodal degrees of freedom are added at nodes.

There are also methods in which the displacements are kept continuous while a discontinuity is considered in the strains.

Other methods resort to the introduction of a non-local continuum in which the stress strain relations do not depend only on the local value of the state variables at a given point but virtually on their value in the entire analysis domain. Nonlocal continua can be divided into two main classes: integral-type non local models and gradient models. Generally speaking, integral-type nonlocal models replace one or more variables (typically state variables) by their nonlocal counterparts obtained by weighted averaging over a spatial neighbourhood of each point under consideration. Gradient models instead can be considered as the differential counterpart of integral nonlocal formulations. Instead of introducing nonlocality through spatial interaction integrals, we can account for it by incorporating higher-order gradients into the constitutive model [52].

The possibilities mentioned do not cover the entire scope of available methods and the choice of the particular strategy should be tailored on the specific problem and on implementation/computational time issues.

5.2.3 Finite element analyses to model localised cracking

The principles explained above are reflected in the new cracking concrete model of LUSAS (multicrack concrete 94). Using the above model the propagation of discrete cracks within a concrete volume has been attempted. The first model analysed was a simple plain concrete specimen with a notch. The geometry of the specimen the applied loads and the supports are reported in Figure 5.5. The same specimen has also been analysed in [51]. The dotted line is the crack path observed experimentally. Typical properties have been assumed for the concrete and are not reported as the results are discussed only qualitatively. We can see from Figures 5.6 and 5.7 that the localization of the strains within a narrow band is effectively achieved. Also the crack pattern is very similar to the one observed experimentally.

In Figure 5.8 we report the load displacement curve showing the progressive softening of the specimen. The results refer to a 1mm thickness of the specimen. Crisfield cylindrical arc-length control strategy has been used to follow the softening branch of the load displacement curve. Some spurious

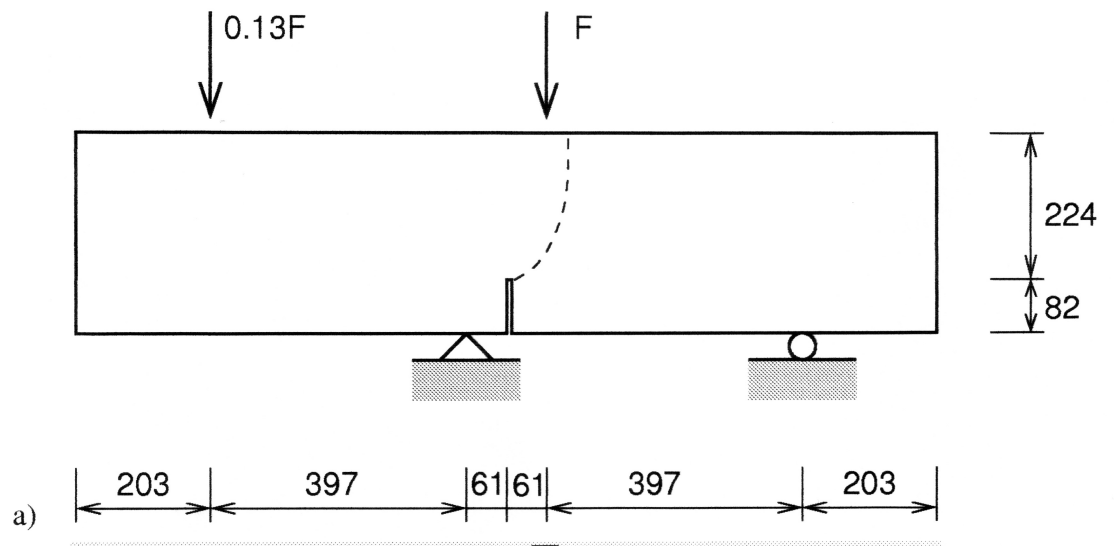


Figure 5.5: Notched plain concrete specimen

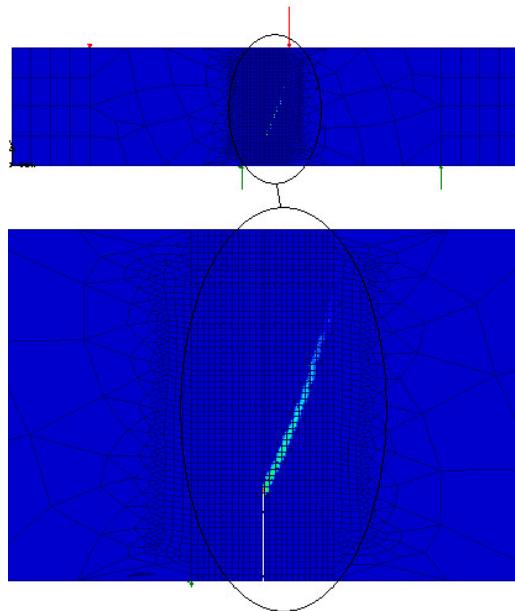


Figure 5.6: Crack path in a notched specimen

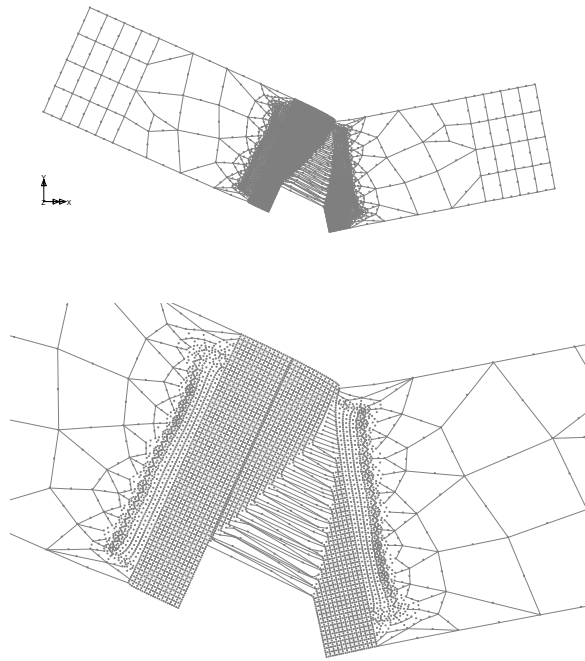


Figure 5.7: Exalted deformed mesh showing crack opening

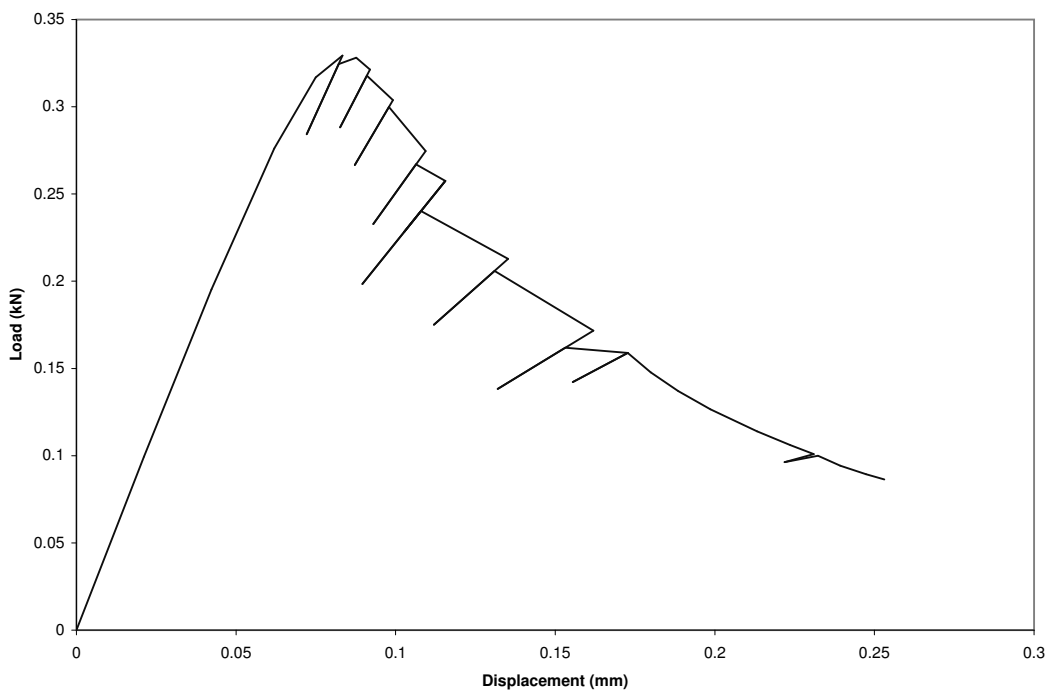


Figure 5.8: Load-Displacement curve for a notched plain concrete specimen under the load conditions shown in Fig. 5.5

algorithmic unloadings are visible but the overall shape of the curve reflects closely the expected one. Although the failure load of the real specimen was not known, we can observe that in this simple case the results are realistic and that there is a potential in the method. This positive result led to the investigation of more complex models. The level of complication has been increased gradually. The first step has been the removal of the crack inducer notch to see whether the model is still capable of capturing the onset of a single localised crack (i.e. whether with a more uniform pre-crack stress field the localization of the strains is still possible). The results are positive again and not too dissimilar from the notched case.

A beam in four points bending was then analysed. It is seen from figure 5.9 that softening outbreaks simultaneously at all points in the constant moment area and discrete cracks fail to appear. Also because a large number of elements is affected by softening at the same time, numerical convergence problems are experienced and the analysis cannot be pushed far beyond the onset of material softening.

The problem with a uniform distribution of stresses is due to the fact that there are no preferential locations for the onset of cracking and the damage tend to accumulate uniformly into a large volume rather than to localize.

In the case of an RC beam retrofitted with FRP under four point bending, in which beside the uniformity of the stresses in the constant moment area there is also an internal force spreading due to the presence of the internal and external reinforcement it is observed that the material undergoes damage uniformly in a large volume and local effects are lost. Also because of loss of stiffness into all the elements attached to the nodes inside the damaged area, the structure becomes unstable and the program fails to converge under relatively modest loads. In the attempt to induce a *non uniformity* a single preset crack was inserted into the model at midspan. In this case, as it is shown in Figure 5.10, one localized crack is visible. The crack is also in the location where it was expected at about 100 mm from the preset one. Unfortunately the model failed to capture the formation of the subsequent cracks.

The conclusion is then that although the model for cracking is realistic and well formulated it is practically inapplicable to our problem due to its inherent indeterminacy. To remove this indeterminacy it is not sufficient to trigger cracking at one single location.

Some authors have suggested to introduce random spatially variable material properties to solve this kind of problem [52]. This would lead to a stochastic approach as a single result involving a random input would not make any sense and a population of results should be generated varying the spatial distribution of the material properties.

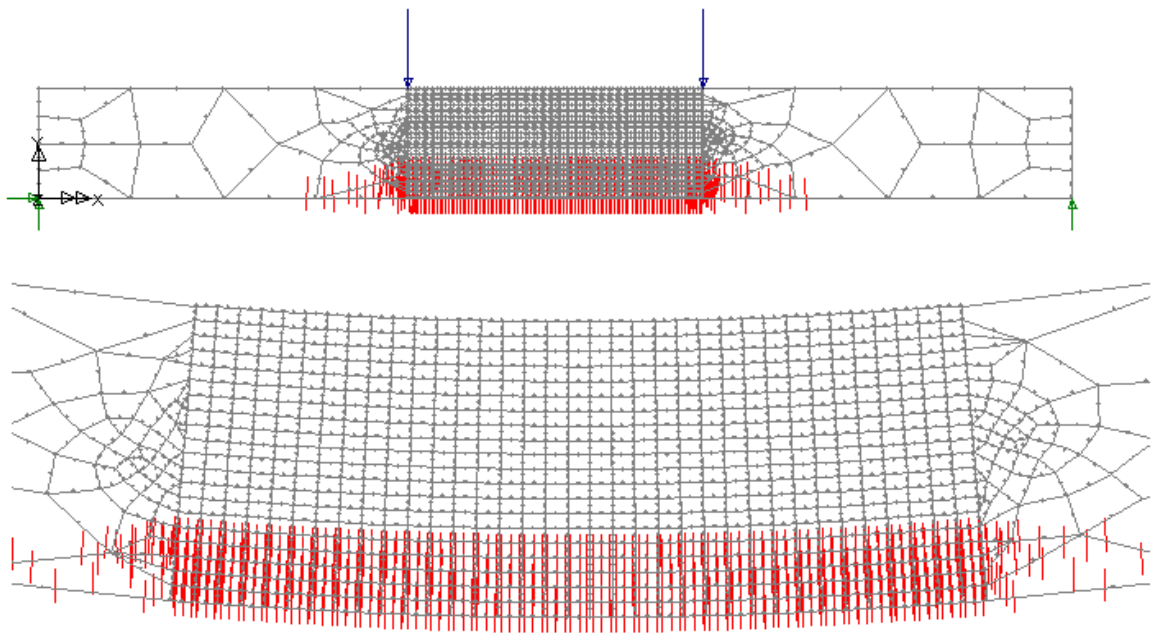


Figure 5.9: Failed concrete in a plain concrete specimen under four point bending

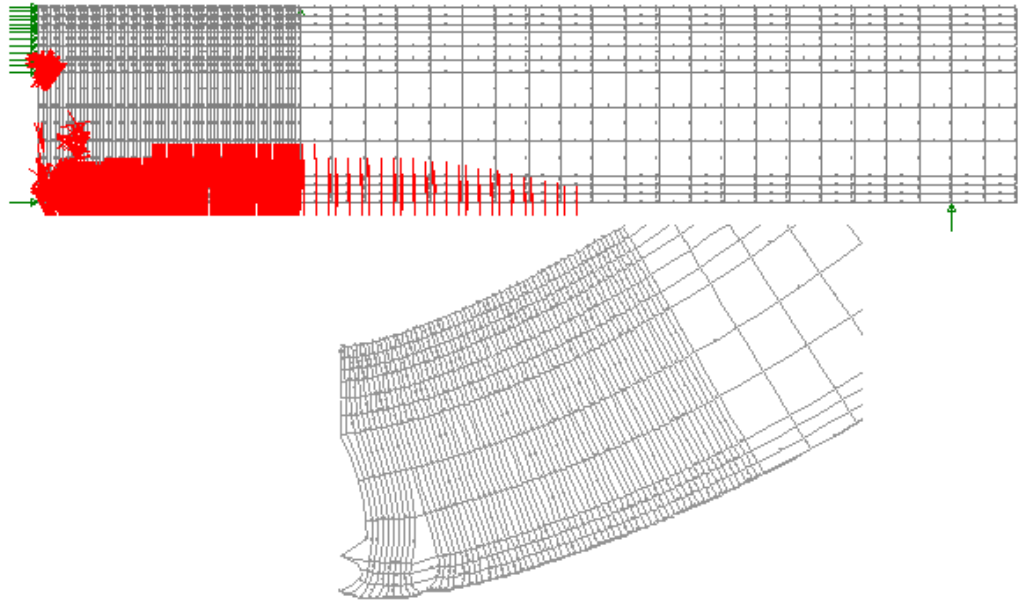


Figure 5.10: Area affected by softening and localization of cracks in full model for analysis of RC beam retrofitted with FRP

For the purpose of the investigation of the interfacial behaviour FRP/concrete, that is the main goal, in relation to a discrete crack modelling, as it will be seen in the next section, good results are obtained with the initial simple approach, consisting in the introduction of preset cracks.

The obvious drawback of this approach is that it requires preliminary knowledge of the specific problem under investigation. This can anyway be obtained within reasonable limits by preliminary analysis. Also as observed before. The fulfilment of all the assumptions can be verified *a posteriori* (The omission of softening for instance is acceptable if in the analysis domain, as defined by the presence of cracks, tensile failure of the material does not occur). Also common practice in engineering is to study a particular aspect in isolation when there are operative difficulties in modelling it together with all the other interrelated ones. Bearing this in mind, we have found a useful

application of the cracking model tested, in the analysis of failure modes of RC beams retrofitted with FRP that cannot be captured by the general model described in chapter 2 and used in the general applications discussed in the next chapter. These failure modes are shear failure due to propagation of a crack triggered at the FRP plate end, and debonding of the covercrete. In order to investigate these failure modes a model of a plain concrete beam with a perfectly bonded FRP plate has been set up and analysed under a uniformly distributed load (UDL). The failure mode mentioned above are the only ones that the model can capture and therefore the model must be used in conjunction with the general one. It is recognised that effects related to the coupling with other aspects are missed, but the model still provides very useful information on potential shear or covercrete debonding failure that is not readily obtainable by other means.

The crack from which the failure originate has been triggered by introducing a small discontinuity at the plate ends. Only half the beam has been modelled because of symmetry. The thickness of the elements along the reinforcement line has been slightly reduced to clear the section from the bars area. This is because direct stresses are not transferred between the reinforcement and the concrete after bond slip has occurred. Besides deformed bars, as seen in Chapter 4, generate conical struts within the surrounding concrete volume, and therefore hoop tensile stresses that determine a preferential line of crack formation. Note that the reduction has been applied to both the model failing in shear and the model failing because of covercrete debonding.

The first series of pictures refer to the shear failure mode (Figures 5.11 to 5.13). In Figure 5.11 we see the mesh and the path of the crack at the the end of the load process. The same crack is shown open in the exalted deformed mesh (Figure 5.12) to bring forward the difference in straining between cracked and uncracked elements. In Figure 5.13 the vector plot of the principal stresses is reported onto the deformed mesh to show that the crack is actually stress free.

To switch to a covercrete debonding mechanism the inclination of the initial *trigger* crack has been reduced. The results are presented again in graphical format in Figures 5.14 to 5.16. In Figure 5.14 we see the crack path on the undeformed mesh. As we can see the crack propagate horizontally along the line of the reinforcement. When the debonding approaches the midspan a flexural crack appears in the unreinforced part of concrete above the main crack. As for the previous case the crack is also shown open on the exaggerated deformed mesh (Figure 5.15). Also the vector plot of the principal stresses at the end of the loading process is given (Figure 5.16), to show a stress free crack.

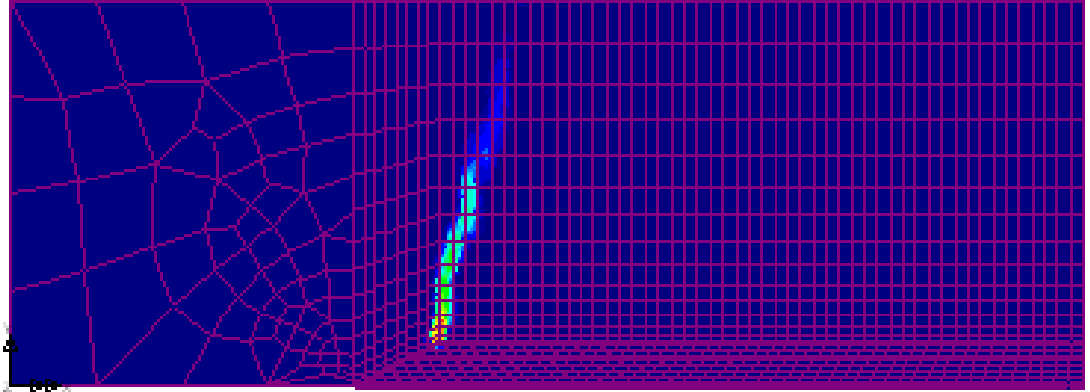


Figure 5.11: Crack path in a concrete beam retrofitted with FRP failing in shear; Crack path shown on undeformed mesh

Finally in Figure 5.17 we report the load displacement curves for the two failure modes. We stress that the only difference between the two models is the inclination of the initial trigger crack, set at the plate end. The loads refer to a 1 mm thickness of the specimens. We note that the two load path are quite different, reflecting the completely different nature of the failure mechanism. It is of concern that the peak resistance is significantly different as well. In fact, only a little difference in the two situations, switching from one failure mode to an other, determines this distinct difference. The model can therefore be usefully adopted to investigate the probability of unforeseen failure modes and therefore improve the reliability of the design predictions.

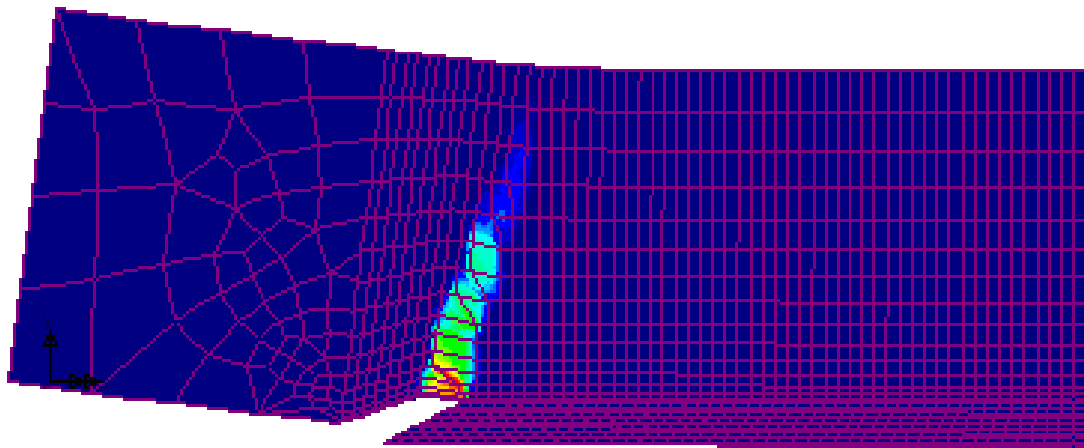


Figure 5.12: Crack path in a concrete beam retrofitted with FRP failing in shear; Crack path shown on deformed mesh

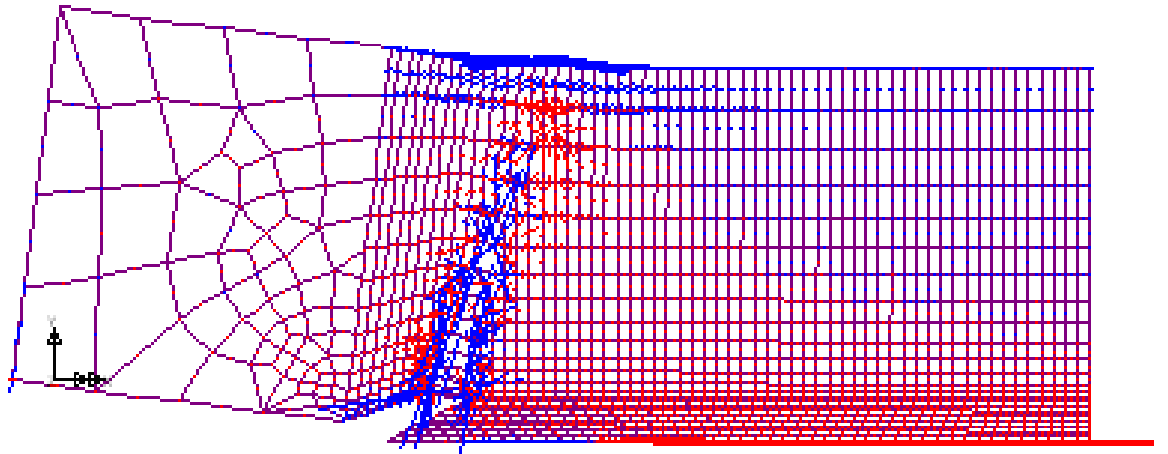


Figure 5.13: Vector plot of principal stresses in a concrete beam retrofitted with FRP; at the end of the loading process on deformed mesh

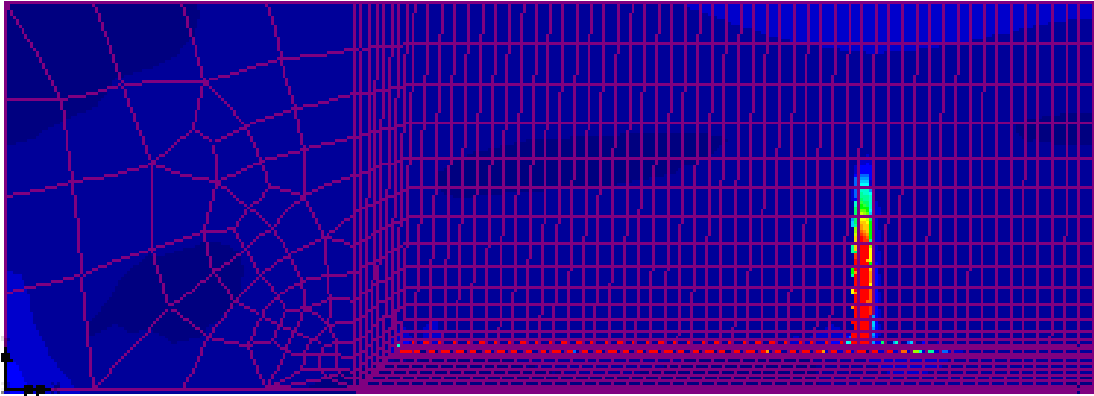


Figure 5.14: Crack path in a concrete beam retrofitted with FRP failing because of covercrete debonding; Crack path shown on undeformed mesh

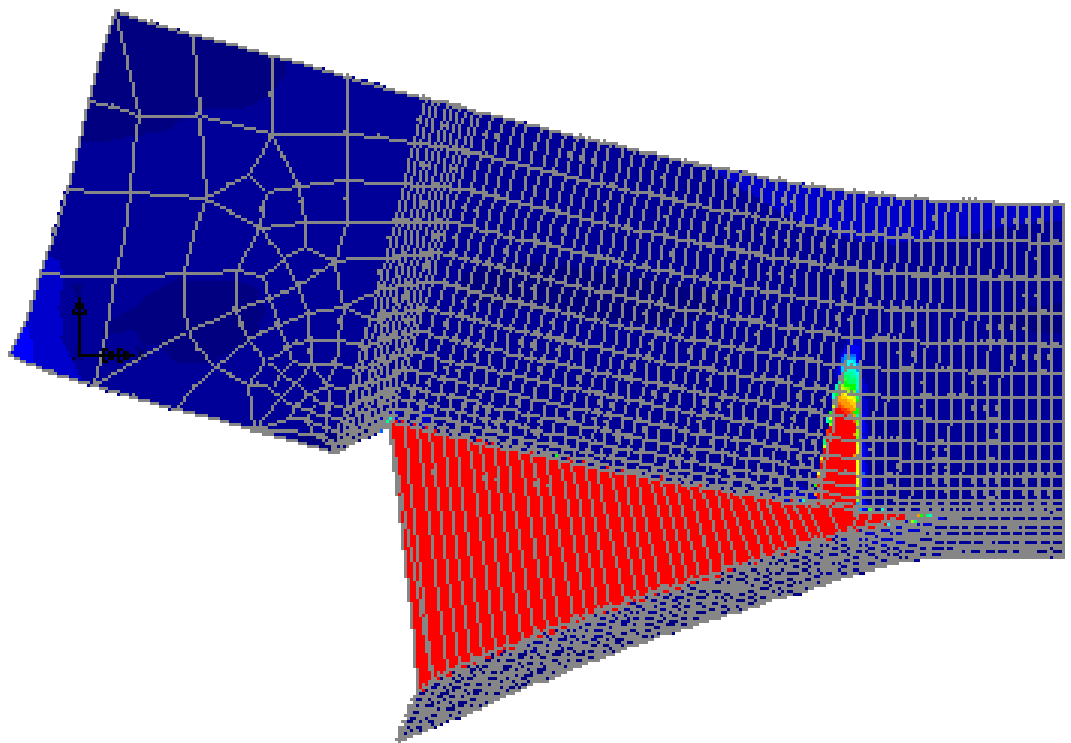


Figure 5.15: Crack path in a concrete beam retrofitted with FRP failing because of covercrete debonding; Crack path shown on undeformed mesh

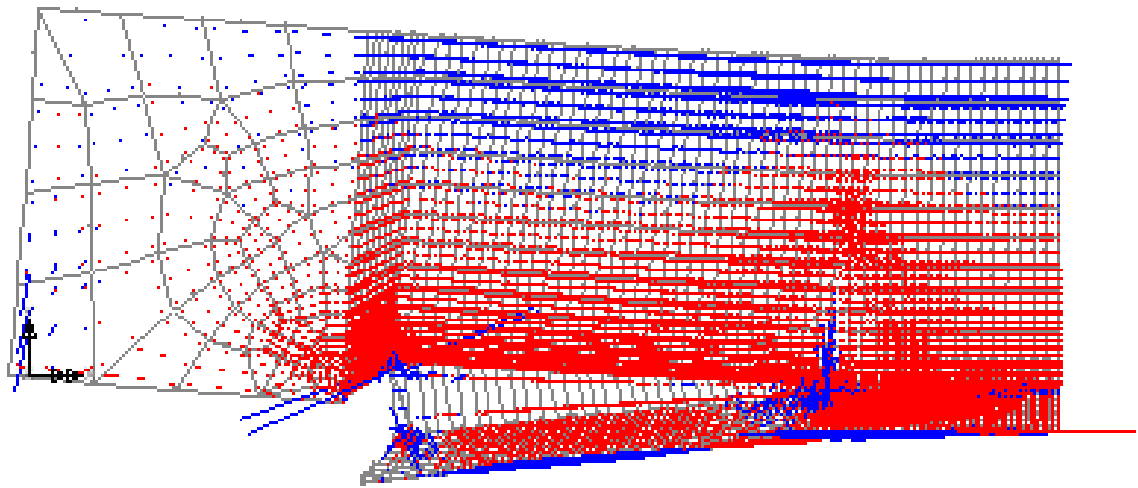


Figure 5.16: Vector plot of principal stresses in a concrete beam retrofitted with FRP; at the end of the loading process on deformed mesh

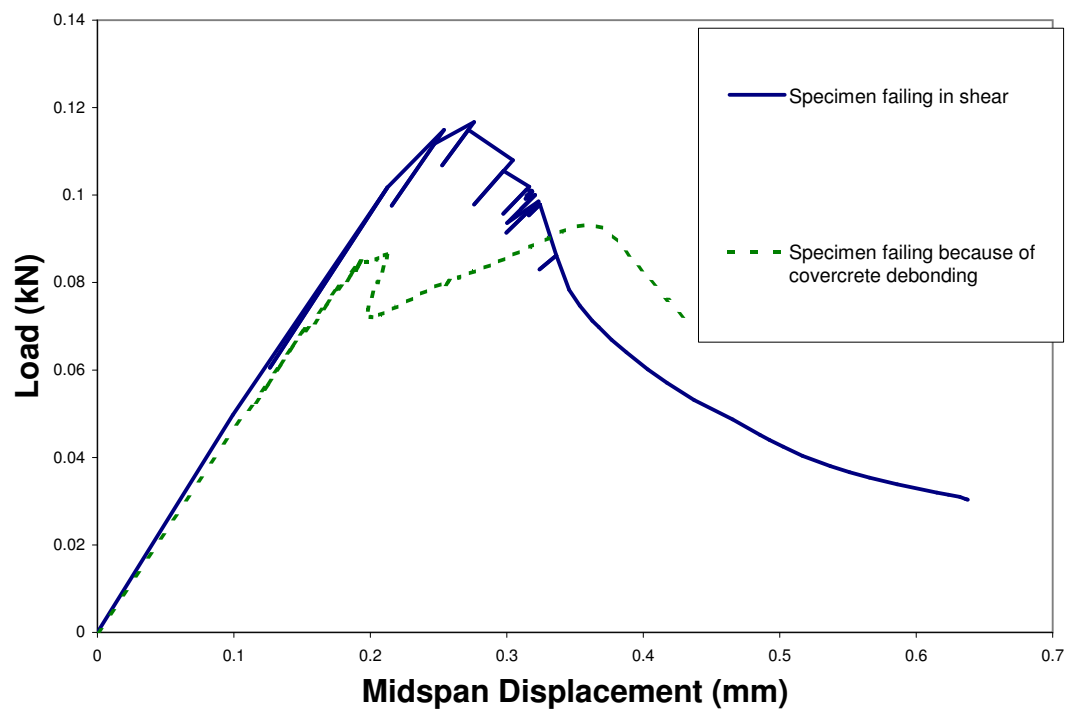


Figure 5.17: Load-Displacement curves for concrete beams retrofitted with FRP failing in shear and by covercrete debond

Chapter 6

Applications

6.1 Introduction

Nonlinear finite-element analyses of reinforced concrete (RC) beams retrofitted with fiber-reinforced-polymers (FRP) have been carried out up to failure. Unlike the previous sections, in which specific aspects have been numerically investigated in isolation, we present here models and results referring to a complete structural element.

These analyses are intended to provide a good appreciation of the importance of the different features of a model for the analysis of this type of systems and to get a better insight into their behaviour through simulations including failure modes not observed in ordinary RC beams.

The isotropic elasto-plastic model with the Menetrey-Willam yield criterion [68] is used for concrete. This model provides, as explained in Chapter 3 a fair representation of the tensile/cohesive strength of cementitious materials, as well as a reasonable description of shear strength of frictional materials, by making the yield function also depend on the third invariant J_3 of the stress deviator.

In order to take into account the bond-slip interaction between the reinforcing steel bars and the concrete, and therefore the tension-stiffening effect, use has been made of the cohesive-zone model proposed in Chapter 4, which for the pure-mode-II case at hand specialises to a piece-wise linear, elastic-damage model. The same model has been adopted to take into account the possible debonding of the FRP sheet.

Localised cracks have been modelled by introducing vertical interfaces with unilateral contact at preset locations along the beam span. In particular, it is shown that the shear stress profile at the FRP/concrete interface is largely affected by these cracks and is characterised by shear stress concen-

trations which can indeed determine the onset of delamination. It is further shown that smeared crack approaches can fail to capture this effect.

Numerical results are presented for the simply supported beam studied experimentally in [131] and a comparison is made between the numerical and experimental results in order to test the efficiency of the analysis. Different modelling options are compared and discussed.

6.2 Numerical results

The experimental tests carried out by White et al. in [131] have been chosen for a case history.

The problem analysed in [131] has been chosen both because it represents a typical case of engineering interest and because the experimental setup and the results are reported with a level of detail which is sufficient to attempt reproducing them numerically.

A set of 9 beams was considered in [131]. All of them were characterised by the same geometry and steel reinforcement, which are reported here in Figure 6.1, and were tested in four-point bending.

One of the beams was used as a control beam (CB) and no FRP reinforcement was applied to it. The remaining 8 beams were divided into two groups of 4 beams, for which two types of carbon FRP (CFRP) reinforcement were used, one of them consisting of pultruded laminates, and the other one consisting of prepreg sheets. The four beams of each group were then subjected to four different loading rates and one of the cases also involved cyclic loading.

Stress-strain curves for steel and concrete are affected by strain rate and appropriate laws for representing this rate dependence were provided by the authors of the experimental study[131]. The numerical analysis has been carried out for a monotonic loading with a fast loading rate of 0.0167 mm s^{-1} because this is the type of loading which has been applied to the control beam (CB) and hence the one for which comparison between results obtained for the control and the retrofitted beams is possible. The beams reinforced with the pultruded laminates, referred to as S-type (SB), have been reinforced with two sheets of laminate 50 mm wide and 1.2 mm thick. The beams retrofitted with the pre-prep sheets, referred to as R-type (RB), have been reinforced with 5 sheets of FRP, each of them being 135 mm wide and 0.11 mm thick.

Therefore, these three types of beam, that is the CB, SB and RB, have been considered in the simulations. They have been analysed with a two-dimensional model in the hypothesis of plane strain.

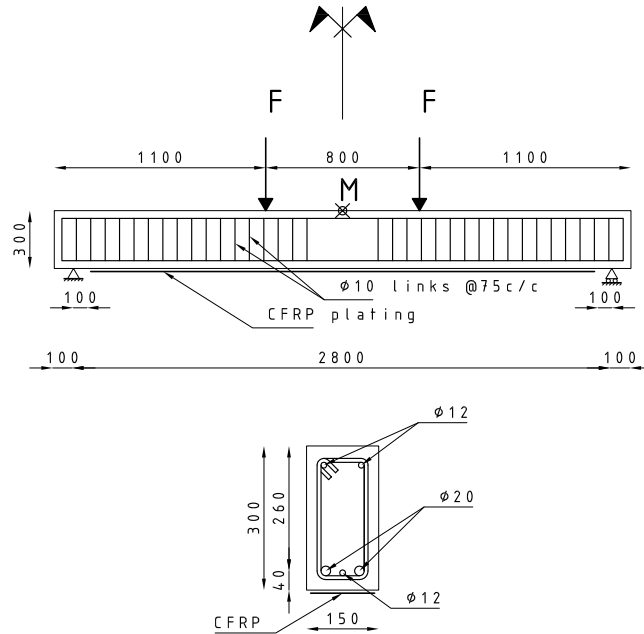


Figure 6.1: RC beam: geometry and loading.

6.2.1 Material properties

The material parameters selected for concrete are reported in Table 6.1. Setting $e = 1$, and the other parameters as given in the table, the Menetrey-Willam yield function specialises to the Drucker-Prager one. The uniaxial compressive and tensile strengths are $f_c = 38.5 \text{ MPa}$ and $f_t = 3.2 \text{ MPa}$, as for the material used in the tests [131] for the case of a fast loading rate, derived according to [111] estimating that a loading rate of 0.0167 mm s^{-1} results in a magnitude of the strain rate of 10^{-3} s^{-1} , both in the concrete and in the steel rebars.

The Drucker-Prager model accounts for the different tensile and compressive strengths of concrete but is not consistent with the experimental evidence that the nonlinear behaviour of concrete depends on the Lode angle. Hence, the eccentricity parameter e has also been given the values 0.8 and 0.6 so as to change the shape of the deviatoric sections (see Chapter 3) and to investigate its importance.

Linear elastic-perfectly plastic behaviour has been assumed for the concrete and, for the elastic range, the Young's modulus has been chosen as a secant modulus which approximates the initial part of the nonlinear behaviour in compression with a linear elastic relationship.

Concrete					
Elastic properties	Young modulus (GPa)		Poisson ratio		
	20		0.18		
Plastic properties	A (MPa ⁻¹)	B (MPa ⁻¹)	C (MPa ⁻¹)	m	e
	0.0	0.2	0.42	1	0.6 ÷ 1.0

Table 6.1: Material properties for the concrete.

	Young modulus (GPa)	Yield/Failure stress (MPa)*
Steel bars	205	470
S-type FRP	155	2400
R-type FRP	160	3000

* This value refers to yield for steel and to failure for FRP

Table 6.2: Material properties for the steel rebars and the CFRP laminate.

	G_c (N/mm)	τ_o (MPa)	s_o (mm)
Concrete/rebar interface	24	12	0.8
Concrete/S-type FRP interface	0.35	3.5	0.0001
Concrete/R-type FRP interface	0.33	3.3	0.0001

Table 6.3: Material properties for the concrete-rebar and concrete-FRP interfaces.

For the steel rebars a linear elastic-perfectly plastic model has been adopted. The material properties as indicated in [131] are reported in Table 6.2. The

yield stress of 470 MPa is obtained, for the case of a fast loading rate, by using a model proposed in [111]. The behaviour of the FRP laminates has been assumed as linear elastic up to failure.

Not enough information is given in [131] about the interface properties required in the model. For the interface parameters entering the rebar bond-slip relationships, introduced in Chapter 4, the values of Table 6.3 represent estimated values which have been chosen on the basis of similar cases reported in the literature [41, 56, 101]. The properties of the concrete/FRP interface have been selected in accordance with the indications provided in [34, 33] (see chapter 4). Accordingly, the following relations have been used to estimate the interface parameters in terms of the geometrical and mechanical properties of the adherend materials:

$$\tau_o = 0.3 K_b \sqrt{f_c f_t} \quad G_c = 0.03 K_b \sqrt{f_c f_t} \quad K_b = \sqrt{\frac{2 - \frac{b_f}{b}}{1 + \frac{b_f}{400}}} \quad (6.1)$$

where b_f and b denote the widths of the FRP sheet and of the beam, respectively, expressed in mm .

The remaining parameter s_o is related to the interface stiffness K . In absence of detailed information on the thickness and properties of the employed adhesive, s_o has been evaluated with a view to obtaining a high penalty stiffness value which approximately models the almost rigid behaviour of the undamaged interface.

The values so obtained for the interface parameters are reported in Table 6.3. The scaled values which have actually been inserted in the finite-element model have then been obtained from the values of Table 6.3 by smearing the interface relationship over the unit beam width, consistently with the plane-strain hypothesis.

6.2.2 Two-dimensional Finite-element models

Because of the symmetry of the problem only one half of the geometry has been analysed. The finite-element model used is shown in Figure 6.2.

A crack pattern has been predefined and 14 vertical cracks have been introduced in the model with a spacing of 100 mm , which is approximately the same as that observable from the experimental results reported in [131]. Such pattern represents an approximation, which is admittedly somewhat coarse in the right-hand region of the model where inclined cracks develop because of shear. In the finite-element model the cracks have been inserted by doubling the set of nodes, so as to introduce a possible discontinuity.

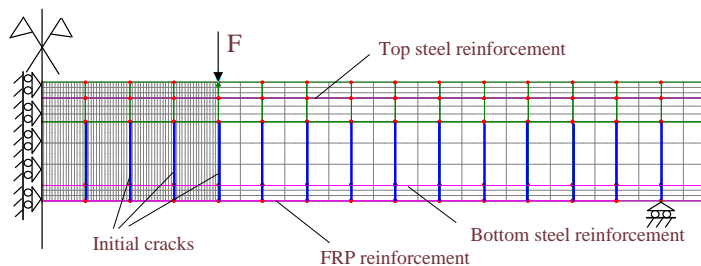


Figure 6.2: RC beam: finite-element model.

Furthermore, in order to prevent material overlapping, contact-type interface elements supplemented with a unilateral contact law with no friction have been used (see also [5] for a more detailed description of such elements).

The experimental results of [131] refer to beams retrofitted before any loading is applied. Hence, the *a priori* introduction of the cracks entail some inaccuracies of the results in the very early stage of the analysis. However, this is accepted because the aim of the analyses is to investigate on the behaviour of the beam after that cracking has developed, up to failure. In particular, in order to analyse in detail the key role played by the presence of cracks, it was considered important to model the crack pattern which has actually been found during the experiments.

For the concrete and the FRP reinforcement 8-noded quadrilateral plane-strain and plane-stress elements have been used, while the steel rebars have been modelled with 3-noded bar elements. Finally, 6-noded interface elements have been used on the concrete-rebar and on the concrete-FRP interface. Small displacements and small deformations have been considered.

The cylindrical arc-length method [27], in its modified version described in [50], has been used in order to follow the structural behaviour beyond the possible points of unstable delamination between concrete and FRP or unstable bond-slip between concrete and rebars. Although local-control arc-length schemes typically perform better in presence of delamination or debonding, in this case the cylindrical arc length gave better results than the local-control procedure developed in [5].

This issue will be discussed in more detail in the following section. More precisely, the results reported in Figures 6.4-6.6 will allow to explain a drawback related to the cylindrical arc-length method, while from the results reported in Figure 6.11 it will be possible to explain the overall better performance of the cylindrical arc-length method with respect to the local-control arc-length method.

Results and discussion

In the two dimensional analyses both the plane strain and the plane stress formulations have been used for elements representing concrete. The main reason for this is associated with work programming issues. In fact, the implementation of the new material model for concrete in the LUSAS and the investigation work on retrofitted beams have been carried out in parallel. As, due to the complications discussed in Chapter4, the routines for the implementation of the Menetrey Willam material model in plane stress have become available in a late stage of the research work, the model in plane strain has been used for most of the investigations carried out using two dimensional models. However, the use of the plane strain assumption is not unjustified due to the confinement action of the links on the concrete in the compression zone. This confinement is expected to have a considerable effect on the plastic behaviour of the material (see Chapter4). The results obtained with the plane strain assumption have been subsequently compared with those obtained with the plane stress one. The difference between the two cases will be shown to be negligible and therefore it was not possible to ascertain which assumption is the most appropriate.

Concrete in plane strain

Figure 6.3 shows the load-displacement curves obtained for the control beam by plotting the value of each force F vs. the displacement of point M at the midspan (see Figure 6.1). Three values have been assumed for the eccentricity parameter e and a comparison with the experimental results reported in [131] is considered. The sharp elbow of the curves at a load level of about 75 KN is due to steel yield, and one can observe that the eccentricity parameter has little influence on the pre-yield part of the curves, and almost no influence after steel yield has occurred. The best results are achieved with $e = 0.6$. In general, quite good agreement is obtained with the experimental results and, in particular, the values of the load and of the displacement at which yield occurs in the steel rebars are well approximated.

In Figures 6.4 and 6.5 the same curves as in Figure 6.3 have been reported for the two types of reinforced beams SB and RB, and show very good agreement between experimental and numerical results. In these cases the eccentricity parameter e has higher influence on the results. This could be related to the fact that shear is the prevalent component of stress at the interface and e influences the shape of the deviatoric sections of the yield surface.

It should also be borne in mind that the assumed interface model is

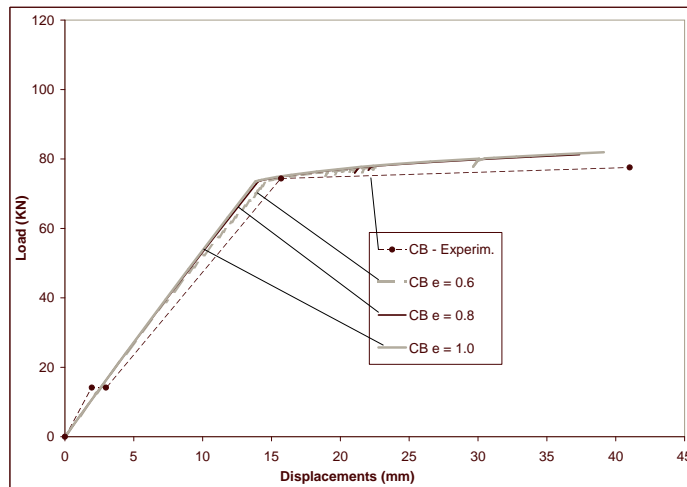


Figure 6.3: Applied load P vs deflection of the midpoint of the beam for the control beam (CB): comparison between the experimental data and the numerical results obtained with different values of the eccentricity parameter e .

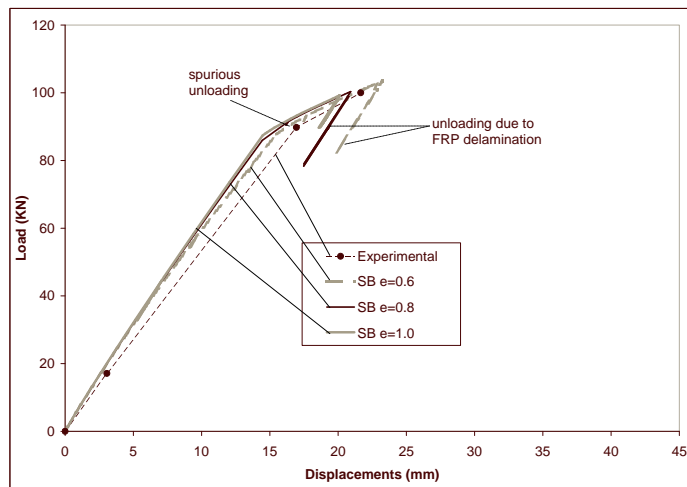


Figure 6.4: Applied load P vs deflection of the beam midpoint for the reinforced beam (SB): comparison between the experimental data and the numerical results obtained with different values of the eccentricity parameter e .

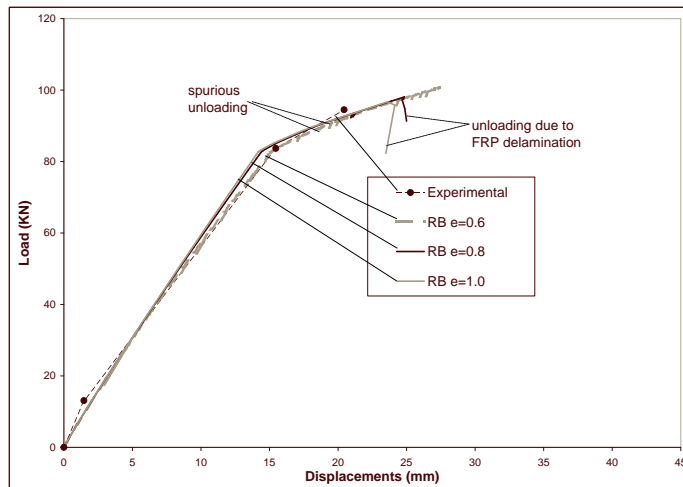


Figure 6.5: Applied load P vs deflection of the beam midpoint for the reinforced beam (RB): comparison between the experimental data and the numerical results obtained with different values of the eccentricity parameter e .

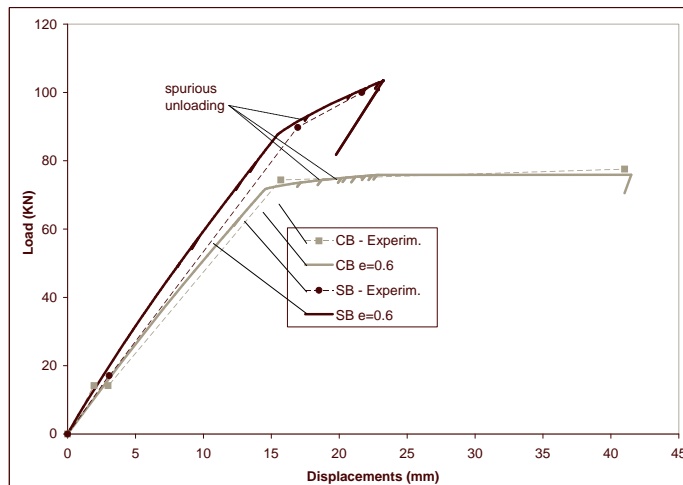


Figure 6.6: Applied load P vs deflection of the beam midpoint: comparison between the experimental data and the numerical results ($e = 0.6$) for the control beam and S-type the reinforced beam.

representative of what happens in a finite volume including the bonding

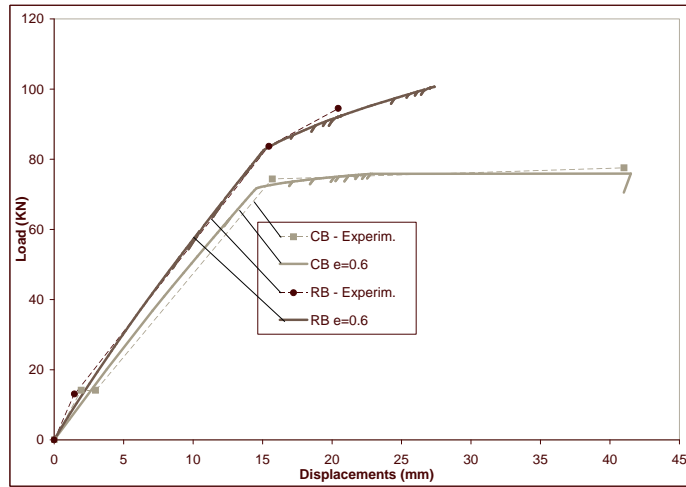


Figure 6.7: Applied load P vs deflection of the beam midpoint: comparison between the experimental data and the numerical results ($e = 0.6$) for the control beam and R-type the reinforced beam.

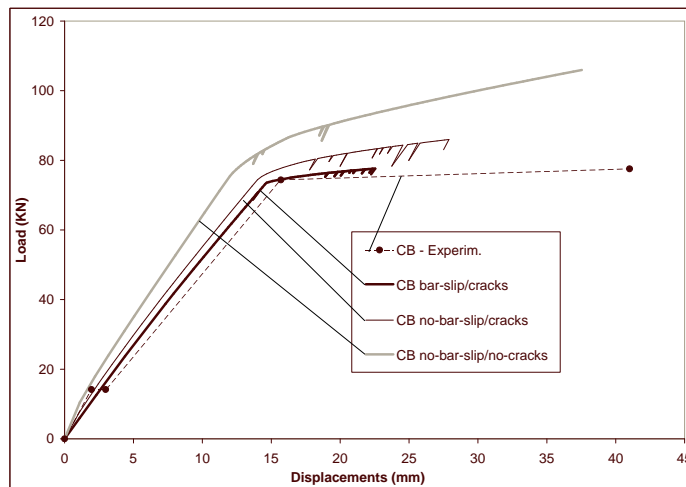


Figure 6.8: Applied load P vs deflection of the beam midpoint for the control beam (CB): comparison between the experimental data and the numerical results ($e = 0.6$) obtained with different sets of hypotheses.

material and a layer of concrete, whose thickness is generally estimated as 20-30 mm, and that the fracture energy and the peak stress of the interface

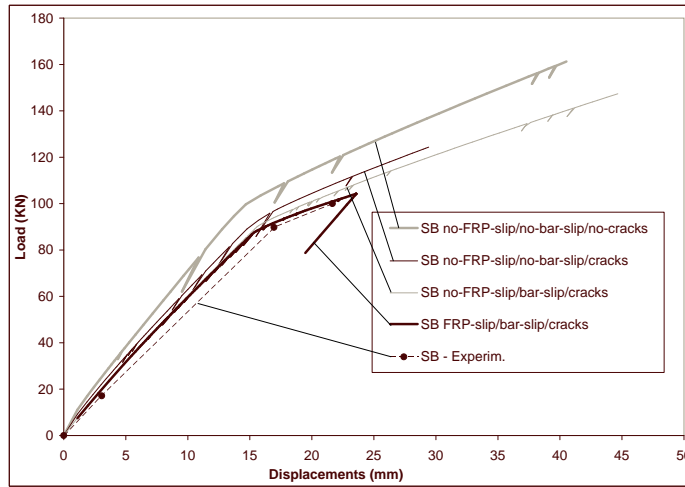


Figure 6.9: Applied load P vs deflection of the beam midpoint for the reinforced beam (RB): comparison between the experimental data and the numerical results ($e = 0.6$) obtained with different sets of hypotheses.

are dependent on the properties of the concrete. Hence, as the boundary between what is concrete and what is interface is somewhat vague, it is reasonable to believe that a refined modelling of the layer of concrete adjacent to the interface can be important for the accuracy of the results. Further investigation on this aspect will be the subject of future research work.

Figures 6.6 and 6.7, for the case $e = 0.6$, show a comparison between the results obtained for the control beam CB and for the reinforced beams SB and RB. It is apparent that the retrofitted beams increase in strength and decrease in ductility with respect to the control beam, as correctly predicted by the numerical model.

Remark 6.2.1 A drawback of the cylindrical arc length is that, in some increments, it may provide some spurious unloading. This is because, at each iteration, the solution to the quadratic arc-length equation gives two roots, and the optimal choice between them is problem dependent. In his famous paper [27] Prof. Crisfield introduced the so-called ‘angle criterion’ as an effective way of avoiding ‘doubling back’ in many problems. However, Crisfield himself and Hellweg in [50] introduced an alternative method, which turned out to give better results for the composite delamination problems studied therein, whereby the root associated with the minimum norm of the iterative out-of-balance forces is chosen.

In these analyses the ‘angle criterion’ has been found to be more effective. Nevertheless it was not possible to completely avoid cases of little spurious unloading, which have been indicated in Figures 6.4-6.6. Instead, the more evident snap-backs which are found at the end of the curves numerically obtained for the reinforced beams are caused by the propagation of delamination at the FRP/concrete interface, as is illustrated in more detail later on. ■

Figures 6.8 and 6.9 show the results of some analyses done with a view to understanding the importance of some of the assumptions made in the finite-element model.

In particular, two further analysis have been carried out for the control beam. In the first one, referred to as ‘CB no-bar-slip/cracks’ in Figure 6.8, the initial cracks have been retained in the finite-element model but the bilinear bond-slip relationship for the concrete/rebars interface has been replaced with a perfect bond assumption. In the second analysis, referred to as ‘CB no-bar-slip/no-cracks’ in Figure 6.8, the cracks have been eliminated by constraining together, with perfect bond, the couples of nodes initially sharing the same position, and the assumption of perfect bond has also been made for the concrete/rebars interface.

Analogously, three further analyses have been made for the reinforced beam SB. In the first one, referred to as ‘SB no-FRP-slip/bar-slip/cracks’ in Figure 6.9, the initial cracks and the bilinear bond-slip relationship for the concrete/rebars interface have been retained, while a perfect-bond assumption has been made for the concrete/FRP interface. In the second analysis, referred to as ‘SB no-FRP-slip/no-bar-slip/cracks’ in Figure 6.9, the initial cracks have been retained in the finite-element model but the bilinear bond-slip relationships, both for the concrete/rebars interface and for the concrete/FRP interface have been replaced with a perfect-bond assumption. Finally, in the third analysis, referred to as ‘SB no-FRP-slip/no-bar-slip/no-cracks’ in Figure 6.9, the cracks have been eliminated by constraining together the couples of nodes initially sharing the same position, and the assumption of perfect bond has been made for the concrete/FRP and concrete/rebars interfaces.

Furthermore, the analyses reported in Figures 6.3 and 6.5 for the case $e = 0.6$ have also been reported for comparison in Figures 6.8 and 6.9 and have been referred to as ‘CB bar-slip/cracks’ and ‘SB FRP-slip/bar-slip/cracks’, respectively.

It appears from Figures 6.8-6.9 that all of the considered hypotheses, that is the presence of the initial cracks and that of cohesive relationships at the concrete-FRP and concrete/rebars interfaces, are important in order

to achieve a good degree of accuracy in terms of load displacement curve. In particular, the increasing stiffness of the f.e. model associated with the closure of the cracks and with the perfect bond of the concrete with steel and FRP is correctly reproduced in the figures. We now focus on the interfacial

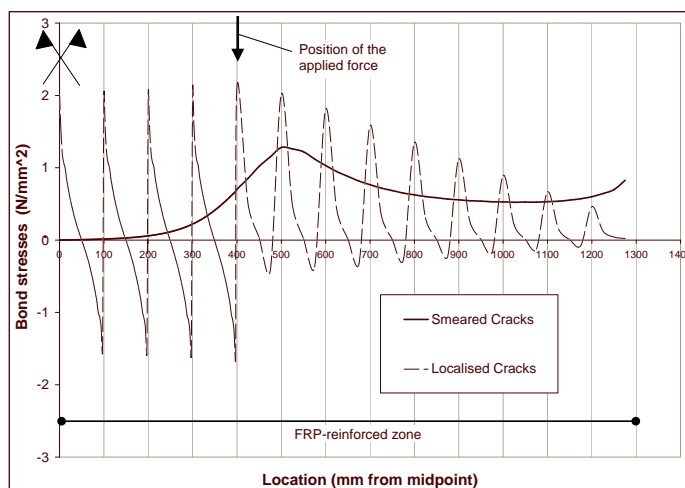
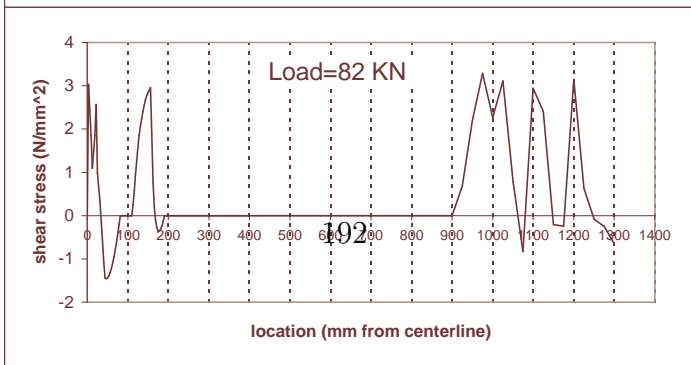
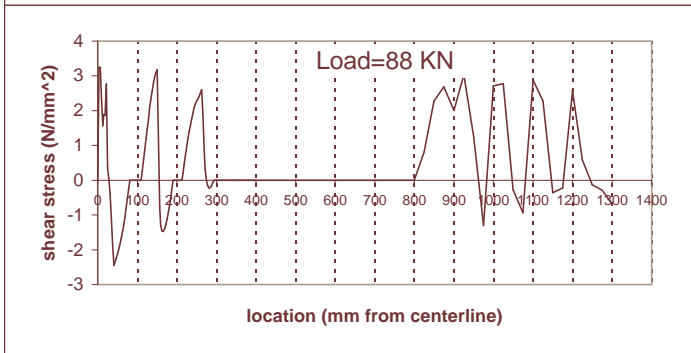
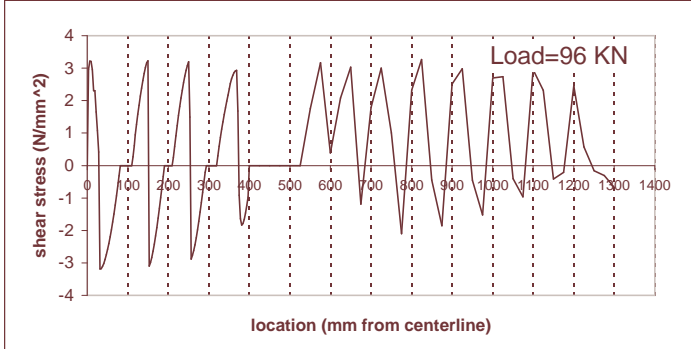
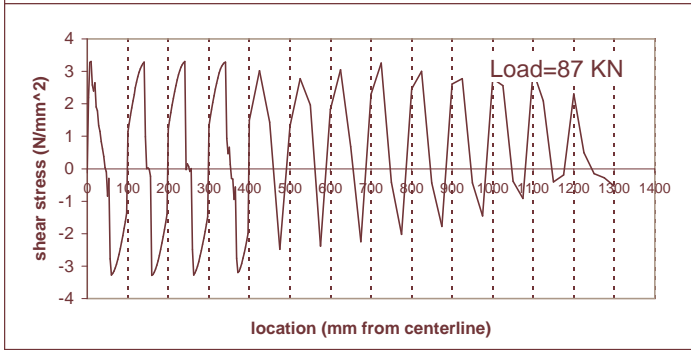
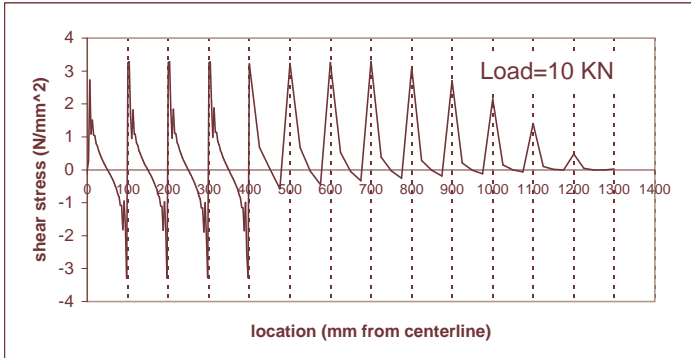


Figure 6.10: Shear stresses at the FRP/concrete interface for localised and smeared cracks.

stresses at the FRP/concrete interface and see that localised cracks have even a more distinct effect on these. A lot of work has been done on the interface performance [101, 137] and analytical solutions, which are only applicable prior to cracking, have been provided. Instead, the nonlinear model developed in this work is capable of capturing the effects of cracking on the interface stresses. This is shown in Figure 6.10, in which the shear stresses at the FRP/concrete interface for a model with localised cracks and those obtained using a smeared crack concept are reported for a load level below delamination initiation and for the reinforced beam RB.

The smeared crack concept has been introduced in the finite-element model using Oliver's material model, as already done in [92]. In this model the non-linear behaviour of concrete is simulated by means of a scalar variable called damage or degradation parameter. Factors like shear retention and anisotropic behaviour of cracked concrete are not included in the model. Degradation is allowed both in tension and compression and the required input parameters are:

$$r_0 = f_t / \sqrt{E_0} \quad r_1 = f_c / f_t \quad \text{and} \quad \alpha = [E_0 / f_t - 0.5]^{-1} \quad (6.2)$$



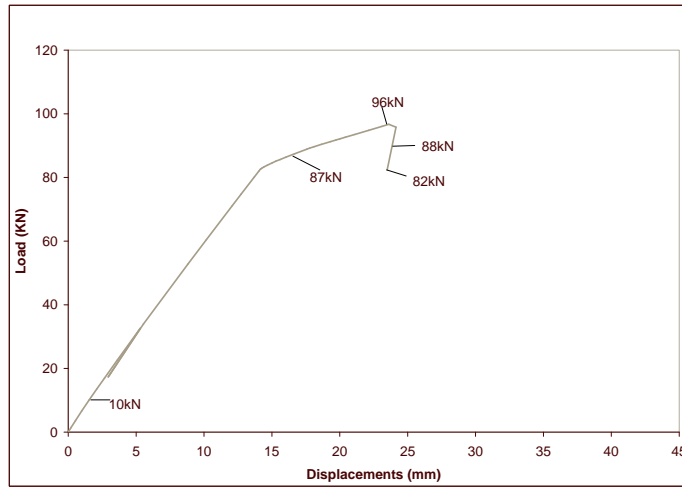


Figure 6.11: Evolution of bond stresses at the interface FRP/concrete for the reinforced beam RB and $e = 1.0$: (a) interface-stress profiles; (b) load-displacement curve with corresponding levels of applied load.

In the above expressions r_0 is the damage threshold, α is a damage accumulation parameter and E_0 is the undamaged Young's modulus. The quantities required for the calculation of these parameters are those reported in Table 6.1. In the smeared crack case shear stresses at the interface quickly tend to zero on the left-hand side of the applied force, i.e. in the constant-moment area of the beam. Moreover, these stresses are smoothly distributed and their value, far from the laminate tips, can be well approximated using Jourawski's approach. However, Figure 6.10 shows that this distribution of stresses is very different from that obtained for a beam with localised cracks. Further work will be carried out and other smeared crack models proposed in the literature will be used in order to fully explore the drawbacks and the potential of this approach in the analysis of the structures under examination. The last set of results presented in Figure 6.11.a represents a series of diagrams showing the stresses at the FRP/concrete interface in the reinforced beam with $e = 1.0$, for several values of the applied load. For the sake of clarity, these values are also reported in Figure 6.11.b near the corresponding points of the load-displacement curve.

The progressive de-cohesion of the laminate from the concrete face, initiating in the area near to the point of application of the load and leading to almost complete delamination and then to failure is evident. In this case delamination is not triggered in the vicinity of the terminal zones of the

laminate. Indeed the shear forces at supports are limited and the stresses generated by crack opening in the span are the critical ones. Stresses in the laminate at the maximum failure load were found to be around 75% of the laminate failure stress of the FRP composite.

Remark 6.2.2 The analysis of the evolution of the interface stresses during delamination explains why a local-control arc-length algorithm, such as that developed in [5], gives worse performance with respect to the Crisfield's cylindrical arc-length method [27]. In fact, there are many points on the FRP/concrete interface which attain, almost at the same time, the peak value of the stress at the beginning of the analysis. Hence, in this early stage, the local-control method fails to determine the actual points of the interface where delamination will initiate and propagate.

As a matter of fact, the key idea of the local-control approach is that the points of the interface where decohesion increases must be detected, so that a weighted sum of the corresponding relative-displacement parameters is adopted as control function in the arc-length scheme. Failing to detect these points does not allow the algorithm to automatically proceed in the direction of increasing, progressive decohesion. This, in turn, does not result in lack of convergence, but rather produces complete unloading.

Such problems do not occur with the cylindrical arc-length method because the control parameter is represented by the norm of the increment of the whole displacement vector, that is the vector including all the degrees of freedom of the f.e. model. On the other hand, as already observed in Remark 4.1, spurious unloading can occur with the cylindrical arc-length method. Furthermore, the cylindrical arc-length algorithm is not always robust and often convergence in our analyses was obtained after a careful and time-consuming tuning of the algorithm parameters such as maximum allowed increment length, maximum allowed number of increment reductions, desired number of iterations [66]. For example, in correspondence of the final point in the load-displacement curve reported in Figure 6.11.b, convergence was not achieved even after many reductions in the increment length so that the analysis was terminated, although delamination had not yet completely propagated along the entire interface.

■

Concrete in plane stress

The analysis carried out in plane strain have been repeated using plane stress elements for the concrete. Only an eccentricity $e = 0.6$ has been considered.

The results show little variation between the two cases, with a better prediction of the ultimate load in the plane stress case.

The number of comparisons carried out does not allow, in the opinion of the author, to establish with certainty that the plane stress model is the most appropriate one, even though the specific results obtained seem to slightly suggest so. We remind the reader that the links have not been considered specifically and that the plane strain model allows for confinement against strains in the out of plane direction due to their presence. This constraint cannot be imposed in any manner, in the two dimensional case, using plane stress elements. For pronounced plastic strains in the compressive area the effect of this confinement is known to be significant for concrete and can be well captured by the Menetrey Willam concrete model. The adoption of the plane stress hypothesis, then, results in lack of exploitation of the potential of the material implemented. It is recognised that the beneficial effects of confinement would be overestimated in plane strain. Also the use of an associated flow rule, as explained in Chapter3 would lead to overestimation of the passive confinement for the links. This effect could be mitigated using fictitious values for the elastic modulus E and the Poisson ratio ν . This route was attempted but the variation observed in the results did not permit to draw any conclusion and therefore the strategy is not discussed further.

However, as it is evident from Figure 6.12, the plane stress model performed much better in terms of numerical convergence. This is clearly seen in Figures 6.12 and 6.13, in which the results for the beam retrofitted with S-type FRP (SB) are reported in terms of stress displacement curves. We see that in the plane stress case the analysis can carry on even after the complete debonding of the FRP. It is interesting to note that the residual capacity of the beam after FRP debonding corresponds to the capacity of the control beam (CB). This is not necessarily the case in reality, because, as higher compressive stresses are attained in the concrete during the loading history, damage to the concrete in compression can significantly reduce the residual capacity. The different crack pattern of the retrofitted beam, compared to the control beam, can also have an effect. The results presented, however, are consistent with the characteristics of the model. In fact, softening of the concrete in compression is not allowed in the model adopted and the crack pattern of the retrofitted and non retrofitted beams are preset and are the same. The consistency of the results yielded with the basic characteristics of the model, adds reliability the finite element solution. Actually they suggest that the numerical solution of the problem as formulated is correct.

The formulation may or may not be fairly representative of the real behaviour but some difference between reality and model is obviously to be accepted.

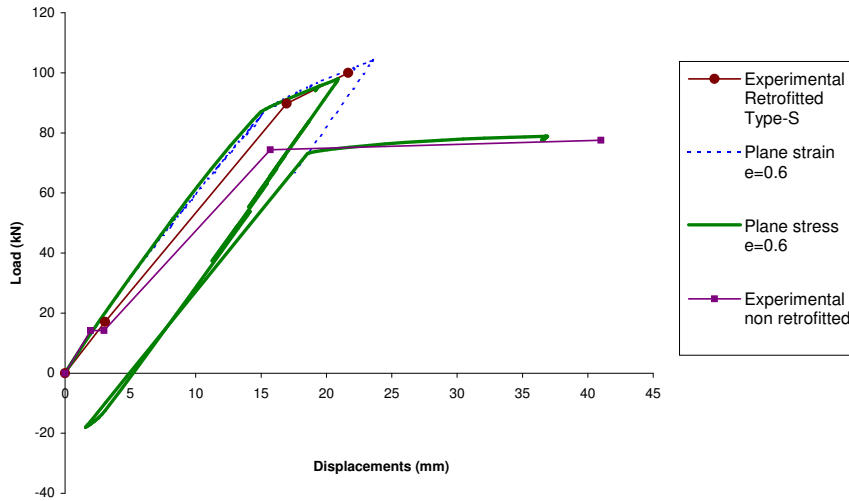


Figure 6.12: Load-Displacement curves for the S-Type retrofitted beam; experimental, plane strain and plane stress.

Finally the interfacial stresses at different load levels are reported in Figure 6.14 as for the plane stress case. We see that the pattern of the stresses is the same as for the plane strain case, as is the debonding mechanism.

6.2.3 Three-dimensional Finite-element models

Full three dimensional models have also been set up. These models have been analysed for the following reasons:

- investigation of the limitations of the two dimensional models as to the results obtainable with these models
- investigation of the limitations of the two dimensional models as to the results not obtainable with these models
- observation of the behaviour of RC beams retrofitted with FRP in three dimension

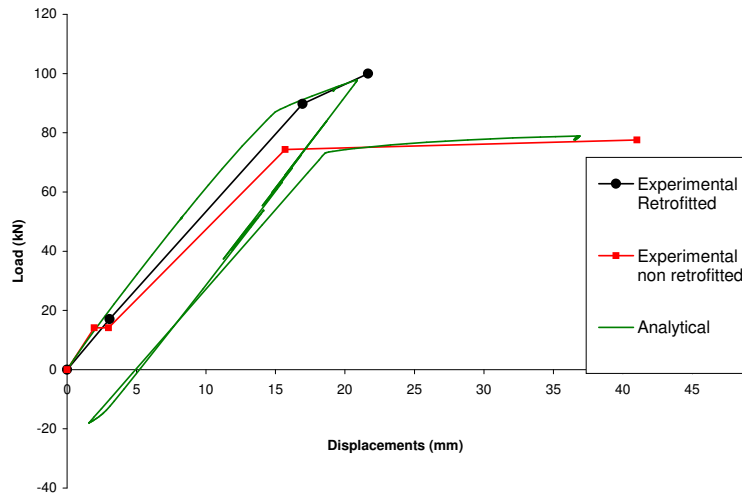


Figure 6.13: Load-Displacement curves for the S-Type retrofitted beam; experimental retrofitted, experimental control beam and plane stress.

- demonstration of the utility of three dimensional finite element models for the integration of experimental results

The results presented in this section are intended to be mainly demonstrative of the potential of the method as its use is at an early stage. Results on the retrofitted beams refer to S-Type beams.

Surly, three dimensional models provide a great wealth of useful data, and all the results are directly related to real quantities. Interface stresses, for instance, are the real local interface stress, and not their resultant over the perimeter of the reinforcement. Also normal stresses are not averaged values along the breadth of the beam but the real local values. As for the distribution of the forces within the volume, not only they can be calculated in detail, but they can also be presented in a convenient graphical format for an easy interpretation (see Figures 6.16 to 6.19). Note that also the input parameters for material and interfaces models are the real parameters as known from the appropriate tests and no manipulation is required.

The basic configuration of the three dimensional model generated is given in Figure 6.15. Only one quarter of the model needs to be represented due to

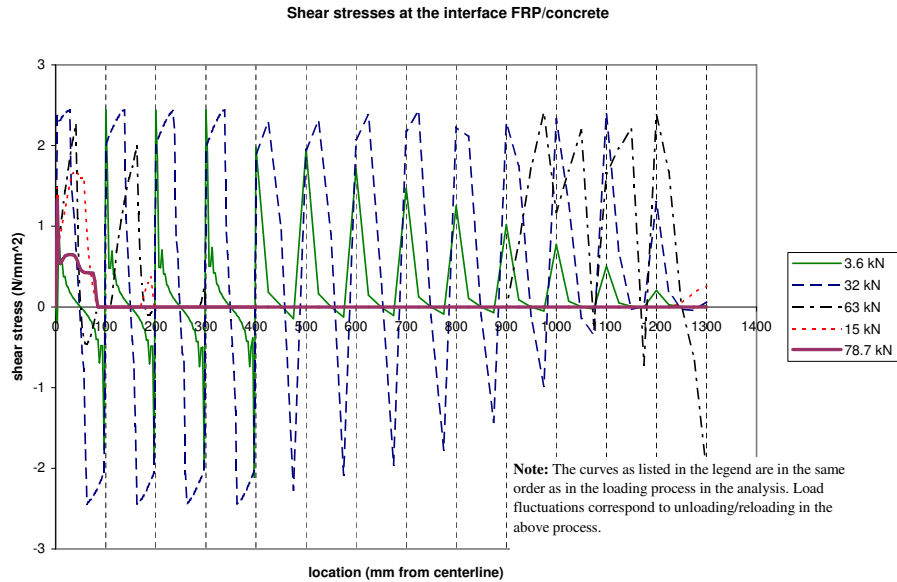


Figure 6.14: Shear stresses at the FRP/concrete interface and Delamination process.

double symmetry conditions. Note that this time the tilt in the shear cracks as we approach the supports has been introduced in the model. Hexahedral 20 node elements have been used for all concrete, FRP and steel, while three dimensional interface elements have been used to connect the different materials together.

Steel has been modelled as usual as elastic perfectly plastic, with yielding governed by Henky-Von Mises criterion. FRP is linear elastic up to failure. The Menetrey Willam model for concrete, although available for the three dimensional case since the early stages of the research carried out, has not been used in these models and concrete is considered linear elastic and infinitely strong. This is because the computational time required for these models is considerable and at this early stage of their exploration the linear elastic assumption has been thought to be an acceptable approximation, since preset cracks are introduced (failure in tension is not expected in analysis domain inclusive of cracks) and the plastic behaviour of concrete in compression has a less distinct impact on the results. Actually computational time, along with practical difficulties in the model generation, is the main drawback of

these models that have generally discouraged their extensive use.

Some of the interesting advantages of using three dimensional models are the automatic inclusion of effects related to the flexural action on the reinforcing bars, that results in non uniform stresses across their section (see Figure 6.17), the explicit representation of the dowel effects and of the contact stresses between concrete and steel, the non uniform transversal distribution of stresses in the FRP yielded by these models and the possibility of investigation of the influence of the ratio b_f/b between the breadth of the beam and that of the retrofit plate, known to be highly influential on the interface properties.

In the last Figure (6.20) we report the load displacement curves for the three dimensional models for the control beam (CB) and an S-Type retrofitted beam. The curves are compared with the experimental ones and those obtained with the two dimensional models. The effect of assuming the concrete as linear elastic infinitely strong is evident. The load displacement curve, in fact, shows an apparent hardening after failure of steel. This expresses, actually, the stiffness of the unreinforced elastic concrete. Obviously the load can be increased at will as failure is not possible. The sharp elbow observed in the two dimensional case at yielding of steel are not visible in the curves related to the three dimensional models. This is due to the use of a large step increment resulting in a graph not including the points in the vicinity of the elbow and is only an apparent effect. The calculated displacements have been bulleted to highlight this.

6.3 Conclusions

From the inspection of the results presented in this section the following conclusive remarks can be drawn:

- the proposed nonlinear numerical model of RC beams retrofitted with FRP in flexure is capable of capturing many important aspects of the behaviour of these structural systems, up to failure;
- delamination failure can be well predicted by the model;
- cracking plays a key role in the development of the stresses at the FRP/concrete interface and often determines the onset of delamination;
- bond-slip between concrete and steel rebars is to be taken into account in order to get accurate results;

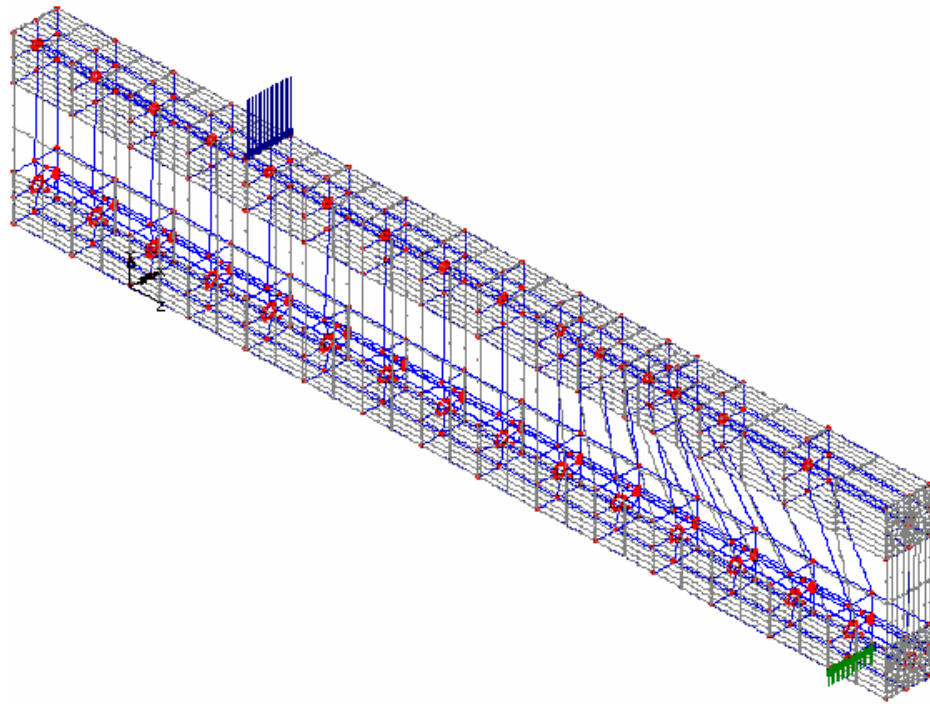


Figure 6.15: RC beam: geometry and loading.

- Crisfield's cylindrical arc-length method performs better than the local-control arc-length algorithm recently developed in [5].

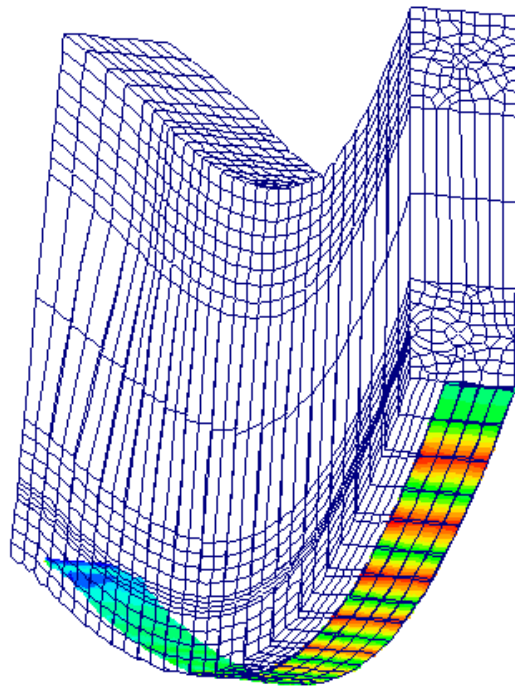


Figure 6.16: Contour diagram of normal stresses in the FRP plate.

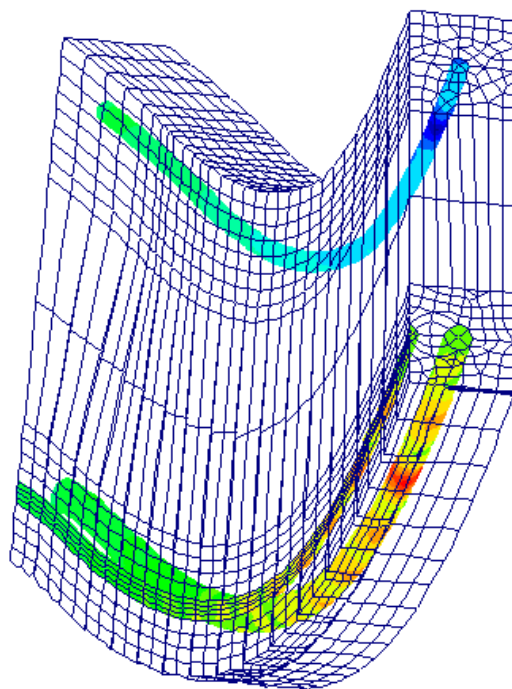


Figure 6.17: Contour diagram of normal stresses in the steel bars.

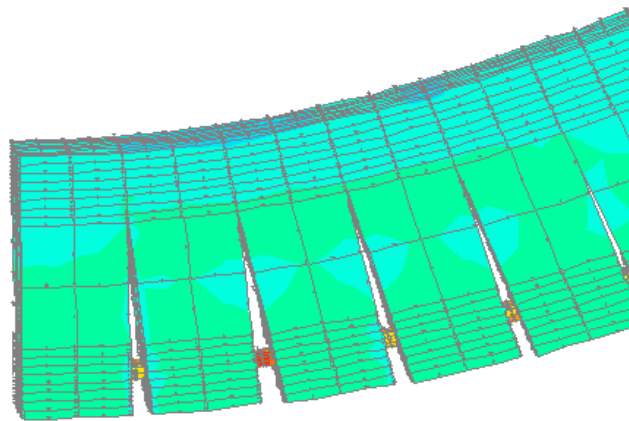


Figure 6.18: Contour diagram of normal stresses on deformed mesh showing cracks and steel bond slip.

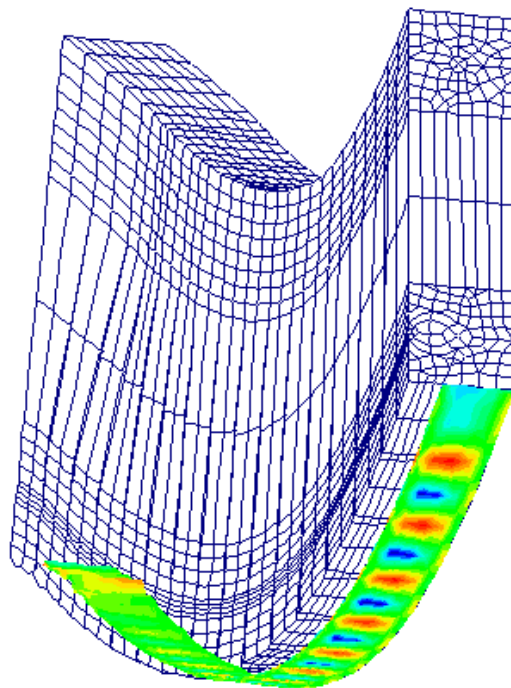


Figure 6.19: Contour diagram of normal stresses in the FRP plate in the transversal direction.

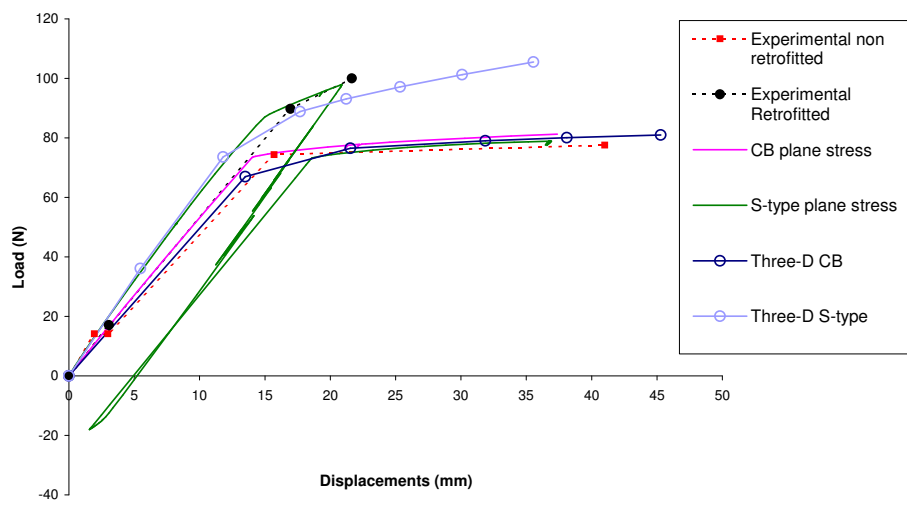


Figure 6.20: Load-Displacement curves; experimental, two dimensional and three dimensional comparison

Conclusive remarks

- An elasto-plastic material model featuring isotropic and kinematic hardening, with yield function of Menetrey Willam has been implemented for use in the finite element program LUSAS. The model has been implemented for the three dimensional case, for use in plane strain problems and for use in plane stress problems.
- Failure modes typical of RC beams retrofitted with FRP are associated with the mechanisms of force transfer between concrete and FRP.
- The above force transfer can be modelled by introducing an interface characterized by an appropriate constitutive law.
- This can be effectively done within the framework of the finite element method and has led to results in good accordance with experimental ones.
- RC beams retrofitted with FRP are structures highly sensitive to cracking of concrete. A discrete crack model should be used to predict the local stress concentrations in the FRP/concrete interface at crack mouths and consequently the correct mechanism of debonding between the two materials.
- The use of preset localized cracks in association with an appropriate bond slip model for steel reinforcement and an appropriate stress slip model for FRP reinforcement proved to be the most effective strategy.
- Three dimensional models can clarify the importance of out of plane components of stress and strains and of uneven distribution of stresses along the breadth of the beam. In particular the influence of the ratio breadth of the beam to breadth of the retrofit plate b/b_f on the bond performance can be investigated.

Bibliography

- [1] J.E.H. Argyris, G. Faust , K.J. Willam, Limit load analysis of thick walled concrete structures - A Finite Element approach structure, *Computer Methods in Applied Mechanics and Engineering*, Vol. 8, North Holland, Co. 1976, pp. 215-243.
- [2] G. Alfano and L. Rosati. A general approach to the evaluation of consistent tangent operators for rate-independent elastoplasticity, *Computer Methods in Applied Mechanics and Engineering*,167(1):75–89, 1998.
- [3] G. Alfano, F. De Angelis, L. Rosati. Closed-form solution of the finite-step constitutive problem in plane elasto/visco-plasticity, *Computer Methods in Applied Mechanics and Engineering, Proc. of ECCM99, Munchen*,Wunderlich KJ. (ed) Elsevier, 1999.
- [4] G. Alfano and M.A. Crisfield. Finite element interface models for the delamination analysis of laminated composites: mechanical and computational issues. *International Journal for Numerical Methods in Engineering*, 50(7):1701–1736, 2001.
- [5] G. Alfano and M.A. Crisfield. Solution strategies for the delamination analysis based on a combination of local-control arc length and line searches. *International Journal for Numerical Methods in Engineering*, 58(7):999–1048, 2003.
- [6] G. Alfano, L. Rosati, and G. Simonelli. Numerical analysis of RC beams retrofitted with FRP strips, ECCOMAS 2004, Jyvskyl, July 2004.
- [7] G. Alfano, L. Rosati, and G. Simonelli. Finite element modelling of the flexural behaviour of RC beams strengthened with FRP. Submitted to ASCE.
- [8] O. Allix, P. Ladveze, and A. Corigliano. Damage analysis of interlaminar fracture specimens. *Composite Structures*, 31(1):61–74, 1995.

- [9] O. Allix and A. Corigliano. Modeling and simulation of crack propagation in mixed-modes interlaminar fracture specimens. *International Journal of Fracture*, 77:111–140, 1996.
- [10] O. Allix and A. Corigliano. Geometrical and interfacial non-linearities in the analysis of delamination in composites. *International Journal of Solids and Structures*, 36(15):2189–2216, 1999.
- [11] G. Bolzon and A. Corigliano. A discrete formulation for elastic solids with damaging interfaces. *Computer Methods in Applied Mechanics and Engineering*, 140:329–359, 1997.
- [12] O. Buyukozturk and B. Hearing. Failure behaviour of precracked concrete beams retrofitted with FRP. *Journal of Composites for Construction*, 2(3):138–144, 1998.
- [13] M.L. Boas. *Mathematical Methods in the Physical Sciences*. Courier Companies, U.S.A. , 1983
- [14] F. Barzegar , Layering of RC membrane and plate elements in non linear analysis, em *Journal of Structural Engineering*, ASCE, Vol. 114, No 11, pp. 2474-92, 1988.
- [15] Z.P. Bazant, L. Cedolin. Fracture mechanics of reinforced concrete, *Journal of the Engineering Mechanics*, ASCE, Vol.106, No.EM6, pp.1287-1306,1980.
- [16] Z.P. Bazant, L. Cedolin. Finite element modelling of crack band propagation, *Journal of Structural engineering*, ASCE, Vol.109, No.1, pp.69-93,1983.
- [17] Z.P. Bazant, B.H. Oh. Crack band theory for fracture concrete, *Materials and structures*, RILEM, Paris, Vol.16, pp.155-176,1983.
- [18] Z.P. Bazant, J. Ozbolt. Nonlocal Microplane Model for Fracture, Damage, and Size Effect in Structures, *Journal of Engineering Mechanics*, ASCE, Vol.116, No.11.
- [19] T. , Goangseup Z. , Chen H. , Jingxiao X. , The extended FEM for static and dynamic problems, ECCOMAS 2004, Jyvskyl, July 2004.
- [20] E.J. Barbero, R. Luciano, and E. Sacco. Three-dimensional plate and contact/friction elements for laminated composite joints. *Computers & Structures*, 54(4):689–703, 1995.

- [21] C. Bedard, M.D. Kotsovos Fracture process of concrete for NLFEA methods, *Journal of Structural Engineering*, ASCE, Vol.112, No.3, pp573-587
- [22] W.F. Chen and A.F. Saleeb. *Constitutive equations for engineering materials*. Wiley, New York, 1992.
- [23] V. Comincioli *Analisi Numerica McGraw-Hill*, Milano, 1995.
- [24] L. Corradi Dell' acqua *Meccanica delle strutture, Mc Graw-Hill* , Milano, 1992.
- [25] R. Baldacci , G. Ceradini , E. Giancreco. *Plasticita' CISIA*, Milano, 1974.
- [26] M.A. Crisfield, Acceleration Solution Techniques and Concrete Cracking, *Computer Methods in Applied Mechanics and Engineering* , Vol.33, pp.585-607, 1982.
- [27] M.A. Crisfield. A fast incremental/iterative solution procedure that handles "snap-through". *Computers & Structures*, 13:55–62, 1981.
- [28] A. Corigliano. Formulation, identification and use of interface models in the numerical analysis of composite delamination. *International Journal of Solids and Structures*, 30(20):2779–2811, 1993.
- [29] A. Corigliano and M. Ricci. Rate-dependent interface models: formulation and numerical applications. *International Journal of Solids and Structures*, 38(4):547–576, 2001.
- [30] N. Chandra, H. Li, C. Shet, and H. Ghonem. Some issues in the application of cohesive zone models for metal-ceramic interfaces. *International Journal of Solids and Structures*, 39(10):2827–2855, 2002.
- [31] L. Champaney and N. Valoroso. Evaluation of interface models for the analysis of non-linear behaviour of adhesively bonded joints. In A. Mota Soares and al., editors, *Proceedings of the European Conference on Computational Mechanics ECCM-2001*, Cracow, Poland, 2001.
- [32] J.L. Chaboche, R. Girard, and A. Schaff. Numerical analysis of composite systems by using interphase/interface models. *Computational Mechanics*, 20:3–11, 1997.

- [33] Istruzioni per la Progettazione, l'Esecuzione e il Controllo di Interventi di Consolidamento Statico mediante l'utilizzo di Compositi Fibrorinforzati,, *CNR-DT 200/2004*, Consiglio Nazionale Delle Ricerche, 2004.
- [34] Design guidance for strengthening concrete structures using fiber composite materials *Concrete Society Technical Report No. 55*, The Concrete Society, 2000
- [35] R. DeBorst, P. Nauta. Non-orthogonal cracks in a smeared finite element model, *Engineering Computations*, Vol.2, pp 35-46, 1985.
- [36] R. DeBorst, The zero-normal-stress condition in plane stress and shell elastoplasticity, *Communication in Applied Numerical Method*, Vol.7, pp. 29-33, 1991.
- [37] R.J. Dodds, Numerical techniques for plasticity computations in finite element analysis, *Computers & Structures* ,Vol 26, pp. 767-779, 1991.
- [38] Del Piero G., Some properties of the set of fourth-order tensors with applications to elasticity, *J. Elasticity* ,Vol 3, pp. 245-261, 1979.
- [39] G. Etse , R.L. Willam, Fracture energy formulation for inelastic behaviour of plain concrete, *International journal for numerical methods in engineering* ,Vol 120 No 9 1983-2011, 1994.
- [40] H. Floegl, H. Mang, Tension stiffening concept based on bond slip , *Journal of Structural Division* , ASCE, Vol. 108, No.ST12, pp. 2681-701, 1982.
- [41] D. Ferretti and M. Savoia. Non-linear model for R/C tensile members strengthened by FRP-plates. *Engineering Fracture Mechanics*, 70:1069–1083, 2003.
- [42] P. Fuschi , M. Dutko, D. Peric, DRJ. Owen, On numerical integration of the five parameter model for concrete, *Computers & Structures* ,Vol 53, pp. 825-838, 1994.
- [43] P. Fuschi , D. Peric, DRJ. Owen, Studies on generalized midpoint integration in rate-independent plasticity with reference to plane stress J2-flow theory, *Computers & Structures* ,Vol 53, pp. 825-838, 1994.
- [44] M. E. Gurtin An introduction to continuum Mechanics, *Academic Press inc.*, San Diego California, 1981.

- [45] A. Brencich, L. Gambarotta. Isotropic damage model with different tensile-compressive response for brittle materials, *International J. of Solids and Structures*, 38, pp 5865-5892, 2001.
- [46] P. Grassl, Modelling of dilation of concrete and its effects in triaxial compression. *Finite Elements in Analysis and Design* , Vol. 40, pp. 1021-1033, Elsevier, 2004.
- [47] T.J.R. Hughes, M. Cohen, M. Haroun, Reduced and selected integration techniques in the Finite Element Analysis of plates, *Nuclear Engineering and Design* , Vol. 46, No1, pp. 203-22, 1978.
- [48] E. Hoek, E.T. Brown , Empirical strength criterion for rock masses, *Journal of the Geotechnical Engineering Division* , V106, No GT9, pp. 1013-1035, 1980.
- [49] Han W., Reddy B.D., *Plasticity: Mathematical Theory and Numerical Analysis*, Springer, New York, 1999.
- [50] H.B. Hellweg and M.A. Crisfield. A new arc-length method for handling sharp snap-backs. *Computers & Structures*, 66(5):705–709, 1998.
- [51] M. Jirasek, B. Patzack Models for quasibrittle failure: Theoretical and computational aspects, ECCM-2001, Cracow,2001.
- [52] M. Jirasek, Z.P. Bazant, *Inelastic Analysis of Structures*, John Wiley & Sons, England, 2002.
- [53] M. Jirasek, T. Zimmermann, Embedded crack model: I. Basic formulation, em *International Journal for Numerical Methods in Engineering*, 50: 1269-1290, 2001.
- [54] M. Jirasek, T. Zimmermann, Embedded crack model: II. Combination with smeared crack, em *International Journal for Numerical Methods in Engineering*, 50: 1291-1305, 2001.
- [55] K.R. Jaafar, Bond in reinforced concrete, Dissertation submitted for the degree of MPhil., University of Cambridge, 2000.
- [56] K.R. Jaafar., *Bond in reinforced concrete*. Churchill College, Cambridge, 2000. M. Phil. Dissertation.
- [57] Klaus-Jurgen Bathe, *Finite Element Procedures* *Prentice-Hall,Inc.*, Englewood Cliffs, New Jersey, USA.

- [58] J. Kolleger, G. Mehlhorn., Material Model for Cracked Reinforced Concrete, IABSE Colloquim on Computational Mechanics of Concrete Structures, Delft, 1987. Report No. 54, pp 63-74.
- [59] J. Kolleger, G. Mehlhorn., Material model for the analysis of reinforced concrete surface structures, Computational Mechanics, 6:341-357, 1990.
- [60] H.G. Kwak, F.C. Filippou., Finite element analysis of reinforced structures under monotonic loads, Structural engineering mechanics and materials, Report No. UCB/SEMM-90/14, Berkeley,1990.
- [61] M. Keuser, G. Mehlhorn., Finite element models for bond problems, Journal of structural engineering, ASCE, Vol.113, No. 10, pp.2160-2173,1987.
- [62] H. Kupfer, H.K. Hilsdorf and H. Rush., Behaviour of concrete under biaxial stresses, ACI Journal, Vol.66, No. 66-62, pp.656-666,1969.
- [63] J. Lemaitre, J.L. Chaboche., Mechanics of solid materials, Cambridge University Press, 1994.
- [64] Lee SW., JW. Yoon, DJ. Yang, A stress integration algorithm for plane stress elasto-plasticity and its application to explicit finite element analysis, Computers & Structures ,Vol 53, pp. 301-311, 1994.
- [65] Y.C. Loo, Y. Yang, Cracking and failure analysis of masonry arch bridges, em Journal of Structural Engineering, ASCE, vol.117, No.6, 1991.
- [66] FEA Ltd. *LUSAS - User Manual*. Kingston-upon-Thames, UK, 1999.
- [67] X.Z. Lu, L.P. Ye, J.G. Teng., J.J. Jiang, Meso-scale finite element model for FRP sheets/plates bonded to concrete. *Engineering Structures*, Vol. 27, pp. 564-575, Elsevier, 2005.
- [68] P. Menetrey and K. Willam., Triaxial failure criterion and its generalization. *ACI Structural Journal*, 92(3):311-317, 1995.
- [69] A. Matzenmiller, R.L. Taylor, A return mapping algorithm for isotropic elastoplasticity, International journal for numerical methods in engineering ,Vol 37, 813-826, 1994.

- [70] Y. Mi, M.A. Crisfield, H.B. Hellweg, and G.A.O. Davies. Finite element method and progressive failure modelling of composite structures. In D.R.J. Owen and et al., editors, *Computational plasticity: Fundamentals and Applications. Part 1*, pages 239–254, Barcelona, 1997. CIMNE.
- [71] Y. Mi, M.A. Crisfield, G.A.O. Davies, and H.B. Hellweg., Progressive delamination using interface elements. *Journal of Composite Materials*, 32(14):1246–1272, 1998.
- [72] Y. Mi, M.A. Crisfield, H.B. Hellweg, G.A.O. Davies, Finite Element Method and progressive failure modelling of composite structures, *DRG Owen at al. Editors*, Computational Plasticity: fundamentals and applications Part I, pp.239-245, Barcelona 1997.
- [73] K. Maekawa, A. Pimanmas, H. Okamura, Non linear mechanics of reinforced concrete, Spon press, 2003.
- [74] S.M. Mirza, J. Houde, Study of bond stress-slip relationship in RC, em *ACI Journal*, Vol.76, No.1, pp. 19-46, January 1979.
- [75] A.M. Malek, H. Saadatmanesh, M.R. Ehsani, Prediction of failure load of RC beams strengthened with FRP plate due to stress concentration at the plate end, em *ACI Structural journal*, 95, No.1, pp. 142-152, 1998.
- [76] N. Möes and T. Belytschko., Extended finite element method for cohesive crack growth. *Engineering Fracture Mechanics*, 69:813–833, 2002.
- [77] D. Meyer and H. Okamura., Finite element analysis of Reinforced Concrete Structures. *Proceedings of the US-Japan Joint Seminar on Finite Element Analysis of Reinforced Concrete*, Tokyo, 1985.
- [78] A. Millard, Numerical algorithms for plane-stress elastoplasticity: review and recommendations, In *Computational Plasticity, Proc. 4th Complas International Conference, Barcelona*, Onate E. (ed). CIMNE, 1995.
- [79] U. Neubauer, F S. Rostasy, Design aspects of concrete structures strengthened with externally bonded CFRP-plates, 1996
- [80] B. Miller, A. Nanni, L. DeLorenzis., Bond of laminates to concrete, *ACI Material J.*, Vol. 98(3), pp 246-254 2001.
- [81] A.H. Nilson, Non linear analysis of reinforced concrete by the FEM, *American Concrete Institute*, Vol. 65, pp. 747-766, September 1968.

- [82] M. Arduini,A. Nanni., Behaviour of precracked RC beams strengthened with carbon FRP sheets, *Journal of Composites for Construction*,No.2, pp 63-70, 1997.
- [83] D. Ngo, A.C. Scordelis , Finite Element Analysis of reinforced concrete beams, *Journal of American Concrete Institute* , Vol. 64, No 3,pp. 152-163, 1967.
- [84] M. Arduini,A. Nanni., Parametric study of beams with externally bonded FRP reinforcement, *ACI structural Journal*,No.5, pp 493-501, 1997.
- [85] M. Arduini,A. DiTommaso,A. Nanni., Brittle failure in FRP plate and sheet bonded beams, *ACI structural Journal*,No.5, pp 363-369, 1997.
- [86] A. Needleman. An analysis of tensile decohesion along an interface. *Journal of the Mechanics and Physics of Solids*, 38(3):289–324, 1990.
- [87] J. Oliver, A.E. Huespe, M.D.G. Pulido , S. Blanco, D. Linero, Recent advances in computational modelling of material failure, ECCOMAS 2004, Jyvskyl, July 2004.
- [88] J. Oliver, M. Cervera, S. Oller, J. Lubliner, Isotropic Damage Models and Smeared Crack Analysis of Concrete, Proceedings of the 2nd International Conference on Computer Aided Analysis and Design of Concrete Structures, Vol.2, BICANIC MANG.
- [89] D.W. Phillips , O.C. Zienkiewicz, Finite Element non linear Analysis of concrete structures, Proceedings of the Institution of Civil Engineers, Part. 2, Vol.61, pp. 59-88, 1967.
- [90] V. Palazzo, L. Rosati , N. Valoroso, Solution procedures for J3 plasticity and viscoplasticity, *Computational methods Appl. Mech. Engrg.*,191, 903-939, Elsevier 2001.
- [91] H. Parisch, A critical survey of the 9 node degenerated shell element with special emphasis on thin shell application and reduced integration , *Computer methods in applied mechanics and engineering*, Vol. 20 No. 3, pp. 1545-1557, 1985.
- [92] H. Rahimi and A. Hutchinson., Concrete beams strengthened with externally bonded FRP plates. *Journal of Composites for Construction*, 5(1):44–56, 2001.

- [93] G. Romano, *Scienza delle Costruzioni*, Vols. I e II, *Hevelius*, Benevento, 2003
- [94] J.N. Reddy, *An Introduction to The Finite Element Method*, *McGraw-Hill International Edition*, Singapore, 1993.
- [95] L. Rosati and Valoroso N., Recent advancements in J3 elastoplasticity ECCM-2001, Cracow, Jun 26-29, 2001.
- [96] L. Rosati and Valoroso N., Direct derivation of the plane stress elastoplastic constitutive algorithm from the three-dimensional one - part1: theoretical formulation, Dipartimento di Scienza delle costruzioni Università di Napoli Federico II, 2003 .
- [97] L. Rosati and Valoroso N., Direct derivation of the plane stress elastoplastic constitutive algorithm from the three-dimensional one - part2: computational issues, Dipartimento di Scienza delle costruzioni Università di Napoli Federico II, 2003 .
- [98] L. Rosati and Valoroso N., A return map algorithm for general isotropic elasto/visco-plastic materials in principal space. *International Journal for Numerical Methods in Engineering*, 2004 In press.
- [99] M. Romano, On Leon's Criterion, *Meccanica*, pp. 48-67, 1969.
- [100] Russo, Romano, Cracking response of R-C members subjected to uniaxial tension, em *ASCE Journal of Structural Engineering*, 118(5), pp.1172-1190.
- [101] H.A. Rasheed and S. Pervaiz., Bond slip analysis of fiber-reinforced polymer-strengthened beams. *Journal of Engineering Mechanics - ASCE*, 128(1):78-86, 2002.
- [102] J.G. Rots, D. Ngo and P.Kuster., Smearred crack approach and fracture localization in concrete. *Journal of Engineering Mechanics - ASCE*, 128(1):78-86, 2002.
- [103] Ritto-Correa M., Camotim D., Integration algorithm for J2 elastoplasticity uder arbitrary mixed stress-strain control, *International Journal for Numerica Methods in Engineering*, 50: 1213-1232, 2001.
- [104] Y.R. Rashid, Analysis of prestressed concrete pressure vessels *Nuclear Engineering and Design*, Vol.7, No.4, pp 334-344, 1968

- [105] M. Savoia, B. Ferracuti, C. Mazzotti, Non-linear bond-slip law for FRP-Concrete interface, Structural Engineering Department, University of Bologna, Italy, 2002 .
- [106] W.M. Sebastian., Significance of midspan debonding failure in FRP-plated concrete beams. *HERON*, Vol. 30, No.1, pp. 3-48, 1985.
- [107] A.C. Scordelis, D. Ngo , H.A. Franklin, Finite Element Study of reinforced concrete beams with diagonal tension cracks, Proceedings of Symposium on shear in reinforced concrete, ACI Publication sp-42, 1974.
- [108] M. Suidam , W.C. Schnobrich, Finite Element Analysis of Reinforced concrete, *Journal of the Structural Division ASCE* , Vol. 99, No ST10, pp. 2109-2122, October 1973.
- [109] S. Somayaji , S.P. Shah, Bond stress versus slip relationship and cracking response of tension members, *ACI Journal* , Vol. 78, No. 3, pp. 217-25, May-June 1981.
- [110] G. Alfano, L. Rosati, and G. Simonelli., Modelling of failure mechanisms in RC beams retrofitted with FRP in flexure, *COMPLAS VIII*, Barcelona, 2005.
- [111] P. Soroushian, K. Choi, and A. Alhamad., Dynamic constitutive behaviour of concrete. *ACI Structural Journal*, 83(2):251–258, 1986.
- [112] S.T. Smith, J.G. Teng, Shear-bending interaction in debonding failure of FRP-plate RC beams, em *Advances in Structural Engineering*, 6, No. 3, 2004.
- [113] Simo JC., Taylor RL., A return map algorithm for plane stress elasto-plasticity, *International Journal for Numerical Methods in Engineering*, 22: 649-670, 1986.
- [114] Simo JC., Govindjee S., Exact close form solution of the return map algorithm for the plane stress elasto-viscoplasticity, *Engineering Computations*, 5: 254-258, 1988.
- [115] Simo JC., Hughe TJR., *Computational Inelasticity*, Springer-Verlag, New York 1998.
- [116] J.C.J. Schellekens and R. de Borst. A non-linear finite element approach for the analysis of mode-*I* free edge delamination in composites. *International Journal of Solids and Structures*, 30(9):1239–1253, 1993.

- [117] J.C.J. Schellekens and R. de Borst. On the numerical integration of interface elements. *International Journal of Solids and Structures*, 36:43–66, 1993.
- [118] N. Point and E. Sacco. A delamination model for laminated composites. *International Journal of Solids and Structures*, 33(4):483–509, 1996.
- [119] S. Tsuchiya, N. Fukuura, K. Maekawa, Dynamic response of R-C piers applied with multidirectional forces using 3D FEM analysis based on fiber model, Proceedings of the Repetition Deterioration Phenomena in the Plasticity Range Symposium, GCI, pp. 359-68, 1998.
- [120] J.G. Teng, W.C. Zhu, C.A. Tang., Mesomechanical model for concrete. Part I: model development, *Magazine of Concrete Research*, Vol.56, No.6, pp 313-330, 2004.
- [121] J.G. Teng, W.C. Zhu, C.A. Tang., Mesomechanical model for concrete. Part II: applications, *Magazine of Concrete Research*, Vol.56, No.6, pp 331-345, 2004.
- [122] V. Tvergaard and J.W. Hutchinson. The relation between crack growth resistance and fracture process parameters in elastic-plastic solids. *Journal of the Mechanics and Physics of Solids*, 40(6):1377–1397, 1992.
- [123] V. Tvergaard and J.W. Hutchinson. The influence of plasticity on mixed mode interface toughness. *Journal of the Mechanics and Physics of Solids*, 41(6):1119–1135, 1993.
- [124] F. Vecchio, M.P. Collins., The response of reinforced concrete to in plane shear and normal stress, Publication N. 82-03, Department of civil engineering, University of Toronto, 1982.
- [125] F. Vecchio, M.P. Collins., The modified compression field theory for reinforced concrete elements subjected to shear, *ACI Struct. J.*, Vol.3(4), pp219-31, 1986.
- [126] R.G. Selby, F. Vecchio, M.P. Collins., Analysis of reinforced concrete elements subject to shear and axial compression, *ACI Struct. J.*, Vol.93, No. 3, pp. 572-582, 1996.
- [127] K.J. Volokh., Comparison between cohesive zone models, *Communications in Numerical Methods in Engineering*, 2004.

- [128] N. Valoroso, Theoretical aspects and computational issues in plasticity and viscoplasticity, Univerita' degli studi di Napoli Federico II, Tesi di dottorato, 1998-1999.
- [129] M.S. Wendel., Significance of midspan debonding failure in FRP-plated concrete beams. *Journal of Structural Engineering - ASCE*, 127(7):792–798, 2001
- [130] R.G. Wight, M.F. Green, and M.A. Erki., Prestressed FRP sheets for post strengthening reinforced concrete beams. *Journal of Composites for Construction*, 5(4):214–220, 2001.
- [131] T.W. White, K.A. Soudki, and M. Erki., Response of RC beams with CFRP laminates and subjected to a high rate of loading. *Journal of Composites for Construction*, 5(3):153–162, 2001.
- [132] K.J. Willam, E.P. Warnke, Constitutive models for triaxial behaviour of concrete, *Int. Ass. for Bridge and Struct. Engng.*, Seminar on concrete structures subjected to triaxial stresses, Paper III-01, pp. 1-30, Bergamo (Italy), 1974.
- [133] G.N. Wells and L.J. Sluys., A new method for modelling cohesive cracks using finite elements. *International Journal for Numerical Methods in Engineering*, 50(12):2667–2682, 2001.
- [134] Z. Wu, J. Yin., Fracturing behaviours of FRP-strengthened concrete structures. *Engineering Fracture Mechanics*, Vol. 70, pp. 1339-1355, Elsevier, 2003.
- [135] J. Yang, J.G. Teng, J.F. Chen, Interfacial stresses in soffit plated reinforced concrete beams, *Proceedings of the Institution of Civil Engineers*, ICE, Vol. 157, pp. 77-89, 2004.
- [136] H. Yoshikawa, T. Tanabe , An analytical analysis for tension stiffness of R-C members, em Trans. of the Japan Concrete Institute, Vol. 8, pp. 473-80, 1986.
- [137] J. Yang, J.G. Teng, and J.F. Chen. Interfacial stresses in soffit-plated reinforced concrete beams. *Proceedings of ICE - Structures and Buildings*, 157(3):77–89, 2004.
- [138] H. Yuan, J.G. Teng., R. Seracino, Z.S. Wu, J. Yao, Full-range behaviour of FRP-to-concrete bonded joints, *Engineering Structures*, Vol. 26, pp. 553-565, Elsevier, 2004.